I. Molecular Simulations of Buckyball Fullerenes

II. Quantum Chemistry Studies on High-T_c Superconductors

Thesis by

Yuejin Guo

In Partial Fulfillment of the Requirements

for the Degree of

Doctor of Philosophy

California Institute of Technology

Pasadena, California

1992

(Submitted May 7, 1992)

To Zezhong and little Audrey

Acknowledgments

I would like to acknowledge many people who have made my stay at Caltech enjoyable and educational.

First, I must thank Bill Goddard for providing me with an opportunity to work in his group. I have benefited greatly from his vast chemistry, physics, and materials science acknowledge and intuition, of course including his computer programming. Because of his constant encouragement and support I have had the chance to explore many exciting projects. These have made my life at Caltech truly unforgettable.

I also thank the past and present WAG group members for their help and friendship. I am grateful to Naoki Karasawa for offering me so much help when I started the molecular simulation program. I would like to thank Guanhua Chen in particular for being a collaborator as well as a good friend. I also want to thank Jean-Marc Langlois for invaluable collaboration on High-Tc project. Also I would like to thank Siddharth Dasgupta for correcting many program bugs. Many thanks go to Kian-Tat Lim, Alan Mathiowetz, Terry Coley and Richard Müller for their patient help to use computer facilities. I owe special thanks to Ann Miller, Charles Musgrave, Kevin Plaxco and Jason Perry for their friendship.

Finally, my greatest debt is certainly to my family, whose continual support and love have made this work possible. I especially thank my wife, Zezhong, for her constant support and inspiration during the course of this work.

Abstract

Part I. In order to interpret and predict the unusual chemical and physical properties of the C_{60} and related fullerenes, fullerites, and molecular/solid state derivatives, we started with the graphite force field (GraFF) developed for sp^2 carbon centers (based on fitting experimental lattice parameters, elastic constants, phonon frequencies for graphite and alkali-intercalated graphite), and successfully predicted vibrational frequencies, fullerite and alkali-doped fullerite crystal structure, density, heat of sublimation, and compressibility, *etc.*, for C_{60}, C_{70} and their derivatives. We also developed a highly accurate force field for C_{60} in excellent agreement with all 14 experimental frequencies within abs error 3.0 cm^{-1}.

Part II. We have applied ab initio electronic methods (GVB and CI) to various clusters representing La_2CuO_4, Nd_2CuO_4, $YBa_2Cu_3O_7$, and Bi and Tl containing high-Tc materials to study their basic electronic structure and magnetic interaction. Particularly, we develop the GVB superexchange CI (GVB – X – CI) method to study the superexchange coupling interaction. Using this method, we can calculate the J_{dd} from the first principle at about the same accuracy as experiment.

Our results indicate that the superconductivity in Cu-O plane of these cuprates arise from a essentially magnetically induced interaction, that is, (i) all Cu have a Cu^{II} d^9 oxidation state with one unpaired spin that is coupled antiferromagnetically to the spins of adjacent Cu^{II} sites; (ii) reduction below the cupric Cu^{II} state leads to Cu^{I} d^{10} sites with a highly mobile Cu(3d) electron, and these extra electrons hop from site to site (while the oxygen remains in the O^{2-} state). The hopping of these extra electrons causes the flipping of the local spin moment of the antiferromagnetic background; (iii) oxidation beyond the cupric Cu^{II} state leads not to Cu^{III} but rather to oxidized oxygen atoms with an highly mobile Op hole, which is ferromagnetically coupled to the adjacent Cu^{II} d electrons despite

the fact that this is opposed by the direct dd exchange. This coupling induces an attractive interaction between conduction electrons that is responsible for the superconductivity

Table of Contents

Part II.
The Quantum Chemistry Studies on High Temperature Superconductors

Part I

Molecular Simulations of Buckyball Fullerenes

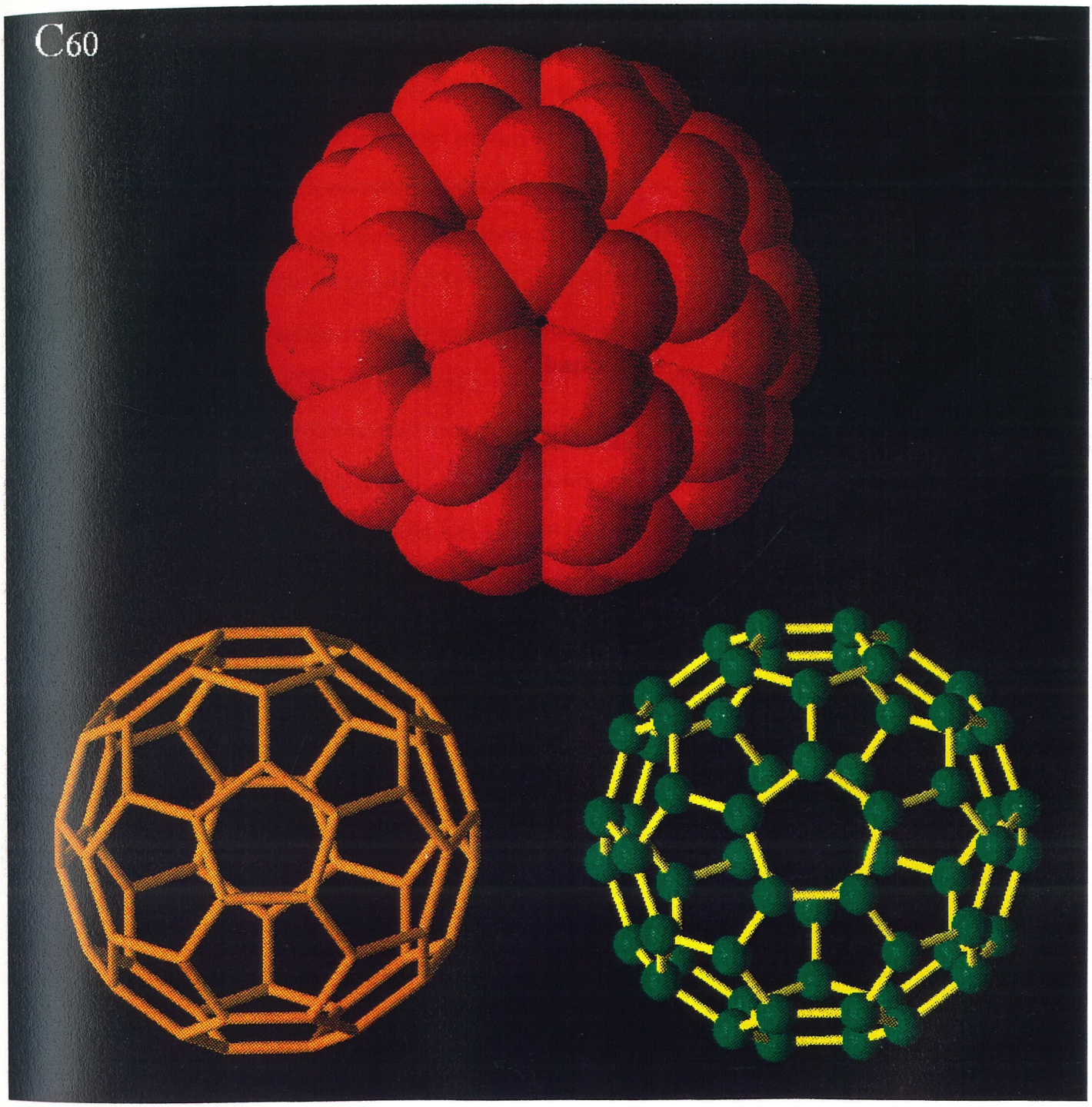
C60

Chapter 1

Introduction

Introduction

Recent breakthroughs in synthesizing macroscopic quantities of C_{60}, C_{70} and other higher fullerenes (buckyballs), the third allotropic form of carbon other than diamond and graphite, reported by Krätschmer and Huffman *et al.*[1,2] by resistive heating of graphite under an inert atmosphere, have led to much activity in characterizing structures and understanding of the physical and chemical properties of these materials and their derivatives by vibrational spectroscopy, crystal structure analysis, NMR, STM, etc..[1-4] Infrared and vibrational Raman spectra, X-ray and electron diffraction strongly support the proposal "soccerball" structure for the C_{60} cluster, and NMR spectroscopy directly confirms its icosahedral symmetry.[4] The cagelike truncated icosahedral structure of C_{60} has been firmly established. This structure was predicted in 1985 by Kroto and Smalley *et al.* to account for the exceptional stability of the C_{60} species in carbon cluster beams produced by laser vaporization of graphite.[5]

After Krätschmer and Huffman *et al.*'s report,[1] there have been a lot of expectation of their unusual chemical, electronic, optical, and tribological properties due to C_{60}'s unique structure. In just one year, many remarkable properties have been revealed one after another, for example, doped with alkali metals it becomes a superconductor second only to the high-T_c oxide superconductors,[6,7] under rapid compression it quickly converts into diamond,[8] unique nonlinear optical properties,[9] C_{60} doped with TDAE becomes an organic molecular ferromagnet at 16.1 K,[10] and chiral buckyballs.[11,12] Furthermore, these fullerene molecules have opened up new unexpected avenues in superconductivity research and an entirely new area of carbon chemistry.

In order to interpret and predict such results, we started with the graphite force field (GraFF) developed for sp^2 carbon centers (based on fitting experimental

lattice parameters, elastic constants, phonon frequencies for graphite), and successfully predicts vibrational frequencies, fullerite and alkali-doped fullerite crystal structure, density, heat of sublimation, and compressibility, *etc.*, for C_{60} and C_{70}.[13-17]

Since in the molecular simulation the force field plays a crucial role,[18] it deserves more discussions.

Molecular mechanics calculations employ an empirically derived set of equations for the Born-Oppenheimer surface whose mathematical form is familiar from classic mechanics. This set of potential functions, called the force field, contains adjustable parameters that are optimized to obtain the best fit of calculated and experimental properties of the molecules, such as geometries, conformational energies, heats of formation, vibration frequencies, or other properties. The assumption is always made in molecular mechanics that corresponding parameters and force constants may be transfered from one molecule to another. In other words, these quantities are evaluated for a set of simple compounds, and thereafter the values are fixed and can be used for other similar compounds.

Simple force field include bond stretching, angle bending, torsion, and van der Waals interactions

$$V = \sum V_{\text{stretch}} + \sum V_{\text{bend}} + \sum V_{\text{torsion}} + \sum V_{\text{vdW}} \ .$$

More elaborate force fields may also include cross-interaction terms (coupling terms, or off diagonal terms), electrostatic terms, and so on.

If we know the equilibrium position of each atom as well as the potential surface in the vicinity of each atom, then we can calculate the vibrational levels within the energy minima (i.e., the vibrational frequencies and their energies). This gives us the frequencies to be expected in the vibrational spectra (IR and Raman spectra), and it also gives us, using a Boltzmann distribution, the populations of the

various ground and excited states. We can thus find the zero-point energy, and the vibrational energy for each conformation. By mixing the conformations according to a Boltzmann distribution, we can find the heat content of the whole system. Further, it is possible to find the entropy of the substance from the populations, as it depends on the total number of occupied Boltzmann-weighted states (translation, rotation, vibration, internal rotation, plus some symmetry corrections). Finally, the thermodynamic functions, which depend on the way the populations change with temperature, can be found.

With molecular mechanics, there are a great many parameters that go into the calculation, which for any given molecule need to be known from previous studies on other molecules of that general class.

These large carbon clusters consist of graphitic hexagonal nets plus 12 pentagons which are necessary to make the net closure. In the structure and bonding sense they are very similar to the graphite, that is, the three valence electrons of each carbon atom are used to form σ bonds with its three neighbors(i.e., sp^2). This leaves one electron on each C in a π orbital. These π orbitals can then be paired in many ways, and form all possible allowed resonance structures. In effect, C_{60} is a spherical analog of graphite: one is curl up to form a finite molecule and the other is a two-dimensional infinite molecule. The idea is to develop the force field from graphite, and then it can be used for C_{60}, since the graphite system is well studied.

In the condensed phase, the interaction between the balls is only van der Waals force. Since our force field already includes this interaction which corresponds to the layer layer interaction in graphite, we would expect that the GraFF should be especially good for the condensed phase properties of C_{60} because the intermolecular interactions in graphite and C_{60} are essentially the same. This can be shown in later chapters by applying this force field to condensed phase, to understand how these balls pack together, and to predict various solid properties such

as elastic constants, cohesive energy, Young's moduli, phonon dispersion, and some thermodynamic properties.

This graphite force field also is a good starting point for the intramolecular properties. Based on the graphite force field, we also develop a force field for these fullerene molecules by introducing extra strain effects.

In this part of the thesis we present the result of our molecular mechanics simulation on the molecule and solid forms of the C_{60} and related fullerenes, fullerites, and molecular/solid state derivatives, and try to understand their unusual chemical and physical properties in gas and condensed phases.

The main content of each chapter has been summarized in the following:

Chapter 2 Molecular Properties A highly accurate force field has been developed for C_{60} in excellent agreement with all 14 experimental frequencies within abs error 3.0 cm^{-1}. If some quantum effect is included, this error can be further reduced to 1.8 cm^{-1}. This force field has also been applied to predict structural and vibrational properties of C_{70} and other fullerenes. Using the force field developed for graphite, we also study the strain energy, heat of formation, and relative stabilities between the fullerenes and graphitic sheets. Heat of formation of C_{60} has been calculated to be 659 kcal mol^{-1} or 10.99 kcal per carbon atom. We find that fullerenes are stable with respect to the finite graphitic sheet from C_{32} to at least C_{600}.

Chapter 3 Prediction of fullerene packing in C_{60} and C_{70} crystals We present a general analysis of the packing of such molecules that predicts C_{60} to have FCC more stable than HCP (by 0.9 kcal/mol), whereas C_{70} has HCP more stable than FCC (by 0.4 kcal/mol). The predicted structure of C_{60} leads to an orthorhombic distortion (*Cmca*) at 0 K. Dynamics calculations indicate that there is rapid reorientation (but not free rotation) of the C_{60} molecules at higher tem-

peratures, suggesting a phase transition from orthorhombic at low temperature to an orientationally disordered form (equal lattice parameters of 14.13 Å) at room temperature. This may correspond to the first order transition observed at 249 K.[19]

Chapter 4 Thermodynamic Properties Using this force field we study thermodynamic properties (including cohesive energy, heat of sublimation, and vapor pressure) for crystals of C_{60} and C_{70} fullerenes (buckyball molecules). For example, our calculations lead to ΔH_{707K} = 40.9 kcal/mol for C_{60} and ΔH_{739K} = 46.4 kcal/mol for C_{70}, in excellent agreement with experimental value of 40.1 ±1.3 kcal/mol[20] and 46.8 ±1.7 kcal/mol[21] for C_{60} and C_{70}, respectively.

Chapter 5 Mechanic Properties Recently Ruoff[22] suggested that at high pressures buckyball such as C_{60} might be harder than diamond. We have tested these ideas by theoretical calculations of the structure and elastic properties of C_{60} and C_{70} crystals at pressures up to 100 GPa. We find that the buckyballs distort significantly at higher pressures, leading to a cubic shaped molecule (buckycube) by 100 GPa! However, even at 100 GPa fullerite crystals remain softer than graphite and diamond. On the other hand the distortions of the C_{60} at higher pressure force the carbon atoms to become more tetrahedral, and we suggest that compression of C_{60} to appropriate pressures and temperatures might lead to the crystal diamonds. This has been confirmed most recently by Regueiro *et al.* crushing C_{60} to diamond at room temperature.[8]

Chapter 6,7 Alkali Doped C_{60} and Superconducting Phase Alkali-doped buckyballs (M_3C_{60}) have been shown recently to be superconductors with the T_c up to 33 K. We report the principles and predictions arising from theoretical structural studies of M_xC_{60} where x = 0, 1, 2, 3, 6 and M = Li, Na, K, Rb, Cs. For M_6C_{60} with M = K, Rb, Cs we confirm the bcc structure reported for M = K, Cs. Particularly, we predicted the crystal structure of superconductor K_3C_{60} where with fcc the tet

site is too small for K, Rb, Cs so that each C_{60} is forced to reorient with the hex ring point at the tet site center, leading to ordered C_{60}'s which was confirmed later by experimental work.[23] Most recently, the experimental linear compressibility[24] of K_3C_{60} has been obtained to be $1.20 \pm 0.09 \times 10^{-3}$ kbar^{-1}, which is in excellent agreement with our predicted value of 1.13×10^{-3} kbar^{-1}. However, we find that this fcc structure is *metastable*! For M_3C_{60} with M = K, Rb, Cs we find the stable structure is bcc with C_{60}'s at the center and corners of a cube and two M on each face, forming chains in the x,y,z directions (A-15), We suggest alternative procedures for synthesizing bcc M_3C_{60}.

Summarizing for M_3C_{60}: With fcc the tet site ($r_M/r_A = 0.225$) is too small for K, Rb, Cs (0.278, 0.307, 0.337, respectively) so that each C_{60} is forced to reorient with the hex ring point at the tet site center, leading to ordered C_{60}'s. With bcc the best C_{60}...C_{60} contacts (hex rings facing each other) allow the C_{60}'s hex rings to simultaneously face all tet sites. Thus bcc M_3C_{60} is well ordered for all Li, Na, K, Rb, Cs. This leads to a strong energetic driving force for orienting the C_{60}, and a large barrier for rotating the C_{60}.

The T_c of the fullerides is not as high as the high-T_c copper oxides which have set the superconductive record at about 125 K. But because the fulleride materials are a much simpler system, they may offer a window into the still mysterious mechanisms of superconductivity which may ultimately lead to a more profound understanding of superconductivity in general.

References

1. W. Krätschmer, K. Fostiropoulos, and D. R. Huffman, Chem. Phys. Lett., **170**, 167 (1990).
2. W. Krätschmer, L. D. Lamb, K. Fostiropoulos, and D. R. Huffman, Nature, **347**, 354 (1990).
3. D. S. Bethune, G. Meijer, W. C. Tang, H. J. Rosen, Chem. Phys. Lett.,

174, 219 (1990); D. S. Bethune *et al. ibid.* **179**, 181 (1991).

4. R. Taylor, J. P. Hare, A K. Abdul-Sade, and H. W. Kroto, JCS Chem. Comm., **20**, 1423 (1990).
5. H. W. Kroto, J. R. Heath, S. C. O'Brien, R. F. Curl, R. E. Smalley, Nature **318**, 162 (1985).
6. A. F. Hebard *et al.*, Nature **350**, 600 (1991).
7. Z. Iqbal *et al.*, Science **254**, 826 (1991).
8. M. N. Regueiro, P. Monceau, and J.-L. Hodeau, Nature **355**, 237 (1992).
9. L. W. Tutt and A. Kost, Nature **356**, 225 (1992).
10. F. Wudl *et al.*, Science **253**, 301 (1991).
11. R. Ettl, I. Chao, F. Diederlich, and R. L. Whetten, Nature, **353**, 149 (1991).
12. F. Diederlich *et al.*, Science, **254**, 1768 (1991).
13. Y. Guo, N. Karasawa, and W. A. Goddard, Nature **351**, 464 (1991).
14. Y. Guo, & W. A. Goddard III, (to be submitted).
15. Y. Guo, & W. A. Goddard, Phys. Rev. Lett. (submitted).
16. Y. Guo, & W. A. Goddard, (to be submitted to JPC).
17. Y. Guo and W. A. Goddard, Nature (submitted).
18. U. Burkert and N. L. Allinger, *Molecular Mechanics;* ACS: Washington, DC, 1982; ACS Monograph 177.
19. P. A. Heiney *et al.*, Phys. Rev. Lett. **66**, 2911 (1991).
20. C. Pan, M. P. Sampson, Y. Chai, R. H. Hauge, and J. L. Margrave, J. Phys. Chem. **95**, 2944 (1991).
21. C. K. Mathews *et al.*, Current Science, **61**, 838 (1991).
22. R. S. Ruoff, & A. L. Ruoff, Nature **350**, 663-664(1991).
23. P. W. Stephens *et al.*, Nature **351**, 632 (1991).
24. O. Zhou *et al.*, Science **255**, 833 (1992).

Chapter 2

Vibrational Frequencies and Strain Energy of C_{60} and Other Fullerenes

Vibrational Frequencies and Strain Energy of C_{60} and Other Fullerenes

Yuejin Guo and William A. Goddard III

Materials & Molecular Simulation Center

Beckman Institute (139-74)

California Institute of Technology, Pasadena, California 91125

Abstract

A highly accurate force field has been developed for C_{60} in excellent agreement with all 14 experimental frequencies within abs error 3.0 cm^{-1}. If some quantum effect is included, this error can be further reduced to 1.8 cm^{-1}. This force field has also been applied to predict structural and vibrational properties of C_{70} and other fullerenes. Using the force field developed for graphite, we also study the strain energy, heat of formation, and relative stabilities between the fullerenes and graphitic sheets. Heat of formation of C_{60} has been calculated to be 659 kcal mol^{-1} or 10.99 kcal per carbon atom. We find that fullerenes are stable with respect to the finite graphitic sheet from C_{32} to at least C_{600}.

2.1 Introduction

The recent breakthroughs[1] in synthesizing large amounts of C_{60}, C_{70} and other fullerenes[1,2] have led to an increased ability to characterize the vibrational frequencies,[1,3] crystal structures[1b] and other properties (e.g., NMR[4]) of molecules. In order to interpret such experimental results, we have developed a force field suitable for predicting vibrational frequencies, strain energies, and other properties. We illustrate this force field by comparing to the observed frequencies of C_{60}, and predicting the vibrational frequencies for C_{70} and other fullerenes.

From both theoretical and experimental molecular spectroscopic point of view, C_{60}, the roundest, and most symmetrical large molecule found so far, provides a great opportunity for theoretical and experimental understanding of vibrational properties of the fullerene molecules because of its unique high symmetry which makes C_{60} spectra much simpler than others with lower symmetry. This can be shown clearly from that the total number of the IR and Raman frequencies increase dramatically when the symmetry is lower: The total number of the IR/Raman frequencies are 4/10, 22/38, 31/53, and 172/228, for C_{60} (I_h), C_{50} (D_{5h}), C_{70} (D_{5h}), and C_{78} (C_{2v}), respectively.

The well-known C_{60} cluster serves as a prototype for the structures and properties of the large carbon closed-shell clusters. Thus one can study the C_{60} cluster to understand the properties of these clusters in general. Particularly, in late 1990, simple synthesis of macroscopic amounts of the C_{60} and C_{70} clusters has made possible spectroscopic studies of these species, and has triggered intense theoretical and experimental research effort to understand the vibrational properties. Though a lot of work has been done, so far no satisfied force field for C_{60} has been developed yet. Since the high resolution IR and Raman experimental spectroscopy data are

available, it is time for elucidation of accurate force fields for the fullerene molecules. So we want to develop a force field mainly for two purposes, one is to understand vibrational properties associated with C_{60}'s high symmetry; another is to apply this force field to characterize other stable higher fullerenes, which have been detected in the carbon soot produced by arc heating of graphite in an inert atmosphere, such as C_{70}, C_{76}, C_{78}, C_{82}, C_{84}, C_{90}, C_{94}, and C_{94} etc,[5,6] and also C_{50}.[2] We believe that the C_{60} will become a standard for testing both experimental and theoretical force fields for large size molecules.

2.2 Topologic Consideration

More than two hundred years ago, Euler already found the relation between the numbers of vertices(N_0), edges(N_1), and faces(N_2) of a simple convex polyhedron

$$N_0 + N_2 = N_1 + 2\ . \tag{1}$$

Equations may be derived relating to special types of polyhedra. Here we are only interested in the sp^2 hybridized carbon case, that is, if 3 edges meet at every vertex (3-connected polyhedron) and f_n is the number of faces with n edges (or vertices):

$$3f_3 + 2f_4 + f_5 + 0f_6 - f_7 - 2f_8 - ... = 12 \tag{2}$$

for carbon only n = 5 or 6 are likely. In this equation, the coefficient of f_6 is zero, suggesting that polyhedra, in which all the faces are pentagons and hexagons, must have 12 pentagons plus arbitrary hexagons.

2.3 Symmetry Analysis

A. $C_{60}(I_h)$ molecule

C_{60} is a spheroidal molecule with the geometry of a truncated icosahedron - a hollow, ball-like molecule with 60 vertices and 32 faces, of which 12 would be regular pentagons and 20 would be regular hexagons(see Figure 1a).[2]

The infrared spectrum of most molecules as large as C_{60} would be expected to be very complex, which has 174 vibrational modes. But according to the group theory, for the highly symmetrical C_{60} truncated icosahedron with I_h point group symmetry, of the 174 (i.e., $3 \times 60 - 6$) vibrational modes of the C_{60} (I_h) structure only 46 modes would be independent. Of these 46 modes, four with T_{1u} symmetry would be infrared-active, while 10 would be Raman-active. It exhibits following symmetrical structure

$$T_{I_h} = 2A_g + A_u + 3T_{1g} + 4T_{2g} + 4T_{1u} + 5T_{2u} + 6G_g + 6G_u + 8H_g + 7H_u \ , \quad (3)$$

i.e., one-, three-, four- and five-fold degenerate modes are involved. According to the selection rules(Wilson), however, only four three-fold degenerate modes of the T_{1u} symmetry are active in the infrared spectrum. The Raman active modes consist of two singly degenerate A_{1g} modes and eight 5-fold degenerate H_g modes.

B. $C_{70}(D_{5h})$ molecule

Similarly, for the C_{70} molecule a fairly symmetrical polyhedron has been suggested, namely one of symmetry point group D_{5h} formed by 12 pentagons and 25 hexagons(Figure 1b). NMR spectrum consists of five lines, and it is clear from NMR spectroscopy that C_{70} possesses five sets of inequivalent carbon atoms. Therefore, the ^{13}C NMR spectrum of C_{70} tended to confirm this structure.[4]

There are 204 vibrational modes for a 70-atom molecule (2N-6), but under D_{5h} symmetry 31 vibrations are allowed in the infrared spectrum and 53 in the Raman spectrum. Vibrational analysis of the $C_{70}(D_{5h})$ molecule to give the values

of its harmonic vibration frequencies has been done. The 204 (3×70-6) normal vibrational modes of this species exhibit the following symmetrical structure

$$T_{D_{5h}} = 12A_1' + 9A_2' + 9A_1'' + 10A_2'' + 21E_1' + 22E_2' + 19E_1'' + 20E_2'' \qquad (4)$$

so that only one- and two-fold degenerate vibrational motions are present. According to the symmetry selection rules, the only IR-active modes of the $C_{70}(D_{5h})$ molecule will be those of the A_2'' and E_1' symmetries, and Raman-active modes will be those of the A_1', E_2' and E_1'' symmetries.

2.4 Force Field

These large carbon clusters consist of graphitic hexagonal nets plus 12 pentagons which are necessary to make the net closure. In the structure and bonding sense they are very similar to the graphite, that is , the three valence electrons of each carbon atom are used to form σ bonds with its three neighbors(i.e., sp^2). This leaves one electron on each C in a p_π orbital. These π orbitals can then be paired in many ways, and form all possible allowed resonance structures. In effect, C_{60} is a spherical analog of graphite: one is curl up to form a finite molecule and the other is a two-dimensional infinite molecule. Here the idea is to develop the force field from graphite, and then it can be used for C_{60}, since the graphite system is well studied.

In the condensed phase, the interaction between the balls is only van der Waals force. Since our force field already includes this interaction which corresponds to the layer layer interaction in graphite, we would expect that the GraFF should be especially good for the condensed phase properties of C_{60} because the intermolecular interactions in graphite and C_{60} are essentially the same. This can be shown in later chapters by applying this force field to condensed phase, to understand how these balls pack together, and to predict various solid properties such

as elastic constants, cohesive energy, Young's moduli, phonon dispersion, and some thermodynamic properties.

As shown in Table 1, the high frequency modes calculated by GraFF are not as good as the low frequency modes due to the strain introduced by the pentagons in C_{60}. But for the intramolecular properties, GraFF is a good starting point. Based on our graphite force field, we develop a force field for these fullerene molecules by introducing extra strain effects.

First, we want to make use of the unique symmetry structure of C_{60} to understand its vibrational properties.

There are two totally-symmetric A_g modes for C_{60}. For these radical breathing and tangential stretching (or pentagonal pinch) modes the pentagons and hexagons of the structure expand and contract in and out of phase, respectively, or we also can say that two different types of the bonds vibrate with same and opposite phases, for the two modes.

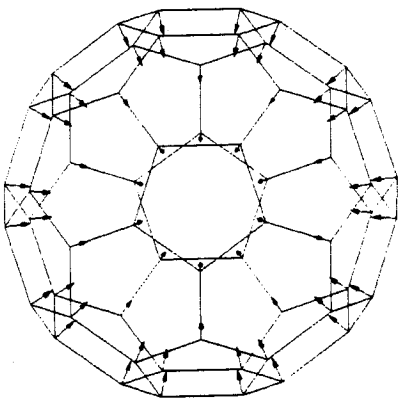

$1A_g$

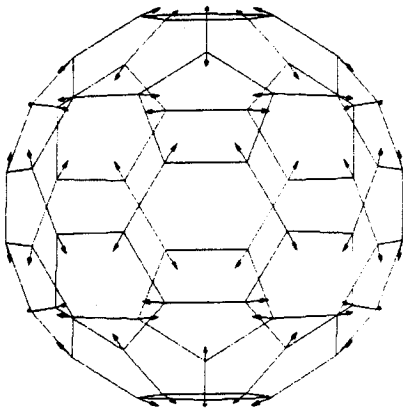

$2A_g$

Because of unusually high symmetry all atoms are equal to each other, and it makes these two modes truly pure stretching modes which means these two modes do not change angles and other terms,so angle and other force constants are not involved. More importantly, for C_{60}, each carbon atom in this structure is exactly equivalent

by symmetry to each of the other 59 carbon atoms, and under the totally-symmetric A_g vibrations, this is still true, which means all atoms move in the same way. This leads to that each of these A_g vibrations is the same as a two particles vibration. So we can analytically solve these two A_g modes by treating them as the effective two particles problem.

In general, given the masses, the structure, and the force constants, complete mathematical procedures exist for calculating the form and frequencies of all the normal modes of vibration of relatively simple molecules. However, as the molecules become more complex the difficulty of the mathematical treatment increases enormously, and it is almost impossible for a molecule as large as 60 atoms.

Consider a molecular model where the nuclei are represented by point masses and interatomic bonds are represented by massless springs which follow Hooke's law. The form and frequencies of the vibrations are determined by classical methods. The diatomic vibrational frequency is given by

$$\nu(\mathrm{sec}^{-1}) = \frac{1}{2\pi}\sqrt{\mathrm{K}\left(\frac{1}{\mathrm{M}_1}+\frac{1}{\mathrm{M}_2}\right)}\,, \tag{5}$$

where the ν, K, and $\mathrm{M_i}$ are the frequency in sec^{-1}, the force constant in dynes/cm, and the mass in united atomic unit, respectively, or

$$\nu(\mathrm{cm}^{-1}) = \frac{1303}{\sqrt{143.88}}\sqrt{\mathrm{K}\left(\frac{1}{\mathrm{M}_1}+\frac{1}{\mathrm{M}_2}\right)}\,, \tag{6}$$

where ν, K, and $\mathrm{M_i}$ are in cm^{-1}, $(\mathrm{kcal/mol})/\mathrm{\AA}^2$, and united atomic unit, respectively. If we know the experimental vibrational frequency, then we can calculate the stretching force constants from this eq., that is,

$$\mathrm{K} = \mathrm{A}\nu^2, \qquad \mathrm{A} = \frac{143.88}{(1303)^2}\cdot\frac{1}{\left(\frac{1}{\mathrm{M}_1}+\frac{1}{\mathrm{M}_2}\right)}\,. \tag{7}$$

For C_{60} A_g modes, because of the extremely high symmetry, we can find analytic solutions for these A_g modes. We can isolate C atoms to the pairs of C

atoms by central inversion symmetry and treat each pair as a isolated diatomic system by projecting force on it: The first A_g mode is

$$\sin^2\theta\left[K_2+\frac{1}{2}K_1\left(\frac{\sqrt{5}-1}{2}\cdot\frac{1}{tg\theta}-1\right)^2\right]=A\nu_1^2\ , \tag{8}$$

and the second A_g mode is

$$\cos^2\theta\left[K_2+\frac{1}{2}K_1\left(\frac{\sqrt{5}-1}{2}\cdot tg\theta+1\right)^2\right]=A\nu_2^2\ , \tag{9}$$

where K_1 and K_2 are related by

$$\frac{K_2}{K_1}=\frac{1}{2}\left(\frac{\sqrt{5}-1}{2}\cdot tg\theta+1\right)\left(\frac{\sqrt{5}-1}{2}\cdot\frac{1}{tg\theta}-1\right)\ , \tag{10}$$

where K_2 and K_1 are stretching force constants for double and single bonds, respectively., and the $\theta=11.43°$ is the angle between the double bond and tangetial stretching (second A_g). If a simple force field were working for C_{60}, the force field used for the first A_g mode could be applied to the second A_g mode, but the simple valence force field calculation for the second A_g mode predicts a 1814 cm^{-1}, which is about 344 cm^{-1} higher than the observed value of 1470 cm^{-1}. The experimental value of 1470 cm^{-1} double-bond stretching "pentagonal pinch" vibration mode in C_{60} is lower than the expected value from the simple standing wave approach, because the electron can partially slip away from the bonds which become longer and into bonds which become shorter during the vibration. The result of this is that the restoring force for the "pentagonal pinch" vibration mode is less than that for the "breath" vibration mode (i.e., first A_g) where this kind of electron redistribution during the vibration cannot occur, that is, $K_1^{2A_g}<K_1^{1A_g}$ and $K_2^{2A_g}<K_2^{1A_g}$. But, in force field method, the motions of the nuclei are studied, and the electrons are not explicitly examined at all, they are simply assumed to find an optimum distribution about the nuclei. So in some normal vibrational modes can cause this potential field change, therefore lead to the change of the force constants in delocalized π-electron

molecules. In molecular mechanics point of view (i.e., force field method), the above phenomena needs the interaction force constant to be taken into account; in the viewpoint of quantum level, this means that the electronic structures of two vibration modes are different.

This result suggests that the π-electron contributed from each carbon atom are delocalized over the entire sphere and C_{60} has aromatic character analog to benzene case. Our results support its three-dimensional delocalized aromatic character and thus imply its nonlinear optical properties.

In general, nonlinear optical properties of conjugated organic and polymeric materials are associated with their delocalized π-electrons, so this highly mobile or delocalized π-electrons in C_{60} are responsible for large nonlinear optical responses.[7]

In a simple valence force field a bending or stretching oscillator can be thought of as a simple spring which exerts forces on its masses equal to a force constant times its distortion from equilibrium. The restoring force does not depend on what the other oscillators in the molecule are doing. However, in reality, if two or more oscillators in a molecule are distorted from equilibrium, they may be able to affect each others restoring forces to some extent because of a change in electronic structure. In this case, a more general valence force field is necessary where the restoring force on one oscillator is equal to a force constant times its own distortion plus a second force constant times the distortion of a second oscillator, and so forth. The second force constant, which can be positive or negative, is called an interaction force constant and is usually about an order of magnitude smaller than the main force constants.

2.5 C_{60} Vibrations

Recently an empirical force field[8] (denoted GraFF) was developed for graphite by requiring that the lattice parameters, elastic constants, and phonon

modes exactly fit experimental data. We have used this force field (Table 2) as the starting point for calculating and assigning vibrational frequencies of fullerenes. In Table 1 we compare the calculations to the all 14 bands that have been assigned from experiments on C_{60}.

Without any corrections there is a good agreement for the out-of-plane bands (lower five), where we find (experiment in parentheses): 261 (273) cm^{-1} for $1H_g$, 435 (434) for $2H_g$, 488 (497) for $1A_g$, 556 (527) for $1T_{1u}$, 574 (577) for $2T_{1u}$. This suggests that the out-of-plane like distortions of C_{60} are well described by the graphite force field. The higher bands correspond to vibrations within the C_{60} membrane and are about 10% lower than experiment: 1113 (1183) for $3T_{1u}$, 1276 (1428) for $2T_{1u}$, 1321 (1426) for $2H_g$, and 1281 (1470) for $2A_g$. The overall abs deviation of frequencies is 62 cm^{-1}. If we modify the GraFF by simply replacing bond stretch terms by analytical solution of two A_g modes, and keep rest terms the same as GraFF, this new force field, denoted Q-graFF, gives much better result (see Table 1), for example, now the abs error of frequencies is 17 cm^{-1}. Because C_{60} has 5-numbered rings not present in graphite, it is plausible that the theory would have greater error for these in-plane modes, and we will empirically readjust our force field to take into account these differences. Before doing this there are some additional factors to consider.

In Table 3 we compare geometrical parameters from GraFF with recent crystallographic results on $C_{60}OsO_4$ and with NMR, *ab initio* Hartree Fock (HF) calculations, and semiempirical MNDO calculations. All methods agree that the CC bond lengths are longer in pentagonal rings than for bonds that are only in hexagonal rings. The difference, ΔR_{CC} is 0.041 Å for GraFF 0.044 for $C_{60}OsO_4$, 0.05 for NMR, and 0.078 for HF, and 0.074 for MNDO. The HF value seems clearly high, probably because of the lack of electron correlation. On the other hand, GraFF leads to CC bond lengths too long by .025 Å. This may be because the π bonds are

bent, a fact not included in the FF.

The most complete vibrational spectra for C_{60} are from studies of condensed C_{60} . Consequently, we calculated the vibrational frequencies both for free C_{60} and for the FCC C_{60} crystal. As indicated in Table 4 these calculations show considerable (11 cm^{-1}) *blue* shifts for the $1H_g$ and $1A_g$ Raman bands, corresponding to the squashing and breathing modes of C_{60} . The other modes all blue shift by a small amount (2 to 4 cm^{-1}). Comparing spectra near 0 K with those at 300K there are red shifts by $\sim$2 to 4 cm^{-1}. Combining these results we expect that the total correction between gas phase C_{60} at 0K and condensed C_{60} at 300K is about 8 cm^{-1} (blue) for $1H_g$ and $1A_g$ and $\sim$ zero for all other modes. The resulting experimental frequencies for gas phase C_{60} at 0K are given in Table 4 as "exact gas phase 0K". For the four out-of-plane modes the theory is now off by -6, $+4$, -4, and $+2$ cm^{-1}.

In order to develop a highly accurate force field for C_{60}, we have to go beyond the graphite force, and add more force field terms to empirically readjust our force field to take into account these differences between graphite and fullerenes, in particular the pentagon. In figure 3 we list almost all possible force field terms for C_{60}, which include about total 27 parameters, of 27 parameters, 22 are force constant parameters and 5 are geometric parameters. We find that only 15 of the them are important for C_{60} vibrational properties (figure 4).

To describe the in-plane modes of C_{60}, adjusted the force constants with the following two requirements:

a) the equilibrium structure of C_{60} is changed to that determined by crystallography (bonds to within 0.001Å, angles to within 0.01°), and

b) all 14 IR- and Raman-active modes.[19,20]

The resulting force field, denoted OptFF, is given in Table 5 and the frequencies for C_{60} are given in Tables 6 and 7. In Table 6 we include only the allowed transitions for Raman (A_g, H_g) and IR (T_{1u}).

The frequencies calculated from the OptFF are in excellent agreement with all 14 experimental frequencies with abs error 3.0 cm^{-1} or less than 1%. During the adjusting the force constants to match the frequencies, the most difficult part is to obtain the right gap between $4T_{1u}$ and 2 A_g modes. There are two possibilities to interpret this difficulty: one is assuming the experimental assignment is correct, that is, these two modes are very similar, both are "pentagonal pinch" modes except with different parities which leads to a node plane in $4T_{1u}$,

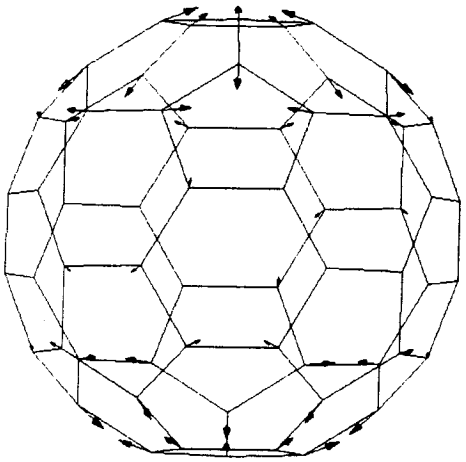

$\mathbf{4T_{1u}}$

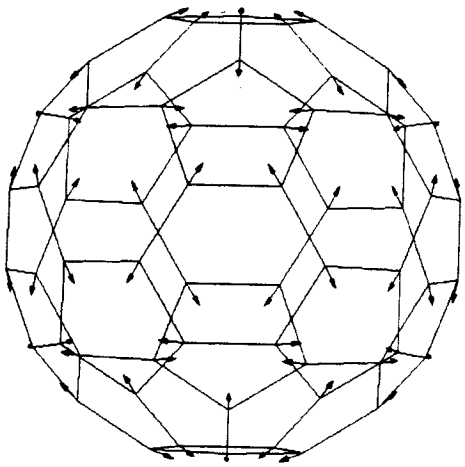

$\mathbf{2A_g}$

but the quantum effect discussed in section 2.4 is not included in the current force field; another is the problem of the experimental assignment on $7H_g$ and $2A_g$. We think that first one is likely, if we do not use $4T_{1u}$ for adjusting the force constants. Then this abs error can be further reduced to only 1.8 cm^{-1}. This force field has also been applied to predict structural and vibrational properties of C_{70} and other fullerenes.

The ten Raman allowed modes and the four IR allowed modes are shown in Figure 2.

There have been several previous calculations of the vibrational frequencies of C_{60}. These are compared in Table 8. These frequencies were calculated from semi-empirical quantum-chemistry methods by Newton[9](MNDO) and Slanina[10](AM1)

or from estimated force constants by Harter[11](spring-mass model) and Cyvin[12] (normal coordinate analysis). The frequencies predicted by these methods are too high, particularly for the in-plane modes, for example, $\sim$1800 cm^{-1} for $2A_g$ mode which is about 30 % too high. The reason is that Hartree Fock quantum chemistry methods generally give frequencies too high by $\sim$ 20%.

2.6 C_{70} Vibrations

C_{70} has a D_{5h} geometry where the 10 extra atoms run around the middle of the cage, related to C_{60} by the addition of a central cylindrical 10-atom belt, producing a structure which looks like an elongated sphere, and leading to a long axis c=8.0 Å, leaving the remaining axes (a = b = 7.1 Å) the same as in C_{60} (where a = b = c = 7.1 Å). In Figure 1b, we show the optimized structure of C_{70} cluster, and this structure is confirmed by NMR[4], and electron diffraction.[13] The numbering system used to list the geometrical parameters is also given in figure 1b. The molecule has 12 degrees of freedom, and 8 of them are bond length parameters and are listed in Table 9. The eight bond lengths fall into three ranges. The bonds defining a pentagon (type 2-2, 2-3, 3-4, and 5-5) are long with an average value of 1.456 Å, which is equal to our value for the equivalent bond in C_{60} (1.455 Å). The bonds joining the apices of two pentagons (type 3-3 and 4-5) are short, with an average value of 1.413 Å, equal to our value for the equivalent bond in C_{60} (1.414 Å). The remaining bonds in C_{70} (type 1-1 and 1-2) have no equivalent in C_{60}. Geometrically, the most interesting aspect of C_{70} corresponds to the nature of the bonding and strain around the 10 added carbon atoms. These atoms are all at the junction of three hexagons and thus most resemble the carbon in graphite. Of them, the five bonds around the equator (type 1-1) are not distorted by the proximity of pentagons, and these bonds have a length of 1.429 Å which is the same as the graphite (1.42 Å). The rest remainder of the 20 (type 1-2) bonds is 1.439 Å,

about the mean value of the long bond in C_{70} and the bond in graphite.

The comparison of the electron diffraction experiment, *ab initio* HF(dzP) and our OptFF bond length parameters is listed in Table 9. For the equivalent bonds in C_{60} (i.e., long and short bonds), experiment, HF(dzP) and our OptFF results are generally consistent with each other, and are equal to their respective values of equivalent bonds in C_{60} with one exception, that is, HF(dzP)'s value of the type 2-2 long bond is too short (1.415 vs. 1.465 Å). For the five bonds around the equator our value is the same as electron diffraction value, but HF(dzP) value of 1.475 Å is exceptionally long, which is the longest bond in all eight distinct types, while for type 1-2 bond all three methods give different values.

Because of the significantly lower symmetry for C_{70} (D_{5h}) than for C_{60} (I_h), there are many more allowed bands (53 Raman and 31 IR compared to 10 and 4). The predicted vibrational modes are tabulated in Table 10, where the IR and Raman allowed transition are placed in the first columns. Early published spectra are mixed with C_{60} spectra,[3] and only very recently have experimental vibrational spectra on C_{70} been obtained by several groups.[18,19,20] No C_{70} vibrations have previously been assigned. In Table 10 we have made assignments of 6 modes (indicated by experimental frequencies in parameters) and have noted 18 other predicted transitions of C_{70} that are obscured by C_{60} vibrations (indicated by square brackets). Since it is now possible to obtain quite pure C_{70}, we would expect IR and Raman data to become available soon, and hope that these predictions will be useful. It is clear from the large number of allowed vibrational modes that it is impossible to make any complete assignments unless the associated intensity information is also available. But based on that the modes of C_{70} which correspond to modes of C_{60} with strong intensity should have comparable strong intensity, we can make partially assignment for C_{70}.

Some selected vibrations are listed in Table 11. Here $1A_1'$ (259), $1E_2'$ (222),

and $1E_1''$ (275) correspond to the $1H_g$ squashing mode of C_{60} (279 cm^{-1}). The $1A_g$ breathing mode of C_{60} (493 cm^{-1}) corresponds to $2A_1'$ (449 cm^{-1}) in C_{70}. The $2T_{1u}$ (581 cm^{-1}) of C_{60} corresponds to $5E_1'$ (546) and $3A_2''$(565) in C_{70}.

2.7 Trends in Vibrational Levels

In Table 12 we list the calculated vibrational transitions for C_{50}. There are no reported spectra for this C_{50}, but we hope these predictions will be useful in searching for this molecule.

The lowest allowed Raman modes in C_{50} at 281(A_1'), 326(E_2'), 303(E_1'') correspond to the squashing H_g (d-like) mode calculated at 279 for C_{60}, while the lowest allowed Raman modes are in C_{70} at 259(A_1'), 222(E_2'), 276(E_1''), respectively. Averaging over these all levels, the energy of the squashing mode changes from 308 (C_{50}), to 279 (C_{60}), to 251 (C_{70}). As indicated in Table 11 similar downward trends are observed for the breathing mode (at 493 in C_{60}), and the out-of-plane mode (at 581 in C_{60}), and the pentagon compression mode (at 1462 in C_{60}).

These downward trends indicate that the strain energy per carbon atom decreases with the size increasing.

2.8 Strain Energies

A purely hexagonal network cannot close perfectly, so we can view fullerenes as finite graphitic fragments plus some strain domains incorporating the pentagons, with these pentagons they have been able to curl into a ball, perfectly tying up all dangling bonds.

Using the graphite force field (see Table 2) for various fullerene molecules (C_N with N = 20, 24, 28, 32, 50, 60, 70, 72, 76, 78, 80, 84, 240, 540) leads[21] to the strain energies in Figure 5 and Table 13. Thus, we find the energy in C_{60} to be 659.6 kcal/mol or 10.99 kcal mol per carbon atom. Because of its edgeless, this

value is also equal to the heat of formation for C_{60}, i.e., $\Delta H_f = 659.6$ kcal/mol. This corresponds to 10.99 kcal/mol per C atom which is significantly larger than zero for graphite, 0.45 for diamond[22] and 1.30 kcal/(mol C) for a graphitic monolayer. On the other hand, the more highly strained C_{20} (I_h) cluster has $\Delta H_f = 24.12$ kcal/(mol C), while $\Delta H_f = 3.46$ kcal/(mol C) for the much less strained C_{540} (I_h) cluster.

In order to understand the significance of this strain energy, and compare relative stabilities between the fullerenes and graphitic sheets, it is necessary to estimate the energy of a flat sheet of 60 carbon atoms and others. In this case, there is no strain but there are broken bonds. In order to estimate the heats of formation for such sheets, we use a Benson-like scheme where A = heat of formation for an isolated edge atom of graphite (radical electron not strongly paired to others) and B = heat of formation for an edge atom of graphite adjacent to a similar such atom. In the latter case the overlap of the radical electrons on the two adjacent atoms leads to a weak "π bond" in the plane as in 1-2 benzyne case.

Experimentally the activation energy for cis-trans isomerization in ethylene is 65 kcal/mol. Since the C=C bond energy of ethylene is 172 kcal/mol, this indicates that the C—C bond energy of

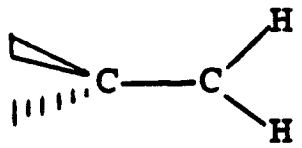

(11)

is D_{298}=107 kcal/mol. we take

$$A = 1/2(\Delta H) = 53.5 \text{ kcal/mol} .$$

To obtain B compare the C−H bond energy in benzyne[23], (12a),

$$(\Delta H_f(C_6H_5) + \Delta H_f(H)) - \Delta H_f(C_6H_6) = 78.6 + 52.1 - 19.8 = 110.9 \text{ kcal/mol}$$

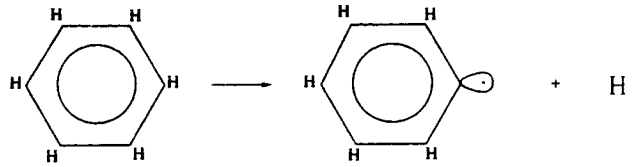

(12a)

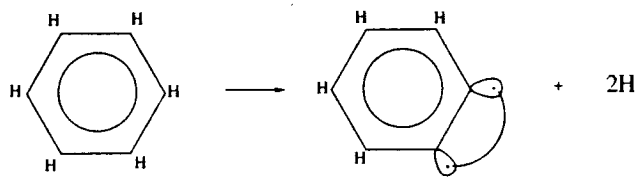

(12b)

to the energy for removing two H's (1-2 benzyne[24]), (12b),

$$(\Delta H_f(C_6H_4) + 2\Delta H_f(H)) - \Delta H_f(C_6H_6) = 106 + 2 \times 52.1 - 19.8 = 190.4 \text{ kcal/mol}.$$

The difference in energy,

$$2 \times 110.9 - 190.4 = 31.4 \text{ kcal/mol}$$

suggests a π bond in the plane between the two radical electrons of 31.4 kcal/mol. This leads to B = 31.4 cal/mol.

The best energy for a flat sheet of 60 atoms is obtained for the structure in Figure 7. This leads to a total energy of broken bonds 20A + 9(−B) = 787.4 kcal/mol. After calibrating the 58.1 kcal/mol vdW interaction energy of graphite force field, a total energy of 845.5 kcal/mol is obtained for this flat sheet of 60 atoms. Thus fullerene C_{60} is more stable than the flat C_{60} sheet by 845.5 - 659.6 = 185.9 kcal/mol or by 3.1 kcal per carbon atom. Thus there is a driving force of 185.9 kcal/mol for C_{60} to have the soccer ball structure rather than a flat graphite sheet, which involves the tendency of the growing clusters to curl in order to minimize the number of dangling bonds. Similar results for other cases are given in Table 13.

These calculations suggest that fullerenes are stable with respect to the graphite sheet between C_{32} and at least C_{600}. Actually, this can be easily understood because the energy of broken bonds per carbon atom in flat sheet is proportional to $2\pi R/\pi R^2$. When N goes to a very high number the edge effect is getting smaller and eventually can be ignored, so for very large N the graphite sheet can be more stable. This is consistent with recent experimental results of detecting the fullerene with the size as large as several hundred carbon atoms.[25] For the small-sized fullerenes, as shown in Figure 6 for $N < 60$ the strain energy increases rapidly as the cluster gets smaller. This leads to very high strain energy for fullerene with $N < 32$, therefore, the graphitic sheets are more stable. This might be why only even-numbered carbon fullerenes larger than C_{32} have been observed in carbon cluster beams produced by laser vaporization of graphite.[26]

Based on the above results, we can correlate these energies with their structures, and reveal the relationship between structure and energy. As shown in Figure 6, at range $N < 60$ the slope is high, which means the average strain per atom dramatically increases as the cluster gets smaller, while at range $N > 60$ the slope is quite low and the strain energy changes more smoothly with the size. Clearly there is a significant turning point in the slope around $N = 60$. This is because C_{60} is the smallest fullerene for which all pentagons can be isolated. When $N < 60$, the fused-pentagon occurs and its number increase with size decreasing, on the other hand, when $N > 60$, the same as C_{60} all pentagons can be isolated, the only difference is a more flat hexagonal network, so the small energy change will be expected.

In general, for all fullerenes the strain of closure tends to concentrate at the vertices of the pentagons, and it is very important that pentagons are isolated as much as possible by hexagons to avoid the instability inherent in fused-pentagon configurations. For example, there are five pairs of fused-pentagons in C_{50}, This may be why the C_{50} cannot be made by Krätschmer *et al.*'s new method, and is only

detected by laser vaporization of graphite and mass spectrometer.[3] It is even worse for smaller fullerenes such as C_{32},C_{28},C_{24}, and C_{20} all of them have the carbon atoms which are shared by pentagons (triplet fused-pentagon configuration) only. The C_{20} dodecahedron would probably be too highly strained to be stable as a bare molecule (although the hydrogen-saturated form $C_{20}H_{20}$, dodecahedrane, is known and very stable species). In fact, with five-membered rings the angles in the flat, regular pentagon are 108°, almost exactly equal to the tetrahedral angle(109.47°), and this is why $C_{20}H_{20}$ is very stable. There is a large strain for this kind of carbon site (even though the bending bond model can reduce the strain a little bit), and this carbon would strongly tend to be sp^3 hybridizing. Therefore, $C_{20}H_{20}$ would be much better, the similar reason accounting for less stable of C_{24}, C_{28} and C_{32}(all of them have carbon atoms which are shared by pentagons only). So balancing the total strain energy and per atom strain energy, C_{60} is the best. This makes it exceptional stable.

For C_{60}, another aspect contributing to its unique stability is the fact that, each carbon atom in this structure is exactly equivalent by symmetry to each of the other 59 carbon atoms. Thus, although there is an appreciable amount of strain in the chemical bonds that is induced by curvature of the sphere, its high symmetry enables it to distribute strain perfectly. There are no " weak links" for chemical attack or photophysical rupture, which account for its extreme chemical and photophysical stability.

It is important to note that for $N \leq 30$, currently, both theory and experiment agree that:[27,28] clusters of intermediate size ($N = 11-30$) exist as monocyclic rings, and in the smallest cluster ($N < 11$), odd clusters ($n = 3,5,7,9$) have linear singlet cumulentic ground states, while even C_n ($n \geq 4$) favor monocyclic rings, although linear isomers are likely to coexist.

2.9 Chiral Buckyballs

After Krätschmer *et al.*'s discovery, the isolation and characterization of the higher fullerenes are becoming possible.[5,6] Recent NMR experiments on C_{76} have been shown that there are 19 different lines each with the same intensity.[29] There is only one buckyball structure of C_{76} compatible with this NMR systems; it is the D_2 structure shown in figure 8. Amazingly the molecule, unlike its highly symmetrical cousins C_{60}andC_{70}, is chiral with helical form, i.e., it has two forms, left handed and right handed. Now theoreticians and experimentists are turning more attention to these higher fullerenes due to their unexpected structure properties. For C_{60} and C_{70}, only one isolated-pentagon fullerene cage is possible, which are C_{60} (I_h) and C_{70} (D_{5h}) structures, respectively. But there are more than one candidate for higher fullerenes, and the number of candidates increase rapidly with the size.

In a previous section we have found that it is very important for energy, that pentagons are isolated as much as possible by hexagons to avoid the instability inherent in the fused-pentagon configurations. Based on this, we apply our graphite force field to higher fullerenes, C_{76}, C_{78} and C_{84}, to study their structures and strain energies (stabilities). We find that C_{76}, C_{78}, and C_{84} could have two, five, and eight possible fullerene structures, respectively. The results are listed in Table 14. In general, we find that the isomers assigned by NMR spectrum[29,30] and qualitative Hückel MO theory[32] are much less stable than the best structures that we have found. The reason is that the C'_{2v}-C_{78}, D'_{3h}-C_{78}, D_{6h}-C_{84}, T_d-C_{84} and D'_2-C_{84} with one, three, two, four, and four flat coronene faces separated by rather sharp edges, respectively, are much more strained than C_{2v}-C_{78}, D_{3h}-C_{78}, D_{2d}-C_{84}, D_2-C_{84}, and C_1-C_{84} structures which do not have quasi-planar coronene face and more uniform curvature over entire ball surfaces. These results strongly suggest that the formation of fullerenes may be a kinetic control process.

2.10 Summary

We have developed a highly accurate force field for C_{60} with abs deviation of frequencies only 3.0 cm^{-1}, if we include some quantum effect, this error can be further reduced to 1.8 cm^{-1}. We also apply this force field to C_{70} and C_{50} and other fullerenes to study their structural, energy, and vibrational properties.

The assignments of the four T_{1u} (IR) modes and the $1H_g$ and $1A_g$ (Raman) bands have been confirmed. We suggest reassigning the 1469 cm^{-1} mode.

We show why the C_{60} and C_{70} molecules are so stable in molecular level. Based on our estimating the ΔH_f, we find that fullerenes are stable with respect to the graphite sheet from C_{32} to at least C_{600}.

The relative stabilities of carbon clusters in the full range are: linear chains for $N < 11$ (although monocyclic ring isomers may coexist for even C_N); monocyclic rings for $11 \geq N \leq 30$; fullerenes for $30 < N < 600$; graphitic sheet for $N > 600$.

References

1a. W. Krätschmer, K. Fostiropoulos, and D. R. Huffman, Chem. Phys. Lett., **170**, 167 (1990).

1b. W. Krätschmer, L. D. Lamb, K. Fostiropoulos, and D. R. Huffman, Nature, **347**, 354 (1990).

2. H. W. Kroto, J. R. Heath, S. C. O'Brien, R. F. Curl, R. E. Smalley, Nature **318**, 162 (1985).

3. D. S. Bethune, G. Meijer, W. C. Tang, H. J. Rosen, Chem. Phys. Lett., **174**, 219 (1990); D. S. Bethune *et al. ibid.* **179**, 181 (1991).

4. R. Taylor, J. P. Hare, A K. Abdul-Sade, and H. W. Kroto, JCS Chem. Comm., **20**, 1423 (1990).

5. F. Diederlich *et al.*, Science, **252**, 548 (1991).

6. K. Kikuchi *et al.*, Chem. Phys. Lett., **188**, 177(1992).

7. L. W. Tutt and A. Kost, Nature **356**, 225 (1992).

8. Y. Guo, N. Karasawa, and W. A. Goddard, Nature **351**, 464 (1991).

9. The Force Field optimization was carried out with FFPARM written by S. Dasgupta, T. Yamasaki, and W. A. Goddard of the MSC/BI.

9. R. E. Stanton and M. D. Newton, J. Phys. Chem., **92**, 2141(1988).

10. Z. Slanina, J. M. Rudzinski, M. Togasi and E. Osawa, J. Mol. Struct. THEOCHEM, **202**, 169(1989).

11. D. E. Weeks and W. G. Harter, J. Chem. Phys., **90**, 4744(1989).

12. S. J. Cyvin, E. Brendsdal, B. N. Cyvin and J. Brunvoll, Chem. Phys. Lett., **143**, 377(1988).

13. D. R. Mckenzie, C. A. Davis, D. J. H. Cockayne, D. A. Muller, & A. M. Vassallo, Nature **355**, 622 (1992).

14. G. E. Scuseria, Chem. Phys. Lett., **180**, 451(1991).

15. K. Raghavachari and C. M. Rohlfing, J. Chem. Phys., **95**, 5768 (1991).

16. F. Negri, G. Orlandi, and F. Zerbetto, J. Am. Chem. Soc., **113**, 6037 (1991).

18. J. P. Hare *et al.*, JCS Chem. Comm., **21**, 412 (1991).

19. T. J. Dennis, J. P. Hare, H. W. Kroto, R. Taylor, D. R. M. Walton, and P. J. Hendra, Spectrochimica Acta, **47A**, 1289 (1991).

20. R. Meilunas R. P. H. Chang, S. Liu, M. Jensen, and M. M. Kappes, J. Appl. Phys., **70**, 5128 (1991).

21. These calculations were all carried out using POLYGRAF (from Molecular Simulations Inc. of Sunnyvale California, formerly known as BioDesign) in conjunction with additional vibrational analysis software written by N. Karasawa, S. Dasgupta, and W. A. Goddard of the MSC/BI.

22. R. C. Weast (ed.) CRC Handbook of Chemistry and Physics, 70th edn. D50-97 (Chemical Rubber Company, Boca Raton, 1989)

23. S. G. Lias, J. E. Bartmess, J. F. Liebman, J. L. Holmes, R. D. Levin, and

W. G. Mallard, J. Phys. Chem. Ref. Data 1988, **17**, Suppl. 1.

24. P. G. Wethold, J. A. Paulino, and R. R. Squires J. Am. Chem. Soc., **113**, 7414 (1991).
25. S. Maruyama, M. Y. Lee, R. E. Haufler, Y. Chai, and R. E. Smalley, Z. Phys. D, **117**, 1 (1991); H. Shinohara *et al.*, J. Chem. Phys., **95**, 8449 (1991).
26. E. A. Rohlfing, D. M. Cox, and A. Kaldor, J. Chem. Phys., **81**, 3322 (1984); Ph. Gerhardt, S. Loffler, and K. H. Homann, Chem. Phys. Lett., **137**, 306 (1987).
27. W. Weltner, Jr. and R. J. Van Zee, Chem. Rev. **89**, 1713 (1989)).
28. K. Raghavachari and J. S. Binkley, J. Chem. Phys. **87**, 2191 (1987).
29. R. Ettl, I. Chao, F. Diederlich, and R. L. Whetten, Nature, **353**, 149 (1991).
30. F. Diederlich *et al.*, Science, **254**, 1768 (1991).
31. K. Raghavachari, Chem. Phys. Lett., **190**, 397 (1992).
32. P. W. Fowler, J. Chem. Soc. Faraday Trans., **97**, 1945 (1991); P. W. Fowler, R. C. Batten, and D. E. Manolopoulos, *ibid.*, 2861 (1991); D. E. Manolopoulos, *ibid.*, 3103 (1991).
33. W. I. F. David *et al.*, Nature **353**, 147 (1991).
34. F. Negri, G. Orlandi, and F. Zerbetto, Chem. Phys. Lett., **144**, 31 (1988).

Figure Captions

Figure 1. C_{60} and C_{70} cluster.

Figure 2. $1A_g$ and $2A_g$ modes of C_{60}(Raman active)

Figure 3. All possible force field terms of C_{60}

Figure 4. Important force field terms of C_{60}

Figure 5. Strain E vs. cluster size.

Figure 6. Strain E vs. cluster size.

Figure 7. Best flat C_{60}.

Figure 8. Chiral

Table 1. Comparison of experimentally assigned vibrational frequencies (cm^{-1}) with those calculated using the GraFF.

Mode	Expt.[a]	GraFF[b]	$\Delta\nu$	Q-graFF[c]	$\Delta\nu$	Active
$1H_g$	273	261	-12	264	-9	Raman
$2H_g$	434	435	1	416	-18	Raman
$1A_g$	496	488	-8	496	0	Raman
$1T_{1u}$	527	556	29	533	6	IR
$2T_{1u}$	577	574	-3	580	3	IR
$3H_g$	710	759	49	713	3	Raman
$4H_g$	774	750	-24	775	1	Raman
$5H_g$	1100	1080	-20	1139	39	Raman
$3T_{1u}$	1183	1113	-70	1182	-1	IR
$6H_g$	1250	1104	-146	1230	-20	Raman
$4T_{1u}$	1428	1276	-152	1460	32	IR
$7H_g$	1426	1321	-105	1476	50	Raman
$2A_g$	1470	1281	-189	1470	0	Raman
$8H_g$	1576	1517	-59	1633	57	Raman

[a] Reference 20.

[b] The force field was optimized for the graphite. The abs error of frequencies is 56.4 cm^{-1}.

[c] The bond stretch terms are from analytical solution of two A_g modes, and rest terms from the GraFF. The abs error of frequencies is 17.1 cm^{-1}.

Table 2. Graphite Force Field Parameters.

Interaction Type[a]	Parameter[a]	GraFF[b]	Q-graFF[c]
VDW (LJ12-6)	R_v(Å)	3.8050	3.8050
	D_v (kcal/mol)	0.0692	0.0692
Bond Stretch[d]	r_b(Å)	1.4114	1.4140[e]
			1.4550[f]
	k_b [(kcal/mol)/A^2]	720.00	823.75[e]
			711.77[f]
	D_b (kcal/mol)	133.00	
Angle Bend (cosine)	θ_a (deg)	120.00	120.00
	k_θ[(kcal/mol)/rad^2]	196.13	196.13
	$k_{r\theta}$ [(kcal/mol)/rad Å]	62.709	62.709
	$k_{rr'}$ [(kcal/mol)/A^2]	68.000	43.940
Torsion (1 fold)	V_t (kcal/mol)	21.280	21.280

[a] For definitions, see S.L. Mayo, B. D. Olafson and W. A. Goddard, J. Phys. Chem., **94**, 8897 (1990).

[b] The force field was optimized for the graphite.

[c] The bond stretch terms are from analytical solution of two A_g modes, and rest terms from the GraFF.

[d] The bond stretches are one Morse and two harmonic For GraFF and Q-graFF, respectively.

[e] Double bond.

[f] Single bond.

Table 3. The detailed Structure[a] of C_{60} Determined by Various Methods

	Experiment			Theory		
	NMR	Neutron[b]	XRD	GraFF	MNDO	HF
	C_{60}	C_{60}	$C_{60}OsO_4$			
C-C Bonds						
R_1	1.40±.015	1.391±.018	1.388±.009	1.414	1.400	1.370
R_2	1.45±.015	1.455±.012	1.432±.005	1.455	1.474	1.448
ΔR	0.05±.020	0.064±.018	0.044±.010	0.041	0.074	0.078

[a] The angles are 108 in 5-membered ring and 120 in 6-membered ring.

[b] Reference 33.

Table 4. Comparison of experimentally assigned vibrational frequencies (cm^{-1}) with those calculated using the GraFF.

	Calculations			Exact Gas	Experiment		
	C_{60} Molecule	C_{60} crystal	shift	Phase[a]	crystal[b] C_{60}	Matrix C_{60} in Ar	Gas Phase
	0K	0K		0K	300K	10K	1065K
out-plane							
$1H_g$	259	270	+11.4	265	273		
$1A_g$	493	504	+11.1	489	497		
$1T_{1u}$	523	528	+4.6	527	527	530	527
$2T_{1u}$	579	581	+2.2	577	577	579	570
in-plane							
$3T_{1u}$	1126	1130	+3.5	1182	1182	1185	1169
$4T_{1u}$	1362	1366	+3.9	1429	1429	1432	1407
$2A_g$	1375	1379	+4.3	1469	1469		

[a] Based on experiment from condensed phase, corrected using theory.

[b] Reference 1 for IR and reference 3 for Raman.

Table 5. C_{60} Force Field Parameters.

Interaction Type[a]	Parameter[a]	OptFF(14ν)[b]	OptFF(ν)[c]
Bond Stretch	r_2	1.4294	1.4293
	r_1	1.4416	1.4423
	k_{r_2}	809.72	819.38
	k_{r_1}	790.57	790.31
	$k_{r_2r_1}$	42.100	41.835
Angle Bend	θ_{21}	116.28	116.32
	θ_{11}	115.64	115.65
	$k_{\theta_{21}}$	148.20	147.87
	$k_{\theta_{11}}$	165.29	162.83
	$k_{r\theta_{21}}$	78.107	80.632
	$k_{r\theta_{11}}$	39.124	38.275
Inversion	ω	22.867	22.814
	k_ω	13.041	13.060
Bond-x-angle	$c_{r\theta}$	14.698	13.911
angle angle 4c	$k_{\theta\theta'}$	-57.470	-59.301

[a] The Polyene option is used. For definitions, see Table 1.

[b] Optimized for geometry (i.e., R_2 and R_1) and all of 14 Raman and IR modes of C_{60}.

[c] Optimized for geometry (i.e., R_2 and R_1) and all of the modes except $4T_{1u}$ mode.

Table 6. Allowed IR and Raman transitions (cm^{-1}) predicted with the C_{60} OptFF. Comparison with experimental transitions known to be C_{60}.

Mode	Expt.[a]	OptFF(14ν)	$\Delta\nu$	OptFF(13ν)	$\Delta\nu$	Active
$1H_g$	273	279	6	279	6	Raman
$2H_g$	434	430	-4	430	-4	Raman
$1A_g$	496	493	-3	493	-3	Raman
$1T_{1u}$	527	528	1	528	1	IR
$2T_{1u}$	577	581	4	581	4	IR
$3H_g$	710	711	1	711	1	Raman
$4H_g$	774	774	0	774	0	Raman
$5H_g$	1100	1099	-1	1098	-2	Raman
$3T_{1u}$	1183	1183	0	1182	-1	IR
$6H_g$	1250	1250	0	1250	0	Raman
$4T_{1u}$	1428	1439	11	1445[c]	17	IR
$7H_g$	1426	1423	-3	1427	1	Raman
$2A_g$	1470	1462	-8	1469	-1	Raman
$8H_g$	1576	1576	0	1576	0	Raman

[a] Reference 20.

[b] Optimized for geometry (i.e., R_2 and R_1) and all of 14 Raman and IR modes of C_{60}. The abs deviation of frequencies is 2.5 cm^{-1}.

[c] Optimized for geometry (i.e., R_2 and R_1) and all of the modes except $4T_{1u}$ mode. The abs deviation of frequencies is 1.86 cm^{-1}.

Table 7. Vibrational frequencies (cm^{-1}) of C_{60} (I_h) calculated using the C_{60}FF.

A_g	A_u	T_{1g}	T_{2g}	T_{1u}	T_{2u}	G_g	G_u	H_g	H_u
Raman				IR				Raman	
493	1261	558	642	528	352	453	370	279	425
1462		983	863	581	721	635	819	430	491
		1402	900	1183	963	796	865	711	721
			1524	1439	1304	1170	1011	774	840
					1502	1486	1417	1099	1180
						1537	1551	1250	1483
								1423	1573
								1576	

Table 8. Comparison of vibrational frequencies from other calculations.

	Exper[a]	OptFF[b]	GraFF[c]	Harter[d]	Newton[e]	Slanina[f]	Cyvin[g]	Negri[h]
$1T_{1u}$	527	528	556	478	577	574	472	544
$2T_{1u}$	577	581	574	618	719	776	618	637
$3T_{1u}$	1183	1183	1113	1462	1353	1405	1119	1212
$4T_{1u}$	1428	1439	1276	1868	1628	1753	1434	1437
$1A_g$	496	493	488	510	610	660	388	513
$2A_g$	1470	1462	1281	1830	1667	1798	1409	1442
$1H_g$	273	279	261	274	263	284	218	258
$2H_g$	434	430	435	413	447	463	435	440
$3H_g$	710	711	759	526	771	730	645	691
$4H_g$	774	774	750	828	924	830	743	801
$5H_g$	1100	1099	1080	1292	1261	1325	1004	1154
$6H_g$	1250	1250	1104	1575	1407	1442	1221	1262
$7H_g$	1426	1423	1321	1910	1596	1686	1468	1465
$8H_g$	1576	1576	1517	2085	1722	1816	1601	1644
abs error		3	62	211	124	166	49	29

[a] Reference 20.

[b] The force field was optimized for the graphite.

[c] Optimized for geometry (i.e., R_2 and R_1) and all of 14 Raman and IR modes of C_{60}.

[d] MNDO, see reference 9.

[e] AM1, see reference 10.

[f] Spring-mass model, see reference 11.

[g] Normal coordinate analysis, see reference 12.

[h] QCFF/PI, see reference 34.

Table 9. The detailed Structure[g] of C_{70} Determined by Various Methods

Type	Expt.[a]	OptFF[b]	GraFF[c]	HF(dzP)[d]	MNDO[e]	QCFF/PI[f]
1 – 1	1.41	1.429	1.461	1.475	1.484	1.492
1 – 2	1.39	1.439	1.426	1.407	1.430	1.435
2 – 2	1.47	1.460	1.457	1.415	1.442	1.447
2 – 3	1.46	1.464	1.446	1.457	1.478	1.475
3 – 3	1.37	1.411	1.406	1.469	1.389	1.398
3 – 4	1.47	1.448	1.454	1.446	1.469	1.464
4 – 5	1.37	1.415	1.414	1.375	1.402	1.414
5 – 5	1.464	1.455	1.455	1.451	1.473	1.468

[a] Electron diffraction, see reference 13.

[b] Optimized for geometry and all of 14 Raman and IR modes of C_{60}.

[c] The force field was optimized for the graphite.

[d] Reference 14.

[e] Reference 15.

[f] Reference 16.

[g] the angle $\angle$ 2-1-2 =117.3°.

Table 10. Vibrational frequencies (cm^{-1}) of the C_{70} fullerene (D_{5h}).

IR Allowed		Raman Allowed			Other		
A_2''	E_1'	A_1'	E_2'	E_1''	A_2'	A_1''	E_2''
327	314	259	222	276	344	381	335
439	334	363	268	393	564	508	396
565	356	450	395	461	608	695	437
701	437	474	451	520	781	813	463
883	514	686	506	568	899	992	657
1070	537	703	567	687	1162	1070	671
1241	546	1022	695	735	1276	1346	698
1419	707	1168	728	780	1446	1478	730
1478	755	1294	747	879	1569	1671	836
1492	797	1442	782	887			878
	910	1493	839	1088			950
	966	1523	871	1181			1091
	1128		992	1186			1207
	1173		1104	1401			1278
	1252		1184	1428			1396
	1366		1294	1458			1457
	1435		1421	1486			1484
	1481		1455	1543			1541
	1498		1487	1657			1559
	1527		1518				1614
	1582		1541				
			1581				

[a]Raman-active modes.

[b]Infrared-active modes.

[c]ref

Table 11. Trends of vibrational frequencies with cluster size. Parentheses indicate observed transitions.

Type[a]	C_{50}	C_{60}	C_{70}
Raman			
squashing mode	281(A_1')	279 (273)(1H_g)	259 (260)(A_1')
	303(E_1'')		276 (E_1'')
	326(E_2')		222 (226)(E_2')
breathing mode	540(A_1')	493 (496)(1A_g)	450 (456)(A_1')
pentagon compression	1491(A_1')	1462 (1470)(2A_g)	1442 (1449)(A_1')
Ifrared			
out-of-plane mode	603(A_2'')	581 (577)(2T_{1u})	565 (565)(A_2'')
	650(E_1')		546 (535)(E_1')
out-of-plane mode	1435(A_2'')	1439 (1428)(4T_{1u})	1419 (1414)(A_2'')
	1440(E_1')		1435 (1430)(E_1')

[a] Refer to C_{60} molecule.

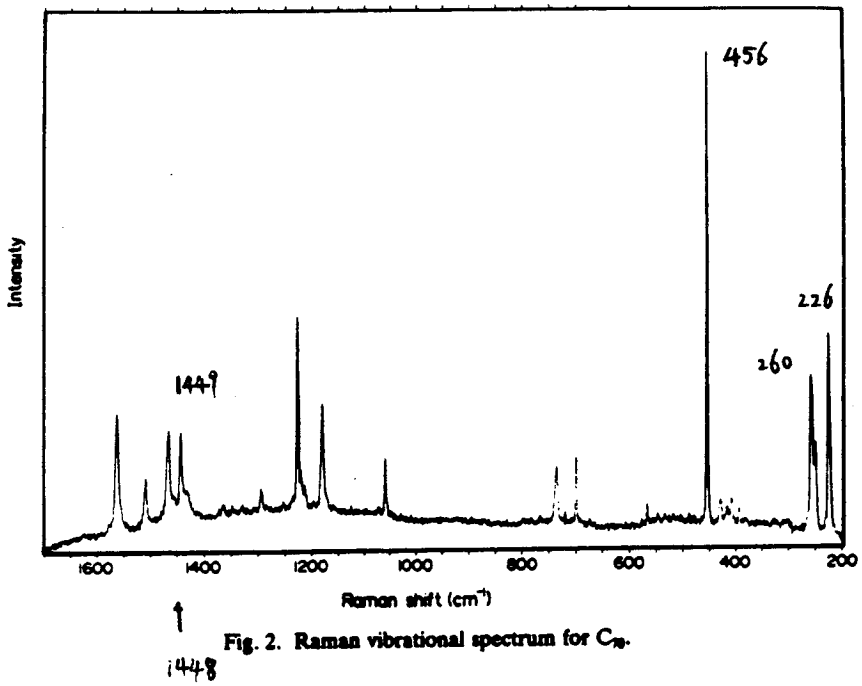

Fig. 2. Raman vibrational spectrum for C_{70}.

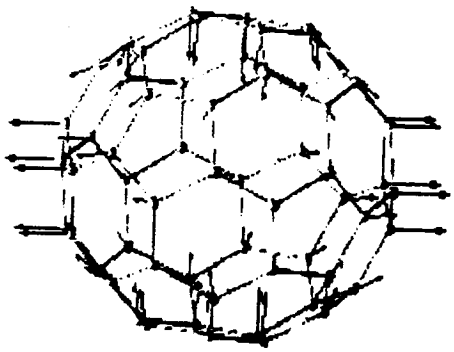

1Hg
273

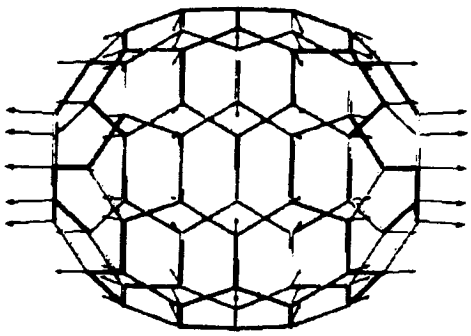

1A′1
2[illegible]

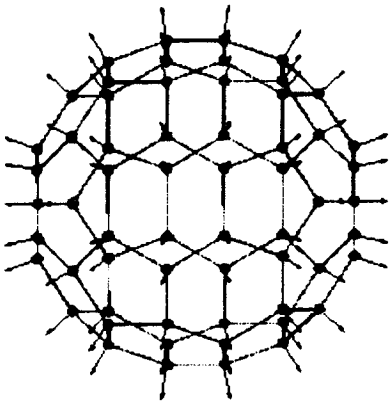

1Ag
496

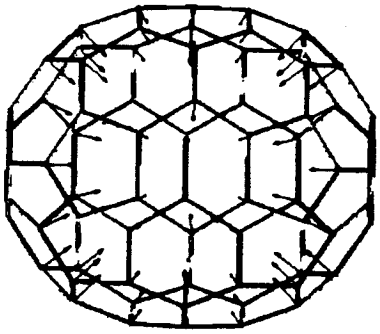

3A′1
45[illegible]

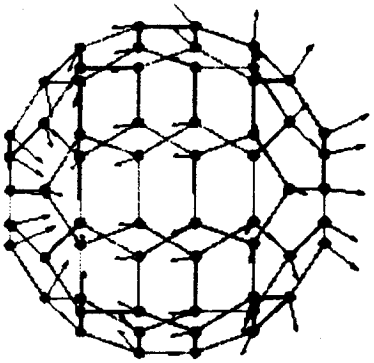

2T1u
577

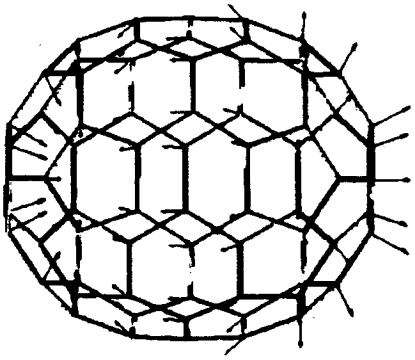

3A″2
565

Table 12. Vibrational frequencies (cm^{-1}) of C_{50} (D_{5h}) molecule.

IR Allowed		Raman Allowed			Other		
A_2''[b]	E_1'[b]	A_1'[a]	E_2'[a]	E_1''[a]	A_2'	A_1''	E_2''
373	396	281	326	303	571	512	401
603	456	515	430	468	721	673	436
701	526	540	521	605	987	871	496
1014	563	776	642	704	1110	1045	659
1227	650	839	762	772	1321	1431	718
1435	826	1129	812	834	1491	1592	840
1498	900	1299	837	903			889
	952	1444	904	1158			1055
	1059	1491	934	1221			1149
	1184		1047	1417			1291
	1232		1181	1480			1429
	1399		1303	1516			1518
	1440		1404	1598			1545
	1467		1472				1588
	1555		1501				
			1571				

[a]Raman-active modes.

[b]Infrared-active modes.

Table 13. Heat of formation[a] vs. size of fullerene and graphitic sheet.

Cluster Size[b]	Fullerene Energy/atom	Sheet Energy/atom	ΔE
C_{20} (I_h)	24.123		
C_{24} (D_{6d})	22.160	19.668	−2.492
C_{28} (T_d)	19.491		
C_{32} (D_3)	18.192	18.339	0.147
C_{48}		15.114	
C_{50} (D_{5h})	12.922	15.168	2.246
C_{60} (I_h)	10.993[c]	14.092	3.098
C_{70} (D_{5h})	10.117	13.322	3.205
C_{72} (D_{6d})	10.434	12.989	2.555
C_{76} (T_d)	9.589		
C_{78} (D_{3h})	9.409	12.652	3.243
C_{80} (I_h)	9.115		
C_{84} (D_{2d})	9.147	11.842	2.695
C_{180}		8.691	
C_{240} (I_h)	5.101		
C_{540} (I_h)	3.463		
Graphite layer[d]		1.304	
Graphite		0.000	

[a] Heat of formation in kcal (mol C)$^{-1}$.

[b] Symmetry for fullerenes only.

[c] Available experimental value is 9.82 kcal (mol C)$^{-1}$ (H-D. Beckhaus, C. Ruchardt, M. Kao, F. Diederich, and C. S. Foote, Angew. Chem. Int. Ed. Engl. **31**. 63 (1992)).

[d] Graphitic monolayer.

Table 14. Heat of formation[a] for C_{76}, C_{78}, and C_{84}.

Structure		ΔH_f (kcal mol^{-1})	$\Delta(\Delta H_f)$ (kcal mol^{-1})		
			GraFF	MM3[e]	MNDO[f]
C_{76}	T_d	728.74	0.00		
	D_2[b]	747.09	18.35		
C_{78}	D_{3h}	733.87	0.00	3.5	
	C_{2v}	744.37	10.50	0.0	
	D_3[c]	759.65	25.78	3.5	
	C'_{2v}[c]	760.71	26.84	1.4	
	D'_{3h}	782.48	48.61	8.0	
C_{84}	D_{2d}	768.38	0.00		0.0
	D_2	768.70	0.32		0.3
	C_1	771.66	3.28		-
	D_{3d}	776.45	8.07		-
	C_s	779.26	10.88		-
	D_{6h}	782.77	14.39		8.0
	T_d	808.88	40.50		31.4
	D'_2[d]	820.68	52.30		58.0

[a] Heat of formation zero for graphite and 659.59 kcal mol^{-1} for C_{60} by GraFF.

[b] NMR assignment, see reference 29.

[c] NMR assignment, see reference 30.

[d] Tentative NMR assignment, see reference 29.

[e] Reference 30.

[f] Reference 31.

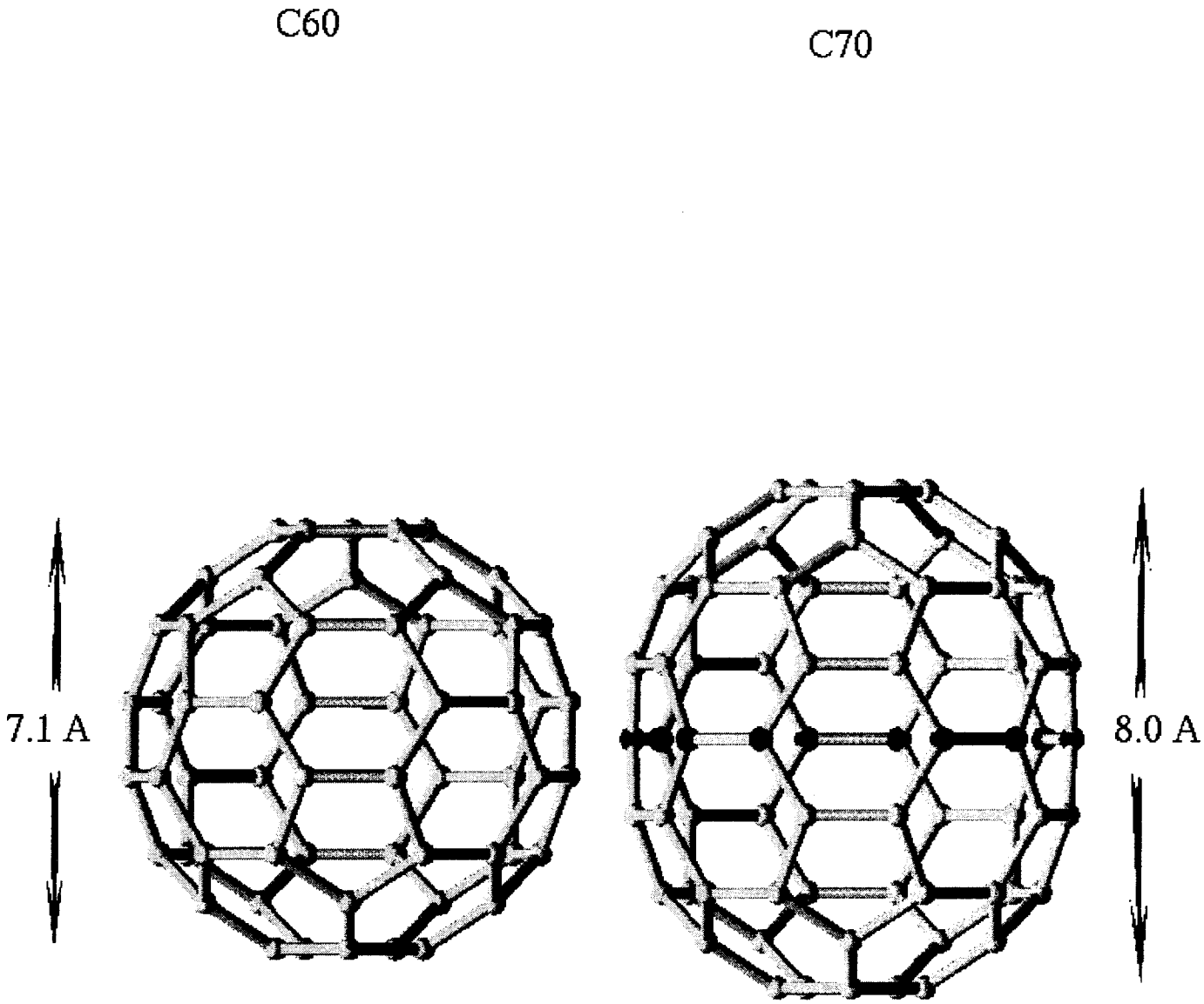

Figure 1.

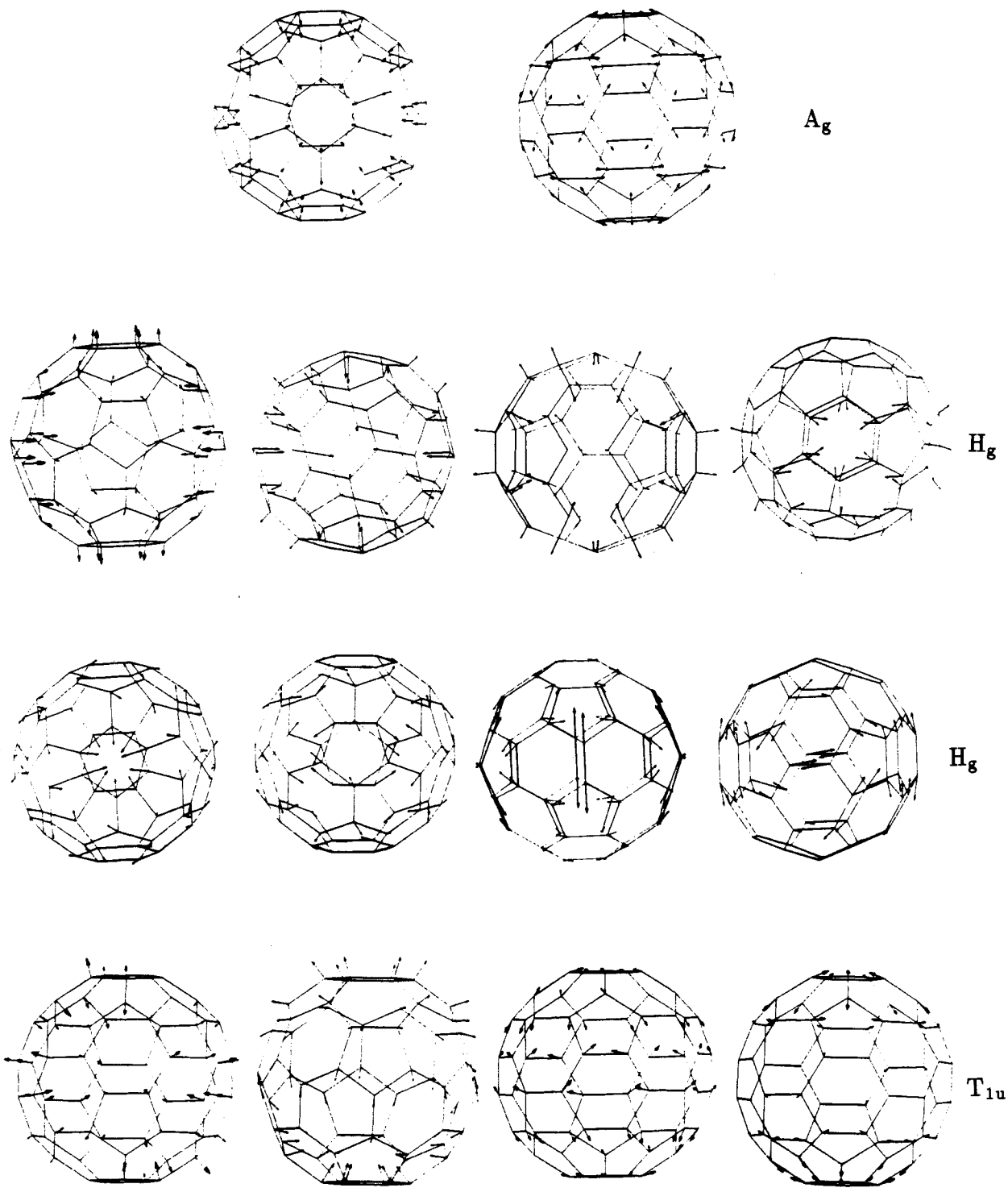

Figure 2.

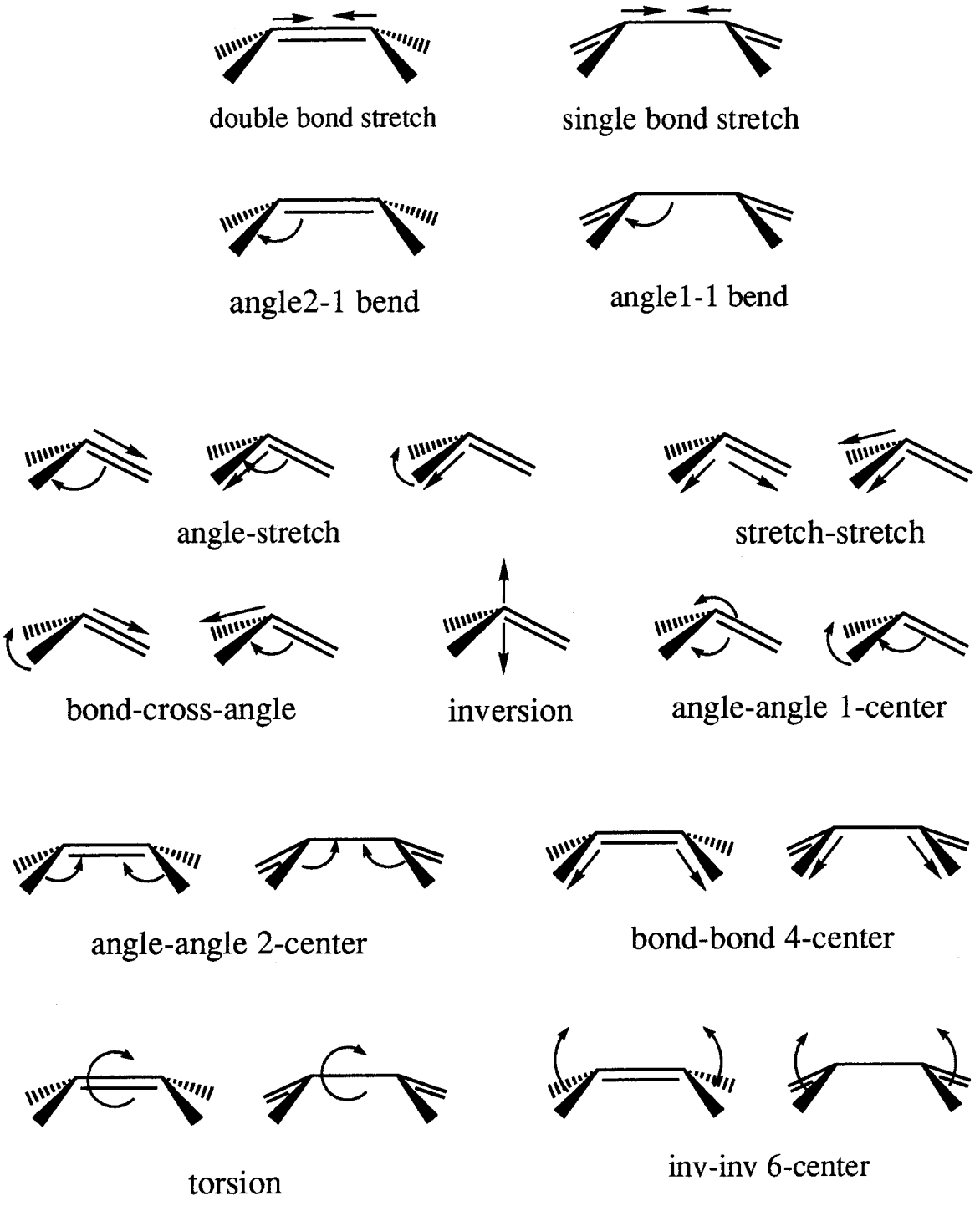

Figure 3. Force field terms for C_{60}

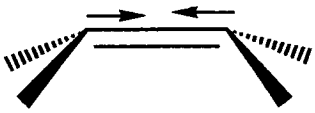

double bond stretch

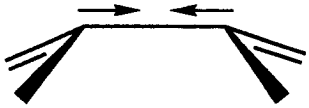

single bond stretch

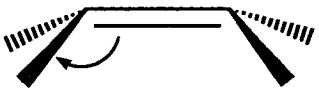

angle2-1 bend

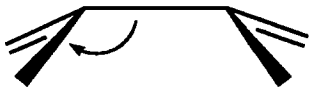

angle1-1 bend

angle2-1-stretch

angle1-1-stretch

stretch2-stretch1

bond-cross-angle

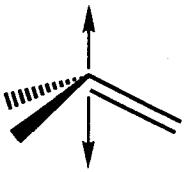

inversion

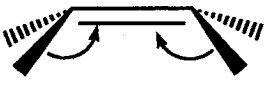

angle-angle 2-center

Figure 4. Force field terms for C_{60}

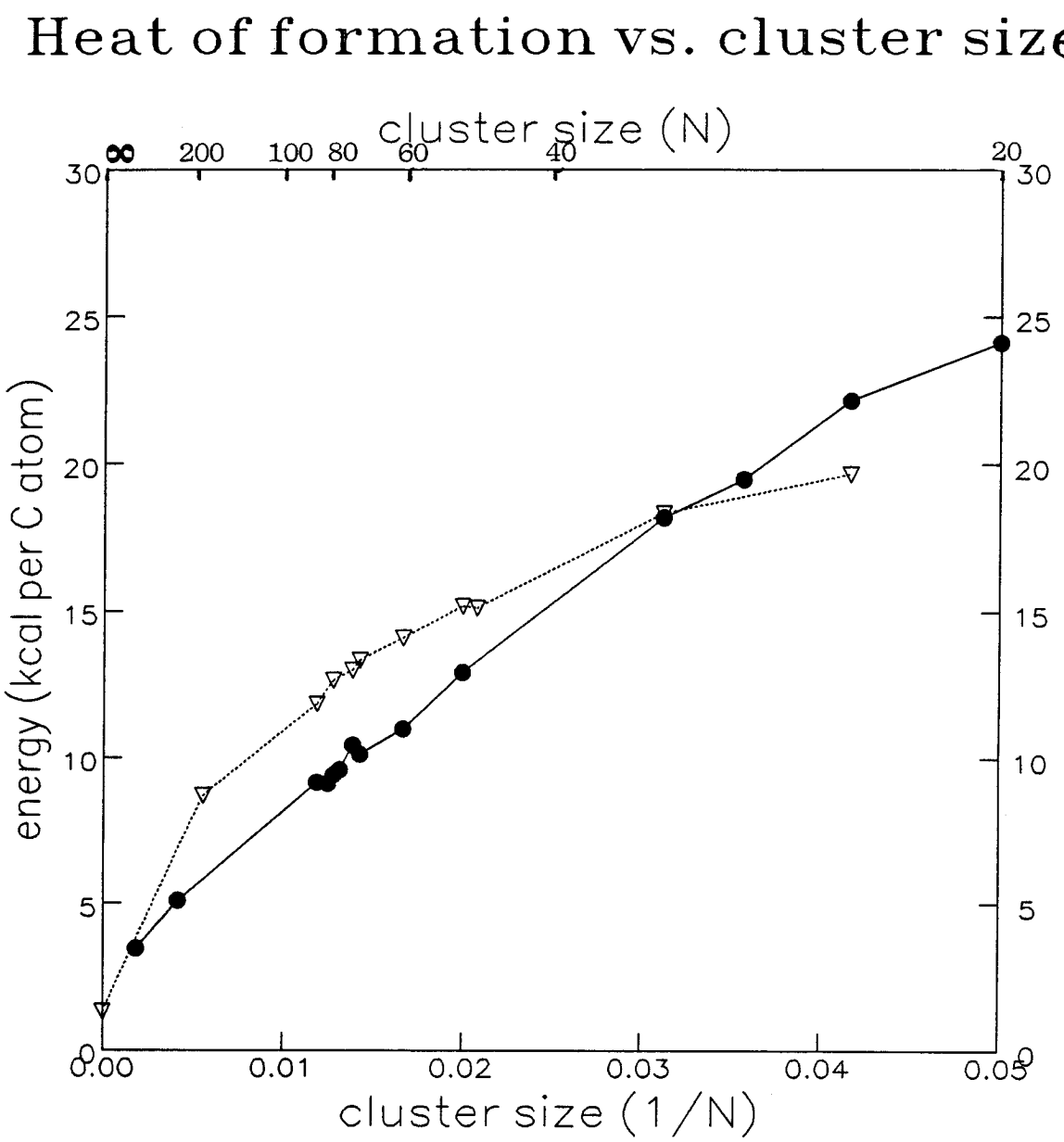
Heat of formation vs. cluster size
cluster size (N)
∞
200
100
80
60
40
20
energy (kcal per C atom)
0
5
10
15
20
25
30
0.00
0.01
0.02
0.03
0.04
0.05
cluster size (1/N)

Figure 5.

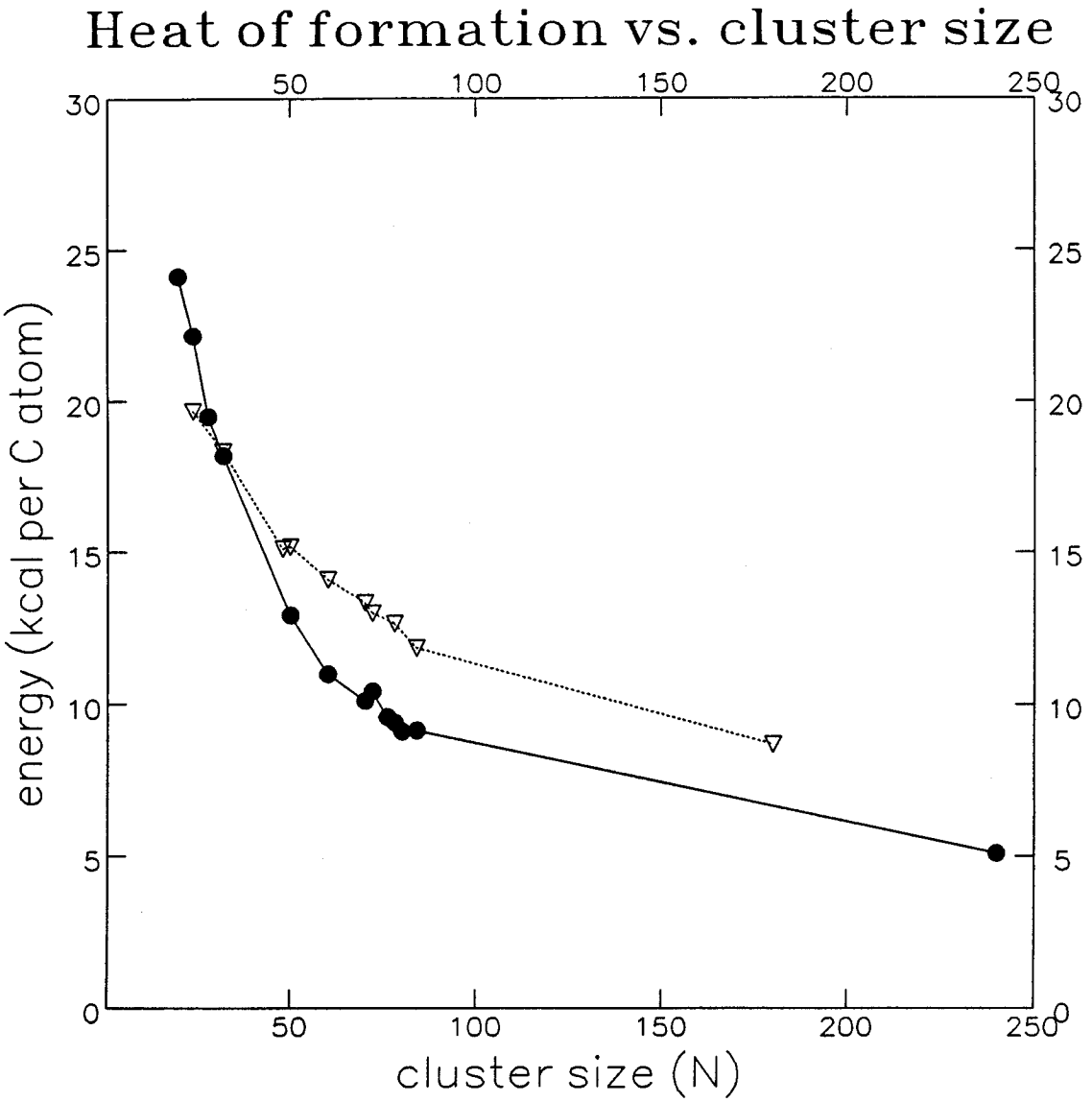
Heat of formation vs. cluster size
energy (kcal per C atom)
cluster size (N)
0
5
10
15
20
25
30
50
100
150
200
250

Figure 6.

C_{60}SHEET

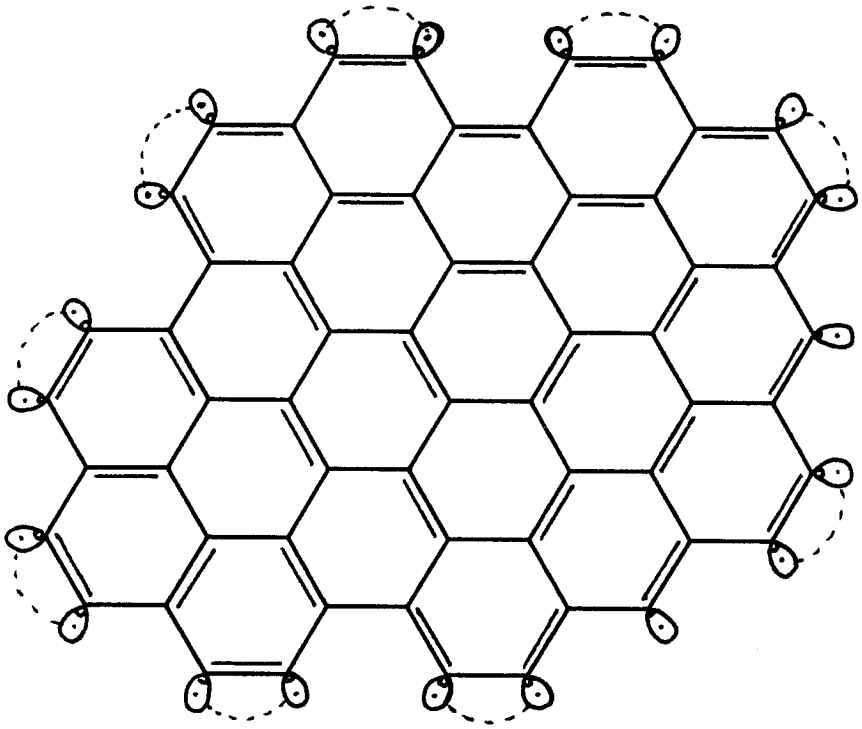

Figure 7.

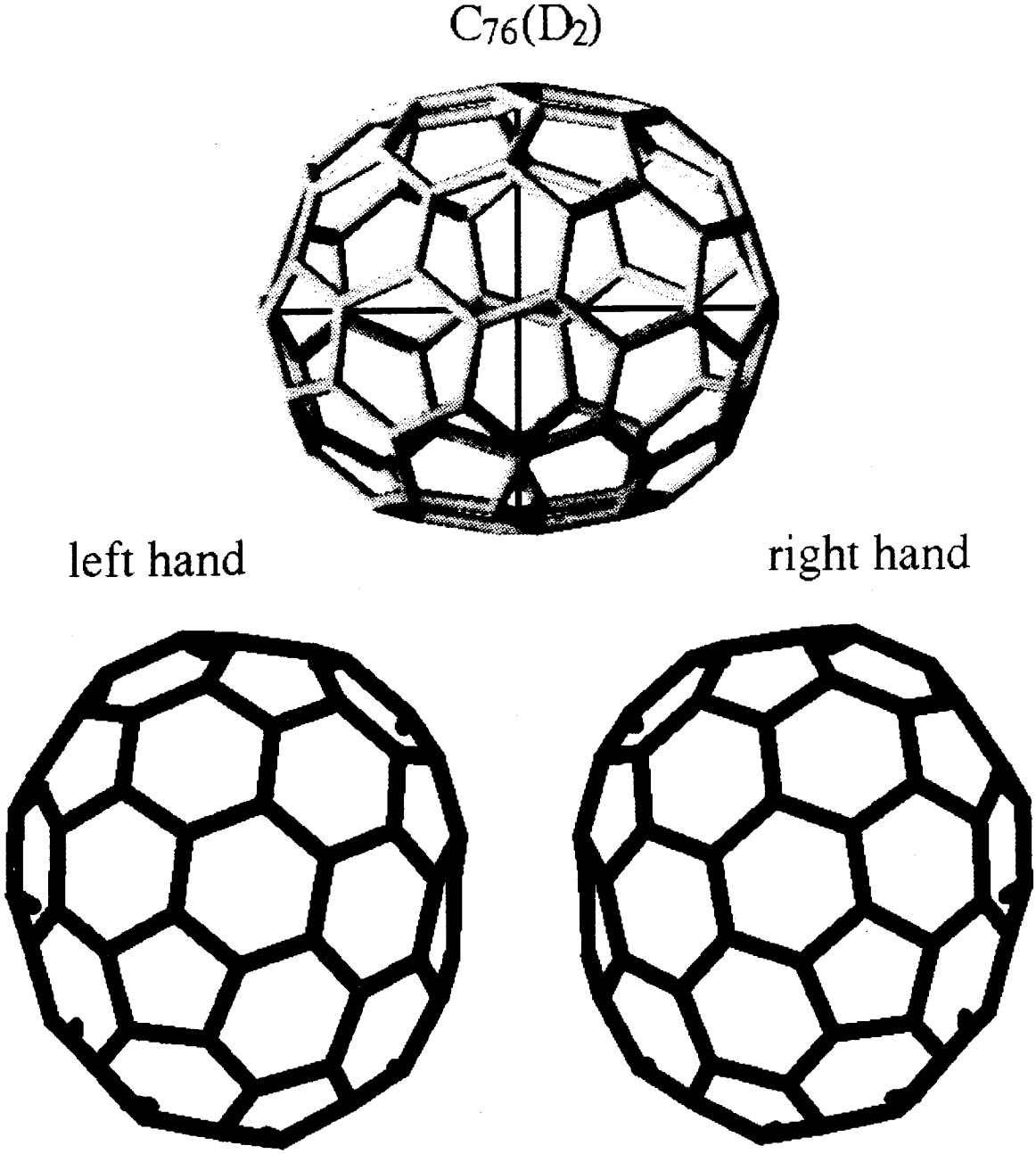

Figure 8.

Chapter 3

3.1 Packing of Buckyballs; Prediction of Fullerene C_{60} and C_{70} Crystals

Packing of Buckyballs; Prediction of Fullerene C_{60} and C_{70} Crystals

Yuejin Guo, Naoki Karasawa, and William A. Goddard III

Materials & Molecular Simulation Center

Beckman Institute (139-74)

California Institute of Technology, Pasadena, California 91125

Abstract

Recent breakthroughs[1,2] in synthesizing large amounts of C_{60}, C_{70} and other fullerenes (buckminsterfullerenes or buckyballs)[3] have led to copious quantities of material; however, there is very little data or understanding of the structures and properties of fullerene crystals. We present a general analysis of the packing of such molecules that predicts C_{60} to have cubic closest packing (FCC) and predicts C_{70} to have hexagonal closest packing (HCP). Using a force field developed recently for sp^2 carbon centers, we predict here the crystal structures and cohesive energies for closest packed crystals of C_{60} and C_{70} fullerenes. We find, as expected, that C_{60} has FCC *more* stable than HCP (by 0.90 kcal/mol), whereas C_{70} has HCP more stable than FCC (by 0.35 kcal/mol). The predicted structure of C_{60} leads to an orthorhombic distortion (*Cmca*) at 0 K. Dynamics calculations indicate that there is rapid reorientation (but not free rotation) of the C_{60} molecules at higher temperatures, suggesting a phase transition from orthorhombic at low temperature to an orientationally disordered form (equal lattice parameters of 14.13 Å) at room temperature. This may correspond to the first order transition observed[4] at 249 K. The ideal FCC structure with 3-fold axes of C_{60} oriented along the body diagonals, leads to a much higher energy (by 5.08 kcal/mol).

To understand the packing of fullerenes it is useful to consider the energetics of fullerene dimers in various orientations. For C_{60} dimer the best interaction is with two hexagonal faces in contact (same orientation, but with the centers shifted by 0.92 Å toward one edge) as in Figure 1a. The bond distance is R_e = 9.84 Å (center to center) and the bond energy is D_e = 7.20 kcal/mol. This leads to a separation of the faces of 3.27 Å and a closest atom-atom distance of 3.36 Å. The worst orientation leads to an energy of 6.10 kcal/mol, about 1 kcal/mol higher than the best.

For C_{70} dimer the optimum interaction is with the long axes parallel. The midriff involves both concave and convex graphite-like regions, and the best interaction (D_e = 8.97 kcal/mol, R_e = 9.94 Å) has a convex side matched with a concave side. Here the worst orientation leads to an energy of 6.09 kcal/mol, about 3 kcal/mol worse than the best.

Because of noncrystallographic symmetries (five fold axes), it is not possible for these fullerenes to retain the optimal dimer orientation in closest packed structures. However the symmetry of the fullerene **does** affect the packing. To understand why C_{60} prefers FCC whereas C_{70} prefers HCP, consider a closest packed layer B and the optimized closest packed layer A on top as in Figure 2. The fullerenes orient so as to have the best average interactions both within and between layers. For C_{60} (symmetry I_h) this leads to hexagonal faces almost in contact (see molecules a and b in Figure 2a, also Figure 1b). The inversion symmetry of C_{60} implies that the optimum interaction of the molecule b in layer B with molecules of layer C is to have each c molecule *on the opposite side of* the optimal b-a interaction. Thus we expect C_{60} to prefer ABCABC or FCC packing, as in Figure 2a.

For C_{70} (symmetry D_{5h}) optimal packing within a closest packed plane leads to the long axis (5-fold) perpendicular to the plane (see Figure 2b), with the horizontal reflection σ_h in the plane. In this case the optimum interaction of molecules

b and c is *on the same side* as the optimum b-a interaction. Thus the best packing is for layers C and A to be the same, leading to ABABAB or HCP packing for C_{70}, as in Figure 2b.

There are no definitive crystal structures published for C_{60} or C_{70}. Reference 1 concluded that the structure for C_{60} is HCP; however, the data did not really distinguish between HCP and FCC. Stoddart[5] quoted unpublished work by Diederich, indicating that FCC is more stable for C_{60}. Indeed, Diederich (private communication) observes only cubic crystal habits for C_{60} and only hexagonal habits for C_{70}, as would be expected from our predictions (the crystals do not lead to sufficient quality diffraction data for structural analysis). [The referee suggested that other unpublished experimental studies supporting FCC structure for C_{60} are in circulation.] The predicted differences in energy between HCP and FCC suggests that compression annealing might be used to obtain more highly crystalline samples of fullerenes. The calculated density for FCC C_{60} of 1.745 g cm^{-3} (0 K) and 1.697 g cm^{-3} (300 K) (from molecular dynamics) are in agreement with the observed density of 1.678 g cm^{-3} at room temperature.[1]

In order to interpret and predict various properties for fullerene molecules and crystals, (including vibrational spectroscopy,[1,2,6] crystal structure analysis,[1] NMR,[7] STM,[8,9] etc.), we developed a force field[10] for sp^2 carbon centers by fitting experimental lattice parameters, elastic constants, and phonon frequencies for graphite. This force field uses Lennard-Jones 12-6 van der Waals interactions [R_v = 3.8050, D_v = 0.0692], Morse bond stretches [R_b = 1.4114, k_b = 720., D_b = 133.0], cosine angle bends [θ_a = 120, $k_{\theta\theta}$ = 196.13, $k_{r\theta}$ = 62.71, k_{rr} = 68.], and a two fold torsion [V_t = 21.28], where all distances are in Å, all angles in degrees, and all force constants and energies in kcal/mol, Å, radian units. For more details on the forms of these potentials, see reference 11. All calculations in this paper were all carried out using POLYGRAF from Molecular Simulations Inc. of Sunnyvale California

(formerly known as BioDesign) in conjunction with additional vibrational analysis software written by N. Karasawa, S. Dasgupta, and W. A. Goddard of the Materials & Molecular Simulation Center at Caltech. The calculations were carried out on Silicon Graphics 4D/380 and 4D/25 graphics workstations.

Using this force field and allowing four independent molecules per unit cell (permitting the molecules to reorient with respect to each other), we calculated the optimum crystal structures for both simple types of closest packing, HCP and FCC. We also considered BCC packing (8 neighbors instead of 12), but this led to much higher energies. In these calculations we used periodic boundary conditions with accuracy bounded convergence acceleration[12] for the long range vdW interactions. All $4 \times 60 \times 3 = 720$ internal degrees of freedom plus the six cell degrees of freedom were simultaneously optimized. We calculated all second derivatives of the energy with respect to these 726 degrees of freedom in order to determine whether the structures are locally stable (all second derivatives positive).

The optimum structure for C_{60} is in Figure 2a and Figure 3 where the blue lines indicate the unit cell. The unit cell distorts, leading to the *Cmca* space group (orthorhombic symmetry). Although four independent C_{60} molecules were allowed, we find that the optimum structure has two independent molecules, as indicated in Figures 2a and 3. We found three other locally stable FCC structures (all second derivatives positive) at 0.31, 0.51 and 0.66 kcal/mol higher (per C_{60}). The HCP structure was 0.90 kcal/mol higher (also locally stable).

Based on symmetry one might have expected FCC C_{60} to orient the diagonal (3-fold) axes of each C_{60} so as to correspond to the 3-fold axes of a cubic crystal (this orients the 2-fold axes of C_{60} along the cubic axes). The optimum such structure is shown in Figure 4; it is not stable (leading to three imaginary frequencies all corresponding to rotations of the C_{60}'s). We will refer to this as the *ideal FCC* structure. As shown in Table 1, the energy of the ideal FCC structure is quite high,

5.08 kcal/mol. This is close to BCC and five times as high as HCP! The reason is that this packing does not allow the hexagonal faces to contact. Instead it leads to poor nearest neighbor interactions as in Figure 1d.

In Figure 1b and 1c we show the nearest neighbor interactions for C_{60} crystal. Each C_{60} leads the eight good interactions (Figure 1b) corresponding closely to the optimum dimer and four (Figure 1c) that are worse by about 1 kcal/mol. The average energy and distance for the good interactions is 7.11 kcal/mol and 9.83 Å (versus 7.20 and 9.84 for the dimer), whereas the average values for the four bad interactions is 6.12 kcal/mol and 10.06 Å. On the other hand, the ideal FCC structure leads to 12 interactions (Figure 1d) that are nearly the worst possible (6.01 kcal/mol and 10.06 Å). This difference of $8 \times 1.10 \times \frac{1}{2}$ accounts for 4.40 kcal/mol of the 5.08 kcal/mol difference in energy. [Interestingly, for K_3C_{60} we find[13] a FCC unit cell with exactly this ideal structure of the C_{60} units; here the electrostatic and vdW interactions between K and C_{60} dominate.]

The optimum FCC structures leads to a distorted, orthorhombic crystal structure at 0 K, and the other low lying structures with FCC packing (at 0.3 to 0.7 kcal/mol) also distort at low temperature. Carrying out molecular dynamics calculations for short periods (20 ps) shows that at low temperature (100K-200K), the C_{60} molecules librate locally around the equilibrium and do not rotate. However near room temperature (300-400K), the C_{60} molecules tunnel from one favored orientation to another. Such orientational fluctuations lead to an average structure that is cubic (A = 14.13 Å at 300 K) with orientational disorder (but *not* free rotation) among the C_{60} molecules. [Note that this cubic structure is *not* the ideal FCC structure.] Thus we expect a phase transition between the distorted orthorhombic form (at low temperature) and the cubic, orientationally disordered form (at room temperature). The first-order transition observed[4] at 249 K might correspond to this transition. This transition temperature should increase and the

lattice parameter should decrease as better quality crystals are produced.

For C_{70} the interactions in the crystal are much more anisotropic than for C_{60}. The interactions within the plane have R_e = 9.92 to 10.06 Å (10.00 average) and D_e = 8.23 to 8.79 kcal/mol (8.47 average) while those out-of-plane have R_e = 10.83 to 10.96 Å (10.91 average) and D_e = 6.75 to 7.18 kcal/mol (6.90 average). This can be compared to the optimum dimer interactions of R_e = 9.94 Å and D_e = 8.97 kcal/mol.

We also calculate the intermolecular vibrational properties of $(C_{60})_2$ and $(C_{70})_2$ dimers, and the frequencies are summed in Table 2. For $(C_{60})_2$, as shown in Figure 5a, the best interaction is with two 6-fold faces in contact (same orientation but with the centers shifted by 0.92 Å toward one edge). This leads to C_{2h} symmetry (yz symmetry plane with z as the dimer axis). The bond distance is 9.84 Å (center to center) and the bond energy is 7.19 kcal/mol. This leads to a separation of the faces of 3.27 Å and a closest atom-atom distance of 3.36 Å. The stretching vibration is at 28.7 cm^{-1} while the shear mode (rotation of molecules about the dimer axis in opposite direction) is at 0.9 cm^{-1}. The other (rolling) modes are at 2 to 8 cm^{-1} (see Table 2) and correspond to rotations in the xy and yz planes, either synchronously (syn, both clockwise) or antisynchronously (anti, one clockwise, one counter clockwise).

For C_{70} dimer the optimum interaction is with the long axes parallel (Figure 5b). The midriff involves both concave and convex regions, and the best interaction (bond energy 8.97 kcal/mol, R_e = 9.1 Å) has a convex side matched with a concave side. This leads to C_{2v} symmetry with C_2 axis in dimer axis. The stretching vibrational frequencies is the same as for C_{60} but the other modes are ~50% higher.

After submission of this manuscript, a paper from the Margrave[14] group reported heats of sublimation of ΔH_{707K} = 40.1 ± 1.3 kcal/mol for C_{60} and ΔH_{739K} = 43.0 ±2.2 kcal/mol for C_{70}. Our calculations lead to a cohesive energy of 43.9

kcal/mol for C_{60} and 49.5 kcal/mol for C_{70}. Correcting for zero point energy and temperature dependence of C_v, S, and H for both the crystal and free molecule, we calculate $\Delta H_{707K} = 40.9$ kcal/mol for C_{60} and $\Delta H_{739K} = 46.4$ kcal/mol for C_{70}, in excellent agreement with experiment.

The research was funded by the Air Force Office of Scientific Research (AFOSR-88-0051). This is contribution 8445 from the Division of Chemistry and Chemical Engineering at Caltech.

References

1. Krätschmer, W., Lamb, L. D., Fostiropoulos, K. & Huffman, D. R. *Nature* **347**, 354-358 (1990).
2. Krätschmer, W., Fostiropoulos, K. & Huffman, D. R. *Chem. Phys. Lett.* **170**, 167-170 (1990).
3. Kroto, H. W., Heath, J. R., O'Brien, S. C., Curl, R. F. & Smalley, R. E. *Nature* **318**, 162-164 (1985).
4. Heiney, P. A. *et al. Phy. Rev. Lett.* (submitted). Quoted by Sleight, A. W. *Nature* **350**, 557-558 (1991).
5. Stoddart, J. F. *Angew. Chem. Int. Ed. Engl.* **30**, 70-71 (1991).
6. Bethune, D. S., Meijer, G., Tang, W. C. & Rosen, H. J. *Chem. Phys. Lett.* **174**, 219-222 (1990).
7. Taylor, R., Hare, J. P., Abdul-Sade, A. K. & Kroto, H. W. *JCS Chem. Comm.* **20**, 1423-1425 (1990).
8. Wilson, R. J. *et al. Nature* **348**, 621-622 (1990).
9. Wragg, J. L., Chamberlain, J. E., White, H. W., Krätschmer, W. & Huffman, D. R. *Nature* **348**, 623-624 (1990).
10. Goddard, W. A. & Karasawa, N. *J. Phys. Chem.* (submitted).
11. Mayo, S. L., Olafson, B. D. & Goddard, W. A. *J. Phys. Chem.* **94**, 8897-8909 (1990).
12. Karasawa, N., & Goddard, W. A., *J. Phys. Chem.* **93**, 7320-7327 (1989).
13. Guo, Y & Goddard, W. A. *Science* (submitted).
14. Pan, C., Sampson, M. P., Chai, Y., Hauge, R. H. & Margrave, J. L. *J. Phys. Chem.* **95**, 2944-2946(1991).

Figure Captions

Figure 1. Optimum interactions between adjacent molecules. (a): free dimer; (b) and (c): the optimal interactions in FCC C_{60} [of the 12 nearest neighbor interactions the 8 in (b) are similar to the dimer (a)]; and (d): interactions for ideal FCC.

Figure 2. (a) Calculated crystal structure of C_{60} fullerene (buckyball). Shown (in blue) is one of the four molecules of the FCC unit cell, surrounded by its optimum 12 neighbors. (b) Calculated crystal structure of C_{70} fullerene (buckyball). Shown (in blue) is one of the four molecules of the HCP unit cell, surrounded by its optimum 12 neighbors.

Figure 3. Optimum FCC. The FCC unit cell of C_{60} is projected along the three axes. The orthorhombic unit cell is shown with blue lines. Balls of different color are in different planes.

Figure 4. Ideal FCC. In this structure 3-fold axes of C_{60} lie along diagonal axes of the cube.

Figure 5. $(C_{60})_2$ and $(C_{70})_2$ dimers

Table 1. Properties of fullerene crystals.

Structure[a]	Energy (kcal/mol)	Density (g/cm^3)	Cell Parameters (Å and degree.) A	B	C	α	β	γ
C_{60} FCC-best	0.000[b]	1.745	14.22[d]	14.22	13.56	90.01	90.00	90.00
FCC-2nd	0.312	1.740	14.27	14.28	13.50	90.01	90.00	90.01
FCC-3rd	0.505	1.737	14.32	14.26	13.50	90.00	90.00	89.72
FCC-4th	0.660	1.736	13.89	14.26	13.92	89.70	89.99	89.83
HCP	0.903	1.732	9.84	19.77[f]	16.31	90.44	90.98	119.39
FCC-ideal	5.078	1.662	10.06	10.06	10.06	60.00	60.00	60.00
BCC	5.279[e]	1.662	9.78	9.78	9.77	109.47	109.47	109.47
C_{70} HCP	0.000[c]	1.740	9.92	20.09[f]	18.52	90.01	90.00	119.61
FCC	0.351	1.736	14.84	14.84	14.76	85.44	85.44	84.23
BCC	10.682[e]	1.604	10.13	10.26	10.19	107.41	107.33	107.68

[a] All calculations allowed four independent molecules per cell (except BCC where there was only one independent molecule per rhombrohombic cell).

[b] Total cohesive energy is 43.8826 kcal/mol using the minimum energies for gas phase and crystal. Correcting for zero point energy and the temperature dependence of C_v, S, and H, we obtain $\Delta H_{707K} = 40.9$ kcal/mol.

[c] Total cohesive energy is 49.5057 kcal/mol using the minimum energies for gas phase and crystal. Correcting for zero point energy and the temperature dependence of C_v, S, and H, we obtain $\Delta H_{739K} = 46.4$ kcal/mol.

[d] Averaging the lattice parameters leads to A = B = C = 14.00 Å at 0K and A = B = C = 14.13 Å at 300K.

[e] BCC is not locally stable and we restricted the calculation to ideal angles.

Table 2. Fullerene dimers

	Bond			Vibrational Modes				
Mole.	R_e	D_e	Shear	Roll				Stretch
				XZ s	XZ a	YZ s	YZ a	
C_{60}	3.37	7.19	0.9	8.3	2.1	7.0	7.8	28.7
C_{70}	3.30	8.97	1.2	7.2	3.2	3.5	12.4	28.6

[a]Z is the dimer axis.

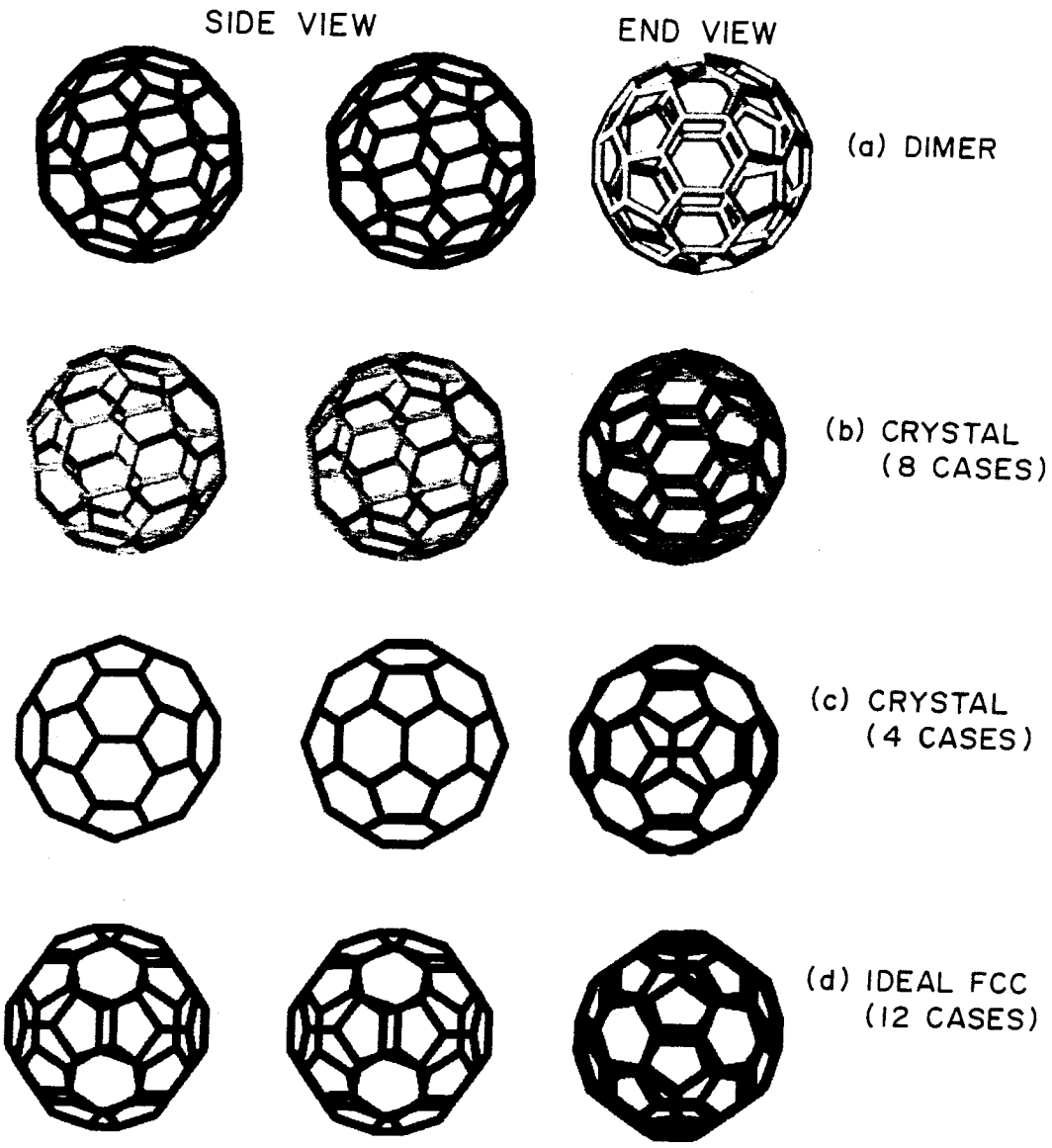
SIDE VIEW
END VIEW
(a) DIMER
(b) CRYSTAL
(8 CASES)
(c) CRYSTAL
(4 CASES)
(d) IDEAL FCC
(12 CASES)

Figure 1.

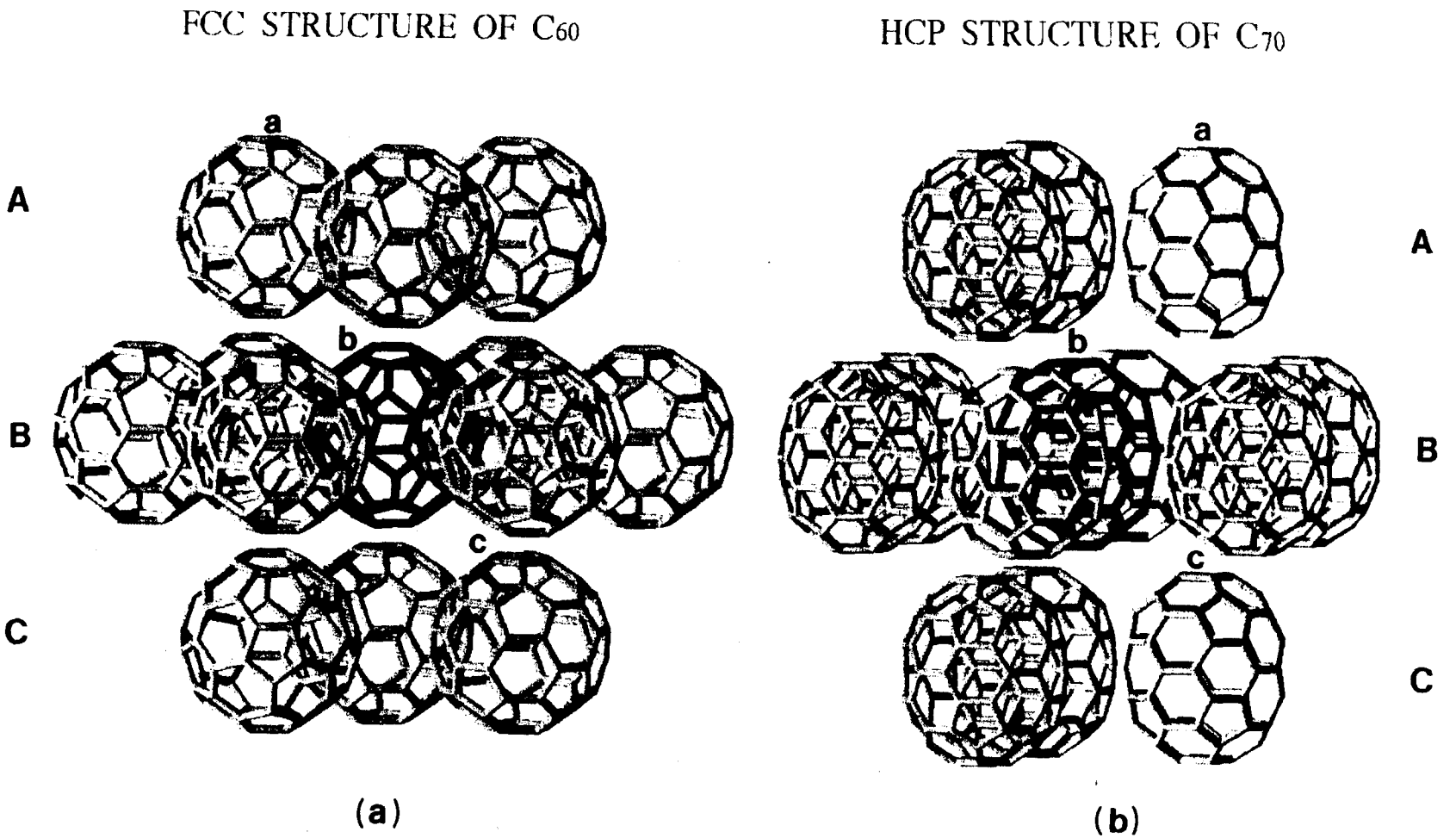

Figure 2.

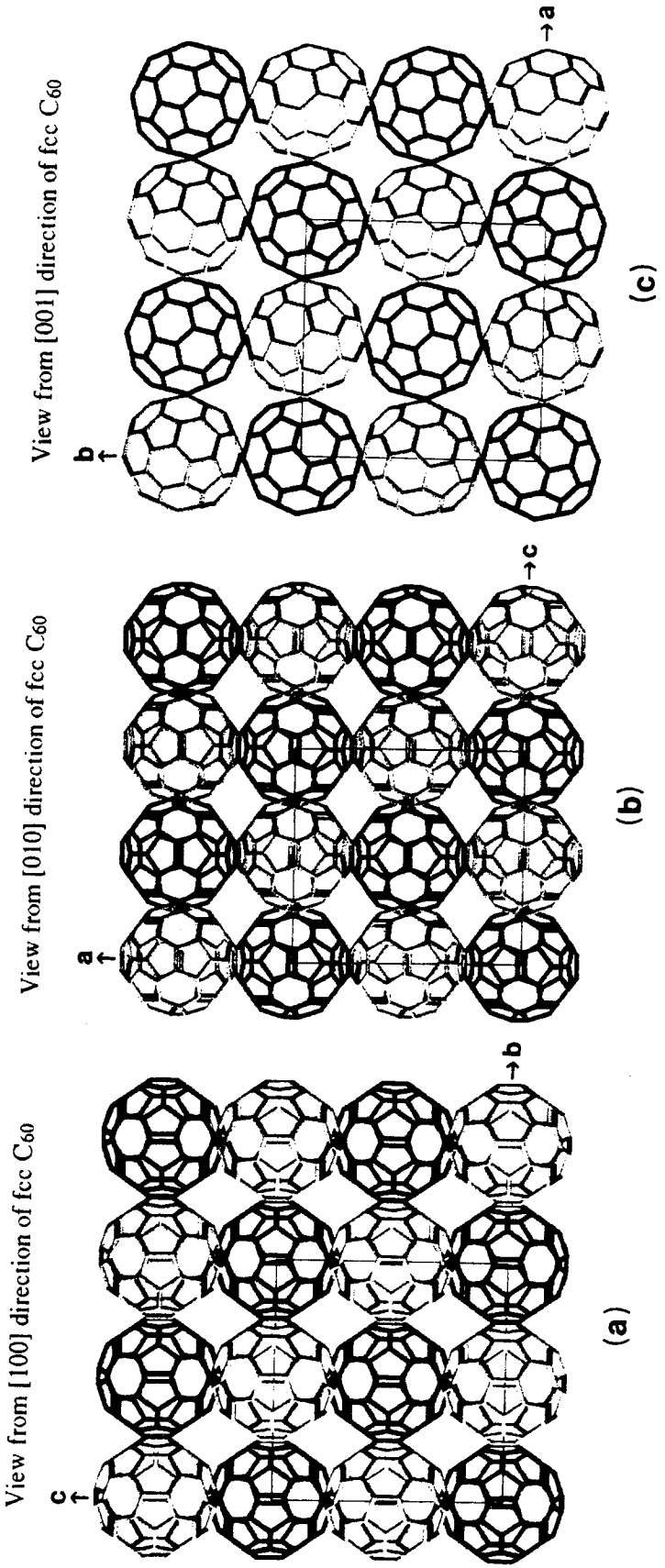
View from [100] direction of fcc C_{60}
c
b
(a)
View from [010] direction of fcc C_{60}
a
c
(b)
View from [001] direction of fcc C_{60}
b
a
(c)

Figure 3.

View from [111] direction of perfect fcc C_{60}

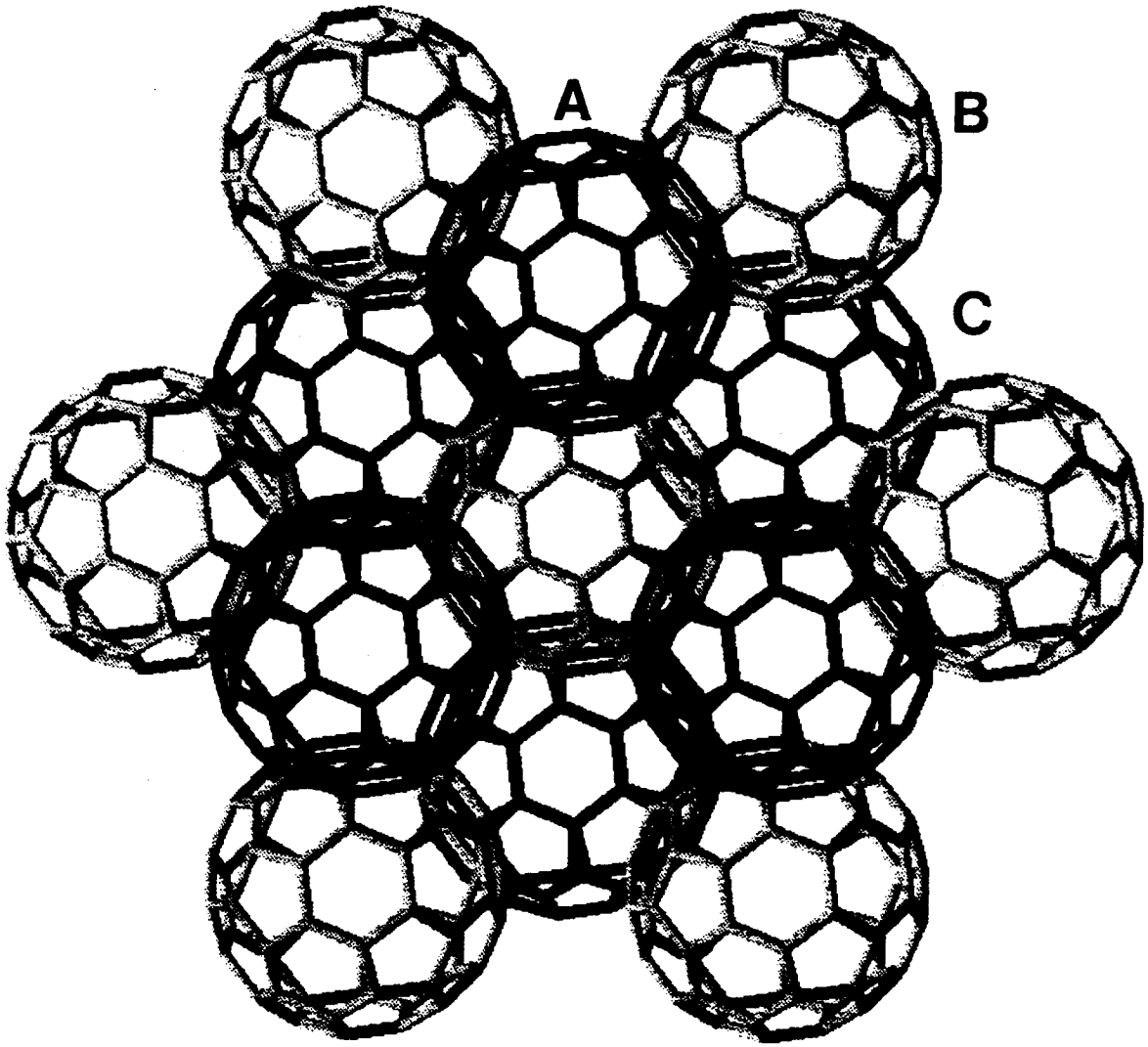

Figure 4.

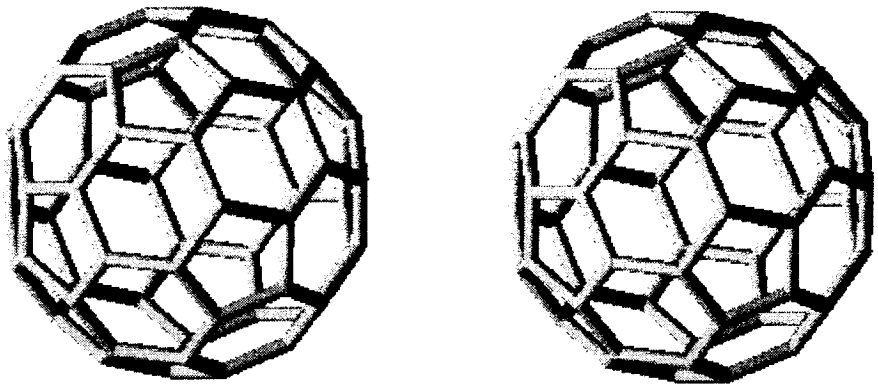

C_{60} DIMER

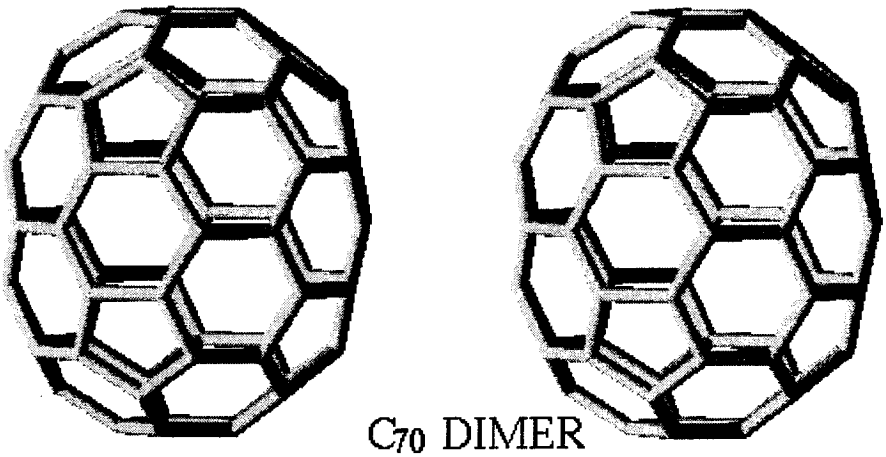

C_{70} DIMER

Figure 5.

Chapter 3

3.2 The hcp Structure of C_{70} Fullerite Crystal

The hcp Structure of C_{70} Fullerite Crystal

Yuejin Guo, Naoki Karasawa, and William A. Goddard III

Materials & Molecular Simulation Center

Beckman Institute (139-74)

California Institute of Technology, Pasadena, California 91125

Recent breakthroughs[1,2] in synthesizing and separating large amounts of C_{60}, C_{70}, C_{76}, C_{78}, C_{84}, and C_{94} have made it possible to study the structures and properties of fullerite crystals. However, there is little data or understanding of the structures and properties of fullerite crystals, except for C_{60} fullerite. We previously presented[3] a general analysis of the packing of such molecules that predicted C_{60} to have cubic closest packing (fcc) and predicted C_{70} to have hexagonal closest packing (hcp).

Recent X-ray and TEM studies by Gu *et al.*[4] showed that C_{60} molecules form either fcc or hcp crystals, depending on the substrate and sublimation conditions (also impurities). More interesting, X-ray and TEM studies on sublimated samples show a new phase with A = 10.01 and C = 18.58 Å at 300 K, but no specific assignment was made. We propose that this new phase is hcp C_{70}. Our predicted structure for hcp C_{70} has A = 10.0 Å and C = 18.5 Å (0 K), almost exactly the same as the experimental lattice parameters (we expect increases by 0.05 to 0.10 Å for 0 to 300 K). The Gu *et al.* results also confirmed our predictions[3] (experiment in parenthesis, T = 300 K) of A=14.0 Å (14.2) for fcc C_{60} , A=9.9 (10.1) and C=16.3 Å (16.4) for hcp C_{60}, at T=0 K (Krätschmer *et al.* originally reported that A=10.02 and C=16.36 Å).[2]

For C_{60} theory[3] and experiment[5,6] agree that the basic packing is fcc with a low temperature ordered phase and a high temperature cubic phase (phase transition[5] $\sim$ 249K) having orientational disorder. However, C_{70} fullerite is much less well characterized. In this report we will mainly focus on C_{70} fullerite.

For C_{70} (symmetry D_{5h}) the optimal packing within a closest packed plane leads to the long axis (fivefold) perpendicular to the plane (see Figure 3b of), with the horizontal reflection σ_h in the plane. In this case, by the symmetry, the optimum interaction of molecules between this close-packed layer and the above layer is the same as the optimum interaction between this close-packed layer and the below layer. Thus the best packing is for above and below layers to be the same, leading to ABABAB or hcp packing for C_{70}, as in Figure 3b. This is expected from the results of calculations on the C_{70} dimer which shows that the most attractive interactions are between hexagonal faces on the side.

To understand the packing of fullerenes it is useful to consider the energetics of fullerene dimers in various orientations. For C_{70} dimer the best interaction is with the long axes parallel. The midriff involves both concave and convex graphite-like regions, and the optimum interaction has a convex side matched with a concave side, The bond distance is R_e = 9.94 Å (center to center) and the bond energy is D_e = 8.97 kcal/mol. The most weakly bound C_{70} dimer is with the two C_{70} in contact along the long axes (long axis 5-fold faces in contact) leading to a distance of 11.24 Å and an energy of 6.48 kcal/mol, about 3 kcal/mol worse than the best. These provide the basic physics why in condensed phase the C_{70} tends to align in the close-packing plane with the long axes parallel.

For FCC C_{60} the distances are R = 9.82 to 10.09 A (9.91 average) while the dimer energies (in the crystal) are D = 6.08 to 7.11 kcal/mol (6.76 average). Thus, of the 43.88 kcal/mol cohesive energy, 40.58 or 93% comes from nearest neighbor interactions. In contrast for FCC structures of noble gases, about 67% generally

comes from nearest neighbors. This indicates that the cohesive energy is dominated by the nearest neighbor interactions in the condensed phase of fullerenes. This is why impurities or substrates can easily induce the hcp C_{60} phase. For C_{70} the interactions in the condensed phase are much more anisotropic than for C_{60}. The interactions within the plane have R = 9.92 to 10.06 (10.00 average) D = 8.26 to 8.82 (8.50 average), and this can be compared to the optimum dimer interactions of R_e = 9.94 Å and D_e = 8.97 kcal/mol. While those out-of-plane have R = 10.83 to 10.96 (10.91 average) and D =6.78 to 7.21 (6.93 average). Averaging the interactions within the plane and out-of-plane leads R = 10.46 Å and D = 7.71 kcal/pair. Thus, similarly, of the 49.51 kcal/mol cohesive energy, 46.28 or 93% comes from nearest neighbor interactions. Hence the nearest neighbor interaction dominating and higher anisotropy of C_{70} will lead to the orientational disorder and different phases in C_{70} fullerite depending on process conditions and initial structure, and this is consistent with recent report by Vaughan *et al.*.[7] The calculated densities are 1.74 g/cc for FCC C_{60} and 1.74 g/cc for HCP C_{70}. This is in good agreement with the observed density of 1.70 g/cc at room temperature.

Our calculations lead to an average fcc lattice parameter of A = 14.0 Å and hcp lattice parameter of A = 9.9 and C = 16.3 Å (C/A = 1.65) for C_{60}, and hcp lattice parameters A = 10.0 and C = 18.5 Å (C/A = 1.85) for C_{70}. The C/A ratio of HCP C_{70} is 1.85 which deviates considerably from the ideal value of 1.633 for closest packing of spheres (hcp C_{60} has C/A = 1.65). This occurs because of the higher anisotropy in C_{70} and can be understood by simply considering difference in molecular dimensions between C_{60} and C_{70}. In C_{70} molecule, the 10 extra atoms run around the middle of the cage, related to C_{60} by the addition of a central cylindrical 10-atom belt, producing a structure which looks like an elongated sphere, and leading to a long axis c=8.0 Å, leaving the remaining axes (a = b = 7.1 Å) the same as in C_{60} (where a = b = c = 7.1 Å). Since the long axis in C_{70} fullerite

aligns in (111) direction, the C lattice parameter (18.5 Å) is about (8.0−7.1)/7.1 = 12.7 % longer than for hcp C_{60}. This shows that the molecular shape differences are precisely reflected in the lattice structure differences.

Recently Dravid *et al.*[8] reported the hcp structure for C_{70} with A = 10.1 and C = 16.8 Å from TEM measurements. Very obviously, this result is wrong. Firstly, if this lattice structure were for the C_{70} fullerite, it would lead to a density of 1.88 g cm^{-3} which is far too high. Secondly, the C_{70} molecule is very anisotropic which, as pointed out above, should lead to a high value of C/A, however, the experiment leads to C/A = 1.66 which is near the ideal C/A ratio. This is unlikely for the anisotropic C_{70} molecule. Since this lattice structure agrees with our predicted hcp C_{60} structure very well, we think that the SAED pattern might have found a small phase of hcp C_{60} in the C_{70} fullerite sample.

References

1. Krätschmer, W., Lamb, L. D., Fostiropoulos, K. & Huffman, D. R. *Nature* **347**, 354-358 (1990).
2. Krätschmer, W., Fostiropoulos, K. & Huffman, D. R. *Chem. Phys. Lett.* **170**, 167-170 (1990).
3. Y. Guo, N. Karasawa, and W. A. Goddard, Nature **351**, 464 (1991).
4. Z. Gu *et al.*, *Chem. Phys. Lett.* **95**, 9615 (1991).
5. P. A. Heiney *et al.*, Phys. Rev. Lett. **66**, 2911 (1991); R. Sachidanandam and A. B. Harris *ibid.* 67, 1467 (1991).
6. W. I. F. David *et al.*, Nature **353**, 147 (1991).
7. G. B. M. Vaughan *et al.*, Science **254**, 1350 (1991).
7. V. P. Dravid, S. Liu and M. M. Kappes, *Chem. Phys. Lett.* **185**, 75 (1991).

Chapter 4

Thermodynamic Properties (Including Vapor Pressure) of Fullerite C_{60} and C_{70} Crystals

Thermodynamic Properties (Including Vapor Pressure) of Fullerite C_{60} and C_{70} Crystals

Yuejin Guo and William A. Goddard III

Materials & Molecular Simulation Center

Beckman Institute (139-74)

California Institute of Technology, Pasadena, California 91125

Abstract

We report the cohesive energies, vapor pressures, and other thermodynamic properties from calculations on the crystals and free molecules of fullerites, C_{60} and C_{70}. These calculations use graphite force field (GraFF) and lead to ΔH_{707K} = 40.9 kcal/mol for C_{60} in excellent agreement with experiment ($\Delta H_{707K} = 40.1 \pm 1.3$ kcal/mol). For C_{70} we obtain ΔH_{739K} = 46.4 kcal/mol in good agreement with experiment (ΔH_{739K} = 45.2 and 41.8 from two sets of experiments).

4.1 Introduction

Recent breakthroughs[1] in synthesizing large amounts of C_{60}, C_{70} and other fullerenes (buckminsterfullerenes or buckyballs),[2] have led to much activity in characterizing these materials by vibrational spectroscopy,[2,3] crystal structure analysis,[2] NMR,[4] STM,[5] etc. In order to interpret and predict such results we used experimental lattice parameters, elastic constants, phonon frequencies for graphite to develop the GraFF force field[6-8] for sp^2 carbon centers. This force field successfully predicts the packing, density, and co-pressibility for C_{60} and C_{70} fullerites. Using this force field we report here thermodynamic properties (including cohesive energies, heats of sublimation, and vapor pressure) for crystals of C_{60} and C_{70} fullerites (buckyball molecules).

4.2 Crystal Structures

4.2.1 Calculations

We calculated[8,9] the optimum crystal structures for both simple types of closest packing: HCP (closest packed planes in the sequence ABABAB) and FCC (closest packed planes in the sequence ABCABC) as indicated in Tables I and II we find that for C_{60} FCC is 0.90 kcal/mol *more* stable than HCP, whereas for C_{70} HCP is 0.35 kcal/mol more stable than FCC.[8]

Because of noncrystallographic symmetries (five fold axes), it is not possible for these fullerites to retain the optimal dimer orientation in closest packed structures. However the symmetry of the fullerite *does* affect the packing.[8] Consider an optimized closest packed layer B interacting with closest packed layers above and below. Any fullerene in B oriented to have the optimum face toward A molecules in layer A above will (because of the inversion symmetry of C_{60}) have the equivalent

faces *on the opposite side* below, leading to ABCABC or FCC packing for C_{60}. On the other hand, a closest packed plane of C_{70} (symmetry D_{5h}) has the 5-fold axis perpendicular to the plane, leading to reflection symmetry in the plane. In this case the optimum interaction with the layers above and below is *on the same side*, leading to ABABAB or HCP packing for C_{70}.

The molecular distances in FCC C_{60} are R = 9.82 to 10.09 Å (9.91 average) while the dimer energies (in the crystal) are D = 6.07 to 7.10 kcal/mol (6.75 average). This compares with R = 9.84 Å and D = 7.19 kcal/mol for the optimal dimer. The calculated density of 1.745 g cm^{-3} for FCC C_{60} at 0K is in good agreement with the observed density of 1.678 g cm^{-3} at room temperature.[1b]

For C_{70} the interactions in the crystal are much more anisotropic than in C_{60}. The interactions within the plane have R = 9.92 to 10.06 Å (10.00 average) and D = 8.23 to 8.79 kcal/mol (8.47 average) while those out-of-plane have R = 10.83 to 10.96 Å (10.91 average) and D = 6.75 to 7.18 kcal/mol (6.90 average). This can be compared to the optimum dimer interactions of R = 9.94 Å and D = 8.97 kcal/mol.

The cell parameters distort due to the incompatibility of the 5 fold axis with the closest packing. Above 300K, we find rapid reorientation of the molecules.[8,10] For 0K the average FCC lattice parameter for C_{60} is a = 14.0 Å and HCP lattice parameters for C_{70} a = b = 9.98 Å and c = 18.52 Å (c/a = 1.86). The asymmetry of C_{70} molecules leads to rhombohedral symmetry for the FCC form. The c/a ratio of HCP C_{70} is 1.86 which deviates considerably from the ideal value of 1.633 for closest packing of spheres (HCP C_{60} has c/a = 1.65).

We calculate a bulk modules of 16.6 GPa which is within the range of experiment, 18.1 ± 1.8 GPa for Duclos *et al.*[13] and 14.6 ± 2.1 GPa from Fischer *et al.*[14] The volume compressibility calculated for C_{70}, 17.6 GPa is similar to C_{60}, but quite anisotropic.

4.2.2 Comparison with Experiment

Both X-ray[15] and neutron diffraction[16] structures are now available for C_{60}. Theory and experiment agree that the basic packing is FCC. Also both agree that there is a phase transition with orientational averaging above the transition with a cubic lattice (experimentally the transition is at 249K, calculations indicate that it is between 300K and 350K). Theory and experiment agree that the high temperature structure has a cubic lattice with a = 14.18 Å (theory) and a = 14.24 Å (exper) at 300K. At low temperature, the theory indicates that the lowest energy structure has long range orientation order with an orthorhombic distortion. On the other hand, the experimental diffraction patterns indicate a cubic lattice at low temperature. The theory finds that the orientation from the neutron diffraction structure is stable (a 2nd derivatives positive) but that it is 2.0 kcal/mol higher than the minimum energy structure. Compressing the optimum orthorhombic structure to cubic of the same density costs 0.8 kcal/mol and leads to a = 14.00 Å in excellent agreement with experiment. Based on the theoretical results, we expect that quenching C_{60} from room temperature would lead to an orientational glass with cubic symmetry and frozen orientations but no long range order. This could explain the discrepancy in the interpretation of theory and experimental low temperature results.

4.3 Thermodynamic Properties

4.3.1 Calculations

In order to obtain the thermodynamic properties as a function of temperature, we calculated the vibrational frequencies (phonons) for both crystalline and gas phase C_{60} and C_{70}. In these calculations we allowed all atoms to move. Thus for C_{60} we allowed one molecule per FCC primitive cell (Z = 1) and calculated 180 vibrational modes for each of 27 points in the brillouin zone (BZ) (fixed volume). Based on the above results and using the quantum partition function for

harmonic oscillators, we calculated ΔH, ΔS, and ΔG as a function of temperature and pressure.

Allowing four independent molecules per cell lowers the energy by 0.50 kcal/mol for FCC C_{60} and by 0.27 kcal/mol for C_{70}. Thus in calculating vapor pressure, we correct the above temperature dependent properties (calculated using FCC with Z = 1 with the energy differences between the Z = 1) FCC structure and the lowest energy crystal (Z = 4). These properties for crystalline C_{60} and C_{70} are reported in Tables III and IV.

Similar calculations on gas phase C_{60} and C_{70} molecules were carried out at various pressures for 0.001 atm (0.76 torr) to 1 atm (760 torr) with the results at 1 atm in Tables V and VI. In the crystal calculations the rotational modes of the free molecule become librations; however, at temperatures above 300K the molecules in the crystal rapidly average over various orientations. Rather than correcting the crystal properties for this degeneracy, we instead calculated the gas phase free energies using a rotational number of g = 1 for C_{60} and C_{70} (rather than g = 60 and g = 10, respectively).

The free energies in Tables III-VI are all relative to the energy at 0K. The calculated quantities are corrected for zero-point energy and temperature dependent enthalpies, as illustrated in Figure 1 for C_{70}. The results are shown in Tables VII and VIII.

4.3.2 Discussion

For graphite the cohesive energy calculated for separating into separate graphite planes[7] is 1.299 kcal/mol (per C atm), whereas for C_{60} we find 43.883/60 = 0.731 and for C_{70} we find 49.506/70 = 0.707 kcal/(mol C). Since the atoms in graphite can interact with sheets on both sides, but fullerenes can only interact outside the fullerene, we should compare the fullerite numbers with half the graphite

energy or 0.650 kcal/mol. Thus the sublimation energies for fullerenes are quite consistent with those on graphite. The excellent agreement with experiment for the sublimation energy of C_{60} and C_{70} confirms the validity of the van der Waals parameters for C GraFF. This in turn leads to a prediction of the sheet cohesive energy is graphite (currently there is no real data on the sheet-sheet cohesive energy of graphite).

4.4 Vapor Pressure

4.4.1 Calculations

In Figure 2 we compare the free energy for C_{60} crystal (Table III) and for C_{60} molecule (Table V) at p=1 atm. The free energies are equal at T = 937K. To calculate the equilibrium vapor pressure as a function of temperature, we assumed that the free energy of the crystal is independent of pressure (reasonable for pressures below 1 atm) and carried out calculations similar to Figure 2 at various pressures. The results are tabulated in Table IX.

For example, with C_{60} we obtain ΔH_{0K} = 42.51 kcal/mol (after correcting for the difference in zero point energy for crystal and molecule, 0.87 kcal/mol) and ΔH_{937K} = 40.26 kcal/mol (the enthalpy difference between the condensed and gas phase changes 2.25 kcal/mol from T = 0 to T = 937 K). The calculated vapor pressure for crystalline C_{60} is in Figure 3. The predicted vapor pressure is 1 torr at 714 K and 1 atm at 937 K.

For crystalline C_{70} the vapor pressure curve is also in Figure 4. Thus ΔH_{0K} = 48.06 kcal/mol (after correcting for the differential zero point energies of 0.95 kcal/mol) and ΔH_{1037K} = 45.72 kcal/mol ($\Delta H_0 - \Delta H_{797}$ = 2.34 kcal/mol). The predicted vapor pressure is 1 torr at 797 K and 1 atm at 1039 K.

The vapor pressure is related to thermodynamic properties

$$\ln p_T = -\frac{\Delta H_T}{RT} + \frac{\Delta S_T}{R}, \qquad (1)$$

where ΔH_T and ΔS_T are the enthalpy and entropy changes from gas to solid. Indeed, as shown in Figure 3, the temperature dependence of p is accurately fitted with the two term function

$$\ln p = -\frac{\overline{\Delta H}}{RT} + \frac{\overline{\Delta S}}{R}, \tag{2}$$

where the average values of $\overline{\Delta H}$ and $\overline{\Delta S}$ are given in Table X.

4.4.2 Comparison with Experiment

While this manuscript was in preparation, results were published by Margrave *et al.*[12] that provide exceptionally good confirmation of our results. Using Knudson cell mass spectrometry of vapor in equilibration with a polycrystalline mixture C_{60} and C_{70}, Margrave *et al.* finds $\Delta H_{707K} = 40.1 \pm 1.3$ kcal/mol for C_{60} and $\Delta H_{739K} = 43.0 \pm 2.2$ kcal/mol for C_{70} (second law heat of sublimation). In comparison our calculations leads to $\Delta H_{714K} = 40.259$ kcal/mol for C_{60} at 1 atm and $\Delta H_{797} = 45.721$ kcal/mol at 1 atm.

The Margrave experiments were based on six runs with the first three and last three separated by a period of two weeks during which the sample was at room temperature. The data for the first three sets lead to 40.3 and 45.2 kcal/mol for C_{60} and C_{70} respectively while the second set of three leads to 40.0 and 41.8 kcal/mol. Margrave *et al.* suggest that the big change for C_{70} might be due to selective oxidation of C_{70}, leading to fewer C_{70} and therefore the measured ΔH might refer to C_{70} in a C_{60} environment rather than in a C_{70} environment. This explanation is plausible and we would like to believe it since the results from the first set are in truly excellent agreement with the theory (experiment in parentheses): 40.3 (40.1) kcal/mol and 45.7 (45.2) kcal/mol.

4.5 Discussion

Now that our force field is established to provide accurate interaction energies, we can use this force field to study disordered and liquid C_{60} systems, mixtures

with toluene and other solvents, monolayers and multilayers on graphite, etc. Thus this force field should be useful for simulating many experiments now in progress.

Given that the interaction energy per C is similar for fullerenes and graphite, it might be that buckyballs would have good tribiological properties and could serve as balls for nanoscale bearings.

Acknowledgements

The research was initiated with funding from the Air Force Office of Scientific Research (AFOSR-88-0051) and completed with funding from NSF-CHE. The facilities of the MSC/BI are supported by by grants from DOE-ECUT, NSF-DMR-MRG, NSF-CHE, BP America, Allied-Signal Corp., Asahi Chemical, Asahi Glass, Chevron, General Electric, Geneal Motors Research, Xerox Corp., and Beckman Institute.

Contribution number 8549.

References

1. (a) W. Krätschmer, K. Fostiropoulos, and D. R. Huffman, Chem. Phys. Lett., **170**, 167 (1990). (b) W. Krätschmer, L. D. Lamb, K. Fostiropoulos, and D. R. Huffman, Nature, **347**, 354 (1990).
2. H. W. Kroto, J. R. Heath, S. C. O'Brien, R. F. Curl, and R. E. Smalley, Nature **318**, 162 (1985).
3. D. S. Bethune, G. Meijer, W. C. Tang, and H. J. Rosen, Chem. Phys. Lett., **174**, 219 (1990).
4. R. Taylor, J. P. Hare, A. K. Abdul-Sade, and H. W. Kroto, JCS Chem. Comm., **20**, 1423 (1990).
5. R. J. Wilson, G. Meijer, D. S. Bethune, R. D. Johnson, D. D. Chambliss, M. S. de Vries, H. E. Hunziker, and H. R. Wendt, Nature **348**, 621 (1990);

J. L. Wragg, J. E. Chamberlain, H. W. White, W. Krätschmer, and D. R. Huffman, ibid. **348**, 623 (1990).

6. The force field used in Lennard-Jones 12-6 potential [R_v = 3.8050, D_v = 0.0692)], a Morse bond stretch [R_b = 1.4114, k_b = 720., D_b = 133.0], cosine angle bend [Θ_a = 120, $k_{\theta\theta}$ = 196.13, $k_{r\theta}$ = 62.71, k_{rr} = 68.] and a two fold torsion [V_t = 21.28], where all distances are in A, all angles in degrees, and all force constants and energies in kcal/mol, A, radian units. For more details see reference 7 and 8.
7. S. L. Mayo, B. D. Olafson, and W. A. Goddard, J. Phys. Chem. **94**, 8897 (1990).
8. Y. Guo, N. Karasawa and W. A. Goddard, Nature **351**, 464 (1991).
9. These calculations were all carried out using POLYGRAF from Molecular Simulations Inc. of Sunnyvale California (formerly known as BioDesign) in conjunction with additional vibrational analysis software written by N. Karasawa, S. Dasgupta, and W. A. Goddard of the Materials & Molecular Simulation Center, Caltech.
10. N. Karasawa, Y. Guo, and W. A. Goddard, unpublished.
11. C. I. Frum, R. Engleman Jr., H. G. Hedderich, P. F. Bernath, L. D. Lamb, and D. R. Huffman, Chem. Phys. Lett. **176**, 504 (1991).
12. C. Pan, M. P. Sampson, Y. Chai, R. H. Hauge, and J. L. Margrave, J. Phys. Chem. **95**, 2944 (1991). (1991).
13. S. J. Duclos, K. Brister, R. C. Haddon, A. R. Kortan, and F. A. Thiel, *Nature* **351**, 380-382 (1991).
14. J. E. Fischer et al., *Science* **252**, 1288-1290 (1991).
15. P. A. Heiney *et al.*, Phys. Rev. Lett. **66**, 2911 (1991); R. Sachidanandam and A. B. Harris *ibid.* 67, 1467 (1991).
16. W. I. F. David *et al.*, Nature **353**, 147 (1991).

Table I. Cohesive energies of C_{60} crystals (12-6).

Structure	Z[c]	Energies (kcal/mol)		Density
		Total[a]	Relative[b]	(g cm^{-3})
FCC	1	43.3778	0.0000	1.7371
	4	43.8826	0.0000	1.7451
HCP	2	42.8592	0.5187	1.7286
	4	42.9792	0.9034	1.7319
BCC	1	38.5582	4.8196	1.6518

[a]Referenced to the free C_{60} molecule.

[b]FCC as reference point.

[c]Molecules per cell.

Table II. Cohesive energies of C_{70} crystals (12-6).

Structure	Z[c]	Energies (kcal/mol)		Density
		Total[a]	Relative[b]	(g cm^{-3})
HCP	2	49.2365	0.0000	1.7350
	4	49.5057	0.0000	1.7400
FCC	1	49.0101	0.2264	1.7334
	4	49.1551	0.3506	1.7357
BCC	1	38.8236	10.4129	1.6035

[a]Referenced to the free C_{70} molecule.

[b]HCP as reference point.

[c]Molecules per cell.

Table III. Thermodynamic properties of FCC C_{60} (1 molecule/cell).

Temp (K)	C_v (cal/mol K)	S (cal/mol K)	U[a] (kcal/mol)	F (kcal/mol)
0	0	0	0	0
100	20.0938	26.3485	1.1292	-1.5057
200	62.5557	52.0761	5.0841	-5.3311
300	115.9873	87.4602	13.9917	-12.2464
400	166.1836	127.8847	28.1641	-22.9899
500	207.1373	169.5534	46.9139	-37.8630
600	238.5558	210.2295	69.2718	-56.8662
700	262.2029	248.8656	94.3660	-79.8402
750	271.7320	267.2883	107.7199	-92.7465
800	280.0212	285.0963	121.5185	-106.5588
850	287.2531	302.2944	135.7044	-121.2461
900	293.5839	318.8964	150.2289	-136.7783
950	299.1454	334.9218	165.0500	-153.1261
1000	304.0490	350.3932	180.1324	-170.2611
1050	308.3884	365.3350	195.4455	-188.1566
1100	312.2422	379.7719	210.9632	-206.7863
1150	315.6771	393.7288	226.6628	-226.1257
1200	318.7490	407.2299	242.5248	-246.1515

[a] Using the structure calculated at T = 0 K and p = 0 atm. The absolute energy for the minimized structure is 637.7327 kcal/mol which leads to a cohesive energy of 43.3778 kcal/mol (referenced to free C_{60} molecules). The total zero point energy is 236.2338 kcal/mol.

Table IV. Thermodynamic properties of FCC C_{70} (1 molecule/cell).

Temp (K)	C_v (cal/mol K)	S (cal/mol K)	U[a] (kcal/mol)	F (kcal/mol)
0	0	0	0	0
100	23.1246	28.6856	1.2170	-1.6519
200	73.9219	58.9958	5.8812	-5.9185
300	136.0614	100.6432	16.3634	-13.8306
400	194.1824	147.9556	32.9494	-26.2343
500	241.6681	196.6005	54.8382	-43.4641
600	278.1776	244.0420	80.9149	-65.5127
700	305.7080	289.0904	110.1743	-92.1918
750	316.8149	310.5695	125.7439	-107.1863
800	326.4828	331.3318	141.8319	-123.2369
850	334.9223	351.3834	158.3717	-140.3077
900	342.3135	370.7406	175.3066	-158.3636
950	348.8094	389.4261	192.5881	-177.3706
1000	354.5389	407.4662	210.1748	-197.2955
1050	359.6109	424.8892	228.0311	-218.1068
1100	364.1167	441.7243	246.1265	-239.7747
1150	368.1337	457.9994	264.4346	-262.2693
1200	371.7270	473.7444	282.9328	-285.5652

[a] Using the structure calculated at T = 0 K and p = 0 atm. The absolute energy for the minimized structure is 684.3154 kcal/mol which leads to a cohesive energy of 49.0101 kcal/mol (referenced to free C_{70} molecules). The total zero point energy is 275.9543 kcal/mol.

Table V. Thermodynamic properties of gas phase C_{60} at p = 1 atm. All calculations use a rotational symmetry number of g = 1 for ease in comparison with the disordered crystal (g = 60 is the correct gas phase value).

Temp (K)	C_p (cal/mol K)	S (cal/mol K)	H[a] (kcal/mol)	G (kcal/mol)
0	7.9488	– – –	0.0000	0.0000
100	16.9233	76.7489	0.9789	-6.6968
200	59.5080	100.3300	4.6251	-15.4419
300	112.9127	134.4740	13.2271	-27.1165
400	163.0390	174.0043	27.0888	-42.5147
500	203.9073	214.9614	45.5198	-61.9630
600	235.2430	255.0404	67.5505	-85.4763
700	258.8183	293.1600	92.3098	-112.9051
750	268.3160	311.3476	105.4937	-128.0201
800	276.5770	328.9337	119.1207	-144.0295
850	283.7834	345.9225	133.1338	-160.9038
900	290.0915	362.3249	147.4841	-178.6119
950	295.6324	378.1611	162.1301	-197.1267
1000	300.5178	393.4518	177.0365	-216.4192
1050	304.8399	408.2203	192.1726	-236.4628
1100	308.6792	422.4926	207.5123	-257.2337
1150	312.1006	436.2901	223.0335	-278.7045
1200	315.1604	449.6387	238.7164	-300.8545

[a] The absolute energy of the minimized structure is 681.1105 kcal/mol and the zero point energy is 235.3656 kcal/mol.

Table VI. Thermodynamic properties of gas phase C_{70} at p = 1 atm. All calculations use a rotational symmetry number of g = 1 for comparison to the disordered crystal (g = 10 is the correct gas phase value).

Temp (K)	C_p (cal/mol K)	S (cal/mol K)	H[a] (kcal/mol)	G (kcal/mol)
0	7.9488	– – –	0.0000	0.0000
100	20.0687	79.1297	1.0578	-6.8559
200	71.0117	107.3898	5.4271	-16.0519
300	133.0964	147.8491	15.6160	-28.7402
400	191.1245	194.2961	31.9011	-45.8193
500	238.5072	242.2477	53.4789	-67.6473
600	274.9204	289.1046	79.2346	-94.2310
700	302.3690	333.6443	108.1642	-125.3901
750	313.4404	354.8917	123.5659	-142.6064
800	323.0762	375.4349	139.4842	-160.8674
850	331.4871	395.2792	155.8532	-180.1381
900	338.8525	414.4395	172.6156	-200.3842
950	345.3254	432.9377	189.7234	-221.5717
1000	351.0342	450.7979	207.1352	-243.6672
1050	356.0876	468.0500	224.8160	-266.6412
1100	360.5764	484.7205	242.7348	-290.4626
1150	364.5783	500.8384	260.8655	-315.1036
1200	368.1579	516.4314	279.1855	-340.5374

[a] The absolute energy of the minimized structure is 733.3255 kcal/mol and the zero point energy is 275.0020 kcal/mol.

Table VII. Changes in thermodynamic quantities from FCC C_{60} crystal to gas phase C_{60} at 1 atm.

Temp (K)	ΔC_p (cal/mol K)	ΔS (cal/mol K)	ΔH^a (kcal/mol)	ΔG (kcal/mol)
0	7.9488	– – –	43.0134	43.0134
100	-3.1705	50.4004	42.8631	37.8223
200	-3.0477	48.2539	42.5544	32.9026
300	-3.0746	47.0138	42.2488	28.1433
400	-3.1446	46.1196	41.9381	23.4886
500	-3.2300	45.4080	41.6193	18.9134
600	-3.3128	44.8109	41.2921	14.4033
700	-3.3846	44.2944	40.9572	9.9485
750	-3.4160	44.0593	40.7872	7.7398
800	-3.4442	43.8374	40.6156	5.5427
850	-3.4697	43.6281	40.4428	3.3557
900	-3.4924	43.4285	40.2686	1.1798
950	-3.5130	43.2393	40.0935	-0.9872
1000	-3.5312	43.0586	39.9175	-3.1447
1050	-3.5485	42.8853	39.7405	-5.2928
1100	-3.5630	42.7207	39.5625	-7.4340
1150	-3.5765	42.5613	39.3841	-9.5654
1200	-3.5886	42.4088	39.2050	-11.6896

[a] Using a cohesive energy 43.8826 kcal/mol and correcting for the differential zero point energy of 0.8692 kcal/mol.

Table VIII. Changes in thermodynamic quantities from FCC C_{70} crystal to gas phase C_{70} at 1 atm.

Temp (K)	ΔC_p (cal/mol K)	ΔS (cal/mol K)	ΔH^a (kcal/mol)	ΔG (kcal/mol)
0	7.9488	– – –	48.5534	48.5534
100	-3.0559	50.4441	48.3942	43.3494
200	-2.9102	48.3940	48.0993	38.4200
300	-2.9650	47.2059	47.8060	33.6438
400	-3.0579	46.3405	47.5051	28.9684
500	-3.1609	45.6472	47.1941	24.3702
600	-3.2572	45.0626	46.8731	19.8351
700	-3.3390	44.5539	46.5433	15.3551
750	-3.3745	44.3222	46.3754	13.1333
800	-3.4066	44.1031	46.2057	10.9229
850	-3.4352	43.8958	46.0349	8.7230
900	-3.4610	43.6989	45.8624	6.5328
950	-3.4840	43.5116	45.6887	4.3523
1000	-3.5047	43.3317	45.5138	2.1817
1050	-3.5233	43.1608	45.3383	0.1990
1100	-3.5403	42.9962	45.1617	-2.1345
1150	-3.5554	42.8390	44.9843	-4.2809
1200	-3.5691	42.6870	44.8061	-6.4188

[a] Using a cohesive energy of 49.5057 kcal/mol and correcting for the differential zero point energy of 0.9523 kcal/mol.

Table IX. Equilibrium temperature for crystal and vapor at various pressures.

p (atm)	C_{60}	C_{70}
1.0	927.2	1050.6
0.1	839.0	950.2
0.01	766.5	868.0
0.001	706.0	799.0

Table X. Vapor pressure functions for C_{60} and C_{70}, $\ln p = \frac{\overline{\Delta H}}{RT} + \frac{\overline{\Delta S}}{R}$ where $p_o =$ 1 atm.

	$\overline{\Delta H}$	$\overline{\Delta S}$
C_{60}	39.4	0.055
C_{70}	45.3	0.057

Figure Captions

Figure 1. Illustration of the energetics for C_{60}

Figure 2. Illustration of the energetics for C_{70}

Figure 3. Determination of temperature, T_o for equilibrium of the solid and gas (at p=1 atmosphere) (a) C_{60}, (b) C_{70}.

Figure 4. Predicted vapor pressure for C_{60} and C_{70} crystals.

C_{60}Energy Diagram (kcal/mol)

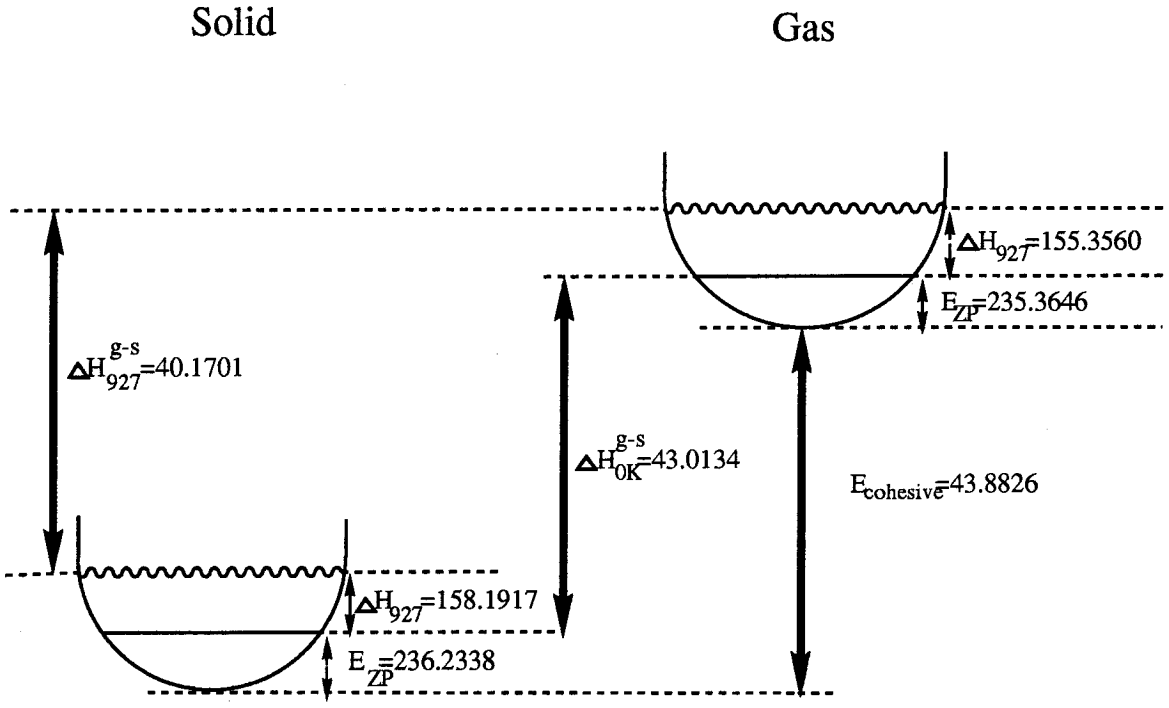

Figure 1.

C_{70} Energy Diagram (kcal/mol)

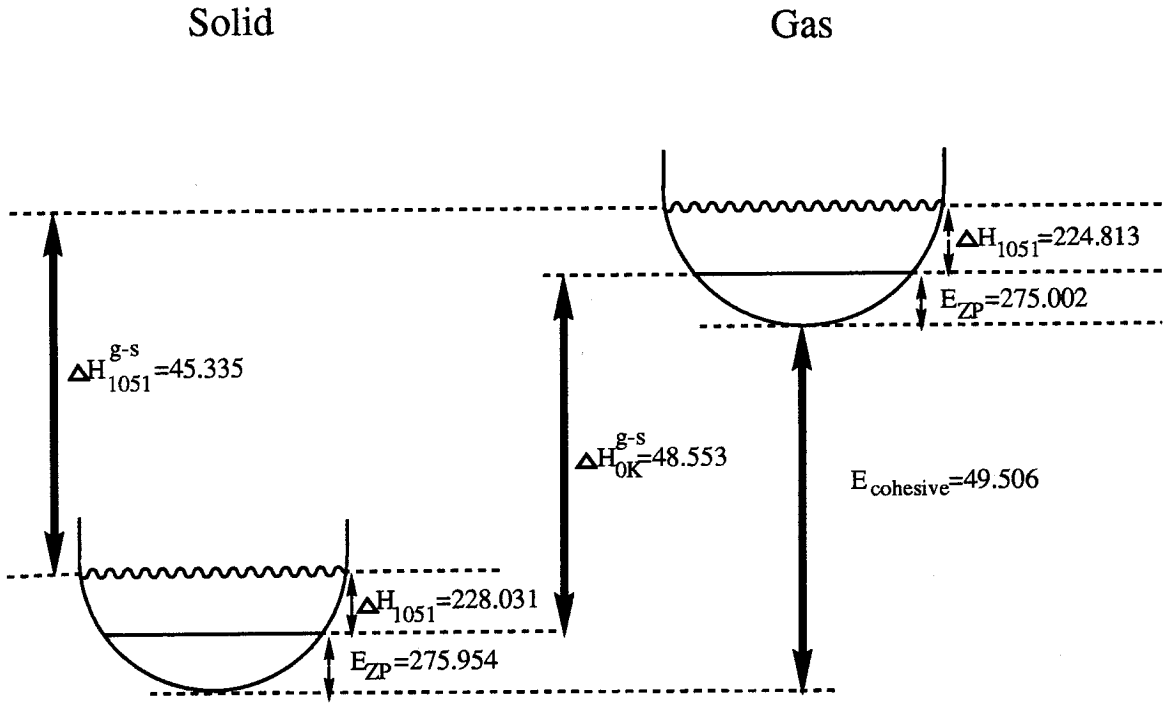

Figure 2.

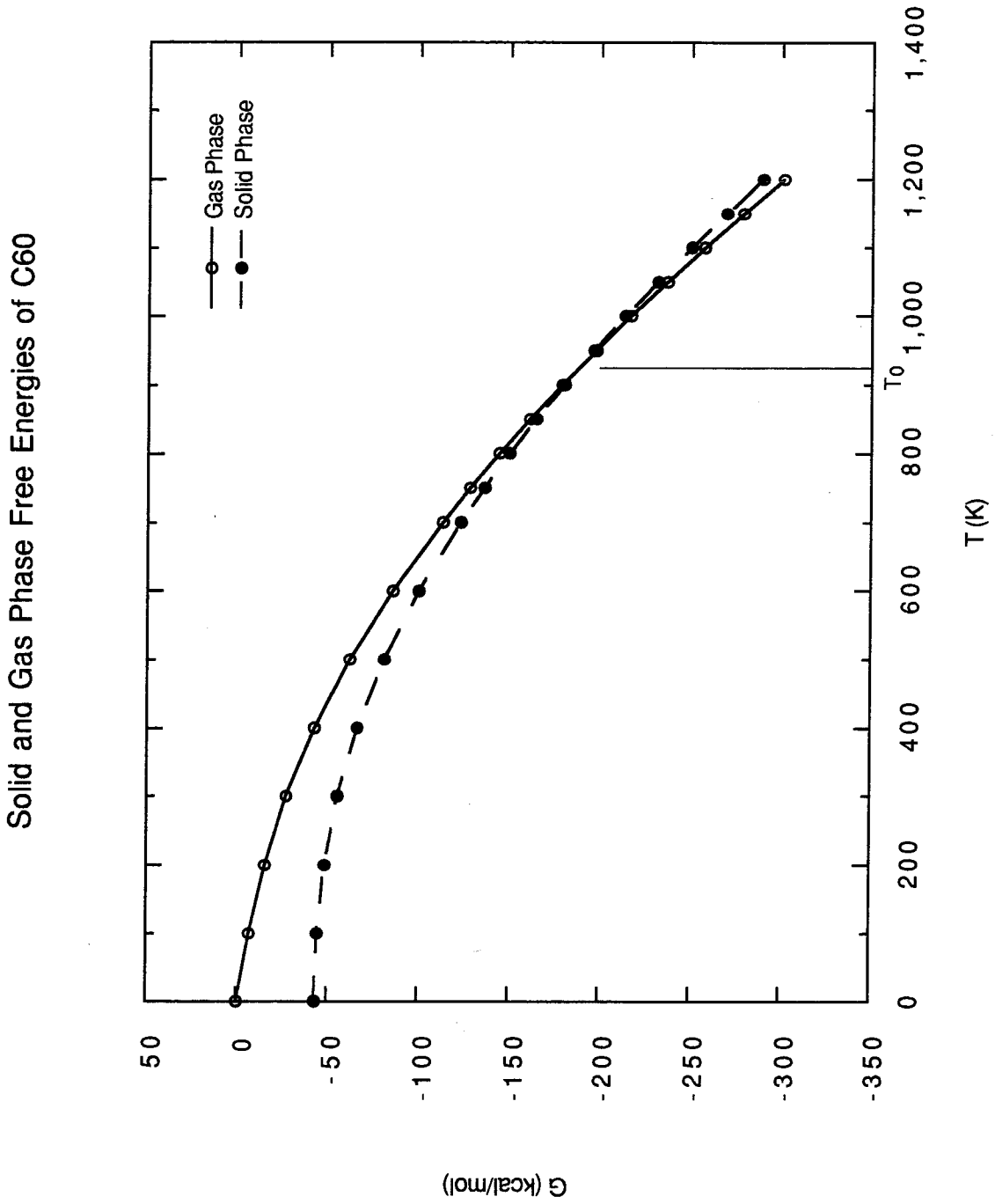
Solid and Gas Phase Free Energies of C60
Gas Phase
Solid Phase
50
0
-50
-100
-150
-200
-250
-300
-350
G (kcal/mol)
0
200
400
600
800
1,000
1,200
1,400
T (K)
To

Figure 3a.

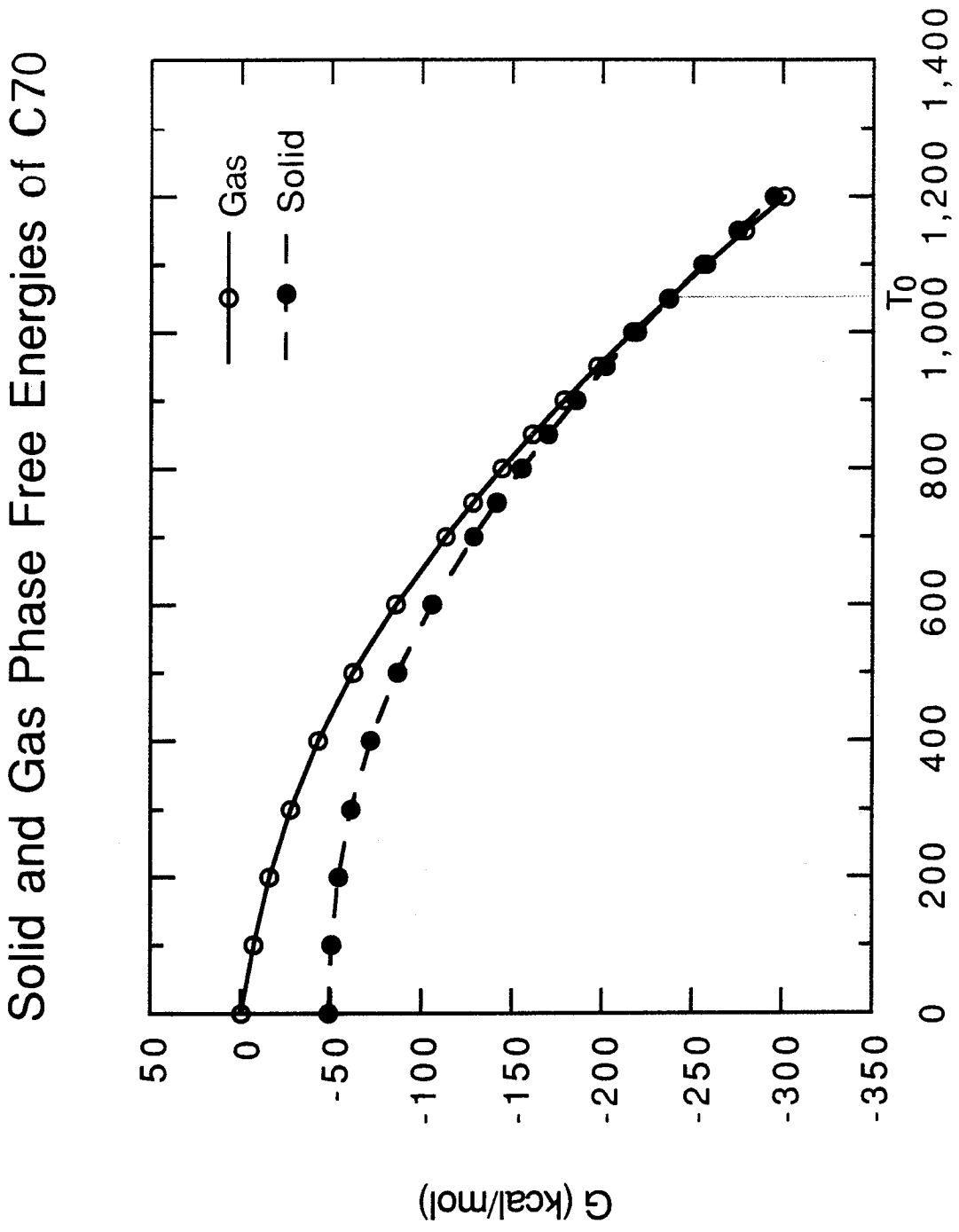
Solid and Gas Phase Free Energies of C70
Gas
Solid
G (kcal/mol)
50
0
-50
-100
-150
-200
-250
-300
-350
0
200
400
600
800
1,000
1,200
1,400
T (K)
T0

Figure 3b.

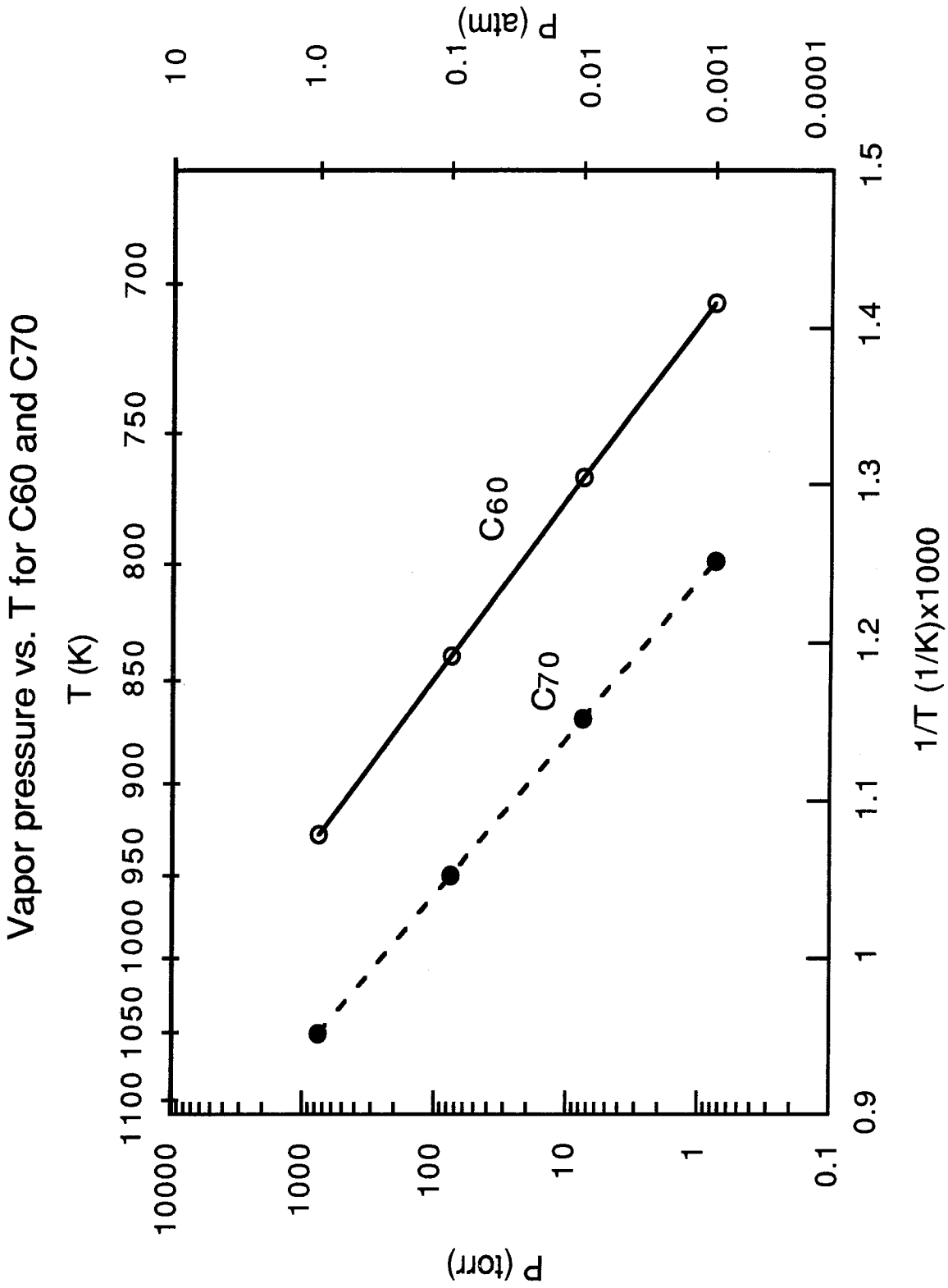
Vapor pressure vs. T for C60 and C70
T (K)
1100 1050 1000 950 900 850 800 750 700
P (torr)
10000 1000 100 10 1 0.1
1/T (1/K)x1000
0.9 1 1.1 1.2 1.3 1.4 1.5
P (atm)
10 1.0 0.1 0.01 0.001 0.0001
C60
C70

Figure 4.

Chapter 5

Compressibility and Distortion of Buckyball Crystals (C_{60}, C_{70}) at High Pressure: Harder than Diamond or Sources of Diamond?

Compressibility and Distortion of Buckyball Crystals (C_{60}, C_{70}) at High Pressure: Harder than Diamond or Sources of Diamond?

Yuejin Guo and William A. Goddard III

Materials & Molecular Simulation Center

Beckman Institute (139-74)

California Institute of Technology, Pasadena, California 91125

Abstract

Recently Ruoff[1] suggested that at high pressures buckminsterfullerene (buckyball) molecules such as C_{60} might be harder than diamond. We have tested these ideas by theoretical calculations of the structure and elastic properties of C_{60} and C_{70} crystals at pressures up to 100 GPa (1 megabar). We find that the buckyballs distort significantly higher pressures, leading to a cubic shaped molecule (buckycube) by 100 GPa! However, even at 100 GPa fullerite crystals remain softer than graphite and diamond. On the other hand the distortions of the C_{60} molecules at higher pressure force the carbon atoms to become more tetrahedral, and we suggest that compression of C_{60} to appropriate pressures and temperatures might lead to a useful alternative way of synthesizing diamonds required for many applications (high temperature electronics, radar domes).

As the procedures for synthesizing large amounts of buckminsterfullerenes (buckyball) molecules (C_{60}, C_{70} etc) have progressed.[2-4] Attention has begun to focus on the properties of such fullerites.[5,6] One novel suggestion is that C_{60} crystals (fullerites) might be harder than diamond at high pressures.[1] The idea here is that interactions between buckyballs are described by van der Waals forces (e.g., Lennard Jones 6-12) in which there is a very stiff inner wall. Thus at sufficient compression the stiffness of the inner wall might exceed the stiffness of diamond (where the inner walls are dominated by bonded interactions).

We have tested these ideas by explicit calculations (at pressure up to 100 GPa) of the density and mechanical properties of C_{60} crystals. The force field used for these calculations was developed by fitting to the experimental lattice parameters, elastic constants, and phonon frequencies for graphite.[7] As indicated in Fig. 1, this force field leads to excellent agreement with the experimental compressibility of graphite.[8] This graphite force field has also been used to predict crystal structures and thermodynamic properties of C_{60} and C_{70} ,[7] where it leads to density and heats of sublimation in good agreement with experiment. Thus the calculated cohesive energy for C_{60} fullerite is 43.9 kcal/mol.[7] Using this force field to calculate the zero point energy and temperature dependence of C_v, S, and H for both the crystal and free molecule leads to ΔH =40.9 kcal/mol at T = 707 K in excellent agreement[7] with the value of 40.1 $\pm$1.3 at 707 K recently reported.[9] Similarly the predicted structure[7] leads to a density of 1.745 g cm^{-3} at 0 K and 1.697 g cm^{-3} at 300 K in good agreement with observations of 1.730 g cm^{-3} at 11 K and 1.682 g cm^{-3} at 300 K.[10]

To study the properties of C_{60} fullerites as a function of pressure, it is es-

sential to allow the atoms within the buckyball to distort in response to the intermolecular interaction. Thus our calculations allow all 180 internal coordinates of each C_{60} molecule to optimize simultaneously with the cell coordinates for various external pressures (following the methodology of Parrinello and Rahman[11]). All calculations in this paper were carried out using POLYGRAF from Molecular Simulations Inc., Sunnyvale, California in conjunction with additional vibrational analysis software written at the MSC/BI. For simplicity we used the Rhombohedral description of the face-centered cubic unit cell with one C_{60} molecule per unit cell. For C_{70} (which has the hcp structure) we included four independent molecules per hexagonal unit cell.

In Fig. 1 and 2 we compare the bulk modulus and density of C_{60} fullerite with the properties of graphite and diamond. Clearly the C_{60} fullerites remain softer than graphite at all pressures and never approach the hardness of diamond. At 20 GPa the bulk modulus is 170 GPa for C_{60} fullerite, 219 GPa for graphite, and 441 GPa for diamond.

It would appear that the major flaw in the estimates by Ruoff[1] was in treating the compressibility of the C_{60} balls. Indeed keeping the size and shape of the C_{60} molecules rigid leads to the *hard ball* C_{60} curve in Fig. 1 and 2. This *does* lead to a very hard crystal at high pressure, with a bulk modulus comparable to diamond at 30 GPa. The misestimate of the compressibility is partly due to a general misconception[3,12,13] about the C_{60} crystal: namely that the $C_{60}...C_{60}$ intermolecular interactions are well up the C...C repulsive wall. This results from assuming that the C...C nonbond distance is $\sim$ 2.9 Å (derived by subtracting the diameter of C_{60}, 7.1 Å, from the $C_{60}...C_{60}$ distance in the crystal, 10 Å), whereas graphite has a minimum C...C of 3.35 Å. In fact, C_{60} fullerite has a shortest C...C distance of 3.36 Å (3.27 Å hexagonal face-face distance), just as in graphite. The reason for the confusion is that buckyball is not quite round. The hexagonal faces

form facets with a minimum distance about 0.3 Å closer to the center than the atoms; these facets are then fitted together in forming the crystal.

Based on Fig. 1 and 2, C_{60} fullerites remain softer than graphite at all pressures; however, for higher pressures (> 10 GPa) the compressibility of the C_{60} molecule makes C_{60} crystal considerably softer than graphite (cf. the hard ball curve). The calculations give an inflection in the bulk modulus around 60 GPa. This occurs at a point where the buckyball is becoming a buckycube (see Fig. 3), which causes a stiffening associated with the cubic shape.

The hard ball results indicate that synthesizing the fullerite with an appropriate atom inside might lead to a material harder than diamond at high pressure. The limiting hardness would be given by the hard ball C_{60} curve in Fig. 2, leading to a bulk modulus exceeding diamond above 30 GPa.

We calculate a bulk modulus of 16.6 GPa which is within the range of experiments: 18.1±1.8 GPa from Duclos *et al.*[12] and 14.6±2.1 GPa from Fischer *et al.*[13] In Fig. 4 we compare our results with experimental data for various pressures. Our calculated compressibilities are in good agreement with the low pressure region and with the upper edge of the experimental results for high pressure. The experimental data exhibits a wide range which might be due to inclusions of solvent, impurities, voids, or other imperfections in many samples. Such defects would tend to give a higher compressibility, and hence it is the *less* compressible samples that might correspond most closely to the perfect crystal studied with theory. Our predictions represent the properties of well ordered crystals and suggest annealing fullerite at high pressure and temperature in order to remove impurities and defects.

To test the dependence of compressibilities on the van der Waals parameters, we considered three sets of parameters, all based on fits to the lattice parameters and elastic constants of graphite. Our standard potential Lennard Jones 12-6 has a well depth of D_e=0.06921 kcal/mol at R_e=3.8050 Å.[7] For graphite this leads to c =

6.6721 Å, C_{33} = 40.70 GPa, and a sheet-sheet cohesive energy of 1.299 kcal/mol. We also use an exponential six potential (D_e = 0.07372 kcal/mol, R_e = 3.8013 Å and a scale factor of 14.255) which leads to the same properties of graphite, and a second exponential six potential (D_e = 0.08444, R_e = 3.8837 and a scale factor of 12.0) which leads to the same c and C_{33} for graphite but a sheet-sheet cohesive energy of 1.719 kcal/mol [N. Karasawa and W.A.G. private communication]. Denoting these potentials as LJ, X6 (14.255), and X6 (12.0) we find that the heat of sublimation at 707K is 40.9, 39.9, and 57.0 kcal/mol. Since experiment is $\sim$ 40.1$\pm$1.3 at 707 K, the X6 (12.0) is definitely less accurate than the other two. These potentials lead to compressibilities of 16.6, 17.1, and 15.6 GPa. Based on such comparisons we estimate that the compressibility is 16.8$\pm$0.4 GPa.

A second issue relating to the accuracy of predictions is the compressibility of the buckyballs themselves. To test our predictions we calculated the vibrational frequencies of C_{60} in the crystal. The lowest three Raman transitions are $1H_g$ (squashing mode), $2H_g$, and $1A_g$ (breathing mode), which are observed at 273, 435, and 497 cm^{-1} in the condensed phase.[14] Our calculations lead to 272, 439, and 499 cm^{-1} for the fcc crystal , in excellent agreement with experiment. Thus the distortion energies of buckyballs should be well described with our force field.

Our calculations on the crystal structure of C_{60} indicate that the most stable structure is orthorhombic[7]; however the powder diffraction data are consistent with a cubic lattice[10]. We believe that this discrepancy is due to static orientational disordering of the C_{60}'s in the experimental samples. With optimum orientations each C_{60} has eight good interactions and four fair interactions with its 12 neighbors, leading to an orthorhombic distortion of the unit cell. We find three other locally stable (orthorhombic) structures with differing distributions of orientations, but with the total energies within 0.7 kcal/mol of the ground state. Forcing the orthorhombic form into a cubic cell with the same volume costs 0.8 kcal/mol (this

leads to a = 14.00 Å whereas the value deduced from experiment is a = 14.04 Å). Our conclusion is that preparing these samples at room temperature or above leads to randomization of the orientations which lock into various locally favorable orientations as the sample is quenched. The resulting structure would not have a favored axis, leading to a powder diffraction pattern indexable in terms of cubic symmetry.

In order to determine the generality of these results for fullerites, we also examined the compressibility of C_{70} fullerite up to 100 GPa. These results are shown in Fig. 5 where we see that the compressibilities of C_{60} and C_{70} are nearly identical up to 100 GPa! The changes in the c and a axes show that C_{70} is quite anisotropic, being less compressible along the long(c) axis and more compressible along the short (a) axis.

For C_{60} fullerite, we estimate the heat of formation to be 10.3 kcal/mol C atom (based on our calculated values of: strain energy = 11.0 kcal/(mol C), ΔH_{subl} = 43.9 kcal/mol C_{60}, and graphite cohesive energy = 1.3 kcal/mol C to separate into sheets). This places fullerite significantly above either diamond (0.45 kcal/mol) or graphite (0 kcal/mol).

In Figure 3 we show the structure of the buckyball as a function of pressure. By 100 GPa (1 megabar) *the soccer ball has become a soccer cube*! This distortion of the balls into cubes (Fig. 3) should lead to a dramatic increase in the resistance to shear deformation at high pressure. By the nature of the force field used in these calculations, new covalent bonds cannot be formed. However the changes in shape of the C_{60} framework due to the van der Waals interactions with other C_{60}'s has clearly distorted the bond angles toward the tetrahedral values appropriate for diamond at high pressure. Based on these calculations we believe that the bonds of C_{60} will rearrange to form diamond (rather than into graphite or amorphous carbon) at pressures well below 100 GPa. This is is because the structure of C_{60} keeps the carbon atoms in a non-planar configuration more compatible with the

diamond structure. Full electronic structure calculations (and experiments) should be able to test these ideas.

Given that the energy of C_{60} starts 10.3 kcal/mol above diamond (whereas graphite starts at 0.45 kcal/mol below diamond) and that the local structure of C_{60} tends toward the tetrahedral coordination with pressure, we suggest that at appropriate temperature and pressure the rearrangement of fullerene to form large crystals of diamond might be quite favorable. This could be a most significant application for buckyballs since the alternatives (the GE process[15] of subjecting graphite to high pressure and high temperature in the presence in the metal catalysts and the CVD of diamond from low pressure CH_4/H_2) lead to small crystallites. Using buckyballs it might be possible to use lower pressure and temperature than with graphite, and it should be possible to reduce or eliminate the catalysts. If so the importance of potential applications requiring large crystals (high temperature electronic materials, highly insulating-thermal conducting substrates, radar domes) might justify the higher costs inherent in first converting the graphitic carbon electrodes to C_{60} and then applying high pressure to form diamond.

Acknowledgement: This research was funded in part by the Air Force Office of Scientific Research (AFOSR-88-0051) and by the Office of Naval Research (N00014-91-J- 1671). The MSC/BI is also funded by grants from DOE-ECUT, NSF-DMR-MRG, NSF-CHE, BP America, Asahi Chemical, Asahi Glass, Allied-Signal, and Xerox Corp. and the Beckman Institute. This is contribution # 8461 from the Division of Chemistry and Chemical Engineering at Caltech.

References

1. Ruoff, R. S. & Ruoff, A. L. *Nature* **350**, 663-664 (1991).
2. Krätschmer, W., Fostiropoulos, K. & Huffman, D. R. *Chem. Phys. Lett.* **170**, 167-170 (1990).
3. Krätschmer, W., Lamb, L. D., Fostiropoulos, K. & Huffman, D. R. *Nature* **347**, 354-358 (1990).
4. Kroto, H. W., Heath, J. R., O'Brien, S. C., Curl, R. F. & Smalley, R. E. *Nature* **318**, 162-164 (1985).
5. Hebard, A.F., Rosseinsky, M.J., Murphy, D.W., Glarum, S.H., Palstra, T.T.M., Ramirez, A.P. & Kortan, A.R. *Nature* **350**, 600-601 (1991).
6. Holczer, K. *et al. Science* **252**, 1154-1157 (1991).
7. Guo, Y., Karasawa, N. & Goddard, W. A. *Nature* **351**, 464-467 (1991).
8. Zhao, Y.-X. & Spain, I. L. *Phys. Rev. B* **40**, 993-997 (1989).
9. Pan, C., Sampson, M. P., Chai, Y., Hauge, R. H. & Margrave, J. L. *J. Phys. Chem.* **95**, 2944-2946(1991).
10. Heiney, P. A. *et al. Phys. Rev. Lett.* **66**, 2911-2914 (1991).
11. Parrinello, M. & Rahman, A. *J. Appl. Phys.* **52**, 7182-7190 (1980).
12. Duclos, S. J., Brister, K., Haddon, R. C., Kortan, A. R., & Thiel, F. A. *Nature* **351**, 380-382 (1991).
13. Fischer, J. E. et al. *Science* **252**, 1288-1290 (1991).

14. Bethune, D. S., Meijer, G., Tang, W. C. & Rosen, H. J. *Chem. Phys. Lett.* **174**, 219-222 (1990).

15. Bundy, F. P., Hall, H. T., Strong, H. M., & Wentorf, Jr., R. H., *Nature* **176**, 51-53(1955).

FIGURE CAPTIONS

(1) Equation of state for C_{60} fullerite and for graphite. For graphite we compare the theoretical (long dash line) and experimental (dots) results. For fullerite we also show how the compressibility would be changed if C_{60} were completely rigid (hard ball C_{60}).

(2) The bulk modulus for diamond, graphite, and fullerite. We also show how the bulk modulus would be changed if each C_{60} were rigid (hard ball C_{60}).

(3) Optimum structure of the C_{60} fullerene molecule in crystalline fullerite as a function of pressure.

(4) Comparison of calculated equation of state for fullerite with various experimental data[12,13]. Solid symbols indicate data under hydrostatic conditions while open symbols indicate nonhydrostatic (less accurate) results.

(5) Equation of state for C_{70} fullerite (compared with C_{60}). Here a and c refer to the axes of this hcp crystal.[7]

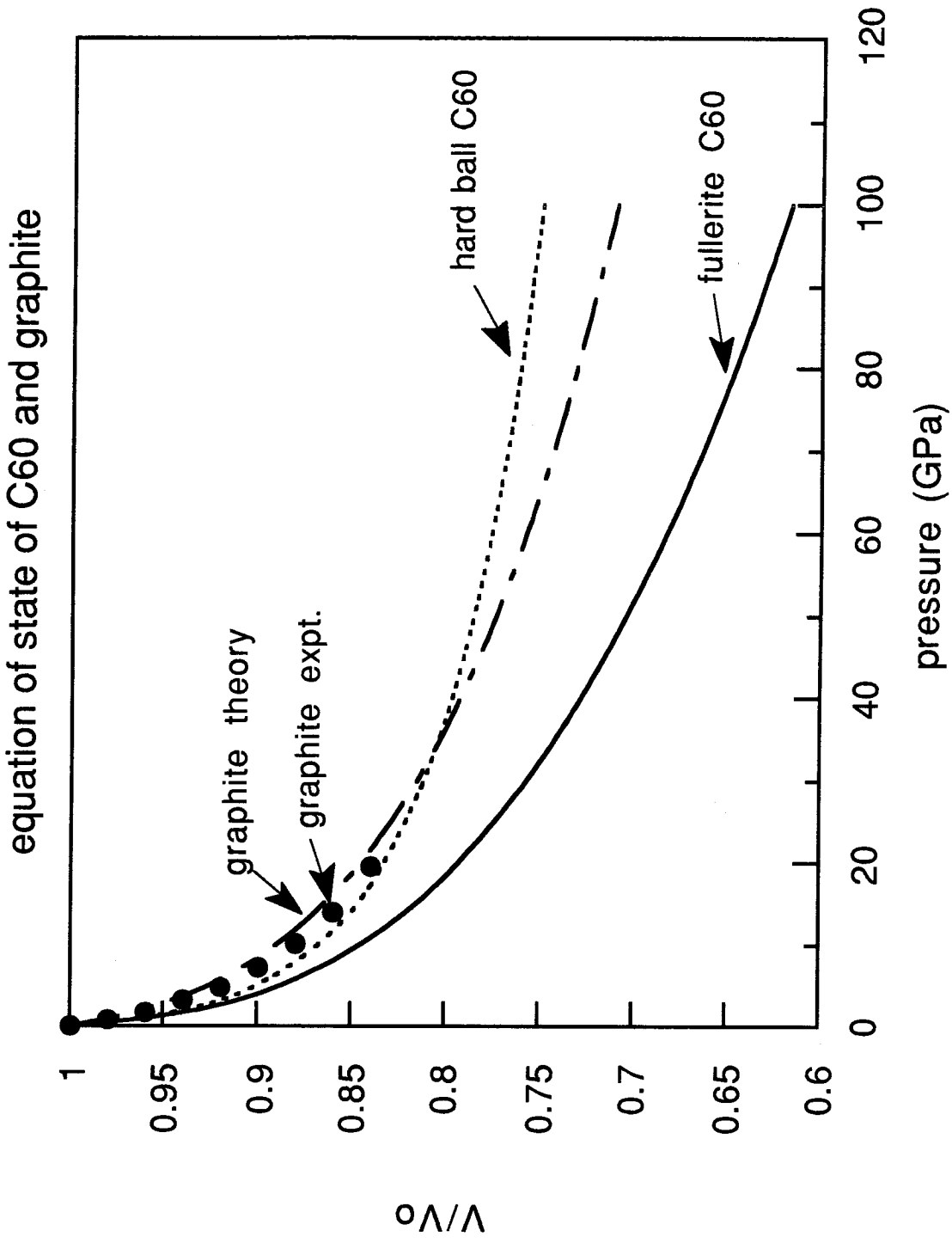
equation of state of C60 and graphite
graphite theory
graphite expt.
hard ball C60
fullerite C60
V/Vo
pressure (GPa)
1
0.95
0.9
0.85
0.8
0.75
0.7
0.65
0.6
0
20
40
60
80
100
120

Figure 1.

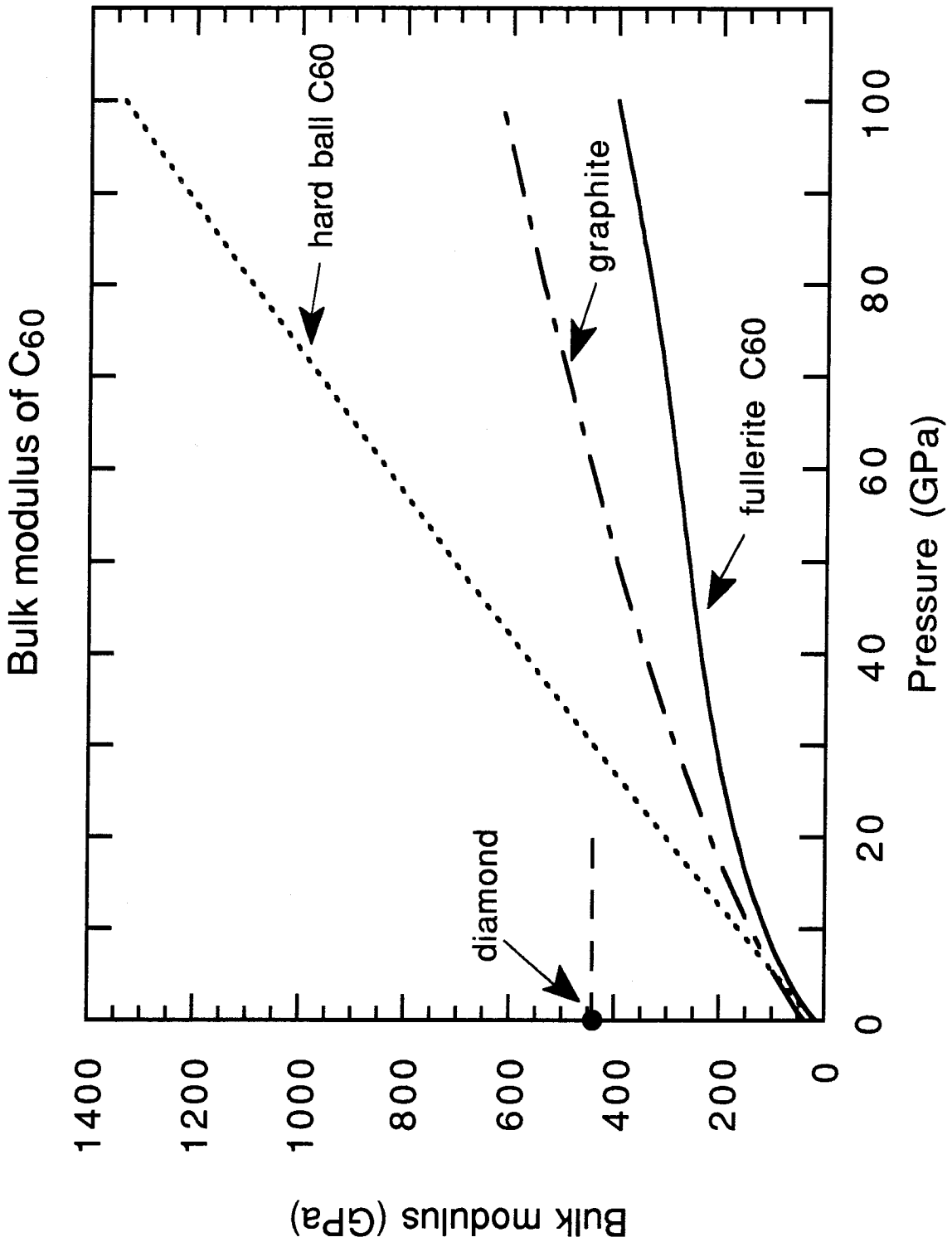
Bulk modulus of C60
hard ball C60
graphite
fullerite C60
diamond
Pressure (GPa)
0
20
40
60
80
100
Bulk modulus (GPa)
0
200
400
600
800
1000
1200
1400

Figure 2.

Structures of fullerite C_{60} under pressure

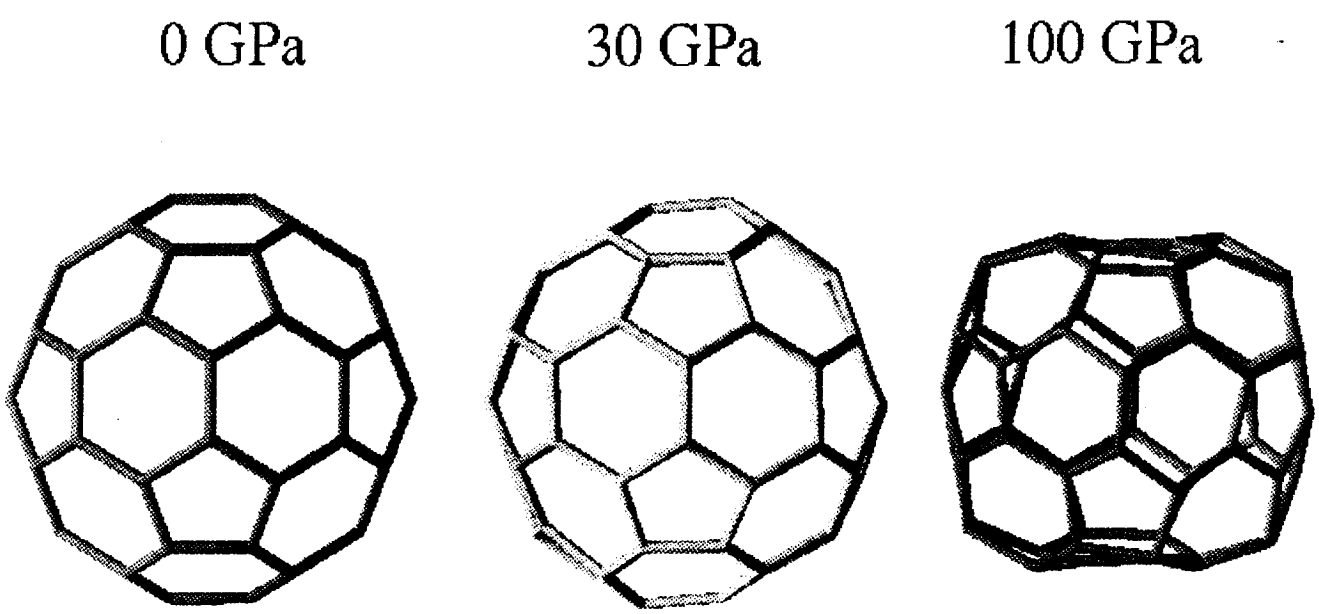

Figure 3.

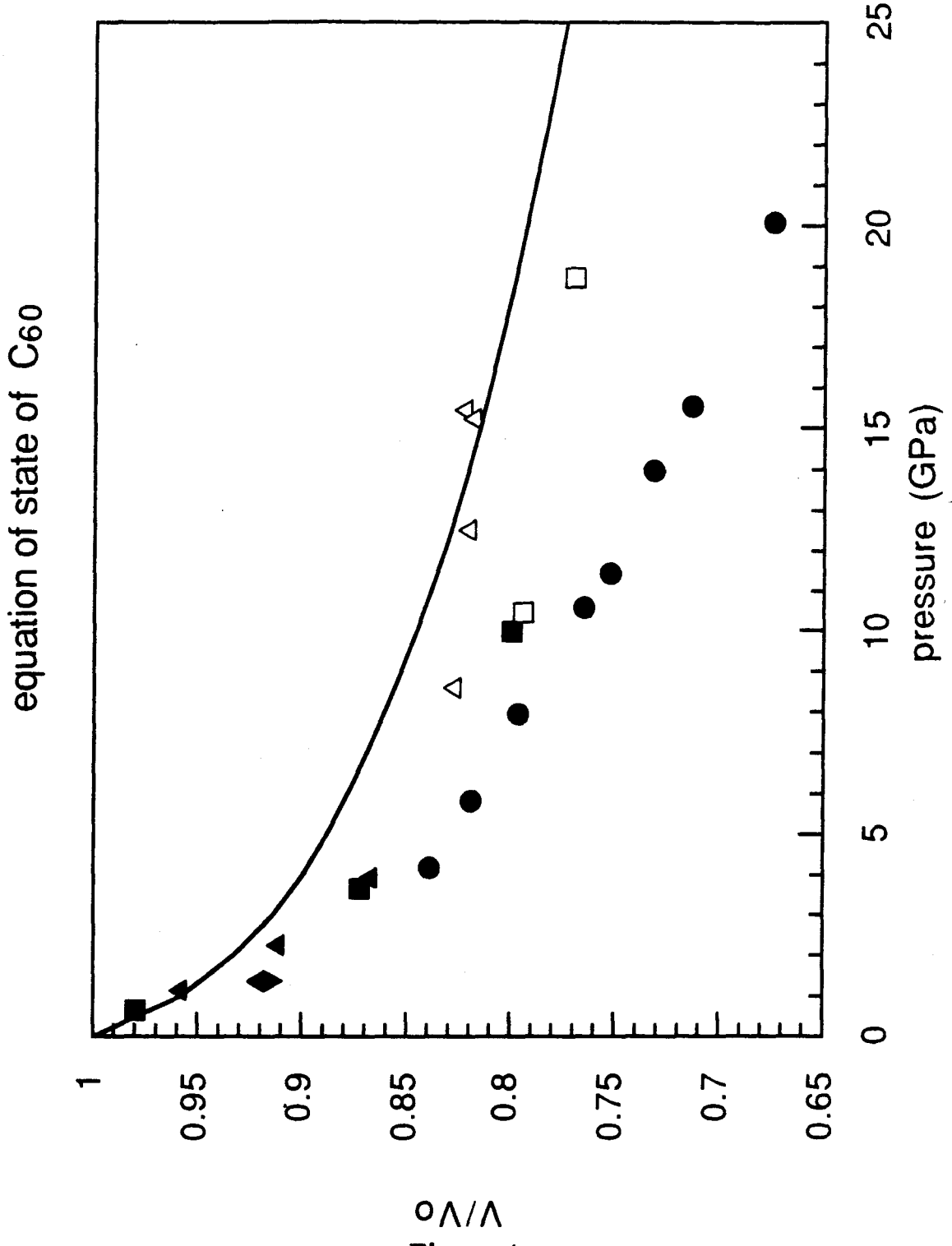
equation of state of C60
V/Vo
1
0.95
0.9
0.85
0.8
0.75
0.7
0.65
0
5
10
15
20
25
pressure (GPa)

Figure 4.

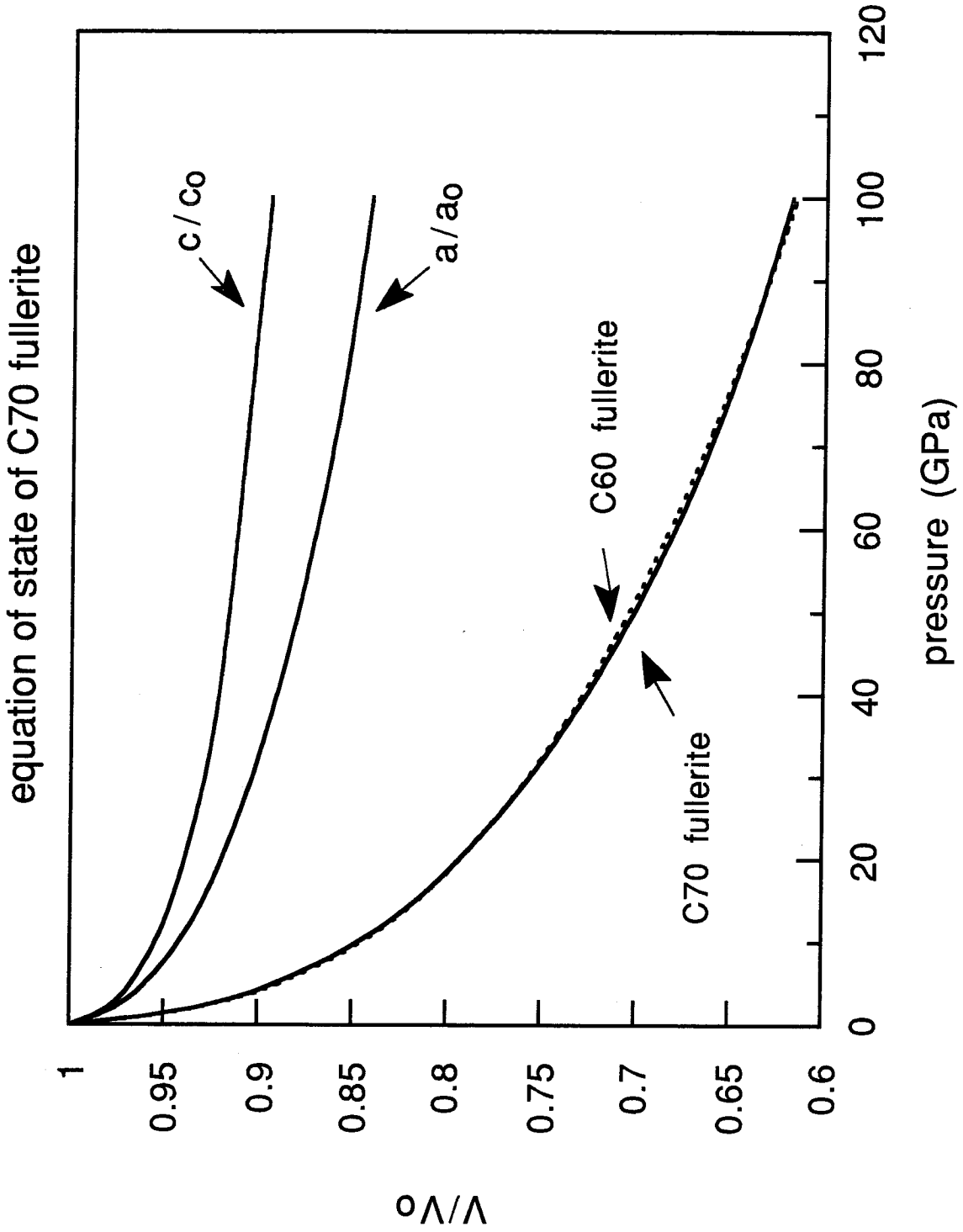
equation of state of C70 fullerite
c / co
a / ao
C60 fullerite
C70 fullerite
V/Vo
pressure (GPa)
1
0.95
0.9
0.85
0.8
0.75
0.7
0.65
0.6
0
20
40
60
80
100
120

Figure 5.

Chapter 6

Crystal Structures, Energetics, and Superconductivity for K_xC_{60} Fullerenes (Buckyballs)

Crystal Structures, Energetics, and Superconductivity for K_xC_{60} Fullerenes (Buckyballs)

Yuejin Guo and William A. Goddard III

Materials & Molecular Simulation Center

Beckman Institute (139-74)

California Institute of Technology, Pasadena, California 91125

Abstract

Recently, Hebard *et al.* reported that K_xC_{60} fullerene (buckyball) is superconducting with a transition temperature of 18K! We report here crystal structures for K_3C_{60}, K_2C_{60}, and KC_{60} predicted using force fields developed for graphite and for K intercalated graphite. We find that K_3C_{60} is FCC with K at all tetrahedral(tet) and octahedral(oct) interstices. Addition of three K per C_{60} greatly stabilizes the FCC structure, and K in the tet sites leads to orientational ordering of the C_{60}, suggesting that it may be much easier to obtain good quality crystals of K_3C_{60} than of pure C_{60}. For K_0C_{60} the space in the tet hole is 1.24 Å , whereas the space in the oct hole is 1.65 Å . Since K^+ is 1.38 Å , it is under compression in the tet site and tension in the oct site. We find that KC_{60} and K_2C_{60} also favor FCC. For KC_{60} the structure with K occupying all oct sites is best; however, for K_2C_{60} occupation of all tet sites is best. This leads to nonmonotonic changes of lattice parameter with doping (a = 9.93 Å for x = 0, 9.86 Å for x = 1, 10.13 Å for x = 2, and 10.02 Å for x = 3) and should lead to nonmonotonic behavior for other properties. These structural results are used to suggest the mechanism of superconductivity in these systems. This mechanism(which is BCS-like) suggests dependences of T_c on x and pressure that would help test the mechanism.

Recently Haddon *et al.*[1] of AT&T Bell Laboratories, reported that alkali doped C_{60} fullerene solids are metallic (with a conductivity of up to 500 Scm^{-1} for K_xC_{60}). This has now been followed by the announcement from Hebard *et al.*[2] of AT&T Bell Laboratories, that K_xC_{60} is superconducting with a transition temperature of 18K! This is the highest T_c yet reported for an organic system and past experience would suggest that this T_c might increase substantially as this new class of superconductors is studied further.

As a first step toward understanding the metallic and superconducting properties of these systems, we report here crystal structures for K_3C_{60}, K_2C_{60}, and KC_{60} predicted using force fields developed for graphite[3] and for K intercalated graphite.[4,5] For K_3C_{60} we examined three distinct packings of the C_{60} molecules:

a. FCC (face centered cubic or cubic closest packed) with K at all tetrahedral(denoted tet) and octahedral(denoted oct) interstices.

b. HCP (hexagonal closest packed) with K at all tet and oct interstices.

c. BCC (body centered cubic) with two K on each cube face to yield the A-15 structure (same structure as Nb_3Sn and other high T_c metallic alloys).

The results are summarized in Table I.

We recently found[6] that C_{60} prefers FCC over HCP by a small amount ($\sim$ 0.5 kcal/mol), but that BCC C_{60} is much higher (4.8 kcal/mol). We find that addition of three K per C_{60} *greatly stabilizes the FCC structure* (9.1 kcal/mol lower than BCC, 14.3 kcal/mol lower than HCP). This strong preference for FCC results from the more uniform distribution of K sites, leading to a shortest K...K distance of 6.166 Å. In contrast, the HCP structure leads to a very short distance of 4.08 Å(because adjacent tetrahedra share a face), destabilizing the HCP structure. It is interesting that the BCC structure (which for C_{60} is far higher than FCC or HCP) is stabilized with respect to HCP by packing the K to obtain the A-15 structure

characteristic of Nb_3Sn type metallic superconductors. Here the K...K distance is 5.75 Å.

This structure for K_3C_{60}, with cubic closest packing of C_{60}'s and occupation by K of all tet and oct interstices is new (no analogs have previously been reported). The C_{60} molecules orient so that each tet K faces six-membered rings from each of the four C_{60} and such that each oct K faces the middle bond of a fused pair of six-membered rings of each of the six C_{60} as shown in Figure 1.

We find that KC_{60} and K_2C_{60} also favor FCC over HCP and BCC. However, since FCC has one oct and two tet interstitial sites per C_{60} molecule, there are several choices of putting one or two K into these sites. We studied several cases shown in Table II.

For KC_{60} we find that *the structure with* K *occupying all oct sites* (NaCl structure) *is best,* 5.9 kcal/mol lower than the structure with K occupying tet sites (GaAs or sphalerite structure). The reason is that the tet site is too small for K, leading to higher van der Waals(vdW) repulsion (by 9.9 kcal/mol).

However for K_2C_{60}, *occupation of all tet sites* (Li_2O or antifluorite structure) *is more stable* (by 13.2 kcal/mol) than occupation of all oct plus half of tet sites. This is because the shortest K...K distance in the oct + tet structure is shorter by about 1 Å than in the tet + tet structure, which causes higher Coulomb repulsion between K^+ cations.

These calculations suggest an interesting sequence of K site occupation as doping is increased from $x = 0$ to $x = 3$. Thus $0 \leq x \leq 1$ has K filling oct sites; $1 \leq x \leq 2$ has each oct site converted to a pair of tet sites; and $2 \leq x \leq 3$ has an additional K in the oct site. In each of these regions there could be additional ordered phases. For example, $K_{1.5}C_{60}$ could have alternate regions with two K in tet sites (compression) and with one K in the oct site (tension), leading to a stable ordered structure. Because K^+ is too large for tet sites and too small for oct sites,

we find a nonuniform change in lattice parameters with doping: 9.93 Å for x = 0, 9.86 Å for x = 1, 10.13 Å for x = 2, and 10.02 Å for x = 3. It is likely that other properties (e.g., conductivity, compressibility, lattice phonon modes, T_c for superconductivity) will have similar non-monotonic behavior with x.

For K_3C_{60} the shortest C – K distance is 3.21 Å in tet sites and 3.65 Å in oct sites; this can be compared with the shortest distances in K intercalated graphite of 3.01 Å for C_8K and 3.06 Å for $C_{24}K$. [Measured to the centers of the C_{60}, the K...C_{60} separations are 6.14 Å at the tet sites and 7.09 Å at the oct sites.] Assuming the vdW radius of carbon to be 1.90 Å (half the vdW minimum) leads to a K^+ radius of 1.31 Å in the tet site and 1.75 Å in the oct site. Correcting for the changes in lattice spacings, we find that the tet hole is 3.14 Å for K_0C_{60} (room for an ion of radius 1.24 Å) which expands to 3.29 Å for K_1C_{60} and K_2C_{60} when K is *only* in tet sites (room for an ion of radius 1.39 Å , quite close to the standard radius of 1.38 Å for K^+). For the oct site we find a hole of 3.59 Å for K_0C_{60} (room for an ion of radius 1.69 Å). This drops to 1.64 for K_1C_{60} with K in the oct site. Those ion hole sizes in K_0C_{60} of 1.24 Å for the tet and 1.69 Å for oct explain *why vdW interactions favor the oct site* of K_1C_{60} (and K_2C_{60}). The K^+ is too small for the oct hole, and indeed we find that K_1C_{60} has a tendency to distort. On the other hand, the tet sites are a bit too small for K^+, leading to significant compression. The result is that all structures of KC_{60}, K_2C_{60}, and K_3C_{60} that have the tet sites occupied show a strong tendency toward cubic symmetry.

It is important to note that for K in the tet site of K_xC_{60}, the total distance from the K to the center of the C_{60} (6.14 Å for K_3C_{60}) is much smaller than the sum, 6.77 Å , of the radius of C_{60} (3.56 Å) plus the K...C distance (3.21 for K_3C_{60}). This discrepancy of 0.63 Å results because C_{60} is not round, it has hexagonal faces that have to orient so as to accommodate K in the tet sites. This leads to a strong energetic driving force to orient the C_{60}, and a large barrier for rotating the C_{60}.

Thus K in tet sites is like dirt in the C_{60} gears, causing each C_{60} to be ordered. Because of this K_xC_{60} with $2 \leq x \leq 3$ *should have a strong tendency toward ordered* C_{60}, whereas $x < 1$ may lead to little such tendency.

If the C_{60} are not ordered then we would calculate the hole for K based on the K to center-of-C_{60} distance (6.14 for tet, 7.09 for oct). This would lead to a hole of 6.14−3.56−1.9=0.68 Å (big enough only for Li^+ of the alkalis) for the tet site and 7.09−3.56−1.9=1.63 Å for the oct site (big enough for all alkalis).

Films of K_xC_{60} with concentrations of K up to x= 6 can be made (K_xC_{60} is insulating). We have not calculated the structures but believe that these systems do not have such ordered locations for the K. Instead, we visualize distributing the K in the annular region about each C_{60}, with the K...K spacing decreasing as x increases.

In discussing the various structures (FCC, HCP, BCC), we use the terms to indicate overall packing of the C_{60} molecules. The actual space group symmetries are lower because each C_{60} has I_h symmetry, which is incompatible with the point symmetries of the FCC, HCP, and BCC structures. Indeed, for C_{60} crystals these asymmetries can lead to significant distortions of the lattice parameters from ideal. Thus for the FCC structure of C_{60} restricted to have only one C_{60} per primitive unit cell, we obtain cell parameters of 9.84, 10.13, and 9.82 Å and 59.1, 61.7, and 58.9° (instead of A = B = C, $\alpha = \beta = \gamma = 60°$). Allowing more C_{60} per unit cell leads to several different FCC structures depending on orientation, but all with similar energies. At room temperature the small barrier to rotation of a C_{60} in its lattice site leads to some equalization of the lattice parameters, but the presence of slightly different lattice parameters for each packing results in crystals that are not yet sufficiently regular for X-ray diffraction studies.

The presence of K with the associated strong electrostatic component of bonding leads to almost perfect FCC lattice parameters (e.g., for K_3C_{60}: 10.024,

10.024, 10.024 Å and 60.00, 60.00, 60.00 degrees). *This suggests that it may be much easier to obtain good quality crystals of* K_3C_{60} *than of pure* C_{60}. For pure C_{60} there is a strong tendency for the C_{60} molecules to orient such that the five fold axes are perpendicular to two of the four closest packed planes. As discussed above for K_xC_{60} with K in the tet sites, the orientation is dominated by C_{60} ... K ... C_{60} interactions rather than C_{60} ... C_{60} interactions, leading to long range orientational ordering and well defined cubic lattice parameters.

All calculations reported here allowed all atom positions and cell parameters to be fully relaxed in obtaining the various structures.[5] All calculations assumed that each K is fully ionized and that the charge on each C_{60}^{3-} is uniformly distributed (-0.05 e per carbon). [Such multiple ion states have been seen in electrochemical reductions.[7]] Full ionization of the K is plausible since the intercalated graphite system $C_{24}K$ (and more dilute compounds) has the K completely ionized[8] (C_8K might be only partially ionized). The force field for carbon[3] was developed to describe the elastic constants, phonons, and lattice parameters of graphite (at 0K). The K...C vdW parameters were chosen to describe $C_{24}K$, where we find a lattice spacing perpendicular to the sheets of 26.25 Å (expt. 26.25 Å).[9] [For C_8K we find 21.10 Å (expt. 21.60 Å) suggesting that the K should not be fully ionized].

In Table II we tabulate the energetics for the various structures. The preference for FCC K_3C_{60} is dominated by the Coulomb interactions, but van der Waals interactions also favor this structure.

Since the sizes of the holes in the tet and oct sites are quite different (1.24 versus 1.69 Å), we would expect interesting ordered structures for mixed metal systems. Considering just alkali ions [The ionic radii are: $Li^+(0.76Å), Na^+(1.02Å), K^+(1.38Å), Rb^+(1.52Å), Cs^+(1.67Å)$], we expect that Li^+ and Na^+ would favor tet sites while Rb^+ and Cs^+ should prefer oct sites. Thus K_2CsC_{60} might have K in tet sites while Na_2KC_{60} might have K in oct

sites. An important issue in considering these other metals is whether the metal is fully ionized. For alkali metals the ionization potentials are *Li (5.39 eV), Na (5.14 eV), K (4.34 eV), Rb (4.18 eV), Cs (3.89 eV)*[10], and it is known that both Li and Na intercalated graphite lead to only partial ionization. Indeed it is possible that K in oct sites of K_xC_{60}, might be only partially ionized since the hole is somewhat larger than the ion. Because of the much larger ionization potentials, monovalent metals such as Cu, Ag, and Au might not become fully ionized in MC_{60}. However their sizes suggest that K_2MC_{60} might have *M = Cu, Ag, and Au* in oct sites. Ca^{2+} has an ionic radius of 1.00 Å , favoring a tet site; however the first and second IP are 6.113 and 11.871 eV, so that Ca might not be fully ionized. Similarly Sr (R=1.18 Å , IP_I = 5.695 eV, IP_{II} = 11.030 eV) and Ba (R=1.35 Å , IP_I = 5.212 eV, IP_{II} = 10.004 eV) might be partially ionized in oct sites.

These results lead to speculations about the conduction properties in K_xC_{60}. (Band calculations are underway but not completed.[11]) In C_{60}^- the extra electron goes into the empty T_{1u} orbital (triply degenerate). The T_{1u} orbitals on adjacent C_{60} lead to small overlap and hence a narrow conduction band for undoped C_{60}. However the presence of K^+ bridging two C_{60} molecules stabilizes the bonding molecular orbital [of $K(C_{60})_2^-$] but not the antibonding orbital. This leads to a broad conduction band in K_xC_{60} and a good conductor. For K_3C_{60} there are three electrons and three T_{1u} orbitals per C_{60}. Since the oct K are in the $\pm x, \pm y, \pm z$ directions and the T_{1u} orbitals point in the x, y, and z directions, we visualize the conduction band as constructed from 3N K_{oct}-centered $C_{60}...K_{oct}...C_{60}$ bonding orbitals (where N is the number of C_{60} molecules). (The T_{1u} orbitals of C_{60} are fat, so that K_{tet} also play a role in stabilizing these orbitals). Indeed since K_6C_{60} is an insulator, we can visualize the conduction properties of K_xC_{60} from x= 0 to 6 in terms of filling these K stabilized T_{1u} bands.

These considerations suggests a BCS-like mechanism for superconductivity.

Considering that the charge carriers are primarily K^+ stabilized dimer orbitals $(C_{60} - K - C_{60})^-$, then hopping of the charge to and from such sites would lead to alternately attractive and repulsive forces on the K. This electron-phonon coupling would operate via the K lattice frequencies (average value 32 cm^{-1} for oct site and 138 cm^{-1} for tet site). In this model the optimum doping would seem to be K_3C_{60} since this would lead to a K stabilized electron in each of the $\pm x, \pm y, \pm z$ directions.

These considerations suggest that a special role might be played by the oct K (since they stabilize T_{1u} orbitals in the $\pm x, \pm y, \pm z$ directions.) If so, the superconducting T_c of K_xC_{60} might peak at $x = 1$ decrease to zero at $x = 2$, increase to a maximum at $x = 3$, and gradually decrease for higher x. For the same reason, high pressure would have an interesting effect since it would tend to populate oct sites in preference to tet sites. Thus for $1 \leq x \leq 3$ increased pressure would tend to increase T_c (the increased vibrational frequencies might compensate partially for this increase). On the other hand for $x < 1$, T_c would not increase with pressure. Calculations are underway to test these ideas.[12] Based on the relevant vibrational frequencies (32 to 138 cm^{-1} or 46 to 199 K), and assuming strong coupling, a crude estimate for the maximum T_c for the K_xC_{60} system is $\sim 1/5$ the vibration frequencies[12] or 10 to 40 K.

Experiments to determine the dependence of T_c on doping and pressure and to determine the concentration of K at oct and tet sites (e.g. by EXAFS, NMR, IR or Raman) as a function of doping and pressure would be most useful, in testing these ideas.

ACKNOWLEDGEMENTS. The research was funded by the Air Force Office of Scientific Research (AFOSR-88-0051).

References

1. R. C. Haddon *et al.*, *Nature* **350**, 320-322 (1991).
2. A. F. Hebard *et al.*, *Nature* **350**, 600-601 (1991).
3. W. A. Goddard, and N. Karasawa, *J. Phys. Chem.* (submitted). The force field uses Lennard-Jones 12-6 van der Waals interactions [$R_v = 3.8050$, $D_v = 0.0692$], Morse bond stretches [$R_b = 1.4114$, $k_b = 720.$, $D_b = 133.0$], cosine angle bends [$\theta_a = 120$, $k_{\theta\theta} = 196.13$, $k_{r\theta} = -72.41$, $k_{rr} = 68.$] and a two fold torsion [$V_t = 21.28$], where all distances are in Å, all angles in degrees, and all force constants and energies are in kcal/mol, Å, radian units. For more details on these definitions, see S. L. Mayo, B. D. Olafson, W. A. Goddard, *J. Phys. Chem.* **94**, 8897-8909 (1990).
4. We used a K...K Lennard-Jones potential [$R_v = 4.0010$ Å , $D_v = 0.0700$ kcal/mol] and a C...K Lennard-Jones potential [$R_v = 3.9018$ Å , $D_v = 0.0696$ kcal/mol].
5. These calculations were all carried out using POLYGRAF (from Molecular Simulations Inc. of Sunnyvale California, formerly known as BioDesign) in conjunction with additional vibrational analysis software written by N. Karasawa, S. Dasgupta, W. A. Goddard, of the Materials & Molecular Simulation Center/BI.
6. Y. Guo, N. Karasawa, W. A. Goddard, *Nature* (submitted).
7. P.-M. Allemand *et al.*, *J. Am. Chem. Soc.* **113**, 1050-1051 (1991).
8. G. R. Hennig, *J. Chem. Phys.* **43**, 1201-1206 (1965).
9. D. E. Nixon, and G. S. Parry, *J. Phys.* **D1**, 291-298(1968).
10. NSRDS-NBS 34, National Bureau of Standards, Washington, D.C., 1970.
11. J.-M. Langlois, M. N. Ringnalda, R. P. Muller, Y. Guo, W. A. Goddard III, work in progress.
12. G. Chen, Y. Guo, W. A. Goddard III, work in progress.

Figure Caption

(1) The K in tetrahedral(green) and octahedral(red) sites of FCC K_3C_{60}.

(2) The unit cell of FCC K_3C_{60}.

Table I. Predicted crystal structures for K_3C_{60} and C_{60}.

Structure		Z[a]	E[b]	ΔE[c]	Density	Cell Parameters[d]					
			kcal/mol	kcal/mol	(g/cm^3	A	B	C	α	β	γ
FCC	$C_{60}K_3$	1	378.386	0	1.954	10.024	10.024	10.024	60.00	60.00	60.00
	C_{60}	1	637.733	0	1.737	9.840	10.128	9.819	59.08	61.66	58.88
BCC	$C_{60}K_3$	2	387.496	9.110	1.871	11.420	11.417	11.410	90.09	90.09	90.09
	C_{60}[e]	1	642.507	4.774	1.662	9.784	9.780	9.774	109.5	109.5	109.5
HCP	$C_{60}K_3$	2	392.716	14.330	1.863	9.913	10.467	17.051	90.04	95.04	121.90
	C_{60}	2	638.251	0.519	1.729	9.834	10.077	16.235	90.34	91.56	120.55

[a]Number of C_{60} molecules per unit cell.

[b]Energy per C_{60}.

[c]Reference points are FCC K_3C_{60} and C_{60} for K doped and pure phases, respectively.

[d]Å and degrees.

[e]BCC is not locally stable and we restricted the calculation to ideal angles.

Table II. Predicted structure and energies for FCC K_xC_{60}.

Compound	K site	Energies(kcal/mol)					Density	Lattice
		Valence[a]	vdW	Coulomb	Total	ΔE	(g/cm^3)	constant(Å)
$C_{60}K$	octahedra	0	−2.701	−55.712	−58.413	0.000	1.855	9.862
	tetrahedra	0.186	7.171	−59.833	−52.476	5.937	1.716	10.131
$C_{60}K_2$	tet+tet	0.199	9.165	−158.427	−149.062	0.000	1.804	10.131
	oct+tet	0.154	5.117	−141.181	−135.910	13.152	1.856	10.036
$C_{60}K_3$	tet+tet+oct	0.327	9.286	−268.416	−258.804	–	1.954	10.024

[a]The reference point is $C_{60}K$(oct) with a valence energy of 637.189 kcal/mol.

unit cell of f.c.c. K_3C_{60}

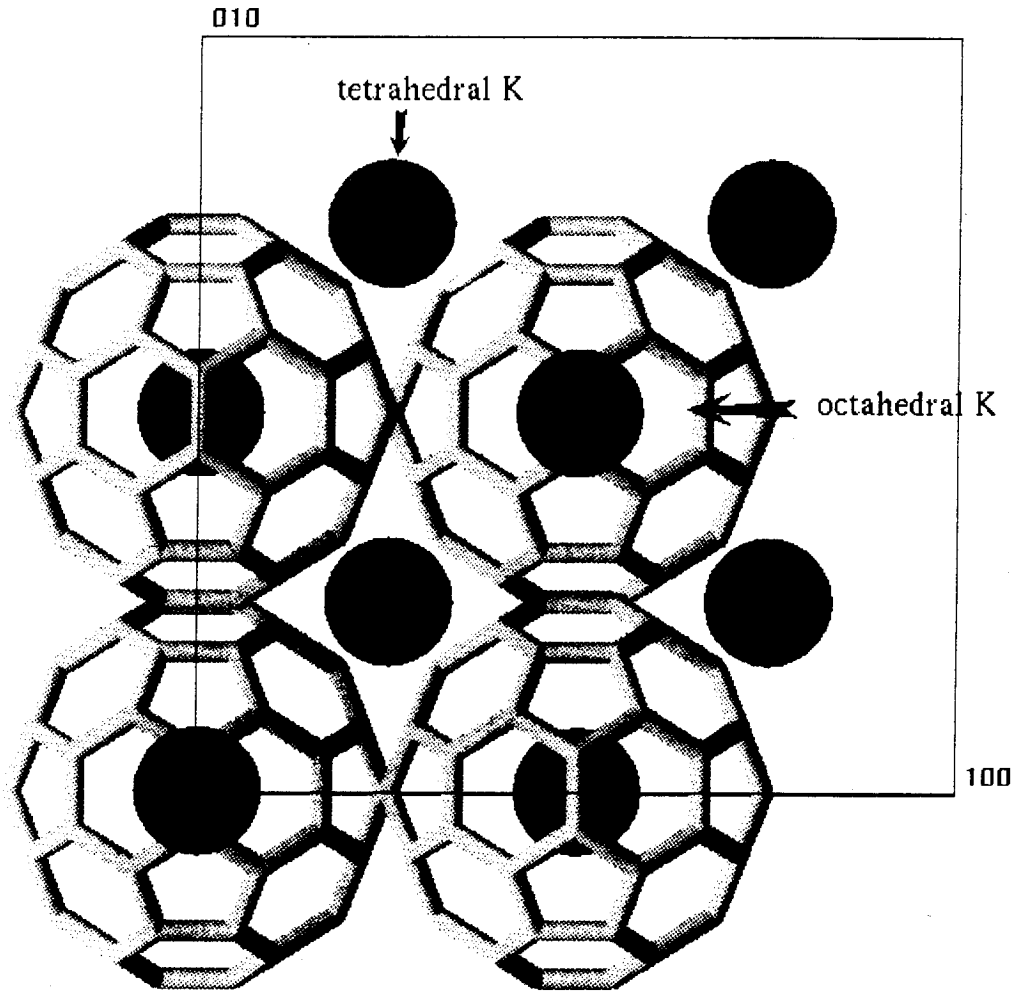

Figure 1.

oct and tet sites of FCC K_3C_{60}

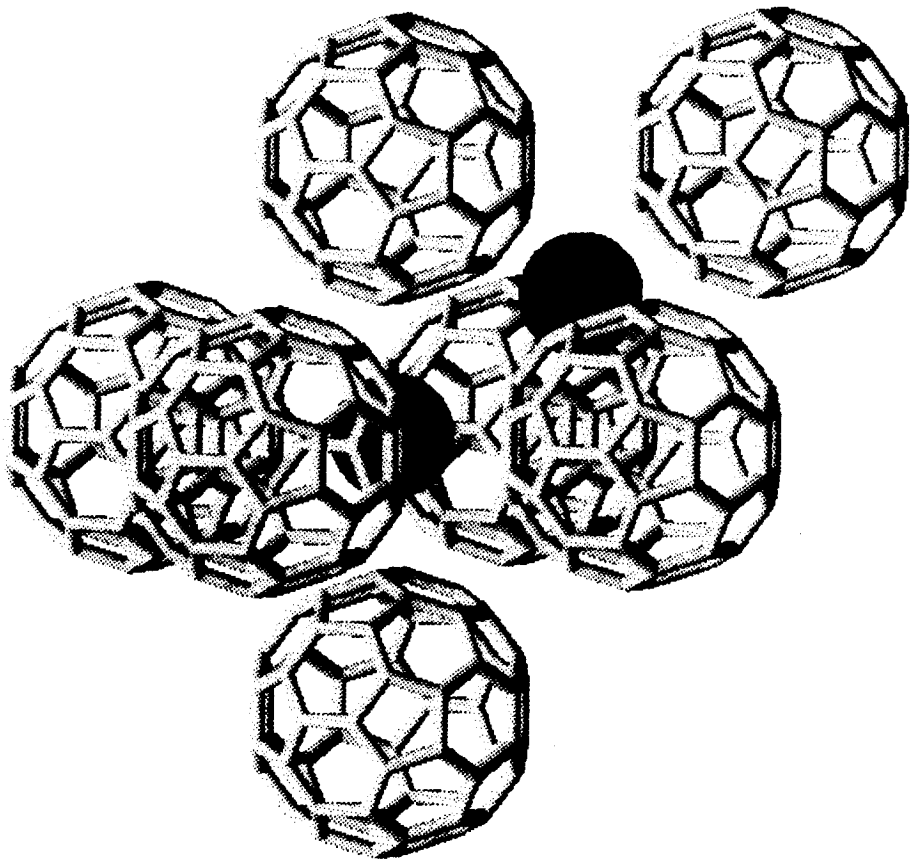

Figure 2.

Chapter 7

A New Structure for Buckyball Superconductors: The bcc (A-15) Structure for M_3C_{60} with $M = K, Rb, Cs$.

A New Structure for Buckyball Superconductors: The bcc (A-15) Structure for M_3C_{60} with M = K, Rb, Cs.

Yuejin Guo and William A. Goddard III

Materials & Molecular Simulation Center

Beckman Institute (139-74)

California Institute of Technology, Pasadena, California 91125

Abstract

We report theoretical structural studies of M_xC_{60} where x = 0, 1, 2, 3, 6 and M = Li, Na, K, Rb, Cs. For M_6C_{60} with M = K, Rb, Cs we confirm the bcc structure reported for M = K, Cs. For M_3C_{60} with M = K, Rb, Cs we find stable fcc and bcc (A-15) structures, *with bcc more stable.* Experimentally fcc has been observed to be superconducting but bcc has not yet been observed. The bcc form is metallic and should have superconductivity properties different from fcc. We suggest procedures for synthesizing bcc M_3C_{60}.

PACS numbers: 61.50.-f, 74.10.+v, 74.70.-b, 61.55.-x

Alkali doped C_{60} fullerites have been shown recently to be superconductors with T_c = 19.3 K for K_3C_{60}[1,2], 28~30 K for Rb_xC_{60}[2,3], and 30~33 K for Cs_xC_{60}[4] and $Cs_xRb_yC_{60}$.[5] In order to establish a structural basis for optimizing and developing new buckyball superconductors, we report the principles and predictions arising from theoretical structural studies of M_xC_{60} where x = 0, 1, 2, 3, 6 and M = Li, Na, K, Rb, Cs. [These studies use a force field which successfully predicts[6,7] the packing, density, heat of sublimation, and compressibility for C_{60} and C_{70}.] We rationalize these results in terms of packing and ion size considerations. These results confirm the bcc structure reported[8] for K_6C_{60} and Cs_6C_{60}, which we find applies also to M = Rb but *not* to Li, Na (they prefer fcc packing). For the superconductor K_3C_{60}, the fcc structure predicted theoretically[6] and determined experimentally[9] is *stable but not the lowest energy*! For M_3C_{60} with M = K, Rb, Cs we find that the most stable structure is bcc with C_{60}'s at the center and corners of a cube and two M on each face, forming chains in the x,y,z directions. This is the A-15 structure associated with the highest T_c intermetallic compounds (Nb_3Sn, Nb_3Ge, etc.). We believe that the metastable fcc structure observed for K_3C_{60} results from the synthetic procedure of diffusing K into the fcc C_{60}, and we suggest alternative procedures for synthesizing bcc M_3C_{60}. We expect that both the fcc and bcc forms of M_3C_{60} are superconducting and that the T_c are different. These results suggest a number of interesting experiments.

We find that the optimum structures of M_xC_{60} with M = Li, Na, K, Rb, Cs (see Table 1) can be rationalized in terms of the following simple packing considerations.

For fcc packing of C_{60} there are two interstitial positions, tet and oct (tetrahedral and octahedral). Assuming that round C_{60}'s are in contact with radius r_A,

the space available for the alkali ion (r_M) is

$$\text{tet}: \frac{r_M}{r_A} = \frac{a\sqrt{3}/4 - a/2\sqrt{2}}{a/2\sqrt{2}} = 0.225 \ \ (2 \text{ per } C_{60})$$

$$\text{oct}: \frac{r_M}{r_A} = \frac{a/2 - a/2\sqrt{2}}{a/2\sqrt{2}} = 0.414 \ \ (1 \text{ per } C_{60}) \ .$$

On the other hand, for bcc packing of C_{60} there are four tet sites on each face (with nearest neighbors being the body centers above and below the face plus two adjacent corners). There is also one squashed oct site for each face and for each edge. The space available for the alkali is

$$\text{tet}: \frac{r_M}{r_A} = \frac{a\sqrt{5}/4 - a\sqrt{3}/4}{a\sqrt{3}/4} = 0.291 \ \ (6 \text{ per } C_{60})$$

$$\text{oct}: \frac{r_M}{r_A} = \frac{a/2 - a\sqrt{3}/4}{a\sqrt{3}/4} = 0.155 \ \ (3 \text{ per } C_{60}) \ .$$

Based on the optimal packing in C_{60} at 0 K (averaged over the 12 neighbors), the effective radius of C_{60} is $r_A = 9.914/2 = 4.96$ Å. Using standard ionic radii[10]: Li (0.76 Å), Na (1.02 Å), K (1.38 Å), Rb (1.52 Å), and Cs (1.67 Å), we obtain

$$\frac{r_M}{r_A} = 0.153(\text{Li}),\ 0.206(\text{Na}),\ 0.278(\text{K}),\ 0.307(\text{Rb}),\ 0.337(\text{Cs}) \ .$$

The above analysis discusses the anions (C_{60}) as if they were round balls, but in fact the hexagonal (hex) and pentagonal (pent) rings lead to facets with hex having an effective radius smaller by 0.3 A. Thus ions too large for the fcc tet site will cause the C_{60}'s to reorient so that the hex faces point at the tet sites (rather than pointing at C_{60} neighbors as in fcc M_0C_{60}).

Consider first M_1C_{60}. We find that $C_{60}...C_{60}$ interactions dominate so that fcc is most stable (for M_0C_{60} bcc is 5 kcal/mol higher than fcc[6]). Since K, Rb, Cs have $r_M/r_A \geq 0.278$, fcc is stable with M in the *oct site.* However Li, Na have $r_M/r_A \leq 0.206$, and hence fcc is stable with M = Li, Na in the *tet site.* In each case

the optimum structure has the C_{60}'s oriented just as for M_0C_{60}. With M in the oct site the lattice constant decreases (since all ions are smaller than the site). However forcing M = K, Rb, Cs into the tet site increases the lattice constant. The relative stability of oct over tet increases for M = K, Rb, Cs since M becomes increasingly larger than the tet site.

For M_2C_{60} we find that the most stable structure is also fcc but with both M in tet sites! This is better than all oct + half tet because of ion-ion repulsion. For the larger ions (M = K, Rb, Cs) there are strong forces orienting the C_{60}'s so that each has hex faces pointing toward each tet K (along each body diagonal).

Next consider M_3C_{60} (Table 1 has energies and other parameters). With all five ions we found locally stable structures (all second derivatives positive) for both bcc and fcc. For Li and Na the ion fits easily into both the tet and oct sites of fcc and the tet sites of bcc, and we find that fcc is stable (by 18.4 and 4.4 kcal/mol for Li and Na, respectively). However, the larger cations (K, Rb, Cs) are too big for the tet site, so that bcc is favored, with increasing stability for larger alkali's (by 1.6, 2.2, 3.1 kcal/mol for K, Rb, Cs, respectively). For fcc the $C_{60}...C_{60}$ separation increases for ions larger than the tet site, but decreases for smaller ions. For bcc similar results are found. Subsequent to these calculations (cited in ref. 6), the experimental structure for fcc K_3C_{60} was reported.[9] Theory and experiment lead to exactly the same structure except that the experiment (at 300 K) finds disorder in the C_{60}'s (90° rotations) whereas we find ordering. The cubic lattice constant is 14.18 Å from theory (0 K) and 14.24 Å from experiment (300 K), about the difference expected from thermal expansion.

One can use simple electrostatic balance considerations[10b] to predict the bcc structure for M_3C_{60}. Assuming that all M are in tet sites, each M transfers 1/4 e^- to each of its four C_{60} neighbors. Thus each C_{60} must have 12 such M neighbors to obtain its charge of −3. Since each M prefers a hex face, this leaves

$20-12 = 8$ faces available for direct $C_{60}...C_{60}$ contacts. This leads to bcc packing of the C_{60} and the optimum structure found in the calculations (Fig. 1). Here the 12 M neighbors to a single C_{60} form an icosahedron with M's sitting above 12 hex faces. The M triangles surrounding the eight empty hex sites then expand to allow better $C_{60}...C_{60}$ contacts. The result is that each C_{60} in bcc K_3C_{60} has 12 K neighbors at R = 6.29 Å (from the center) and 8 C_{60} neighbors at 9.75 Å; each K has four C_{60} neighbors at 6.29 Å, three K neighbors at 5.63 Å and two K neighbors at 6.90 Å. The closest K...C distances are 3.15 Å (24 C per K) which compares well to the value of 3.09 Å (12 C per K) observed in KC_{24} intercalated graphite[11]. The requirement that eight empty hex faces point along the diagonal leads to two possible orientations (rotations of 90°) of each C_{60} about either x, y, or z axes. As indicated in Fig. 1, the optimum corner and center C_{60} must be rotated by 90° in order that each K sees four hex faces.

For the fcc structure of K_3C_{60} the two K in tet sites use 8 hex faces of each C_{60} and transfer two electrons to each C_{60}. (These K sit along the eight diagonal directions of the cube.) The K in oct sites sit along the six cubic axes from each C_{60} and contact the central bond of a fused pair of hex rings (they transfer a total of one electron to each C_{60}). The net result is that each C_{60} has 14 K neighbors (8 at 6.14 Å and 6 at 7.09 Å) with 8 of the hex rings in use. This leaves 12 hex rings available for $C_{60}...C_{60}$ interactions (at 10.024 Å). However, the C_{60} are not optimally oriented for $C_{60}...C_{60}$ interactions. They have the ideal cubic orientation[6] which for M_0C_{60} is 5 kcal/mol higher than the optimum M_0C_{60} fcc structure. Each tet K has four C_{60} neighbors at 6.14 Å, six tet K neighbors at 6.14 Å, and four oct K at 7.09 Å. Each oct K has six C_{60} neighbors at 7.09 Å and eight tet K neighbors at 6.14 Å.

For the hcp structure of M_3C_{60}, there are two tet and one oct interstitial sites just as for fcc. However, for hcp each tet site shares a face with an another tet

site. This results in very close K interactions (4.08 Å for ideal hcp K_3C_{60}; 4.69 Å for distorted hcp K_3C_{60}) and an energy 14 kcal/mol above fcc K_3C_{60}.

Our prediction that the most stable structure of K_3C_{60} is bcc *directly contradicts the recent diffraction study* showing K_3C_{60} to be fcc[9]. We find that both are locally stable (all second derivatives positive), but bcc has an energy 1.6 kcal/mol *lower* than fcc (2.2 and 3.1 kcal/mol lower for Rb_3C_{60} and Cs_3C_{60}, respectively). We believe that these experiments observe metastable fcc K_3C_{60} because the K_3C_{60} was synthesized by diffusing K into fcc C_{60} and carefully equilibrating. Our calculations indicate that fcc is stable with respect to bcc up to at least K_2C_{60}, and we believe that it is plausible that diffusion could lead to fcc K_3C_{60} even though bcc is slightly more stable. Since both experiment and theory agree that K_6C_{60} has bcc packing, (vide infra), we suggest that bcc K_3C_{60} be obtained by first forming K_6C_{60} and then using appropriate vacuum and temperature conditions to remove sufficient K to form K_3C_{60}, which we predict will be bcc. (It may be possible to use K_xC_{60} with $x < 6$ in restructuring the C_{60} from fcc to bcc.) We find that bcc is even more stable for M = Rb, Cs, thus these systems might lead more directly to the more stable bcc packing. A second approach to forming bcc M_3C_{60} would be to anneal at higher pressure (where bcc should be increasingly stable). Our results that bcc is favored for M_xC_{60} with $x \geq 3$, is supported by the recent crystallography result (published after submission of this paper) that M_4C_{60} is distorted bcc[12].

Summarizing for M_3C_{60}: With fcc the tet site ($r_M/r_A = 0.225$) is too small for K, Rb, Cs (0.278, 0.307, 0.337, respectively) causing each C_{60} to reorient so that with the hex ring points at the tet site center, leading to ordered C_{60}'s. For Li, Na (0.153, 0.206) the site is large enough to allow the C_{60} to orient as in fcc M_0C_{60}. With bcc the best $C_{60}...C_{60}$ contacts (hex rings facing each other) allow the C_{60}'s hex rings to simultaneously face all tet sites. Thus bcc M_3C_{60} is well ordered for all Li, Na, K, Rb, Cs. This leads to a strong energetic driving force for orienting the

C_{60}, and a large barrier for rotating the C_{60}.

Next consider M_6C_{60}. For bcc M_6C_{60} there is one M for each tet site (r_M/r_A = 0.291), and we find that K, Rb, Cs (with r_M/r_A = 0.278 to 0.337) strongly prefer bcc to fcc. However, Li, Na are small enough to be accommodated at faces of the oct site (*vide infra*), leading to strongly favored fcc.

For bcc there are a total of 12 tet sites per cell, and placing one M at each site leads to M_6C_{60}. With a transfer of 1/4 e for each K, we must have 24 M neighbors to each C_{60}. This is too many M for the 20 hex faces, and hence the C_{60}'s orient so that each M uses two hex faces and two pent faces for its four neighbors. The result is that each C_{60} has M above all 12 pent faces and above 12 of the 20 hex faces. This leaves eight unused hex faces, just right for the C_{60}...C_{60} contacts of bcc. Each C_{60} has 12 K at 6.18 Å (hex faces, this compares to 6.29 for bcc K_3C_{60} and 6.14 for fcc K_3C_{60}), and 12 K at 6.44 Å (pent faces). Each K has four K at 4.01 Å and one at 5.04 Å. In order that each K be bonded to two hex faces and two pent faces, it is necessary for all C_{60}'s to have either the same orientation or be rotated by 90°. However, the structure calculated for bcc M_3C_{60} with C_{60}'s rotated by 90° is not good for M_6C_{60} since it forces the two pairs of M on each cubic face to have equal distances (increasing the energy by 5.5 kcal/mol for K_6C_{60}). Thus M_6C_{60} has the C_{60}'s parallel whereas M_3C_{60} has them rotated 90°. This structure for bcc M_6C_{60} agrees with the recent experimental study[8]; for both K_6C_{60} and Cs_6C_{60} the experimental lattice constants are slightly larger than the theory (11.39 versus 11.28 Å and 11.79 versus 11.68 Å, respectively), as expected from thermal expansion.

For fcc M_xC_{60} with $x > 3$, the M must be placed in positions other than tet or oct sites. Thus consider the triangular or *delta* sites corresponding to the faces of the tet sites (or equivalently the faces of the oct sites). This leads to 8 delta sites

per C_{60} with the size ratio

$$\text{delta}: \frac{r_M}{r_A} = \frac{a/\sqrt{6} - a/2\sqrt{2}}{a/2\sqrt{2}} = 0.155 \ \ (8 \text{ per } C_{60}) \ .$$

This is ideal for Li (r_M/r_A=0.153) and Li_8C_{60} is calculated to be stable in this structure (which is cubic). Although Na (r_M/r_A = 0.206) might be too large for stable Na_8C_{60}, the fcc Na_6C_{60} is quite stable leading to an energy 58.6 kcal/mol lower than bcc (assuming full ionization for Na). For Li_6C_{60} the fcc form is calculated to be stable by 133.8 kcal/mol. For fcc M_6C_{60} the two opposite triangular faces of the octahedra are missing M's, leading to rhombohedral distortion along this axis.

The force field for carbon[6] was developed to describe the elastic constants, phonons, and lattice parameters of graphite (at 0K). We used M...M and M...C Lennard-Jones potentials developed for studies of M (alkali) intercalated graphite. [e.g., for $C_{24}K$ we calculate a lattice spacing perpendicular to the sheets of 26.25 Å (expt. 26.25 Å).[13]] All calculations[14] reported here allowed all atom positions and cell parameters to be fully relaxed in obtaining the various structures (759 degrees of freedom for fcc K_3C_{60} with four molecular units per unit cell) and should be compared to experiments at 0 K.

Based on the comparison of our calculated lattice parameters with experiment, we estimate that K_3C_{60} (and also M = Rb, Cs) has 100% charge transfer. This is plausible since the intercalated graphite system $C_{24}K$ (and more dilute compounds) has the K completely ionized[15] (C_8K might be only partially ionized). However for M_6C_{60} comparison with experimental lattice parameters suggest charge transfer of 80% for K, 85% for Rb and 90% for Cs. For M = Li, Na there is probably not 100% charge transfer at x=3 and certainly much less by x=6. Electrostatic energies favor fcc over bcc so that less complete charge transfer would lead to a more stable bcc structure.

An important question in assessing the predictions in this paper is their reli-

ability. For bcc M_6C_{60} and fcc M_3C_{60} the calculations correctly predict the lattice parameters and the orientations of the C_{60}'s. For *undoped* C_{60} the three published structures (two experimental[16,17] and one theoretical[6]) agree that the basic packing is fcc with a low temperature ordered phase and a high temperature cubic phase (phase transition[16] $\sim$ 249K) having orientational disorder. However they disagree on the precise orientations in the lower temperature phase. The calculations indicate that these structures are within 2 kcal/mol and suggest that this discrepancy might be due to static orientational disordering of the C_{60}'s in the experimental samples. With optimum orientations, each C_{60} has eight good interactions and four fair interactions with its 12 neighbors, leading to an orthorhombic distortion of the unit cell[6]. Forcing the orthorhombic form into a cubic cell with the same volume costs 0.8 kcal/mol (this leads to $a = 14.00$ Å whereas the value deduced from experiment at 11 K is $a = 14.04$ Å). Our conclusion is that preparing these samples at room temperature or above leads to randomization of the orientations which lock into various locally favorable orientations as the sample is quenched. The resulting structure would not have a favored axis, leading to a powder diffraction pattern indexable in terms of cubic symmetry.

For K_xC_{60} with $x > 1$, the structure is dominated by K...C_{60} interactions and hence we expect the predicted structures to be reliable. Since the predicted energy of bcc M_3C_{60} is 1.6 to 3.1 kcal/mol *lower* than fcc (both stable), we feel that bcc is highly likely to be the most stable structure for M = Cs, likely for M = Rb ($\Delta E = 2.2$ kcal/mol) and reasonably likely for M = K ($\Delta E = 1.6$ kcal/mol). In any case these calculations suggest that bcc M_3C_{60} has a stability comparable to fcc and suggest that it could be formed from M_6C_{60} (which theory and experiment agree is bcc).

What are the implications of the new bcc structure of M_3C_{60} for superconductivity? It is metallic but the M coordination and intermolecular vibrational

modes differ from fcc (in particular only fcc has oct M). Hence if superconductivity is dominated by these modes, Tc could be quite different. For most superconductivity applications one would not want to deal with a metastable structure. If bcc has a higher T_c than fcc, it is possible that results with very high Tc (e.g., 45K in Rb-Tl codoped C_{60})[18] might result from small amounts of bcc that might form in the matrix of fcc (indeed this might play a role in the higher T_c for M_3C_{60} with M = Rb, Cs). The result that fcc M_3C_{60} with M = K, Rb, Cs is metastable, with decreasing stability for larger alkali's, may explain why it is hard to make fcc Rb_3C_{60} and even harder for Cs_3C_{60}. In any case, these results suggest that it will be most interesting to synthesize and test the superconducting properties for bcc M_3C_{60}.

ACKNOWLEDGEMENTS. The research was initiated with funding by the Air Force Office of Scientific Research (AFOSR-88-0051), and completed with funding from NSF-CHE (8544). The facilities of the MSC/BI are also supported by grants from DOE-ECUT, NSF-DMR-MRG, BP America, Allied-Signal Corp., Asahi Chemical, Asahi Glass, Xerox Corp., Chevron, and Beckman Institute. The computer facilities were also funded by DARPA/ONR/UIR.

References

1. A. F. Hebard *et al.*, Nature **350**, 600 (1991).
2. K. Holczer *et al.*, Science **252**, 1154 (1991).
3. M. J. Rosseinsky *et al.*, Phys. Rev. Lett. **66**, 2830 (1991).
4. S. P. Kelty, C.-C. Chen, and C. M. Lieber, Nature **352**, 223 (1991).
5. K. Tanigaki *et al.*, Nature **352**, 222 (1991).
6. Y. Guo, N. Karasawa, and W. A. Goddard, Nature **351**, 464 (1991).
7. Y. Guo and W. A. Goddard, (to be submitted).
8. O. Zhou *et al.*, Nature **351**, 462 (1991).
9. P. W. Stephens *et al.*, Nature **351**, 632 (1991).
10. (a) R. D. Shannon, Acta Cryst. **A32**, 751 (1976); (b) L. Pauling, "The Nature of the Chemical Bond," 3rd ed., Cornell U. Press, Ithaca, N.Y., 1960.
11. N. Caswell, S. A. Solin, T. M. Hayes, and S. J. Hunter, Physica **99B**, 463 (1980).
12. R. M. Fleming *et al.*, Nature **352**, 701 (1991).
13. D. E. Nixon and G. S. Parry, J. Phys. **D1**, 291 (1968).
14. These calculations were all carried out using POLYGRAF of Molecular Simulations Inc. in conjunction with additional vibrational analysis software written at Caltech.
15. G. R. Hennig, J. Chem. Phys. **43**, 1201 (1965).
16. P. A. Heiney *et al.*, Phys. Rev. Lett. **66**, 2911 (1991); R. Sachidanandam and A. B. Harris *ibid.* 67, 1467 (1991).
17. W. I. F. David *et al.*, Nature **353**, 147 (1991).
18. Z. Iqbal *et al.*, Science **254**, 826 (1991).

Figure Caption

1. The bcc (A-15) structure for K_3C_{60}. (a) Shows the unit cell, (b) shows the K ligands of one C_{60}.

Table I. Predicted structure and energies for bcc and fcc M_xC_{60}

structure	energy (kcal/mol)	Z[a]	density (g/cm^3)	$C_{60}...C_{60}$[b] (Å)
C_{60} fcc	0.000[d]	1	1.737	9.914[c]
C_{60} bcc	4.949	2	1.658	9.787
C_{60} fcc-ideal	4.572	4	1.662	10.060
Li_3C_{60} bcc	0.000	2	1.828	9.564
Li_3C_{60} fcc	-18.557	1	1.865	9.790[c]
Na_3C_{60} bcc	0.000	2	1.929	9.593
Na_3C_{60} fcc	-4.395	1	1.968	9.804[c]
K_3C_{60} bcc	0.000	2	1.950	9.751
K_3C_{60} fcc	1.569	4	1.954	10.024
Rb_3C_{60} bcc	0.000	2	2.189	9.875
Rb_3C_{60} fcc	2.176	4	2.193	10.152
Cs_3C_{60} bcc	0.000	2	2.357	10.081
Cs_3C_{60} fcc	3.059	4	2.356	10.372
Li_6C_{60} bcc	0.000	2	1.889	9.371
Li_6C_{60} fcc	-133.79	1	1.942	9.733[c]
Na_6C_{60} bcc	0.000	2	2.213	9.424
Na_6C_{60} fcc	-58.577	1	1.988	10.047[c]
K_6C_{60} bcc	0.000	2	2.213	9.765
K_6C_{60} fcc	10.525[e]	1	1.785	10.792[c]
Rb_6C_{60} bcc	0.000	2	2.740	9.903
Rb_6C_{60} fcc	11.974[e]	1	2.178	10.998[c]
Cs_6C_{60} bcc	0.000	2	3.164	10.116
Cs_6C_{60} fcc	9.462[e]	1	2.499	11.258[c]

[a]Number of independent molecules per unit cell allowed in the calculations (the calculations simultaneously minimized 180Z+6 degrees of freedom).

[b]$C_{60}...C_{60}$ contact distance

[c]These structures distort slightly from cubic.

[d]In reference 6, we allowed 4 independent C_{60} per fcc cell leading to an energy lower by 0.505 kcal/mol.

[e]Based on 80%, 85% and 90% ionization for K, Rb and Cs, respectively. All other calculations assume 100% ionization.

Unit cell of bcc K_3C_{60}

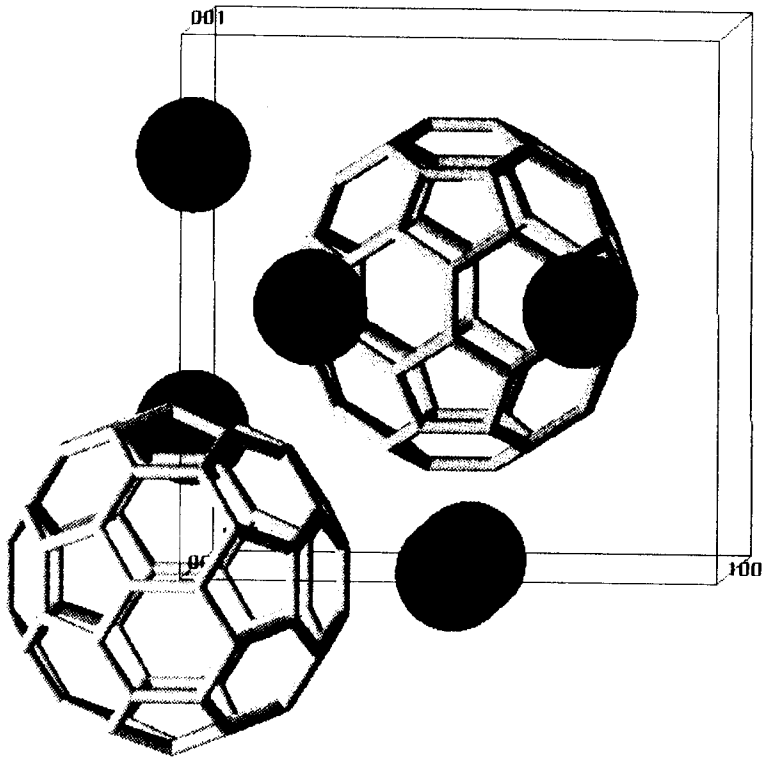

Figure 1a

bcc K_3C_{60}

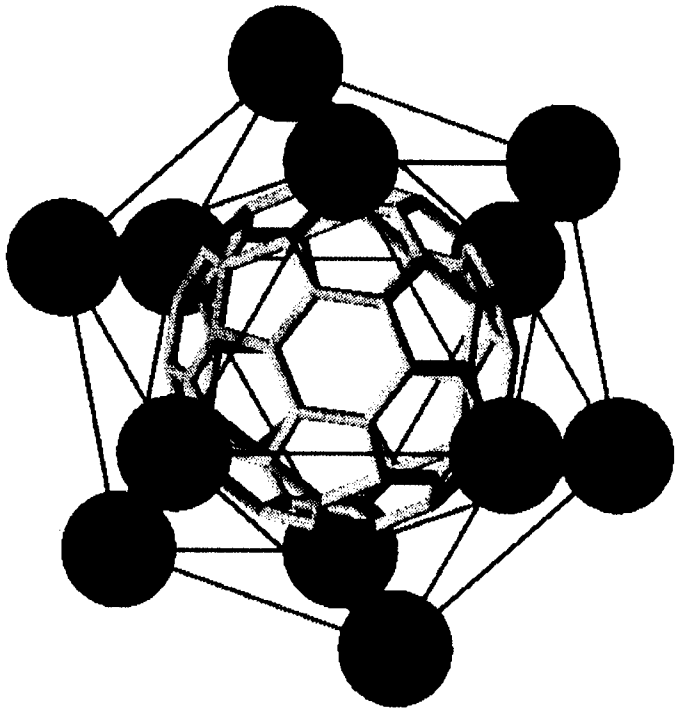

Figure 1b

Figure 1.

Appendix 1

Prediction of Fullerene Packing in C_{60} and C_{70} Crystals

Prediction of fullerene packing in C_{60} and C_{70} crystals

Yuejin Guo, Naoki Karasawa & William A. Goddard III

Materials and Molecular Simulation Center, Beckman Institute (139-74), California Institute of Technology, Pasadena, California 91125, USA

RECENT breakthroughs[1,2] in synthesizing large amounts of C_{60}, C_{70} and other fullerenes[3] have made possible studies of the structures and properties of fullerene crystals. Using a force field developed recently for sp^2 carbon atoms, we predict here the crystal structures and cohesive energies for close-packed crystals of C_{60} and C_{70}. We predict, and confirm from calculations, that for C_{60} face-centred cubic (f.c.c.) packing is more stable than hexagonal close-packing (h.c.p.), by 0.90 kcal mol^{-1}, whereas for C_{70} h.c.p. is more stable than f.c.c. by 0.35 kcal mol^{-1}. The cubic structure of C_{60} undergoes an orthorhombic distortion to space group *Cmca* at 0 K. At higher temperatures there is rapid reorientation (but not free rotation) of C_{60} molecules, suggesting that above about 200 K a phase transition occurs to an orientationally disordered, f.c.c. structure (with a room-temperature lattice parameter of 14.13 Å). This may correspond to the first-order transition observed[4] at 249 K. The threefold axes of the C_{60} molecules in the low-temperature structure are not aligned with the threefold crystallographic axes.

To understand the packing of fullerenes it is useful to consider the energetics of fullerene dimers in various orientations. For the C_{60} dimer the most energetically favourable interaction

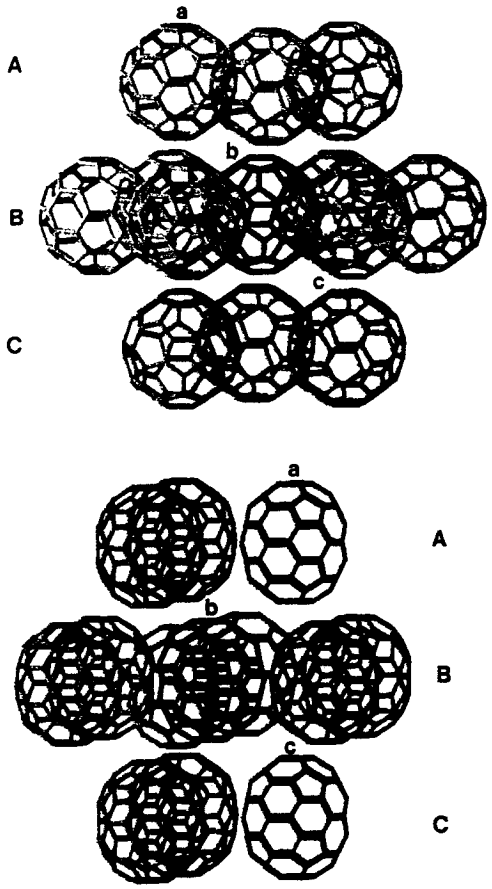

FIG. 1 Top, calculated crystal structure of C_{60} fullerene. Shown (in blue) is one of the four molecules of the f.c.c. unit cell, surrounded by its optimum 12 neighbours. Bottom, calculated crystal structure of C_{70} fullerene. Shown (in blue) is one of the four molecules of the h.c.p. unit cell, surrounded by its optimum 12 neighbours.

occurs for two hexagonal faces in contact (the same orientation, but with the centres shifted by 0.92 Å towards one edge). The equilibrium bond distance is $R_e = 9.84$ Å (centre to centre) and the bond energy is $D_e = 7.30$ kcal mol^{-1}. This leads to a separation of the faces of 3.27 Å and a closest atom-atom distance of 3.36 Å. The least favourable orientation leads to an energy of 6.10 kcal mol^{-1}, about 1 kcal mol^{-1} smaller than the best.

For the C_{70} dimer, the optimal interaction is with the long axes parallel. The waist of the monomer involves both concave and convex graphite-like regions, and the best interaction of the dimer ($D_e = 8.97$ kcal mol^{-1}, $R_e = 9.94$ Å) has a convex side matched with a concave side. Here the worst orientation leads to an energy of 6.09 kcal mol^{-1}, about 3 kcal mol^{-1} worse than the best.

Because of non-crystallographic symmetries (fivefold axes), it is not possible for these fullerenes to retain the optimal dimer orientation in the closest-packed structures. The symmetry of the fullerene does, however, affect the packing. To understand why C_{60} prefers f.c.c. whereas C_{70} prefers h.c.p., consider a closest-packed layer B and the optimized closest-packed layer A on top as in Fig. 1. The fullerenes orientate so as to optimize interactions, on average, both within and between layers. For C_{60} (symmetry I_h) this leads to hexagonal faces almost in contact (see molecules a and b in Fig. 1*a*). The inversion symmetry of C_{60} implies that the optimal interaction of the molecule b in layer B with molecules of layer C is to have each c molecule on the opposite side of the optimal b–a interaction. Thus we expect C_{60} to prefer ABCABC (f.c.c.) packing, as in Fig. 1*a*.

For C_{70} (symmetry D_{5h}), optimal packing in a closest-packed plane is achieved with the long (fivefold) axis perpendicular to the plane (see Fig. 1*b*), with the horizontal reflection σ_h in the plane. In this case the optimal interaction of molecules b and c is on the same side as the optimal b–a interaction. Thus the best packing is for layers C and A to be the same, leading to ABABAB (h.c.p.) packing for C_{70}, as in Fig. 1*b*.

There are no definitive crystal structures published for C_{60} or C_{70}. Krätschmer *et al.*[1] concluded that the structure for C_{60} is h.c.p., but their data did not really distinguish between h.c.p. and f.c.c.. Stoddart[5] quoted unpublished work by F. Diederich, indicating that f.c.c. is more stable for C_{60}. Indeed, Diederich (personal communication) observes only cubic crystal habits for C_{60} and only hexagonal habits for C_{70}, as would be expected from our predictions (diffraction data from the crystals are not of sufficient quality for structural analysis). There are other, as yet unpublished, experimental studies supporting the f.c.c. structure for C_{60} (for example, refs 4, 6). The predicted differences

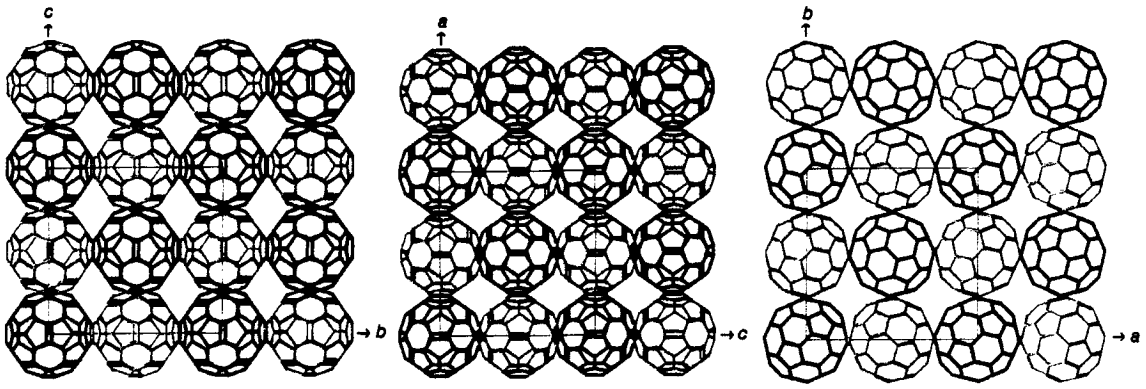

FIG. 2 Optimal f.c.c. structure: the f.c.c. unit cell of C_{60} projected along the three axes: left, [100]; centre, [010]; right, [001]. The orthorhombic unit cell is shown with blue lines. Balls of different colour are in different planes.

TABLE 1 Properties of fullerene crystals

	Structure*	Energy (kcal mol^{-1})	Density (g cm^{-3})	Cell parameters (Å and degree) a	b	c	α	β	γ
C_{60}	f.c.c.-best	0.000†	1.745	14.22§	14.22	13.56	90.01	90.00	90.00
	f.c.c.-2nd	0.312	1.740	14.27	14.28	13.50	90.01	90.00	90.01
	f.c.c.-3rd	0.505	1.737	14.32	14.26	13.50	90.00	90.00	89.72
	f.c.c.-4th	0.660	1.736	13.89	14.26	13.92	89.70	89.99	89.83
	h.c.p.	0.903	1.732	9.84	19.77¶	16.31	90.44	90.98	119.39
	f.c.c.-ideal	5.078	1.662	10.06	10.06	10.06	60.00	60.00	60.00
	b.c.c.	5.279‖	1.662	9.78	9.78	9.77	109.47	109.47	109.47
C_{70}	h.c.p.	0.000‡	1.740	9.92	20.09¶	18.52	90.01	90.00	119.61
	f.c.c.	0.351	1.736	14.84	14.84	14.76	85.44	85.44	84.23
	b.c.c.	10.682‖	1.604	10.13	10.26	10.19	107.41	107.33	107.68

* All calculations allowed four independent molecules per cell (except b.c.c. where there was only one independent molecule per rhombrohombic cell).

† Total cohesive energy is 43.883 kcal mol^{-1} using the minimum energies for gas phase and crystal. Correcting for zero-point energy and the temperature dependence of C_V, S and H, we obtain $\Delta H_{707\,K} = 40.9$ kcal mol^{-1}.

‡ Total cohesive energy is 49.506 kcal mol^{-1} using the minimum energies for gas phase and crystal. Correcting for zero-point energy and the temperature dependence of C_V, S and H, we obtain $\Delta H_{739\,K} = 46.4$ kcal mol^{-1}.

§ Averaging the lattice parameters leads to $a = b = c = 14.00$ Å at 0 K and $a = b = c = 14.13$ Å at 300 K.

‖ b.c.c. is not locally stable, and we restricted the calculation to ideal angles.

¶ This h.c.p. unit cell has four independent molecules per cell.

in energy between h.c.p. and f.c.c. suggests that compression annealing might be used to obtain samples of fullerenes with higher crystallinity. The calculated densities for f.c.c. C_{60} of 1.745 g cm^{-3} at 0 K and 1.697 g cm^{-3} at 300 K (from molecular dynamics) are in agreement with the observed density of 1.678 g cm^{-3} at room temperature[1].

To interpret and predict various properties for fullerene molecules and crystals, (including vibrational spectroscopy[1,2,7], crystal structure analysis[1], NMR[8] and scanning tunnelling microscopy[9,10], we developed a force field[11] for sp^2 carbon centres by fitting experimental lattice parameters, elastic constants and phonon frequencies for graphite. This force field uses Lennard-Jones 12-6 van der Waals interactions ($R_v = 3.8050$, $D_v = 0.0692$), Morse bond stretches ($R_b = 1.4114$, $k_b = 720$, $D_b = 133.0$), cosine angle bends ($\theta_a = 120$, $k_{\theta\theta} = 196.13$, $k_{r\theta} = -72.41$, $k_{rr} = 68$) and a twofold torsion ($V_t = 21.28$), where all distances are in Å, all angles in degrees, all energies in kcal mol^{-1}, and all force constants in kcal mol^{-1}, Å and radian units. For more details on the forms of these potentials see ref. 12. All calculations in this paper were carried out using POLYGRAF (Molecular Simulations Inc., Sunnyvale, California) in conjunction with additional vibrational analysis software written by N.K., S. Dasgupta and W.A.G. The calculations were carried out on Silicon Graphics 4D/380 and 4D/25 graphics workstations.

Using this force field and allowing four independent molecules per unit cell (permitting these molecules to reorientate with respect to each other), we calculated the optimal crystal structures for both simple types of closest packing, h.c.p. and f.c.c. We also considered b.c.c. packing (8 neighbours instead of 12), but this led to much higher energies. In these calculations we used periodic boundary conditions with accuracy-bounded convergence acceleration[13] for the long-range van der Waals interactions. All $4 \times 60 \times 3 = 720$ internal degrees of freedom, plus the six cell degrees of freedom, were optimized simultaneously. We calculated all second derivatives of the energy with respect to these 726 degrees of freedom to determine whether the structures were locally stable (that is, all second derivatives positive).

The optimum structure for C_{60} is shown in Fig. 1*a* and Fig. 2, where the blue lines indicate the unit cell. This structure is an orthorhombic distortion (space group *Cmca*) of f.c.c.. Although we allowed four C_{60} molecules per unit cell to be independent, we find that the optimal structure has two equivalent pairs of molecules, as indicated in Figs 1*a* and 2. We found three other locally stable f.c.c. structures (all second derivatives positive) at energies (per C_{60}) 0.31, 0.51 and 0.66 kcal mol^{-1} higher. The h.c.p. structure (also locally stable) was 0.90 kcal mol^{-1} higher in energy.

From symmetry, one might expect f.c.c. C_{60} to orientate each molecule with the diagonal (threefold) axes parallel to the threefold axes of a cubic crystal (in this orientation, the twofold axes of C_{60} are along the cubic axes). Our calculations show, however, that this structure is not stable (leading to three negative eigenvalues of second-derivative matrix (hessian), corresponding to rotations of the C_{60}s). We will refer to this as the 'ideal' f.c.c. structure. As shown in Table 1, the energy of the ideal f.c.c. structure is fairly high (5.08 kcal mol^{-1}). This is close to that for b.c.c. and five times as high as for h.c.p. The reason is that this packing does not allow contact between the hexagonal faces; instead, it leads to poor nearest-neighbour interactions.

In the optimal f.c.c. structure, each C_{60} leads to eight good interactions (with hexagonal rings in contact as in the optimal dimer) and four contacts that are energetically worse by ~1 kcal mol^{-1}. The average energy and distance for the good interactions are 7.11 kcal mol^{-1} and 9.83 Å (compared with 7.20 and 9.84 for the dimer), whereas the average values for the four poor interactions are 6.12 kcal mol^{-1} and 10.06 Å. On the other hand, the ideal f.c.c. structure leads to 12 interactions that are nearly the worst possible (6.01 kcal mol^{-1} and 10.06 Å). This difference of $8 \times 1.1 \times \frac{1}{2}$ accounts for 4.4 kcal mol^{-1} of the 5.1-kcal mol^{-1} difference in energy. (Interestingly, for K_3C_{60} we find[14] a f.c.c. unit cell with exactly this ideal structure of the C_{60} units; here the electrostatic and van der Waals interactions between K and C_{60} dominate.)

The optimal f.c.c. structure leads to a distorted orthorhombic crystal structure at 0 K, and the other low-lying structures with f.c.c. packing (at 0.3–0.7 kcal mol^{-1}) also distort at low temperature. Molecular dynamics calculations carried out for short periods (20 ps) show that at low temperature (100–200 K), the C_{60} molecules librate locally around the equilibrium and do not rotate. But near room temperature (300–400 K), the C_{60} molecules tunnel from one favoured orientation to another. Such orientational fluctuations lead to an average structure that is cubic (lattice parameter $a = 14.13$ Å at 300 K) with orientational disorder (but not free rotation) among the C_{60} molecules. (Note that this cubic structure is not the ideal f.c.c. structure.) Thus we expect a phase transition to occur between the distorted orthorhombic form (at low temperature) and the cubic, orientationally disordered form (at room temperature). The first-order transition observed[4] at 249 K might correspond to this transition. The transition temperature should increase and the lattice parameter decrease as better-quality crystals are produced.

For C_{70} the interactions in the crystal are much more anisotropic than for C_{60}. The interactions within the plane have $R_e = 9.92$–10.06 Å (10.00 average) and $D_e = 8.23$–8.79 kcal mol^{-1} (8.47 average), whereas those out-of-plane have $R_e = 10.83$–10.96 Å (10.91 average) and $D_e = 6.75$–7.18 kcal mol^{-1} (6.90 average). This can be compared with the optimal dimer interactions of $R_e = 9.94$ Å and $D_e = 8.97$ kcal mol^{-1}.

After submission of this manuscript, ref. 15 reported heats of sublimation of $\Delta H_{707\,K} = 40.1 \pm 1.3$ kcal mol^{-1} for C_{60} and $\Delta H_{739\,K} = 43.0 \pm 2.2$ kcal mol^{-1} for C_{70}. Our calculations lead to a cohesive energy of 43.9 kcal mol^{-1} for C_{60} and 49.5 kcal mol^{-1} for C_{70}. Correcting for zero-point energy and temperature dependence of the specific heat capacity C_v, entropy S and H for both the crystal and free molecule, we calculate $\Delta H_{707\,K} = 40.9$ kcal mol^{-1} for C_{60} and $\Delta H_{739\,K} = 46.4$ kcal mol^{-1} for C_{70}, in excellent agreement with experiment. □

Received 5 April; accepted 17 May 1991.

1. Krätschmer, W., Lamb, L. D., Fostiropoulos, K. & Huffman, D. R. *Nature* **347**, 354–358 (1990).
2. Krätschmer, W., Fostiropoulos, K. & Huffman, D. R. *Chem. Phys. Lett.* **170**, 167–170 (1990).
3. Kroto, H. W., Heath, J. R., O'Brien, S. C., Curl, R. F. & Smalley, R. E. *Nature* **318**, 162–164 (1985).
4. Heiney, P. A. *et al. Phys. Rev. Lett.* (submitted).
5. Stoddart, J. F. *Angew. Chem. Int. Ed. Engl.* **30**, 70–71 (1991).
6. Fleming, R. M. *et al. Proc. Mater. Res. Soc.* (Boston, 1990) (in the press).
7. Bethune, D. S., Meijer, G., Tang, W. C. & Rosen, H. *J. Chem. Phys. Lett.* **174**, 219–222 (1990).
8. Taylor, R., Hare, J. P., Abdul-Sade, A. K. & Kroto, H. W. *J. chem. Soc. Chem. Commun.* **20**, 1423–1425 (1990).
9. Wilson, R. J. *et al. Nature* **348**, 621–622 (1990).
10. Wragg, J. L., Chamberlain, J. E., White, H. W., Krätschmer, W. & Huffman, D. R. *Nature* **348**, 623–624 (1990).
11. Goddard, W. A. & Karasawa, N. *J. phys. Chem.* (submitted).
12. Mayo, S. L., Olafson, B. D. & Goddard, W. A. *J. phys. Chem.* **94**, 8897–8909 (1990).
13. Karasawa, N. & Goddard, W. A. *J. phys. Chem.* **93**, 7320–7327 (1989).
14. Guo, Y. & Goddard, W. A. *Science* (submitted).
15. Pan, C., Sampson, M. P., Chai, Y., Hauge, R. H. & Margrave, J. L. *J. phys. Chem.* **95**, 2944–2946 (1991).

ACKNOWLEDGEMENTS. This research was funded by the Air Force Office of Scientific Research.

Part II

The Quantum Chemistry Studies on High Temperature Superconductors

The Quantum Chemistry Studies on High Temperature Superconductors

Yuejin Guo and William A. Goddard III

Materials & Molecular Simulation Center
Beckman Institute (139-74)
California Institute of Technology, Pasadena, California 91125

Abstract

We have applied ab initio electronic methods(GVB and GVB-X-CI) to various clusters representing the La214, Y123, Nd214, and Bi and Tl containing high-Tc materials. All of them involve a two-dimensional CuO_2 sheet with linear $Cu-O-Cu$ bonds, The GVB calculations show that the spins on adjacent Cu are antiferromagnetically coupled and can be well described by a spin Hamiltonian of the form $H_{dd} = -\sum 2J_{dd}\hat{S}_i \cdot \hat{S}_j$, where $2J_{dd} = E_S - E_T$. The singlet state is stablized because O to Cu charge transfer, which leads to favorable O−Cu bonding. This is called superexchange and we find that to obtain accurate spin-coupling energies requires a CI in which the GVB and superexchange configurations are both included and then single excitations are allowed to all virtual states. This is called GVB superexchange CI, denoted as $GVB-X-CI$. Using this method, we can calculate the J_{dd} from the first principle at about the same accuracy as experiment.

Our results indicate that the superconductivity in Cu-O plane of these cuprates arise from a essentially magnetically induced interaction, that is, (i) all Cu have a Cu^{II} (d^9) oxidation state with one unpaired spin that is coupled antiferromagnetically to the spins of adjacent Cu^{II} sites; (ii) reduction below the cupric Cu^{II} state leads to Cu^{I} d^{10} sites with a highly mobile Cu(3d) electron, and these extra electrons hop from site to site (while the oxygen remains in the O^{2-} state). The hopping of these extra electrons causes the flipping of the local spin moment of the antiferromagnetic background; (iii) oxidation beyond the cupric Cu^{II} state leads *not* to Cu^{III} but rather to oxidized oxygen atoms with an highly mobile Op hole, which is ferromagnetically coupled to the adjacent Cu^{II} d electrons despite the fact that this is opposed by the direct dd exchange. This coupling induces an attractive interaction between conduction electrons that is responsible for the superconductivity.

Chapter 1

Introduction

Introduction

The discovery[1,2] of superconductivity in copper-oxide compounds with transition temperatures up to 125-K has caused a torrent of experimental and theoretical research aimed at defining the characteristics of these materials, understanding the mechanisms involved, and finding materials with transition temperatures even greater than the 125-K or so. It was quickly realized that the theory of conventional superconductivity cannot account for many properties of the new materials,however, there is as yet no generally accepted theoretical explanation of their behavior.

The unprecedented high values of Tc and other unconventional features, such as exceptional short superconducting coherence lengths, small superconducting isotope effects(the small and nearly negligible barium and oxygen isotope effects on Tc), and the proximity of antiferromagnetism to superconductivity, suggest the possibility of a non-phonon paring mechanism, particularly, it should be emphasized that currently the various experiments give a lot of evidence that magnetism plays an important role in the physics of the high Tc cuprates. For instance, as the concentration of the conducting holes(carriers) is increased from zero, magnetic order gives way to short-range magnetic correlations and thence to superconductivity. We believe an electronic mechanism[3,4], namely magnetic in nature, is responsible for the high Tc superconductivity of the copper oxide compounds.

One of the most striking aspects of all known cuprate high Tc superconductors is that they are copper oxides with layered perovskite-like crystal structure, all possessing CuO_2 planes. A key to the behavior of the new materials appears to be the presence of these planes containing copper-oxygen bonding. The special nature of the copper-oxygen chemical bonding in these materials gives rise to a metallic character, that conduct electricity well in some directions, in contrast to the majority of ceramics, which are electrically insulating. so, the chemical bonding and

electronic state of these materials will provide insight into the possible underlying mechanism of superconductivity.

Our goal is to understand the superconducting properties in terms of the electronic state and structure (and chemistry) of these materials so that one can reason about how to modify the pertinent materials to improve properties. Thus we want to understand why small changes in compositions lead to dramatic changes in T_c. Whereas, for example: for $La_{2-x}Sr_xCu_1O_4$ the T_c changes from 0 K for $x \leq 0.06$ to 37 K for x=0.15, back to 0 K for $x \geq 0.34$. Also for

$$(TlO)Ba_2Ca_{n-1}Cu_nO_{2n+2}$$

$$[(Tl,Bi)O]Sr_2Ca_{n-1}Cu_nO_{2n+2}$$

$$(TlO)_2Ba_2Ca_{n-1}Cu_nO_{2n+2}$$

$$(BiO)_2Sr_2Ca_{n-1}Cu_nO_{2n+2}$$

the T_c fluctuates from 0 K to 125 K depending on the number of adjacent CuO planes (N) and upon the distribution of cations (Ca, Ba, Sr, Bi).

In order to understand the mechanism responsible for high temperature superconductivity in the cuprates, clearly, the basic electronic structure and magnetic interaction need first to be established with more precision, particularly on the CuO_2 layers, then based on these we can study the general electronic and magnetic properties of the high-Tc superconducting materials, and also the relationship between magnetism and superconductivity.

For these purposes, we carry out quantum chemical(Generalized Valence Bond or GVB) calculations[3,4] on the model of cuprates to obtain informations about the electronic states and magnetic interactions of the oxidized systems. One of the very basic questions must be addressed, before discussing the detailed properties of high Tc superconducting cuprates, that is, there is strong electron-electron

correlation in the CuO_2 planes of the cuprates for which electron band theory turns out to be a failure. As we know, electron band theory is extremely successful in explaining many solid-state electronic properties, such as the transport properties and optical response of metals and semiconductors. It is most appropriate for materials, such as alkali and alkali earth metals in which the electrons can be treated as virtually independent particles moving in the time-average potential of the crystal lattice. Undoped parent cuprates are antiferromagnetic insulators, but the LDA band structure calculations produce a metallic ground state. The reason for this discrepancy is the strong electron correlations in CuO planes which are not adequately taken into account in a LDA band picture. However the GVB calculations can take these electron correlations into fairly good account, therefore, provide important insight into understanding the mechanism of high Tc superconductivity.

In this paper, we report the results of the first principles quantum chemical calculations on models of the $La_{2-x}Sr_xCuO_4$ (denoted La214), $Nd_{2-x}Ce_xCuO_4$ (denoted Nd214), the $Y_1Ba_2Cu_3O_7$ (denoted Y123), $TlBa_2YCu_2O_7$ (denoted Tl1212), and $Tl_2Ba_2CaCu_2O_8$ (denoted Tl2212).

Our calculation results indicate that in the parent compounds the O(2p) levels are filled and the holes are highly localized in Cu(3d) states, giving Cu^{2+} ions with a spin, and the spins of adjacent Cu^{2+} are coupled antiferromagnetically that is responsible for the observed magnetic behavior. When holes are added by doping they go into (2p) orbitals because the strong Coulomb repulsion makes Cu^{3+} extremely unfavorable energetically. Because the the O(2p) orbitals become partially filled, the added holes can form a conduction band just the same as p-type semiconductor. The electrical conduction in these systems is dominated by hopping of Op holes from site to site in the CuO_2 sheets, and the band structures can be calculated based on these valence bond localized states. In addition, there are important magnetic couplings between spins on adjacent Cu and between the

conduction electrons (oxygen p holes) and the copper spins that are critical in the superconductivity.

One of the most important question is what happens as additional x holes are added to antiferromagnetic background in the CuO_2 layers. In the "single-band" view, each added hole annihilates a localized spin and creates a mobile vacancy which may be regarded as the carrier of the supercurrent. An alternative picture mentioned above associates the localized spins mainly with the Cu sites and the added holes predominantly with O(2p) orbitals. The O hole carries a spin as well as a charge and its interaction with background spins is different from that of a mobile vacancy.

Our results imply the coexistence of bulk superconductivity and short range antiferromagnetic order(or local moments of Cu) because the Cu $d_{x^2-y^2}$ band and O p_π band belong to different bands. Our results indicate that the magnetic moments of the Cu^{2+} persist into the superconducting phase, and also suggest that the charge carriers interact strongly with the local magnetic moments , but do not destroy them. the magnetic correlation lengths will decrease with doping the holes since the moment of mobile oxygen p_π holes tends to couple ferromagnetically with the local moment of Cu^{2+}. This is consistent with that recent neutron experiments in $La_{2-x}Sr_xCuO_4$ with $0.02 \leq x \leq 0.14$ show that as x increases the Cu^{2+} moment is preserved but the basic antiferromagnetic state becomes progressively shorter ranged.

Chapter 2

Cu-Cu Coupling of Undoped Cuprates

Cu-Cu Coupling of Undoped Cuprates

All systems of the hole doped cuprates and of the electron doped systems involve doped two-dimensional Cu-O_2 sheets. In this section we will consider the properties of the undoped sheets. The major points of this chapter are as follows :

a. Oxidation states: The oxygen is O^{--} which means the electron configuration is $(1s)^2(2s)^2(2p)^6$ The copper is Cu^{++} which means that the electron configuration is

$$\underbrace{(1S)^2(2S)^2(2p)^6(3S)^2(3p)^6}_{\text{core}}\ \underbrace{(3d)^9}_{\text{valence}} .$$

There are five d orbitals: $d_{xy}, d_{xz}, d_{yz}, d_{z^2}, d_{x^2-y^2}$ and hence four must be doubly occupied and one is singly occupied. Thus, the Cu^{++} is magnetic, with spin $S = \frac{1}{2}$.

b. Cu geometry: Cu^{++} always prefers four short Cu-O bonds (call this the xy plane), and it may have 0, 1 or 2 oxygen along the z axis. Thus the ground state of Cu^{++} is $(d_{xy})^2(d_{xz})^2(d_{yz})^2(d_{z2})^2(d_{z^2-y^2})^1$ with the unpaired orbital in the sheet pointing at the sheet oxygens.

c. Magnetic structure: The undoped $d_{x^2-y^2}$ orbitals on adjacent magnetic centers have small overlap (S = 0.05). The result is a weak bonding interaction favoring singlet spin pairing and a two-dimensional antiferromagnet.

d. Magnetic Excitations: The excited magnetic states are well described in terms of the Heisenberg Hamiltonian

$$H_{dd} = -\sum 2J_{dd}\hat{S}_i \cdot \hat{S}_j ,$$

where $2J_{dd} \approx 1000$ to 1700 K and the Néel temperature is $T_N \approx 200$ to 400 K.

2.1 Electronic States of Cu^{++}

There are four major classes of the copper oxide systems, La_2CuO_4,[1] Nd_2CuO_4,[5] $YBa_2Cu_3O_7$,[2] and $(AO)_mM_2Ca_{n-1}Cu_nO_{2n+2}$[6,7] (see Figure 1a–1c and 2), and the environment at the Cu is one of the three cases in Figure 3. In all cases there are four short Cu-O bonds ($R \approx 1.94$Å) in the xy plane and between 0 to 2 long bonds ($R \geq 2.3$Å) along the z axis. With Cu^{++} the valence configuration is (3d).[9] The spectrum of excited states were calculated with self-consistent N-electron wavefunctions of each state. The resulting low lying excited states (1 to 2 eV) with the hole in the other d orbitals are given in Figure 4. It is well-known in transition-metal complexes that the d states are split in energy by the surrounding ligands. This effect comes from the bonding interaction of d orbitals with the ligand atoms. The orbitals with the highest energy are antibonding combinations of metal d with σ ligand orbitals. In a regular octahedral environment with d^9 configuration, the e_g hole is doubly degenerate; it can occupy either the d_{z^2} or $d_{x^2-y^2}$ orbitals. However, by the Jahn-Teller theorem, the complex must undergo a tetragonal distortion, for example, the distortion is generally seen as a tetragonal elongation of the octahedron, the e_g levels are split and the hole can then occupy $d_{x^2-y^2}$ orbital to lower the energy. Here the ground state has a $(d_{xy})^2(d_{xz})^2(d_{yz})^2(d_{z^2})^2(d_{x^2-y^2})^1$ configuration, which is denoted as $(d_{x^2-y^2})$. This is expected because the ligands in the xy plane are closer than in the z direction, leading to destabilization of the $d_{x^2-y^2}$ orbital. [Thus, for six-coordinate Cu, the first excited state is (d_{z^2}).] In all cases, the highest energy d orbital for the electron is the $x^2 - y^2$ orbital pointing at the 4 oxygens in the x-y plane (Figure 5), in other words, it is the lowest energy orbital for the hole, as in Figure 4.

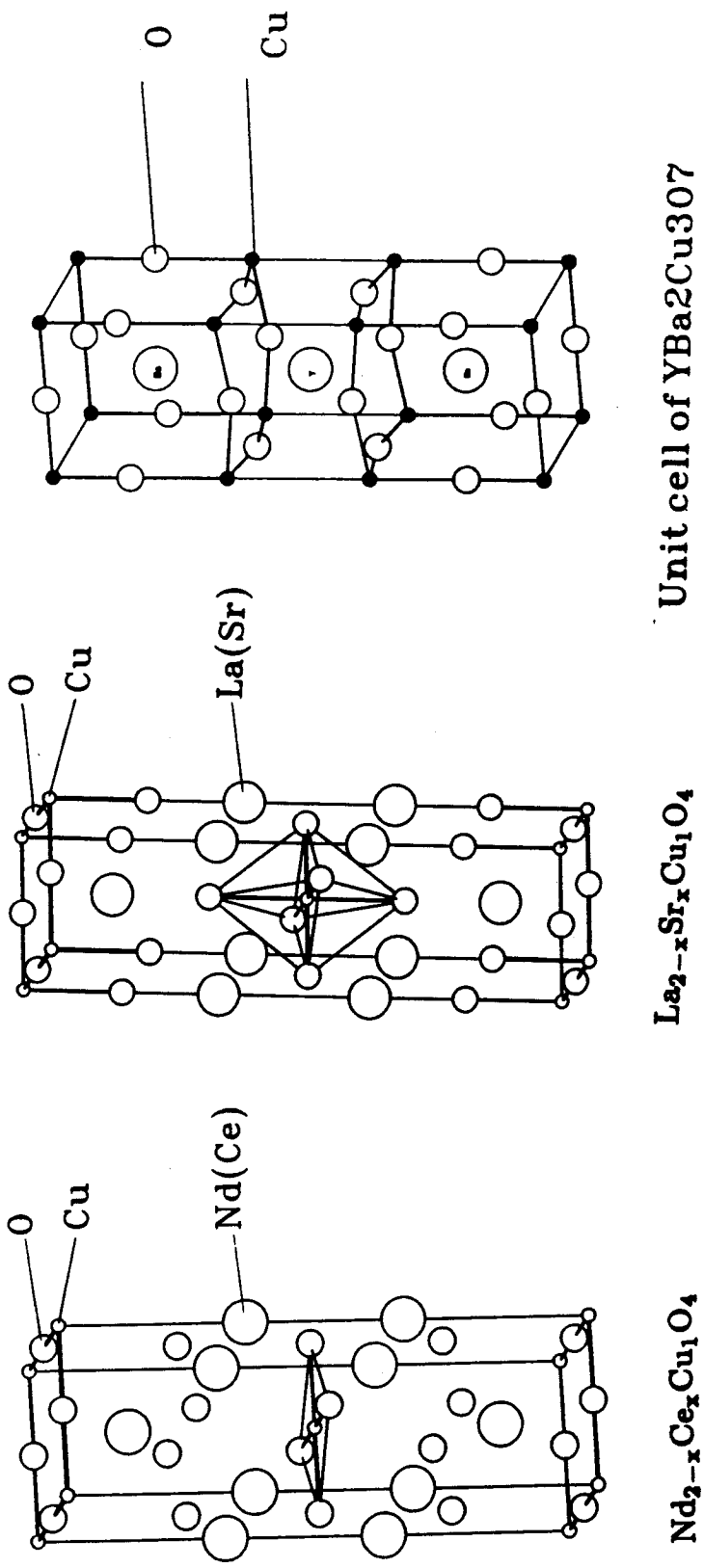
O
Cu
Unit cell of YBa2Cu3O7
O
Cu
La(Sr)
$La_{2-x}Sr_xCu_1O_4$
O
Cu
Nd(Ce)
$Nd_{2-x}Ce_xCu_1O_4$

Figure 1.

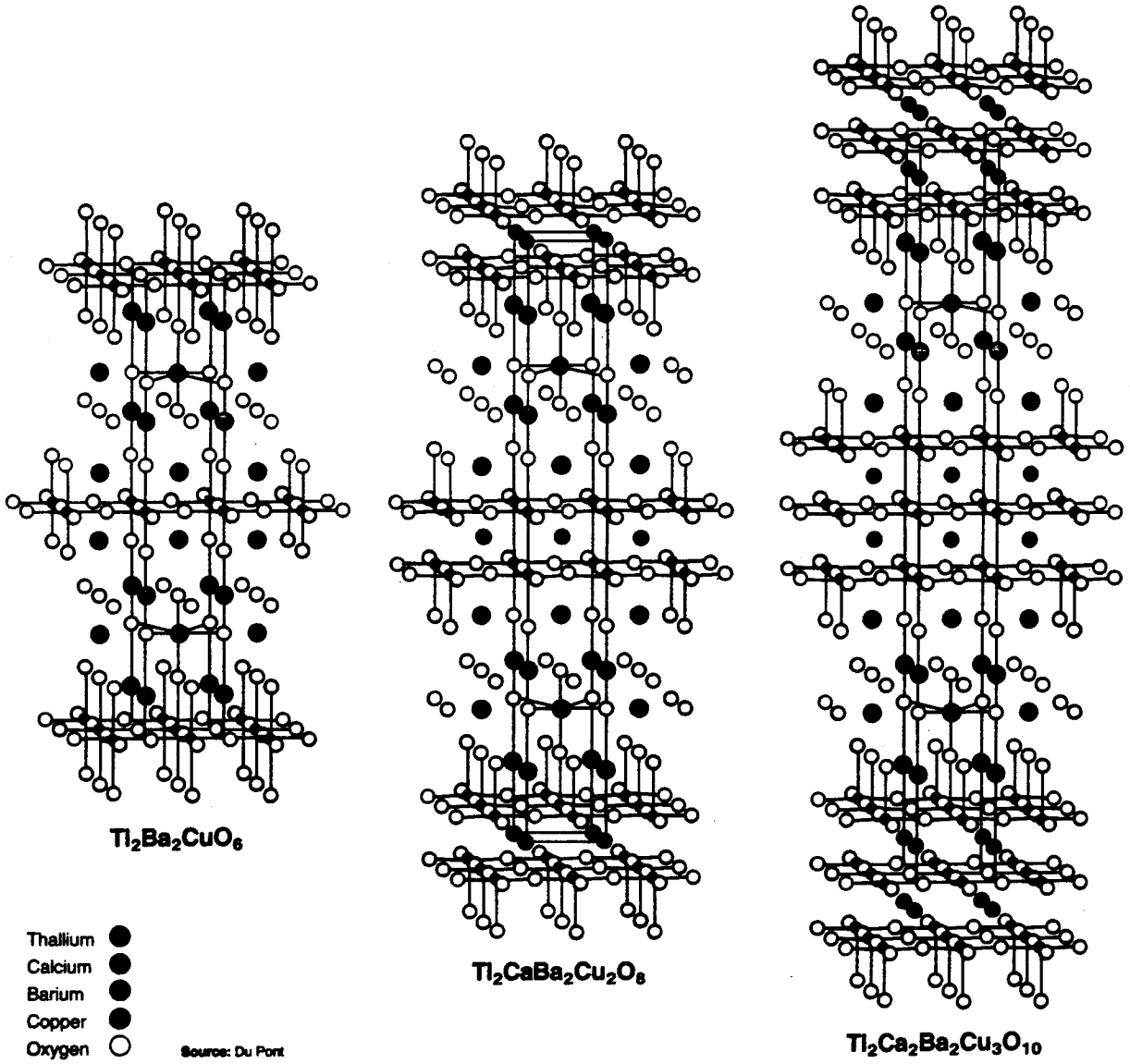
$Tl_2Ba_2CuO_6$
$Tl_2CaBa_2Cu_2O_8$
$Tl_2Ca_2Ba_2Cu_3O_{10}$
Thallium
Calcium
Barium
Copper
Oxygen
Source: Du Pont

Figure 2.

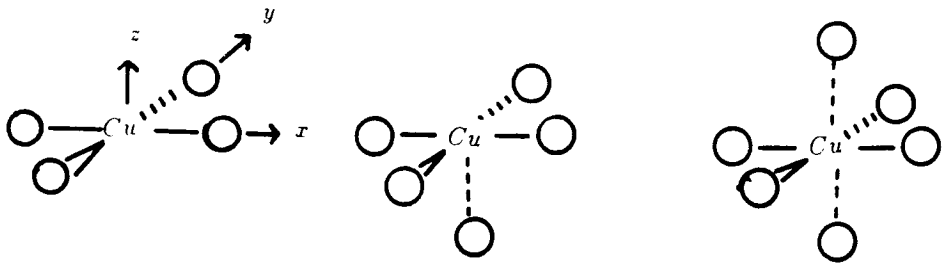

Square Planar	Square Pyramid	Elongated Octahedral
(4-coordinate)	(5-coordinate)	(6-coordinate)
a.	*b.*	*c.*

Figure 3. Cu oxygen sites.

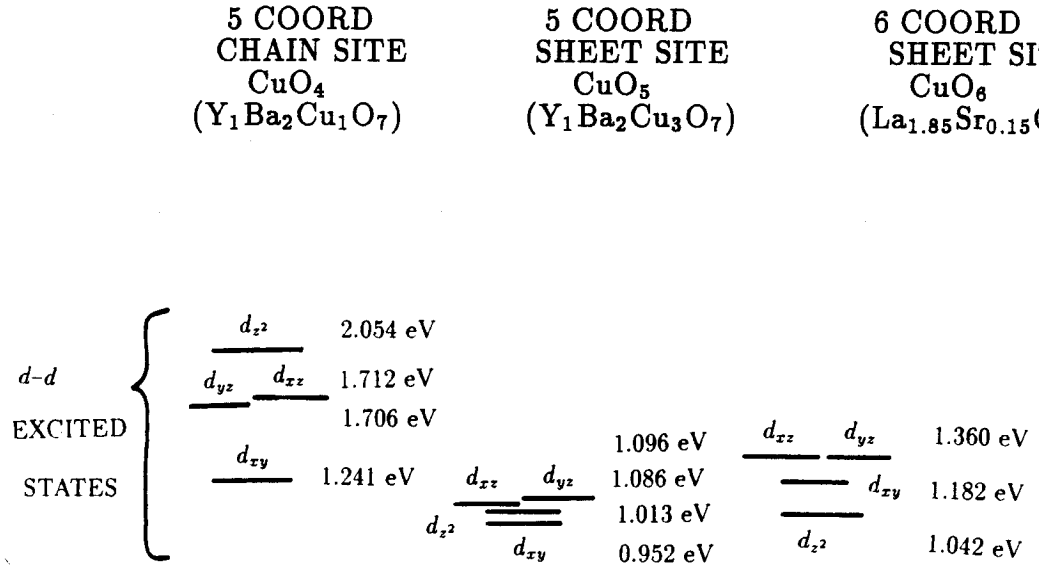

Figure 4. The excited states Cu^{++} in various oxygen environments. The location of the *hole* is indicated.

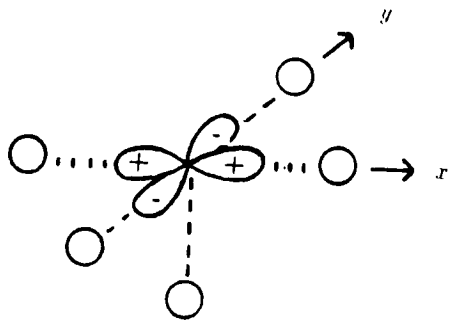

Figure 5. The unpaired Cu d orbital.

2.2 Two-dimensional Copper Oxide Sheets

In general, the magnetic moment of a transition-metal ion is a combination of spin and orbital moments, but in high Tc copper-oxide materials the orbital momentum contribution of Cu^{2+} has been quenched out by the crystal(ligand) field effects. Therefore real freedom is only spin, and the magnetic moment can be calculated by the following "spin-only" formula,

$$\mu = g\sqrt{S(S+1)} \ .$$

Given that each Cu^{++} has one electron in its $d_{x^2-y^2}$ orbital, we will now consider the magnetic states of the two-dimensional sheet, Figure 6.

The $d_{x^2-y^2}$ orbital on adjacent coppers are separated by = 3.8Å leading to very small overlap (S = 0.05). Considering just two such coppers the two electrons can be coupled into either a spin singlet or a spin triplet state, as in Figure 7.

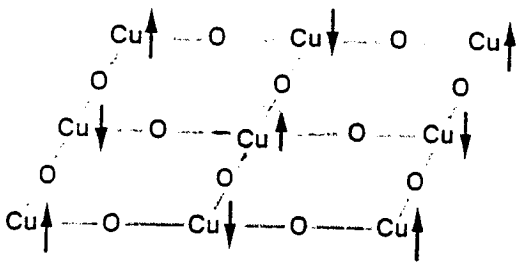

Figure 6. Magnetic structure of two dimensional copper-oxide sheet.

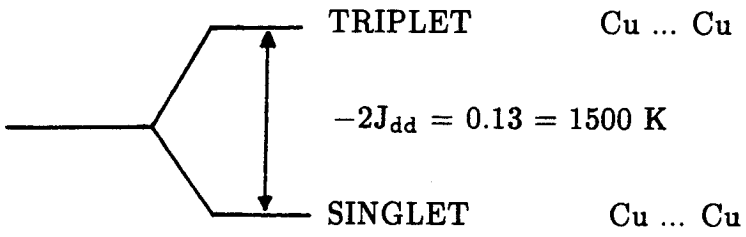

Figure 7. Spin states of a system with two Cu's.

Considering the preference for singlet pairing between all nearest neighbors leads to antiferromagnetic structure as indicated in Figure 6. Before discussing such magnetic interactions, we will consider how one can calculate these splittings using quantum chemistry methods.

2.3 Wavefunctions for Two Electrons

2.3.1 VB Versus MO

There are two distinct ways to build up a two electron wavefunction: VB and MO

a) For valence bond (VB) we start with the two atomic orbitals ϕ_l and ϕ_r as in Figure 8 and form the singlet (bonding) and triplet (antibonding) wavefunctions

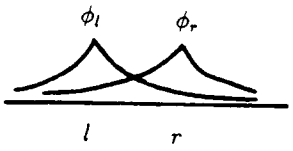

Figure 8. Hydrogen atomic orbitals for H_2.

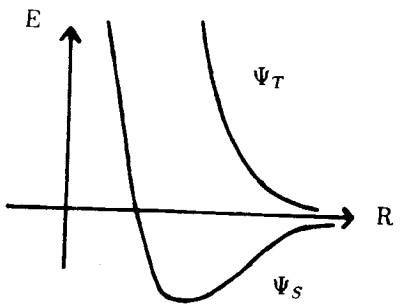

Figure 9.

$$\Psi_S^{VB} = [\phi_l^{(1)}\phi_r{}^{(2)} + \phi_r^{(1)}\phi_l^{(2)}](\alpha\beta - \beta\alpha) = (lr + rl)(\alpha\beta - \beta\alpha) \quad (1)$$

$$\Psi_T^{VB} = (lr - rl)\begin{cases}(\alpha\alpha)\\(\alpha\beta + \beta\alpha)\\(\beta\beta)\end{cases} \quad (2)$$

(ignoring normalization). This leads to energies as in Figure 9.

b) In the molecular orbital (MO) approach we instead start with the MO's of H_2^+

$$\phi_g = (\phi_l + \phi_r)/\sqrt{2(1+S)} = \text{bonding} \quad (3a)$$

$$\phi_u = (\phi_l - \phi_r)/\sqrt{2(1-S)} = \text{antibonding} \quad (3b)$$

(see Figure 10) and build up the wave functions of H_2 in terms of those orbitals

$$\Psi_S^{MO} = \phi_g(1)\phi_g(2)(\alpha\beta - \beta\alpha) = gg(\alpha\beta - \beta\alpha) \quad (4)$$

$$\Psi_T^{MO} = (\phi_g\phi_u - \phi_u\phi_g)\begin{cases}(\alpha\alpha)\\(\alpha\beta + \beta\alpha)\\(\beta\beta)\end{cases} \quad (5)$$

This leads to an energy diagram as in Figure 11 for H_2

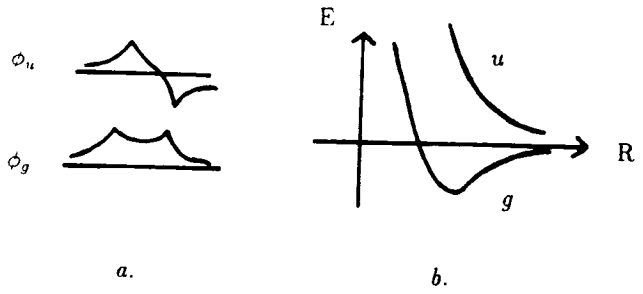

Figure 10. (a) Orbitals and (b) energies of H_2^+.

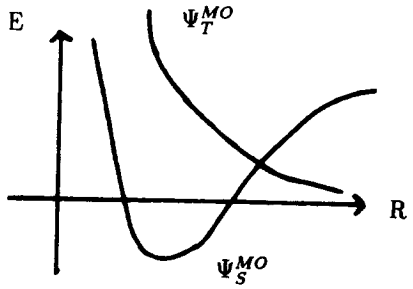

Figure 11. Energies for the MO wavefunctions of H_2.

The salient differences between VB and MO are that MO wavefunctions leads to a better description of ground state properties (bond distance, vibrational frequencies) but a completely wrong behavior as the bond is broken. This is because In MO pictures, the electrostatic repulsion between electrons is treated in an approximate way. It is assumed that electrons move independently, in a potential field that includes the average repulsion from the other electrons. On the other hand, VB leads to a proper description of dissociation but poor properties of ground state properties. Since magnetism involves small overlap (long R), the MO description is not a useful starting point. MO theory can be improved by solving for the orbitals self consistently, leading to the Hartree-Fock wave functions. However, the singlet state still has the form $\phi_g(1)\phi_g(2)$ in (4) and the problem with dissociation remains. The problem with VB at small R is that the atomic orbitals do not respond to the change in potential as the second nucleus is brought up.

With Generalized Valence Bond (GVB) theory[8-16] we allow each electron to

have a different orbital (which may overlap), and we ensure that the spin symmetry and Pauli principle are satisfied. Thus for a singlet state this leads to

$$\Psi_S^{GVB} = (\phi_a\phi_b + \phi_b\phi_a)(\alpha\beta - \beta\alpha) \ . \tag{6}$$

Near R_e the orbitals distort significantly from atomic (Figure 12a), but for long R the optimum shape is that of the atom (Figure 12b).

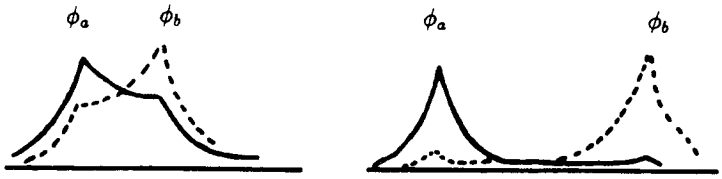

a. Small R *b.* Long R

Figure 12. GVB orbitals of H_2.

The GVB orbitals can be thought of in terms of atomic orbitals as

$$\phi_a \approx \phi_l + \lambda\phi_r \tag{7}$$

$$\phi_b \approx \phi_r + \lambda\phi_l$$

(ignoring normalization), so that

$$\Psi_S^{GVB} = (1 + \lambda^2)(\phi_l\phi_r + \phi_r\phi_l) + 2\lambda(\phi_l\phi_l + \phi_r\phi_r) \ . \tag{8}$$

Thus GVB optimizes the amount of ionic character in the wavefunction (VB requires zero ionic whereas MO requires ionic = covalent). An alternative way to look at the GVB wave function is to define GVB natural orbitals

$$\phi_g^{NO} = (\phi_a + \phi_b)/\sqrt{2(1+S)}$$

$$\phi_u^{NO} = (\phi_a - \phi_b)/\sqrt{2(1-S)} \tag{9}$$

rearranging (9) leads to

$$\phi_a = \sqrt{\frac{1+S}{2}}\phi_g^{NO} + \sqrt{\frac{1-S}{2}}\phi_u^{NO}$$

$$\phi_b = \sqrt{\frac{1+S}{2}}\phi_g^{NO} - \sqrt{\frac{1-S}{2}}\phi_u^{NO} \quad . \tag{10}$$

Substituting (10) into (6) leads to

$$\Psi_S^{GVB} = (1+S)\phi_g\phi_g - (1-S)\phi_u\phi_u \tag{11}$$

(ignoring normalization). Thus the GVB wavefunction can be thought of as having both of the electrons in the bonding orbital part of the time but both electrons in the antibonding orbital part of the time. The net effect on the bonding curve is given in Figure 13.

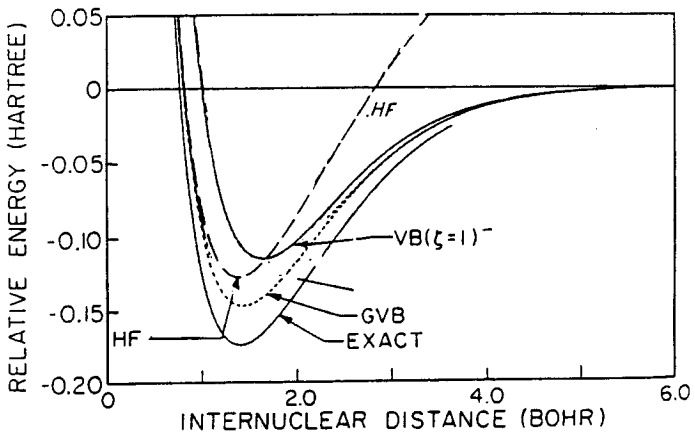

Figure 13.

2.3.2 VB Versus Hubbard

A. Overlapping Orbitals

The energy splitting between the bonding (g) and antibonding (u) states of the one electron bond of H_2^+ molecule is

$$2t_{lr} \equiv E_u - E_g = \frac{-2(h_{lr} - Sh_{ll})}{(1 - S^2)} , \tag{12}$$

where

$$\begin{aligned} h_{lr} &= < \phi_l|h|\phi_r > = < l|h|r > , \\ h_{ll} &= < l|h|l > , \text{ and} \\ S &= < l|r > \end{aligned} \tag{13}$$

(h is the one particle Hamiltonian). Note that t_{lr} is positive.

For two electrons the wavefunctions are

$$\Psi_S = (\phi_l\phi_r + \phi_r\phi_l)(\alpha\beta - \beta\alpha)$$

$$\Psi_T = (\phi_l\phi_r - \phi_r\phi_l) \begin{cases} \alpha\alpha \\ (\alpha\beta + \beta\alpha) \\ \beta\beta \end{cases}$$

and the energy splitting between the bonding (S) and antibonding (T) states is

$$2J_{lr} \equiv E_T - E_S = -2\frac{[-2St_{lr} + (\mathcal{K}_{lr} - S^2\mathcal{J}_{lr}]}{(1 - S^4)} , \tag{14}$$

where

$$\mathcal{J}_{lr} = \int\int \frac{[\phi_l(1)]^2[\phi_r(2)]^2}{r_{12}} = \text{Coulomb Integral} \tag{15}$$

$$\mathcal{K}_{lr} = \int\int \frac{[\phi_l(1)\phi_r(1)][\phi_l(2)\phi_r(2)]}{r_{12}} = \text{Exchange Integral} \tag{16}$$

are always positive. Assuming $S = 0$, (14) leads to $J_{lr} = \mathcal{K}_{lr}$ which is positive, leading to a triplet ground state (ferromagnetism). Retaining terms of order S (14) becomes

$$J_{lr} = \mathcal{K}_{lr} - 2St_{lr} \tag{17}$$

Since the singlet state is lower, the overlap term dominates the exchange term ($\mathcal{K}_{lr}$) leading to a negative J_{lr}.

B. Orthogonal Orbitals

Since MO is a bad starting point for small overlap (long R), Hubbard suggested starting with VB-like wave functions written in terms of *orthogonal* atomic orbitals $\bar{\phi}_l$, $\bar{\phi}_r$ as in (18) and Figure 14

$$\begin{aligned} \bar{\phi}_l &\approx \phi_l - \frac{1}{2}S\phi_r \\ \bar{\phi}_r &\approx \phi_r - \frac{1}{2}S\phi_l \end{aligned} \tag{18}$$

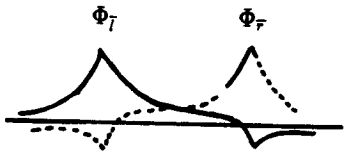

Figure 14. Orthogonalized atomic orbitals (Hubbard).

Using these orbitals one can construct covalent and ionic wavefunctions as in (19).

$$\begin{aligned} \psi_T^{HUB} &= (\bar{l}\bar{r} - \bar{r}\bar{l})/\sqrt{2} \\ \psi_S^{HUB} &= (\bar{l}\bar{r} + \bar{r}\bar{l})/\sqrt{2} \\ \psi_{ion}^{HUB} &= (\bar{l}\bar{l} + \bar{r}\bar{r})/\sqrt{2} \ . \end{aligned} \tag{19}$$

The energy difference between the covalent terms in (19) is

$$E_T^{HUB} - E_S^{HUB} = -2\mathcal{K}_{\bar{l}\bar{r}} \ . \tag{20}$$

Since $\mathcal{K}_{\bar{l}\bar{r}}$ is positive the triplet state is lower and the wavefunction ψ_S^{HUB} does not lead to bonding. The separation between ionic and covalent ($\bar{\phi}_{\bar{l}}\bar{\phi}_{\bar{l}}$ and $\bar{\phi}_{\bar{l}}\bar{\phi}_{\bar{r}}$) is U (the Hubbard parameter). Allowing ψ_S^{HUB} and ψ_{ion}^{HUB} to mix leads to the same energy as for Ψ_S^{VB}, as indicated in Figure 15.

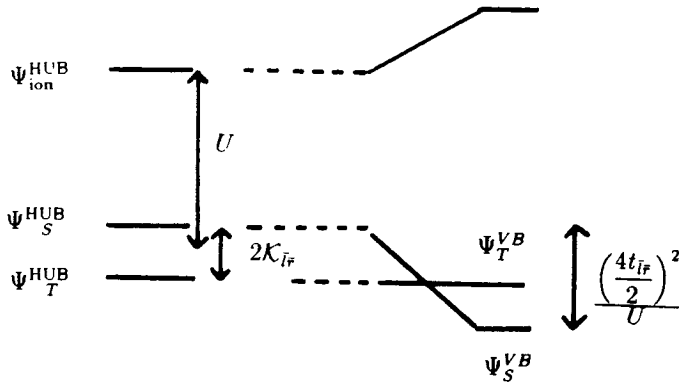

Figure 15. Interactions between Hubbard states.

The net energy splitting is

$$-2J_{lr} = E_T - E_S = -2\mathcal{K}_{\bar{l}\bar{r}} + \frac{4(t_{\bar{l}\bar{r}})^2}{U} \tag{21}$$

leading to

$$J_{lr} = \mathcal{K}_{\bar{l}\bar{r}} - \frac{2t^2_{\bar{l}\bar{r}}}{U} \ . \tag{22}$$

Comparing VB (17) and Hubbard (22), we have

$$\begin{aligned} t_{lr} &\approx t_{\bar{l}\bar{r}} \\ \mathcal{K}_{lr} &\approx \mathcal{K}_{\bar{l}\bar{r}} \\ S &\approx \frac{t_{\bar{l}\bar{r}}}{U} \ . \end{aligned} \tag{23}$$

2.3.3 The Heisenberg Spin Hamiltonian

Since

$$(\hat{S}_1 + \hat{S}_2)^2 = \hat{S}_1^2 + \hat{S}_2^2 + 2\hat{S}_1 \cdot \hat{S}_2$$

then

$$< \psi_T | 2\hat{S}_1 \cdot \hat{S}_2 | \psi_T > = 2 - \frac{3}{4} - \frac{3}{4} = \frac{1}{2}$$

$$< \psi_S | 2\hat{S}_1 \cdot \hat{S}_2 | \psi_S > = 0 - \frac{3}{4} - \frac{3}{4} = -\frac{3}{2}$$

and we can write the excitation energy of this system as

$$-2J_{lr} = E_T - E_S = < T|H_{spin}|T > - < S|H_{spin}|S >$$

where

$$H_{spin} = -2J_{lr}\hat{S}_1 \cdot \hat{S}_2 \tag{24}$$

is called the *Heisenberg Spin Hamiltonian.*

2.4 GVB Calculations

For a general N electron system, the HF wavefunction is given by

$$\mathcal{A}\left[(\phi_1\alpha)(\phi_1\beta)\cdots(\phi_{N/2}\alpha)(\phi_{N/2}\beta)\right] \tag{25}$$

where each orbital is doubly occupied. For the GVB wavefunction, the general form is

$$\mathcal{A}\left[\phi_1\phi_2...\phi_N\chi_{SM}\right] \tag{26}$$

where χ_{SM} is a general spin function for N electrons, which is required to be an eigenfunction of $\hat{S}^2$ and of $\hat{S}_z$,

$$\hat{S}^2\chi_{SM} = S(S+1)\chi_{SM}$$

$$\hat{S}_z\chi_{SM} = M\chi_{SM} \ .$$

Thus for N = 4

$$\chi_{00} = C_1\chi_1 + C_2\chi_2 \tag{27}$$

where

$$\chi_1 = (\alpha\beta - \beta\alpha)(\alpha\beta - \beta\alpha)/2$$

$$\chi_2 = [\alpha\alpha\beta\beta + \beta\beta\alpha\alpha - \frac{1}{2}(\alpha\beta + \beta\alpha)(\alpha\beta - \beta\alpha)]/\sqrt{3} \ .$$

The orbitals $(\phi_1\phi_2..)$ and spin coupling coefficients (C_1, C_2) are then calculated self consistently.

In many cases, only the χ_1 spin coupling is important (perfect pairing), leading to the GVB-PP wavefunction[13]

$$\mathcal{A}\underbrace{[(\phi_1\phi_2+\phi_2\phi_1)(\alpha\beta-\beta\alpha)]}_{\text{GVB pair}}\underbrace{[(\phi_3\phi_4+\phi_4\phi_3)(\alpha\beta-\beta\alpha)]}_{\text{GVB pair}} \tag{28}$$

for which the orbitals are far simpler to optimize.

The GVB calculations[3,4,14] are carried out for a finite cluster involving two or three Cu plus the oxygens bonded to these Cu. In addition, we include about 1000 point charges chosen to mimic the effect of the infinite lattice.[4,14] The criteria is that the Madelung potentials for the clusters match the results from the crystal.

Some clusters are given in Figure 16. In each case we included explicitly all electrons on the atoms shown plus the point charge approximation to all other ions within ~14 Å around each explicit Cu atom. The sphere size was adjusted slightly (up to 0.2 Å) so that balanced sets of ions were included, with the outer boundary always being oxygen. The charge on the outer layer was scaled so that the whole cluster is neutral. All geometries were based on the experimental crystal structures.[17] The Dunning (9s5p/3s2p) double zeta contraction[18] of the Huzinaga Gaussian basis set is used for the O atoms. The Los Alamos core effective potential[19] is used to replace the 18 core electrons of the copper atom. This leads to a (3s,2p,2d) Gaussian basis for the 11 valence electrons of the Cu atom. Figure 17 shows some of the orbitals from such a calculation on Cu_3O_{10}. Each orbital shown has one electron and has the character of a $d_{x^2-y^2}$ orbital on one of the Cu's (these are about 5% delocalization onto the adjacent O's).

Since we treat the atoms around Cu_2O_7 within ~14 Å as simple ionic picture to simulate the Madelung potentials in the crystal, we want to know how the J_{dd} value depends on the radius of the point charge sphere or the size of the point charge cluster. To test this, we have performed the GVB calculation on a series of cluster models of Nd_2CuO_4: Cu_2O_7 + 26ions, Cu_2O_7 + 88ions, Cu_2O_7 + 362ions,

and Cu_2O_7 + 974ions. The results are listed in Table 1, and the J_{dd} vs. radiuses of point charge spheres is plotted on Figure 18. We can see that when the radius of point charge cluster is larger than 6 Å, the J_{dd} is converged. This is because after that point the Madelung potentials of the Cu and O is very close to that of crystal. So we think that near 100 point charges is a minimal requirement for mimicking the effect of the infinite lattice for high-T_c cuprates.

Generally speaking, one way to overcome the difficulties(of infinite systems) is to adopt finite models such as clusters of atoms or ion, real or hypothetical molecules, that can be treated by the same ab initio methods applied to molecules. The means to confine the explicit treatment to those atoms and interactions of significance for the effect under study but to neglect or to only approximately include influences of the environment by suitably chosen boundary conditions, Hence, this "molecular" approach is particularly suited to tackle local phenomena.[12,28] The ground state of parent compounds of high-T_c copper oxides is an antiferromagnetic insulator, so there is one hole in 3d shell for each copper cation, and they are highly localized on Cu sites, the nearest-neighbor interaction of this spins determines their magnetic properties. Because of the highly localized nature of the 3d electrons in CuO_2 layer, we expect that cluster model is good for study magnetic interaction between the localized spins in CuO_2 layer. To show this we have calculated the J_{dd} for two clusters, Cu_2O_7 + 362ions and Cu_3O_{10} + 444ions, and they are 107.3 K and 103.4 K respectively. J_{dd} only change 3.7 %! Therefore, our conclusion is that using finite clusters is farely adequate to model the highly localized electron materials, further more the effects of large correlation energies on electronic structure can be calculated with reasonable accuracy for "small clusters", particularly, in cluster model we can include the strong electron correlation interaction which is crucial for superconducting cuprates.

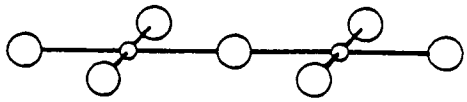

Cu_2O_7+974 ions (Nd214)

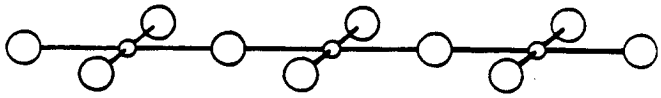

Cu_3O_{10}+444 ions (Nd214)

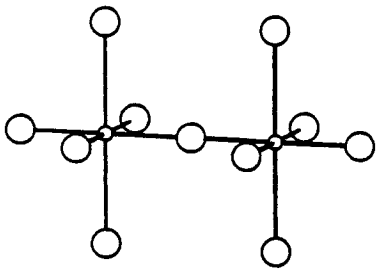

Cu_2O_{11}+986 ions (La214)

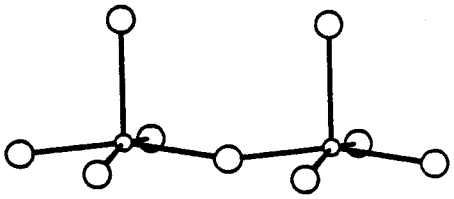

Cu_2O_9+902 ions (Y123)

Figure 16. Clusters used for GVB calculations. Not shown are the 300-1000 point charges used to mimic the electrostatic environment.

Table I. Exchange Energy J vs. size of point charge cluster in CuO_2 Sheet of Nd_2CuO_4[a]

Compound	J_{dd}(°K)	IP(eV)	EA(eV)	V_M^{Cu}(V)	V_M^O(V)	$e\Delta V_M$(eV)
CLUSTER						
Cu_2O_7+26ions	−153.7	7.536	—	−25.4874	19.4591	44.9465
Cu_2O_7+88ions	−135.0	6.016	−5.046	−25.4449	21.9735	47.4184
Cu_2O_7+362ions	−132.2	8.850	−2.447	−23.0866	23.6171	46.7037
Cu_2O_7+974ions	−135.2	8.471	−2.579	−23.6341	22.5830	46.2171
CRYSTAL						
Nd_2CuO_4	—	—	—	−24.4157	21.9404	46.3561

a) The structure data comes from H. Muller-Buromachi and W. Wollschlager's paper, i.e., a=3.946 and c=12.172 Å.

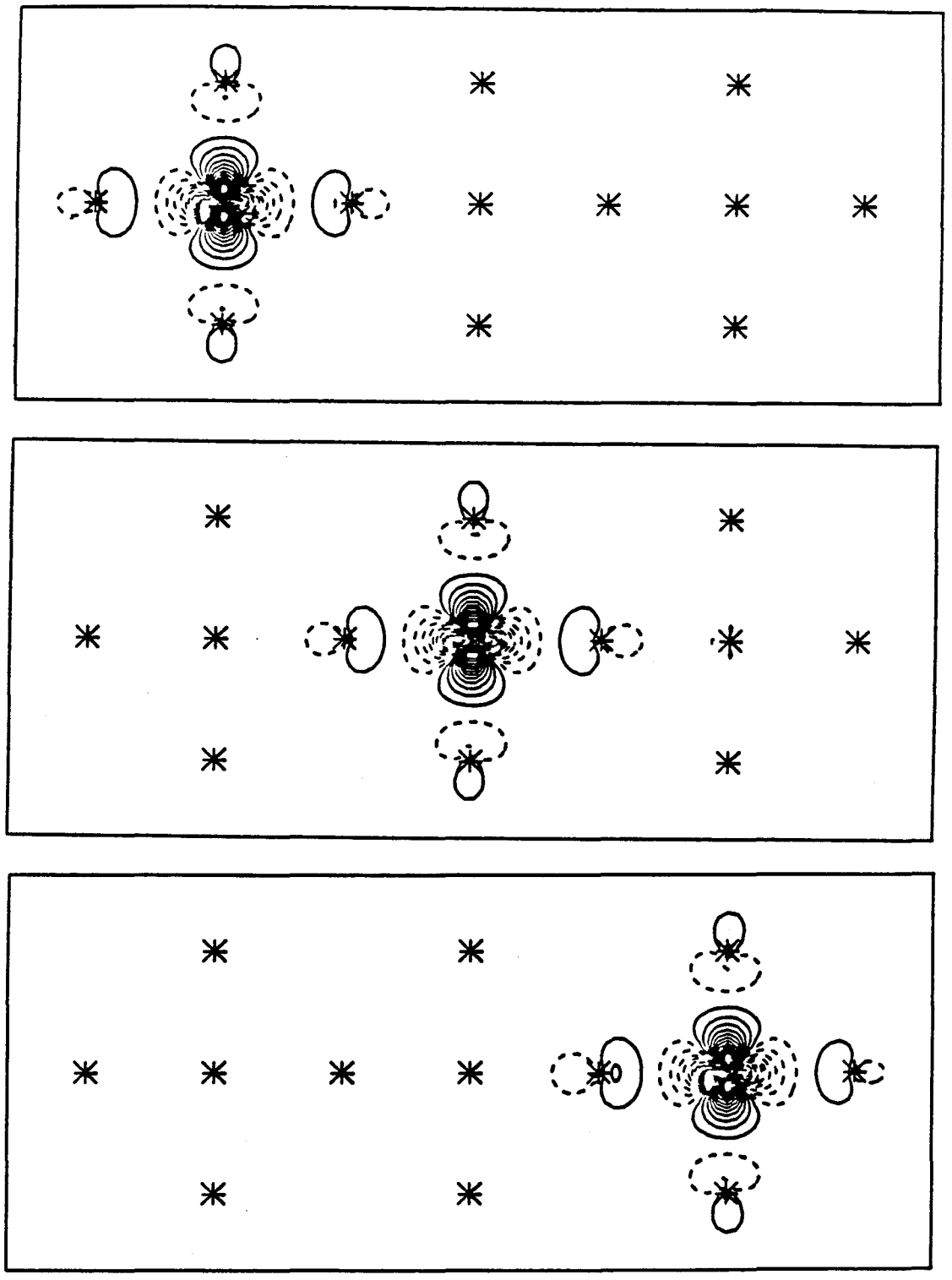

Figure 17.

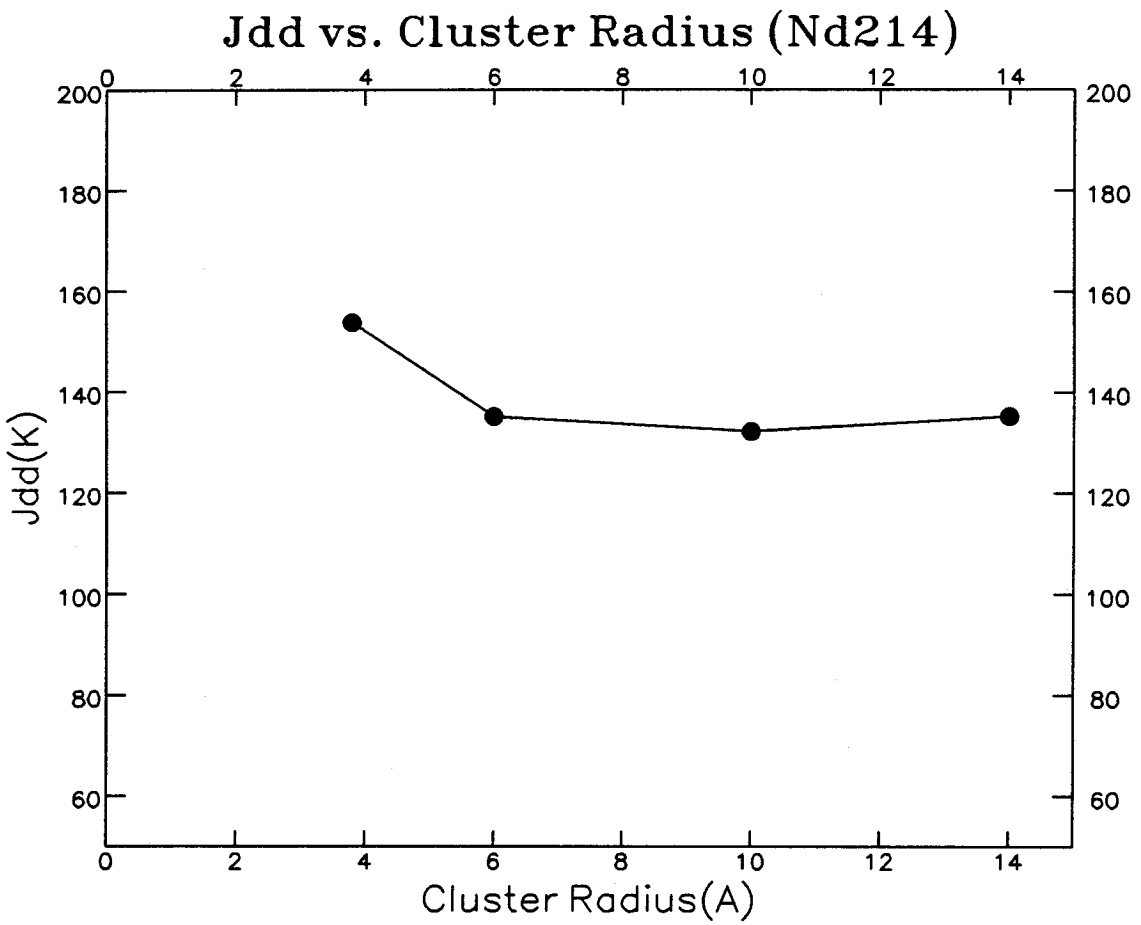

Figure 18. J_{dd} vs. size of point charge cluster.

2.5 Superexchange, Heisenberg Coupling Parameters for the Cuprates

For Cu $d_{x^2-y^2}$ orbitals separated by ~4 Å, the splitting between the singlet and triplet states is less than 1 K = 0.0001 eV. However with an oxygen in between, the splitting is calculated to be $2|J_{dd}| \approx 1500$K (for $La_{2-x}Sr_xCu_1O_4$). The reason for this difference is that the oxygen induces extra overlap or coupling between the d orbitals, as illustrated in Figure 19.

A GVB calculation[3,4] on the covalent singlet and triplet for a Cu_2O_{11} system (mimicking $La_{1.85}Sr_{0.13}CuO_4$) leads to an energy separation of 394 K with the singlet lower; thus $J_{lr}^{GVB} = -197$K. This results from the slight delocalization of the $p\sigma$ orbital of $O^=$ into both adjacent Cu $d_{x^2-y^2}$ orbitals, increasing overlap (to $S \approx 0.05$) and stabilizing the singlet. However, GVB does not account for the charge transfer (CT) processes in Figure 19. To do this we calculate self consistent wavefunctions for the CT states (lying at 8, 15, and 22 eV) and then allow these to mix.[14] This leads to $J_{lr}^{R-GVB} = -593$K (R-GVB for resonance GVB[15]). For an even more complete calculation, we started with the covalent and CT configurations and allowed all single excitations into all orbitals involving Cu-O-Cu. This is denoted as GVB-X-CI and leads to[14] $J_{lr}^{GVB-X-CI} = -778$K.

The $\mathcal{J}_{lr}$ parameter

$$E_T - E_S = -2J_{lr}$$

is reported in Table 2 for several systems. Comparing these results to Raman experiments, it appears that the GVB-X-CI values are good to about 10%.

We have studied the correlation between the J_{dd} and various factors, for example, bonding length, angle, coordination number, and Mulliken population of intervening O atom. We find that there is a very interesting relationship between the J_{dd} and the population of p_σ orbital of the O atom in singly-occupied d orbitals located on the Cu centers, as shown in Fig. 44 and Table 3, it is pretty much a linear correlation. So we do not have to do complicated GVB-X-CI calculations,

but just do the GVB calculation, then we can easily estimate the J_{dd}.

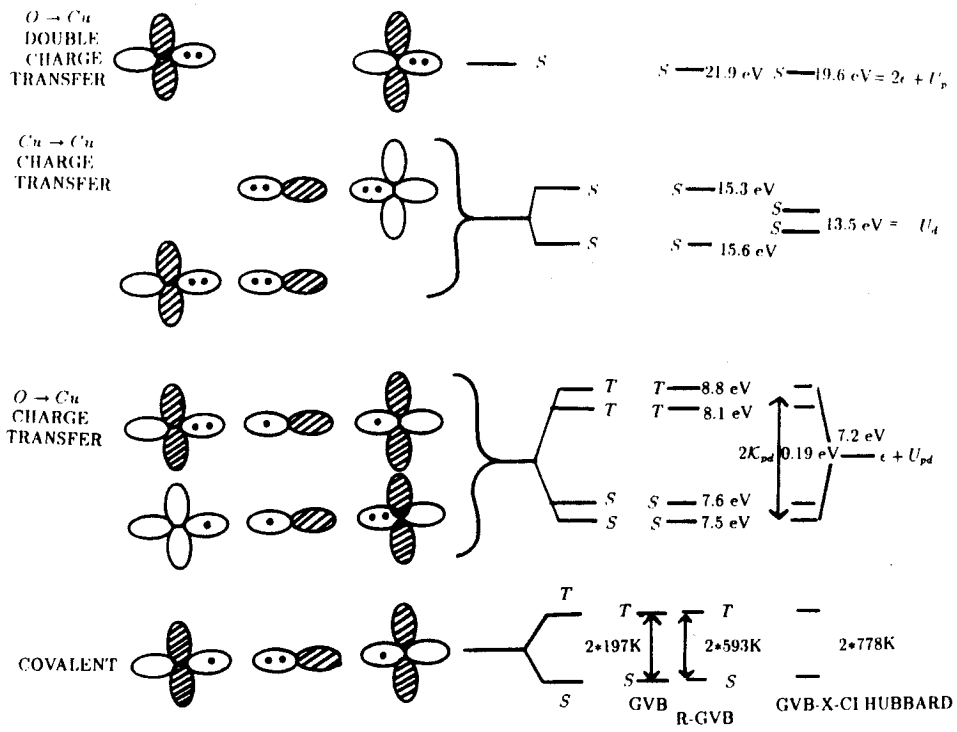

Figure 19. Covalent and ionic states for interaction of two Cu spins relation to Hubbard parameters.

Table 2. Superexchange coupling J_{dd} for one pair of Cu atoms. $E_T - E_S = -2J_{dd}$.

Character	6 Coord.	5-Coord.	4-Coord.
System	La_2CuO_4	$YBa_2Cu_3O_6$	Nd_2CuO_4
Cluster	Cu_2O_{11} + 986ions	Cu_2O_9 + 902ions	Cu_2O_7 + 974ions
GVB	-197 K	-116 K	-135 K
R-GVB	-593 K	-327 K	-399 K
GVB-X-CI	-759 K	-588 K	-722 K
Experiment (Raman)	-741 K*	-570 K	-627K

*This corresponds to -515 cm^{-1} or -0.064 eV or -1.47 kcal/mol or -6.16 kJ/mol.

Table 3. Exchange Energy J vs. 2pσ component

	Nd214 Cu_2O_6[a]	Nd214 Cu_2O_1	Nd214 Cu_2O_3	Nd214 Cu_2O_5	Nd214 Cu_2O_7	La214 Cu_2O_{11}	Y123 Cu_2O_9	Tl1212 Cu_2O_9	Tl2212 Cu_2O_9
Opσ pop.[b]	0.000	.0179	.0174	.0271	.0280	.0300	.0270	.0280	.0311
J_{dd}									
GVB	0.1	−40	−33	−137	−135	−197	−116	−126	−172
GVB-X-CI		−212	−201	−662	−722	−778	−588	−657	−870
EXPT.					−627	−754	−570		

a) No intervening O atom.
b) Where Opσ pop. is Mulliken population of 2pσ orbital of intervening O atom, i.e. 2pσ component of local unpaired d orbital.

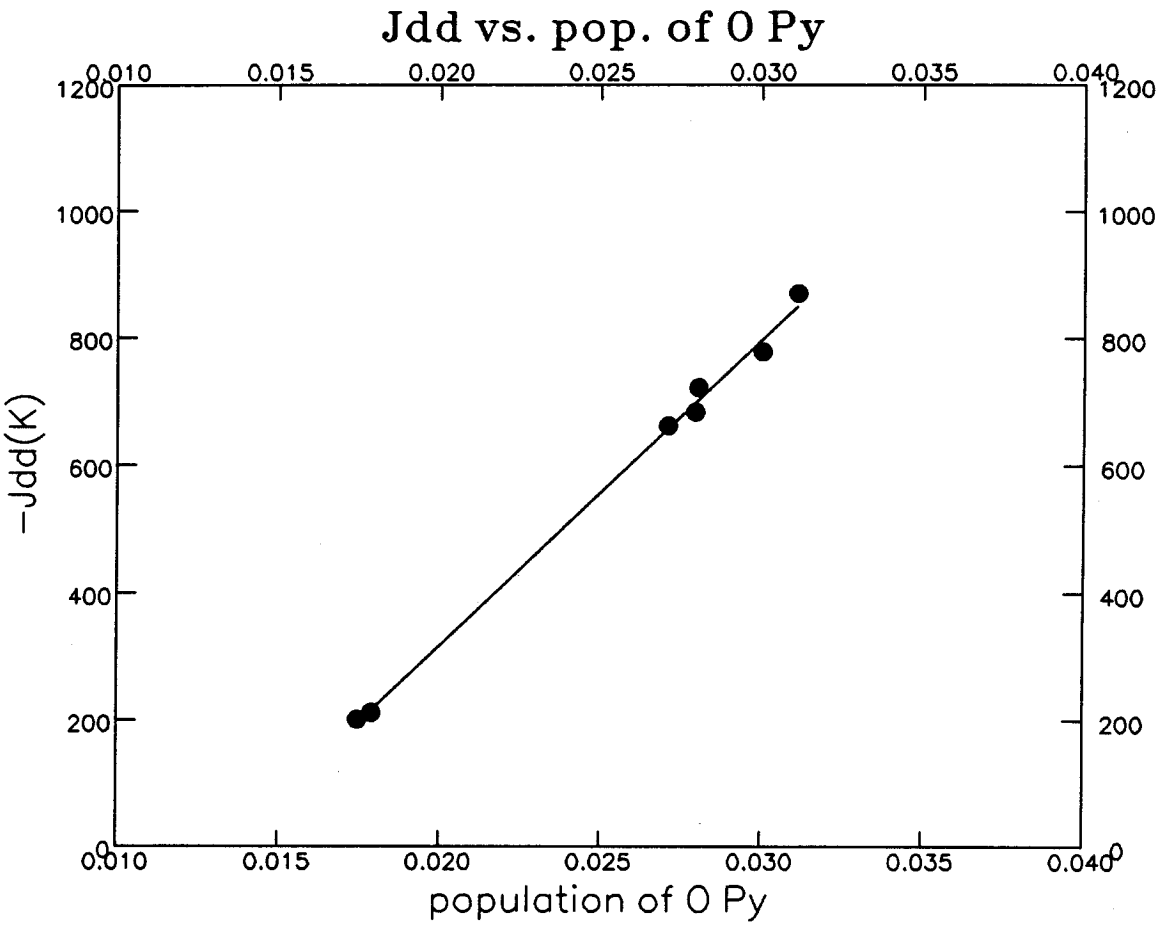

Figure 20. J_{dd} vs. Opσ component in singly d orbital.

Table 4. Calculated and experimental values of J_{dd} (in K).

System (cluster)	Theory		Exper
	GVB	GVB-X-CI	
Semiconductors			
K_2CuF_4 (Cu_2F_{11}+987ions)	3.1 K	6.1 K	8.8 K[a]
			11.3 Neutron[b]
K_2NiF_4 (Ni_2F_{11}+974ions)	−12.8	−45.5	−52 Neutron[c]
$La_2N_iO_4$ (Ni_2O_{11}+966ions)	−44	−136	-
$La_2Cu_1O_4$ (Cu_2O_{11}+986ions)	−197	−759	−741 Raman[d]
			−812 Neutron[e]
$Nd_2Cu_1O_4$ (Cu_2O_7+974ions)	−135	−722	−754 Neutron[e]
			−627 Raman[d]
$Y_1Ba_2Cu_3O_6$ (Cu_2O_9+902ions)	−116	−588	−570 Raman[d]
			−684 Raman[f]
$Y_1Ba_2Cu_3O_{6.2}$			−791 NMR[g]
Conductors			
$La_{1.85}Sr_{0.15}Cu_1O_4$ (Cu_2O_{11}+986ions)	−198	−778	-
$Y_1Ba_2Cu_3O_7$ (Cu_2O_9+986ions)	−94	−501	-
$TlBa_2YCu_2O_7$ (Cu_2O_9+984ions)	−126	−657	-
$Tl_2Ba_2CaCu_2O_8$ (Cu_2O_9+988ions)	−179	−842	-

[a] Reference 20. [b] Reference 21.
[c] Reference 22. [d] Reference 23.
[e] Reference 24. [f] Reference 25.
[g] Reference 26.

2.6 Conduction

To have conduction in the $Cu^{++}O_2$ sheet requires charge transfer configurations. However such excitations are over 3 eV. Thus undoped CuO_2 sheets lead to narrow band semiconductors. Because of the large Coulomb repulsion, U > 10 eV, for two electrons in the same $d_{x^2-y^2}$ orbital, the undoped CuO_2 sheets will be insulating. However, the band gap for conductivity will not be determined by U, that is the $(d^9 - d^9) \rightarrow (d^8 - d^{10})$ process. Rather it is determined by charge transfer between the Cu $d_{x^2-y^2}$ orbital and the Opσ orbitals, the $(d^9 - p^6) \rightarrow (d^{10} - p^5)$ process. Thus upon oxidation (removal of electrons) to form a metal, we expect p-type conduction among the Op orbitals.

Chapter 3

Doping of Cuprates

3.1 Reduced System

Consider reducing the above system by adding one electron. We find that this leads to a Cu^+ (d^{10}) state on one Cu, as shown in Figure 21. On the other hand, similar calculations on the reduced state in LaSrCuO lead to more complex results, with the wavefunction for the extra electron involving strong mixing of Cu d, s, and p basis functions and strong oxygen character. The differences between Nd and La are (1) the six oxygen anions around the Cu for the La make Cu^{2+} relatively more stable with respect to Cu^+ than the four oxygens of the Nd case, and (2) the Cu-O bond distance is 0.08 Å longer for Nd (i.e., 1.89 vs. 1.97 Å), making the $d_{x^2-y^2}$ orbital that accepts the extra electron much less antibonding.

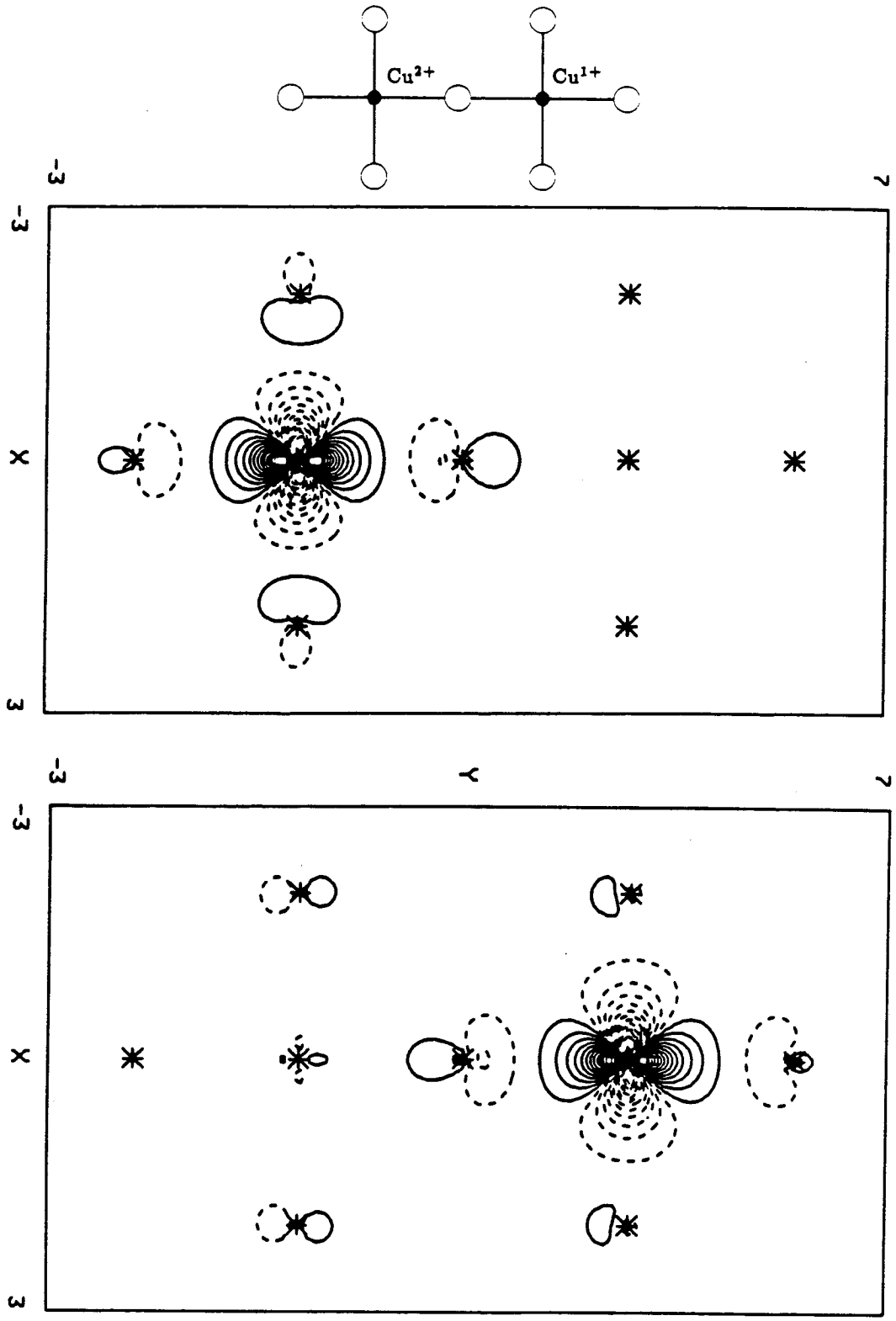

Figure 21. Orbital.

The extra electron in the $Cu^{+}(d^{10})$ site can hop to the $Cu^{2+}(d^{9})$ sites. To calculate the coupling energies, we calculated fully self-consistently the N-electron wavefunction for the Cu_2O_7 system where the left Cu was d^{10}

$$\Psi_\ell : \qquad Cu(d^{10}) - O - Cu(d^{9}) \tag{29a}$$

and also the N-electron wavefunction where the extra electron is on the right

$$\Psi_r : \qquad Cu(d^{9}) - O - Cu(d^{10}) \tag{29b}$$

The orbitals of Ψ_r each overlap in general all orbitals of Ψ_ℓ and the total overlap of the two states is finite

$$S_{\ell r} = \langle \Psi_\ell | \Psi_r \rangle = -0.076 \tag{30}$$

We calculate the matrix element for the hopping $\Psi_\ell \rightarrow \Psi_r$ as

$$h_{\ell r} = H_{\ell r} - S_{\ell r} \left(\frac{H_{\ell\ell} + H_{rr}}{2} \right) = 0.32 \text{ eV} \tag{31}$$

where $H_{ij} = \langle \Psi_i | H | \Psi_j \rangle$, and H is the full one- and two-electron Hamiltonian. [These calculations use the R-GVB program[15] which carries out multiple bioorthogonal transformations to ameliorate the N! overlap problem.]

3.2 Where is the Hole?

The high T_c superconductors all involve oxidation (removal of electrons). We had initially expected that the electron would be removed from Cu, leading from $Cu^{II}d^{9}$ to $Cu^{III}d^{8}$ centers. We carried out self consistent GVB calculations[14] for the same clusters but with one electron removed (and the point charges readjusted to reflect the new charges). The result was always that all Cu were $Cu^{II}d^{9}$ with the electron missing from an oxygen (a singly occupied orbital) as shown in Figure 22 the orbital occupations are summarized in Figure 23. By keeping the excited state orthogonal to this O hole state, we were able to estimate the

excitation energy, leading to the result that an oxygen hole ($O^{=}p^6 \rightarrow O^{-}p^5$) is more favorable than a copper hole ($Cu^{++}d^9 \rightarrow Cu^{++}d^8$) by $\sim$ 1 to 2 eV. There is now ample evidence in support of this oxygen hole character for the doped cuprates.[27] As indicated in Figure 21 the hole on the oxygen can be along the Cu-O axis ($p\sigma$) or perpendicular to the axis and in the plane ($p\pi$). [The pz orbital perpendicular to the sheet is always higher than the others and will be ignored.] Results for various clusters indicate that the $p\sigma$ and $p\pi$ states are generally within 0.5 eV, but the majority have $p\sigma$ lower. The approximation using a cluster to calculate such splitting could shift such levels by 0.1 to 0.5 eV, and hence we consider both $p\sigma$ and $p\pi$ as possible. Which one wins might be determined by the distribution of cations and defects.

Table 5. The ordering of Op holes states for various systems.

$La_2Cu_1O_4$	$Y_1Ba_2Cu_3O_7$	$(TlO)_2Ba_2Ca_0Cu_1O_4$	La_2NiO_4
$p\pi$ .33 eV	$p\pi$ 0.15 eV	$p\sigma$ 0.62 eV	$p\pi$0.54 eV
$p\sigma$ 0	$p\sigma$ 0	$p\pi$ 0	$p\sigma$ 0

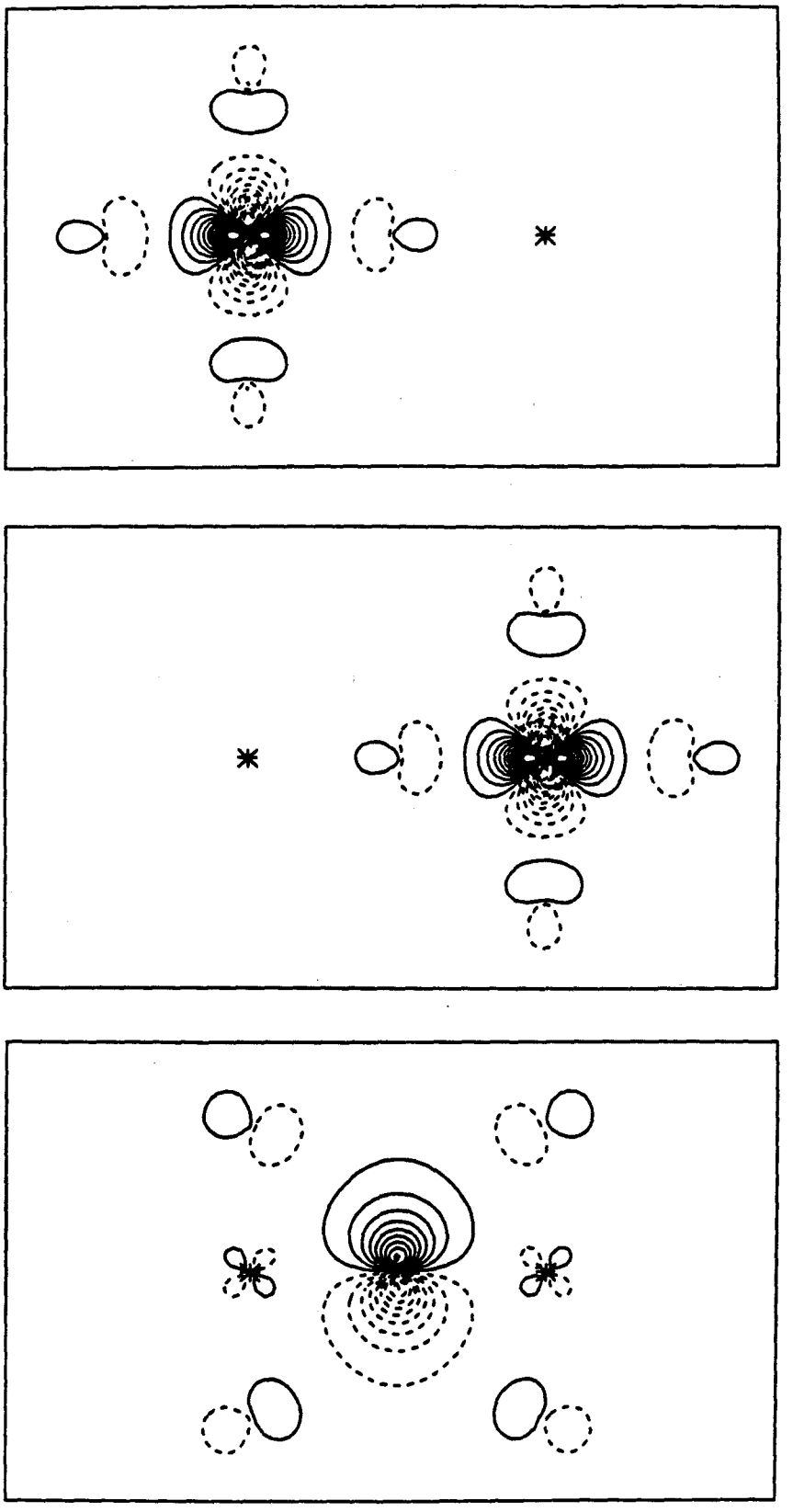

Figure 22. The GVB singly-occupied orbitals

a. Cu^{III} site

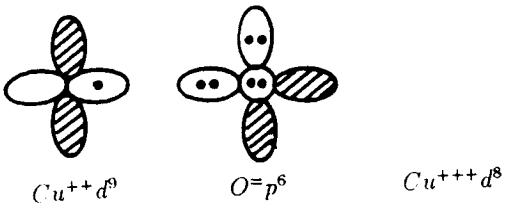

b. Opπ Hole

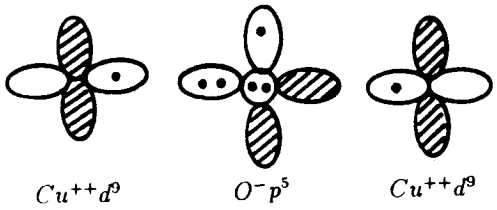

c. Opσ hole

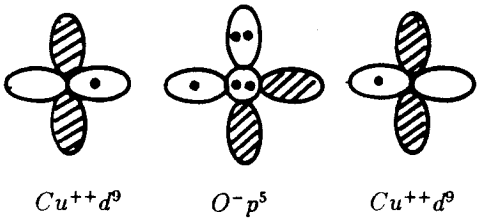

d. Unoxidized

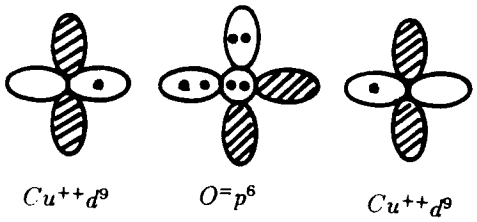

Figure 23.

3.3 Valence Bond Band Structure

Localized Versus Delocalized States

Consider the Cu_3O_{10} cluster modeling the chains of $Y_1Ba_2Cu_3O_7$. Ionizing this cluster leads to two equivalent localized wavefunctions, Ψ_ℓ and Ψ_r,

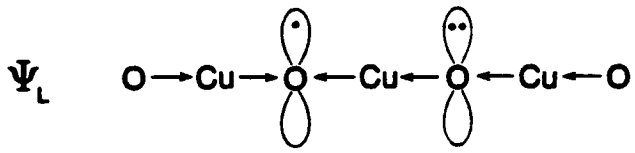

(32a)

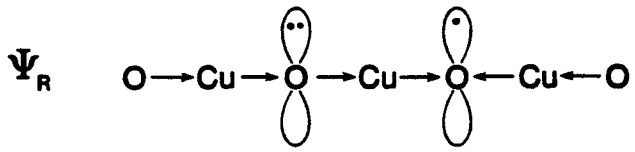

(32b)

The wavefunction localizes because the shape of a doubly-occupied orbital needs to be more expanded (electron repulsion) than that of a singly-occupied orbital and because in Ψ_ℓ the other bonds polarize to stabilize a charge on the left, whereas in Ψ_r they polarize to stabilize a charge on the right. These two wavefunctions overlap with a sizeable matrix element between them,

$$\sigma_{\ell r} = \langle \Psi_\ell | \Psi_r \rangle = -0.1412 \tag{33a}$$

$$H_{\ell r} = \langle \Psi_\ell | H | \Psi_r \rangle \ . \tag{33b}$$

In the resonating-GVB description of these states, the total wavefunction is written

$$\begin{aligned} \Psi_u &= (\Psi_\ell + \Psi_r)/\sqrt{1+S} \\ \Psi_g &= (\Psi_\ell - \Psi_r)/\sqrt{1-S} \ , \end{aligned} \tag{34}$$

We calculate these states using the R-GVB program,[15] which allows every orbital of Ψ_ℓ to overlap every orbital of Ψ_r. This many-electron *resonating generalized valence bond* (R-GVB) hole description of the ion states is equivalent to a polaron-hopping description in which the hole is completely dressed with polarization for

each site. The R-GVB states in (15) lead to a resonance stabilization of 0.33 eV for Ψ_g and destabilization of 0.43 eV for Ψ_u. This leads to a one-dimensional band with bandwidth = 1.62 eV. As a result, holes in the O2pπ bonds of the Cu-O chains or Cu-O sheets lead to high mobility charge carriers for electrical conductivity.

3.4 Cu-O-Cu Coupling

In addition to making the cuprate a conductor, the holes on the oxygens also couple with the spins on the Cu's to modify the magnon spectrum. The reason is that the Op hole has a spin which couples to the spins of the two adjacent Cu's. Here we will consider just the three spin problem

$$\dot{\mathrm{C}}\mathrm{u} - \dot{\mathrm{O}} - \dot{\mathrm{C}}\mathrm{u}$$

The results are given in Figure 24 (for $La_{1.85}Sr_{0.15}CuO_4$).

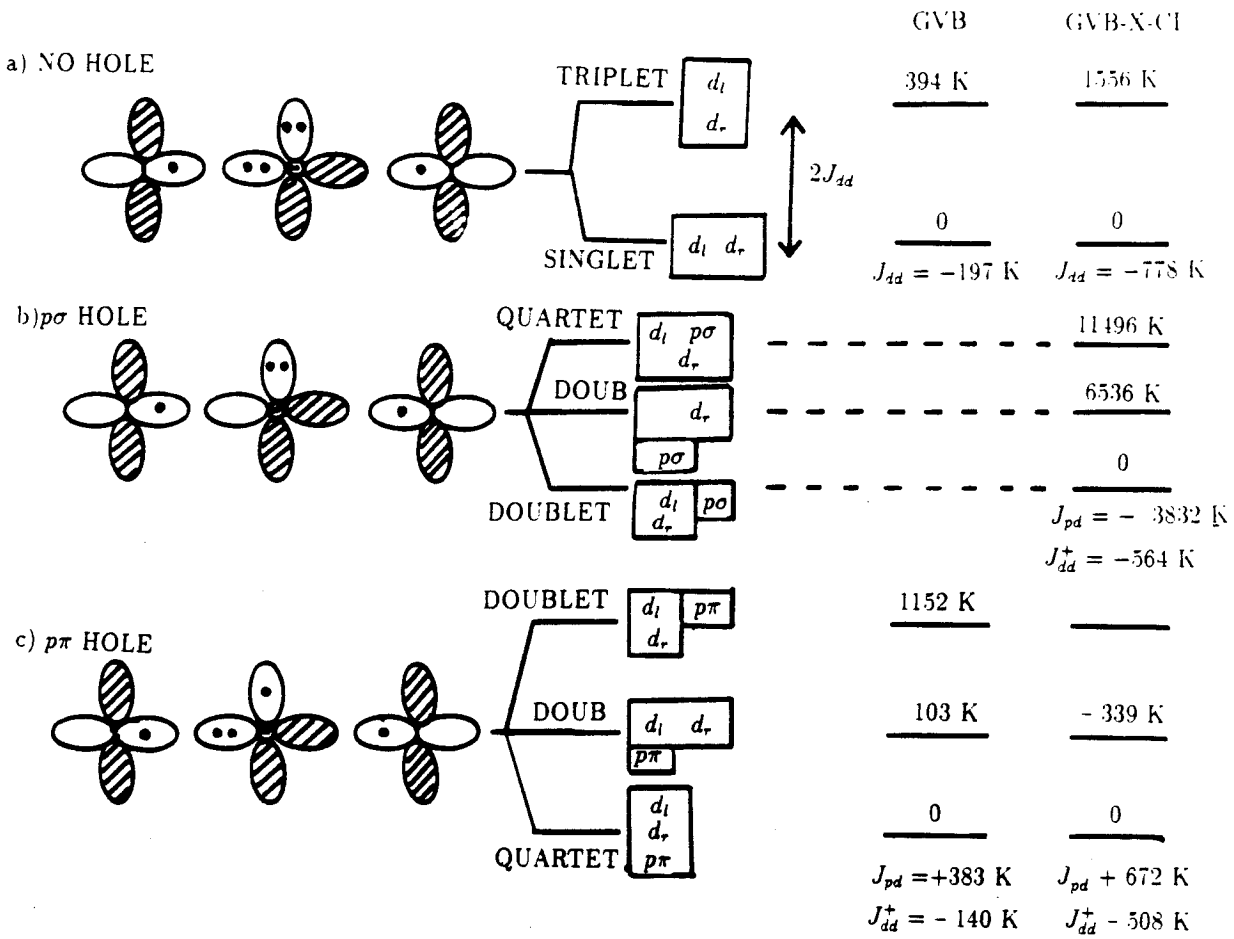

Figure 24. Spin couplings for Cu_2O_{11} clusters mimicking $La_{1.85}Sr_{0.15}CuO_4$.

Without the Op hole, the Cu spins are antiferromagnetically coupled[14]

$$\mathrm{Cu-O-Cu \quad with \quad J_{dd} = -778K}$$

But with an Opσ hole the bonding between pσ and $d_{x^2-y^2}$ leads to a strong preference for the Cu and Opσ spins to be opposite ($J_{pd} = -3832K$). The net effect is to make the Cu spins parallel[14]

$$\mathrm{Cu-Op\sigma-Cu \text{ with } J_{pd} = -3832K \text{ and } J_{dd}^{+} = -564K\ ,}$$

even though the direct coupling between the Cu spins prefers antiferromagnetic pairing ($J_{dd}^{+} = -564K$). Note that J_{dd} is decreased by 28% from the value in the undoped system. This is because the $O^{=}$ of the undoped prefers $O \rightarrow Cu$ excitations more than O^{-} of the doped.

For an Opπ hole the direct interactions of the Op and Cu spins prefer ferromagnetic coupling (since the orbitals are orthogonal). Thus the O – Cu interaction would prefer

$$\mathrm{Cu-Op\pi-Cu \text{ with } J_{pd} = 672K \text{ and } J_{dd} = -508K}$$

These values of J_{pd} and J_{dd} lead to an optimum coupling where the coppers are still slightly antiferromagnetic. However with Opπ the energy to flip the Cu spins parallel is reduced from 1556K to 339K.

Summarizing, an Op hole (pσ or pπ) has a tendency to flip the spins of the adjacent Cu spins from antiparallel to parallel.

3.5 Summary

The important points in this chapter are:

a. Oxidation removes an electron from O, leading to either pσ holes or pπ holes

b. Holes in either pσ or in pπ lead to a valence band structure with the maximum (best place for a hole) at the M point of the Brillouin zone. Thus doping leads to holes around the M point. The result is a high density of states ($N_0 = 1.1$ to $1.4\ eV^{-1}$) and a very nonspherical fermi surface (effective mass $\sim 2\ m_e$)

c. The hole in the oxygen leads to an unpaired spin which prefers for the adjacent Cu spins to be parallel rather than antiparallel.

Chapter 4

Conclusion

4. Conclusion

All high-T_c cuprate systems involve a two-dimensional CuO_2 sheet with linear $Cu-O-Cu$ bonds. The GVB calculations show that the spins on adjacent Cu are antiferromagnetically coupled and can be well described by a spin Hamiltonian of the form

$$H_{dd} = -\sum 2J_{dd}\hat{S}_i \cdot \hat{S}_j$$

where $2J_{dd} \approx 1000$ to 1700 K depending on materials. In order to calculate J_{dd} from first principles we consider a pair of Cu atoms plus the nearest-neighbor oxygen lattice in an environment mimicking the crystal , and find the lowest singlet and triplet states. By eq. (1), the separation of these states gives $2J_{dd}$.

$$E_T - E_S = -2J_{dd}\ .$$

Since the overlap between the d-orbitals is small, one cannot use HF wavefunction which leads to the singlet state ~8eV above the triplet (rather than 1450 K = 0.13 eV below the triplet). On the other hand, the GVB wavefunction treats both levels consistently. The singlet state is stablized because O to Cu charge transfer, which leads to favorable O−Cu bonding. This is called superexchange and we find that to obtain accurate spin-coupling energies requires a CI in which the GVB and superexchange configurations are both included and then single excitations are allowed to all virtual states. This is called GVB superexchange CI, denoted as $GVB-X-CI$. Using this method, we can calculate the J_{dd} from the first principle at about the same accuracy as experiment.

To elucidate the mechanism responsible for high temperature superconductivity in these copper oxide superconductors, it is essential to first understand the

electronic structure and magnetic coupling of these materials. We have applied ab initio electronic methods(generalized valence bond and configuration interaction) to various clusters representing the $La_{2-x}Sr_xCu_1O_4$ (La214), $Y_1Ba_2Cu_3O_7$ (Y123), $Nd_{2-x}Ce_xCu_1O_4$ (Nd214), and Bi and Tl containing high-Tc superconductors materials.

Our results indicate that the superconductivity in Cu-O plane of these cuprates arise from a essentially magnetically induced interaction, that is,

(1) all Cu have a Cu^{II} (d^9) oxidation state with one unpaired spin that is coupled antiferromagnetically to the spins of adjacent Cu^{II} sites;

(2) oxidation beyond the cupric (Cu^{II}) state leads *not* to Cu^{III} but rather to oxidized oxygen atoms (denoted O^+), with an highly mobile O2pπ hole bridging two Cu^{II} sites, $Cu^{II} - O^+ - Cu^{II}$;

(3) reduction below the cupric Cu^{II} state leads to Cu^{I} d^{10} sites with a highly-mobile Cu(3d) electron, and these extra electrons hop from site to site (while the oxygen remains in the O^{2-} state). The hopping of these extra electrons causes the flipping of the local spin moment of the antiferromagnetic background.

(4) in hole-doped systems, the O2pπ hole at these oxidized sites Cu^{II}-O^+-Cu^{II} is ferromagnetically coupled to the adjacent Cu^{II} d electrons despite the fact that this is opposed by the direct dd exchange. This coupling induces an attractive interaction between conduction electrons that is responsible for the superconductivity.

References

1. (a) J. G. Bednorz and K. A. Müller, *Z. Phys. B,* **64,** 189 (1986); (b) J. M. Tarascon, L. W. Greene, W. R. McKinnon, G. W. Hull, and T. H. Geballe, *Science,* **235,** 1373 (1987).
2. M. K. Wu, J. R. Ashburn, C. T. Torng, D. H. Hor, R. L. Meng, L. Gao, Z. J. Huang, Y. Q. Wang, and C. W. Chu, *Phys. Rev. Lett.,* **58,** 908 (1987).
3. (a) Y. Guo, J.-M. Langlois, and W. A. Goddard III, *Science,* **239,** 896 (1988). (b) Chen and W. A. Goddard III, *Science,* **239,** 899 (1988).
4. G. Chen, J-M. Langlois, Y. Guo, and W. A. Goddard III, *Proc. Natl. Acad. Sci. USA*, **86**, 3447 (1989).
5. Y. Tokura, H. Takagi, S. Uchida, **Nature 337**, 345 (1989); H. Takagi, S. Uchida, and Y. Tokura, **Phys. Rev. Lett. 62**, 1097 (1989).
6. H. Maeda, Y. Tanaka, M. Fukutomi, and T. Asano, *Jpn. J. Appl. Phys.,* **28,** L209 (1987).
7. Z. Z. Sheng and A. M. Hermann, **Nature 332**, 55 (1988).
8. W. A. Goddard III, *Phys. Rev.,* **157,** 73 (1967); W. A. Goddard III, *Phys. Rev.,* **157,** 81 (1967); R. C. Ladner and W. A. Goddard III, *J Chem. Phys.,* **51,** 1073 (1969).
9. W. A. Goddard III, *Phys. Rev.,* **174,** 659 (1968).
10. W. A. Goddard III, and L. B. Harding, *Ann. Rev. Phys Chem.,* **29,** 363 (1978).
11. W. A. Goddard III, T. H. Dunning, Jr., W. J. Hunt, and P. J. Hay, *Accts. Chem. Res.,* **6,** 368 (1973).
12. W. A. Goddard III and T. C. McGill, *J. Vac. Sci. Technol.,* **16,** 1308 (1979); W. A. Goddard III *Sciene,* **227,** 917 (1985).
13. P. J. Hay, W. J. Hunt, and W. A. Goddard III, *J. Am. Chem. Soc.,* **94,**

8293 (1972); L. G. Yaffe and W. A. Goddard III, *Phys. Rev. A,* **13,** 1682 (1976).

14. (a) Y. Guo, J.-M. Langlois, and W. A. Goddard III, to be published.

15. A. F. Voter and W. A. Goddard III, *J. Am. Chem. Soc.,* **108,** 2830 (1986). The matrix elements as defined in (14b) would depend on cluster size. We use instead

$$\bar{H}_{ij} = E^{N-1}S_{ij}^{N-1} - H_{ij}^{N-1}$$

where E^{N-1} is the energy of the cluster with one hole, and H_{ij}^{N-1} and S_{ij}^{N-1} are for systems with the hole localized on sites i and j, respectively. The sign chosen in $\bar{H}_{ij}$ is so that $E_k = -IP_k$, where IP_k is the ionization potential out of Bloch state k, leading to band diagrams analogous to one-electron band diagrams.

16. (a) J.-M. Langlois, T. R. Coley, and W. A. Goddard III, to be published.

17. P. Day, M. Rosseinsky, K. Prassides, W. I. F. David, O. Moze, and A. Soper, *J. Phys. C: Solid State Phys.,* **20,** L429 (1987); W. I. F. David *et al., Nature,* **327,** 310 (1987).

18. T. H. Dunning, Jr., and P. J. Hay, In "Modern Theoretical Chemistry" (Plenum Press, New York, 1977), Vol. 2.

19. P. J. Hay and W. R. Wadt, *J. Chem. Phys.,* **82,** 270 (1985).

20. L. J. De Jongh and A. R. Miedema, *Adv. Phys.,* **23** 1 (1974).

21. S. Funahashi, F. Moussa, and M. Steiner, *Solid State Comm.,* **18** 433 (1976).

22. R. J. Birgeneau, *Phys. Rev. B,* **41** 2514 (1990).

23. P. E. Sulewski, P. A. Fleury, K. B. Lyons S-W. Cheong, and Z. Fisk, *Phys. Rev. B,* **41** 225 (1990).

24. T. R. Thurston *et al., Phys. Rev. Lett.,* **65**, 263 (1990).

25. K. B. Lyons *et al., Phys. Rev. Lett.,* **60**, 2736 (1988).

26. C. H. Pennington *et al.*, *Phys. Rev. B,* **39**, 274 (1989).

27. J. Fink, N. Nücker, H.A. Romberg, and J. C. Fuggle, *IBM J. Res. Develop.,* **33**, 372 (1989).

28. J. Sauer, *Chem. Rev.,* **89**, 199 (1989).

Appendix 1

Reprint Series
19 February 1988, Volume 239, pp. 896–899

SCIENCE

Electronic Structure and Valence-Bond Band Structure of Cuprate Superconducting Materials

YUEJIN GUO, JEAN-MARC LANGLOIS, AND WILLIAM A. GODDARD III

Electronic Structure and Valence-Bond Band Structure of Cuprate Superconducting Materials

YUEJIN GUO, JEAN-MARC LANGLOIS, WILLIAM A. GODDARD III

From ab initio calculations on various clusters representing the $La_{2-x}Sr_xCu_1O_4$ and $Y_1Ba_2Cu_3O_7$ classes of high-temperature superconductors, it is shown that (i) all copper sites have a Cu^{II} (d^9) oxidation state with one unpaired spin that is coupled antiferromagnetically to the spins of adjacent Cu^{II} sites; (ii) oxidation beyond the cupric (Cu^{II}) state leads not to Cu^{III} but rather to oxidized oxygen atoms, with an oxygen $p\pi$ hole bridging two Cu^{II} sites; (iii) the oxygen $p\pi$ hole at these oxidized sites is ferromagnetically coupled to the adjacent Cu^{II} d electrons despite the fact that this is opposed by the direct dd exchange; and (iv) the hopping of these oxygen $p\pi$ holes (in CuO sheets or chains) from site to site is responsible for the conductivity in these systems (N-electron band structures are reported for the migration of these localized charges).

TO ELUCIDATE THE MECHANISM RESPONSIBLE for high-temperature superconductivity in various cuprates, we carried out first principles quantum chemical calculations on models of the $La_{2-x}Ba_xCu_1O_4$ (denoted 2-1-4) and the $Y_1Ba_2Cu_3O_7$ (denoted 1-2-3) classes of systems (*1, 2*). The resulting wavefunctions indicate that electrical conduction in these systems is dominated by hopping of oxygen $p\pi$ holes from site to site in the CuO sheets and chains, and we report the band structures based on these valence-bond localized states. In addition, there are important magnetic couplings between spins on adjacent copper atoms and between the conduction electrons (oxygen $p\pi$ holes) and the copper spins that are critical in the superconductivity.

Electronic structure of the reduced (Cu^{II}) system. The electronic wavefunctions were calculated with the generalized valence bond (GVB), Hartree-Fock (HF), or configuration interaction (CI) methods (*3*). Calculations (*4–7*) were carried out on finite clusters as indicated in Fig. 1. In each case we included explicitly all electrons on the atoms shown plus the point charge approximation to all other ions within about 8 Å. The sphere size was adjusted slightly (up to 0.2 Å) so that balanced sets of ions were included, with the outer boundary always being oxygen. The charge on the outer layer was scaled so that the whole cluster is neutral. The number of explicit electrons corresponds to having O^{2-} and Cu^{2+} or Cu^{3+} at each atom shown. The wavefunctions were calculated self-consistently for each state.

We find in all cases (four-, five-, and six-coordinate) that the optimum wavefunctions have nine electrons in d orbitals on each copper, with the singly occupied orbital pointing at the four short bonds. For example, the singly occupied d-like orbitals for the 1-2-3 chain are shown in Fig. 2, a and b (cluster Cu_3O_{10}). The total population in d orbitals on the three copper sites is $d^{9.15}$, $d^{9.17}$, and $d^{9.15}$. The electrons formally considered on O^{2-} are partially shared with the copper so that the total charge on the copper is +0.41, +0.23, and +0.41 for this cluster (rather than +2, +2, and +2). Similar results are obtained for the 1-2-3 stub (Cu_3O_{12}), where the d populations are $d^{9.05}$, $d^{9.17}$, and $d^{9.05}$ (total charges 0.44, 0.45, and 0.44). For the 2-1-4 system (Cu_2O_{11}), the d populations are $d^{9.11}$ and $d^{9.11}$ (total charges −0.23 and −0.23).

With one singly occupied orbital per copper, the Cu_2 systems lead to two low-lying spin states ($S = 0$ and $S = 1$), and the Cu_3 systems lead to three low-lying states ($S = 1/2$, $S = 1/2$, and $S = 3/2$). We solved self-consistently for each of these states using the GVB wavefunction and fitted the resulting energies to a Heisenberg spin Hamiltonian,

$$H = -\sum_{i<j} 2J_{ij}\mathbf{S}_i \cdot \mathbf{S}_j \qquad (1)$$

For the Cu_2 cases, the singlet is lower because the orbitals overlap slightly ($\sigma = 0.05$), leading to an "antiferromagnetic" exchange integral J, where $J = -205$ K for the Cu_2O_{11} sheet and $J = -244$ K for the Cu_2O_7 chain. From the Cu_3 systems we find that $|J_{dd}| < 0.1$ K for second nearest neighbors ($\sigma = 0.0006$). In one and two dimensions, a system described by Eq. 1 with negative J leads to an ordering (Néel) temperature of $T_N = 0$ K (*8*). Hence, long-range order is not expected at finite T. Experimental evidence on La_2CuO_{4-y} suggests that there are strong short-range couplings; however, evidence for long-range order is conflicting, with one report of $T_N = 220$ K (*9*). For the Cu_3 stub (Cu_3O_{12}), the $d_{z^2-y^2}$ orbitals of the center (chain) copper are orthogonal to the $d_{x^2-y^2}$ orbitals of the top and bottom (sheet) copper sites, leading to weak ferromagnetic coupling ($J_{dd} = +11$ K).

Although each system has an array of singly occupied copper d orbitals, it does not lead to electrical conduction. The reason is that the charge transfer state ($Cu^{II} \cdots Cu^{II} \rightarrow Cu^{I} \cdots Cu^{III}$) is very high in energy (about 10 eV for the Cu_2O_{11} cluster). In band language, the system has a large Hubbard U parameter (one center electron-electron repulsion), leading to an exceedingly narrow band.

The oxidized ("Cu^{III}") system. The cuprates exhibiting superconductivity all are oxidized further than Cu^{2+}. Assuming no oxygen vacancies, the copper of $La_{1.85}Sr_{0.15}Cu_1O_4$ is 15 percent oxidized, and the copper of $Y_1Ba_2Cu_3O_7$ is 33 percent oxidized. However, other systems (for example, $La_4BaCu_5O_{13}$ and $La_5SrCu_6O_{15}$) have similar levels of oxidation but do not exhibit superconductivity (down to 5 K) (*10*). For all systems discussed here we find that oxidation of the Cu^{II} (d^9) leads not to Cu^{III} (d^8)

$$O\text{–}Cu^{II}\text{–}O\text{–}Cu^{II}\text{–}O \rightarrow O\text{–}Cu^{III}\text{–}O\text{–}Cu^{II}\text{–}O \qquad (2)$$

but rather to oxidation out of an oxygen $p\pi$ singly occupied orbital (see Fig. 2c) located between two Cu^{II} sites,

$$O\text{–}Cu^{II}\text{–}O\text{–}Cu^{II}\text{–}O \rightarrow O\text{–}Cu^{II}\text{–}O^{+}\text{–}Cu^{II}\text{–}O \qquad (3)$$

Thus, in the oxidized systems, all coppers have the Cu^{II} (d^9) oxidation state, but each oxidation leads to a singly occupied oxygen $p\pi$ orbital that is spin-coupled to the various singly occupied copper d orbitals. We will show below that hopping of such oxygen $p\pi$ holes from site to site leads to electrical conduction if the hole is on the proper oxygen.

The $La_{2-x}Sr_xCu_1O_4$ system has two-dimensional sheets of copper and oxygen as in

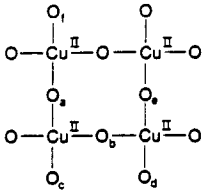

I

where each Cu-O bond is 1.89 Å. In addition, there are apex oxygens 2.40 Å above and below each copper. For $x = 0$, we find that oxidation of the in-plane (sheet) oxygen

Arthur Amos Noyes Laboratory of Chemical Physics, California Institute of Technology, Pasadena, CA 91125.

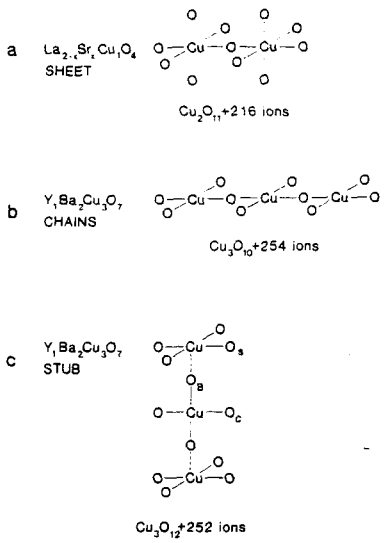

Fig. 1. Clusters used in GVB calculations. The array of point charges extends out to ~8 Å from each copper (adjusted so that the outer shells are oxygens). The charges on the point charges are the nominal values (O^{2-}, Y^{3+}, Ba^{2+}) except for Cu where $Cu^{+2.15}$ was used for $La_{1.85}Sr_{0.15}CuO_4$ and $Cu^{+2.33}$ was used for $Y_1Ba_2Cu_3O_7$. In addition, for $La_{2-x}Sr_xCuO_4$ an averaged charge $Z = 3 - \frac{1}{2}x$ was used for the LaSr system. The number of explicit electrons was based on the nominal charges [for example, $(Cu_3O_{10})^{14-}$ with three Cu^{II}]. In all calculations, all occupied orbitals are strongly bound (lowest IP = 5.4 eV).

is favored by 0.39 eV. Each of these oxygens has two $p\pi$ orbitals perpendicular to the Cu-O-Cu axis, but the $p\pi$ orbital in the plane of structure I is the preferred one for oxidation (by 0.4 eV). This leads to good electrical conduction as discussed below. On the other hand, such a subtle change as replacing part of the La^{3+} with Sr^{2+} can shift the relative ionization potentials (IP) of the apex and sheet oxygens significantly. Thus, with $x = 0.3$, we find that the apex oxygen is preferentially oxidized (by 0.45 eV). We believe that it is subtle shifts in relative IP that lead to a loss in superconductivity above $x = 0.3$ and that this is responsible for the semiconductor character of systems such as $La_4BaCu_5O_{13}$ and $La_5SrCu_6O_{15}$ (which have sheets or chains similar to the 2-1-4 and 1-2-3 systems). Thus, subtle changes in the cations (charges or placement) or in the structure (for example, owing to higher pressure) might change these semiconductors into superconductors.

For the $Y_1Ba_2Cu_3O_{7-y}$ system, there are three types of oxygens, O_C, O_S, and O_B for chain, sheet, and bridge, as indicated in Fig. 1c, but we find a very strong preference for oxidizing the chain oxygens. For $y = 0$, there must be one oxygen hole per central copper and hence an idealized structure would have every bridging O_C oxidized. However, with sufficient positive charge along the chain, it becomes favorable to oxidize sheet oxygens. Holes in O_C can hop easily to adjacent O_C, leading to high mobility if the chain is perfect. Holes in O_S would lead to conduction in the sheets much as in $La_{2-x}Sr_xCu_1O_4$. These two-dimensional sheets should be less sensitive to defects than the chains. Holes in O_B probably serve to communicate between the O_C and O_S sites. Thus, we expect an equilibrium population of holes among O_B, O_C, and O_S, with O_C and O_S important in electrical conduction.

Magnetic coupling in oxidized states. With three singly occupied orbitals, the spins in a Cu^{II}–O^{+}–Cu^{II} triad can be coupled in three ways ($S = 3/2$ and two $S = 1/2$). Since the singly occupied oxygen $p\pi$ orbital is orthogonal to the Cu^{II} orbitals, there is ferromagnetic coupling between the oxygen $p\pi$ and adjacent copper d orbitals. The spin coupling between the Cu^{II} spins still prefers singlet; however, the Cu-O exchange is much stronger, leading to a ferromagnetic (quartet) ground state. Thus the optimal magnetism of a chain is as in

$$O\text{–}Cu^{II}\uparrow\text{–}O^{+}\uparrow\text{–}Cu^{II}\uparrow\text{–}O\text{–}Cu^{II}\downarrow\text{–}O \quad \text{(II)}$$

We solved self-consistently for all possible spin states of the various clusters and fitted the results with Eq. 1 to obtain coupling terms of $J_{OCu} = 383$ K, $J_{dd} = -205$ K, and $J_{dd}^{\pm} = -139$ K for sheets of $La_{2-x}Sr_xCu_1O_4$, and $J_{OCu} = 405$ K, $J_{dd} = -244$ K, and $J_{dd}^{\pm} = -164$ K for chains of $Y_1Ba_2Cu_3O_7$. Here J_{OCu} is for adjacent oxygen $2p$ and copper $3d$ orbitals, $J_{dd}^{\pm}$ is for two copper atoms with the intervening oxygen oxidized (the center and left Cu of structure II), and J_{dd} is for a copper pair where the intervening oxygen is not oxidized (the central and right Cu of structure II). Note that the J_{dd} with an intervening O^{+} is smaller than that for a normal oxygen (164 K versus 244 K); this is because superexchange decreases when the central atom (oxygen) is less negative (*11*).

In the accompanying report (*12*) it is shown that the interplay between the O-Cu and Cu-Cu magnetic couplings is responsible for the superconductivity in these systems.

Electron correlation. It is important to emphasize that the many-body electron correlations implicit in the GVB wavefunction are essential to a proper description of these clusters (*3*). For example, an ordinary HF calculation on the Cu_2O_7 cluster yields a closed-shell singlet state 6.89 eV above the triplet, while the GVB wavefunction puts the singlet 0.04 eV below the triplet. The problem with the HF description for these systems is that separate singly occupied d orbitals as in Fig. 2, a and b, are not allowed. Thus, for Cu_2O_7, the GVB wavefunction has the form

$$\Psi_{singlet}^{GVB} = \mathcal{A}[\Phi(\phi_L\phi_R + \phi_R\phi_L)(\alpha\beta - \beta\alpha)] \quad (4)$$

where ϕ_L and ϕ_R denote $d_{x^2-z^2}$–like orbitals centered mainly on the left and right copper (as in Fig. 2 for Cu_3), Φ contains all other orbitals and spins, and $\mathcal{A}$ is the antisymmetrizer (determinant operator). All orbitals are calculated self-consistently with no restriction on shape, overlap, or character of the orbitals. Similarly, the triplet state is described as

$$\Psi_{triplet}^{GVB} = \mathcal{A}[\Phi(\phi_L\phi_R - \phi_R\phi_L)(\alpha\beta + \beta\alpha)] \quad (5)$$

where all orbitals are solved for self-consis-

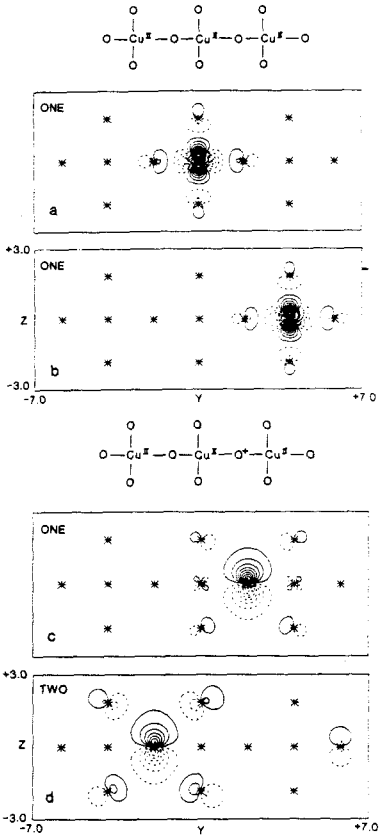

Fig. 2. The GVB orbitals (amplitudes) of Cu_3O_{10} (**a**) and (**b**) show two of the three singly occupied (d-like) orbitals located on the copper centers. Atoms in the plane are indicated with asterisks. Positive contours are solid, whereas negative contours are dotted; the increments are 0.10 atomic units. (**c**) The new singly occupied (oxygen $2p\pi$–like) orbital obtained by ionizing the Cu_3O_{10} cluster. No noticeable change occurs in the other orbitals shown in (a) and (b). (**d**) The corresponding doubly occupied orbital at an adjacent oxygen.

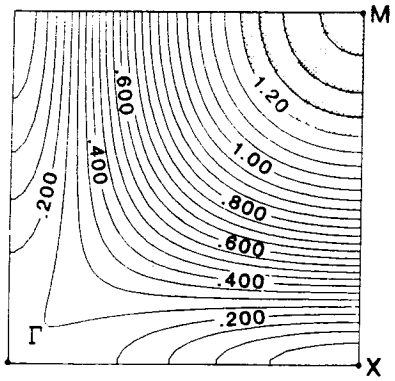

Fig. 3. The upper oxygen $2p\pi$ band for the Cu-O sheets of $La_2Cu_1O_4$ (based on GVB energy band calculations). The contour lines are labeled in electron volts. The Fermi energy for $La_{1.85}Sr_{0.15}Cu_1O_4$ is at the boundary of the dotted and undotted regions.

tently; however, the final orbitals are very similar (indistinguishable in a plot such as Fig. 2) from the optimum orbitals of the singlet. As a result, the Heisenberg-type description (Eq. 1) is suitable. In contrast, the HF functions have the form

$$\Phi^{HF}_{singlet} = \mathcal{A}[\Phi(\phi_g\phi_g)(\alpha\beta - \beta\alpha)] \quad (6)$$

$$\Phi^{HF}_{triplet} = \mathcal{A}[\Phi(\phi_g\phi_u - \phi_u\phi_g)(\alpha\beta + \beta\alpha)] \quad (7)$$

where all orbitals are calculated self-consistently. For the optimum triplet state, the final orbitals have the form

$$\phi_g = (\phi_L + \phi_R) \quad (8)$$

$$\phi_u = (\phi_L - \phi_R) \quad (9)$$

(ignoring normalization), leading to a wavefunction identical to $\Psi^{GVB}_{triplet}$. However, for the singlet state, the HF wavefunction has the form

$$\phi_g\phi_g = (\phi_L\phi_R + \phi_R\phi_L) + (\phi_L\phi_L + \phi_R\phi_R) \quad (10)$$

which includes equal amounts of covalent and ionic character. These ionic terms correspond to equal mixtures of Cu^{III}-Cu^{I} character into the Cu^{II}-Cu^{II} wavefunction, leading to an artificially high energy. This HF wavefunction also leads to strong mixtures between the copper $d\sigma$ and oxygen $p\sigma$ orbitals ($d_{y^2-z^2}$ and p_y in Fig. 2). To remove this difficulty for HF wavefunctions, one can relax the spin symmetry restriction and use a wavefunction of the form

$$\Phi^{UHF} = \mathcal{A}[\Phi(\phi_L\alpha)(\phi_R\beta)] \quad (11)$$

(the unrestricted HF or UHF wavefunction). This leads to much lower energy, but the wavefunction is a mixture of singlet and triplet character and hence one cannot directly obtain parameters for Eq. 1. (The UHF wavefunction leads to singly occupied orbitals that are essentially pure $d_{y^2-z^2}$ in character.) The GVB wavefunction corresponds to converting Eq. 11 into a singlet state (leading to Eq. 4) and then reoptimizing the orbitals self-consistently. In terms of band concepts, the HF description has a half-filled band (ϕ_g occupied and ϕ_u empty), whereas the GVB description has every band orbital half-occupied (ϕ_L and ϕ_R). For the infinite system, localized, singly occupied orbitals such as in Fig. 2 lead to very narrow energy bands. It is well known that such systems are not well described with normal band theory, and an empirical modification (the Hubbard Hamiltonian) is used to obtain UHF-like wavefunctions. For the GVB method, an N-body approach to band calculations is required.

Valence bond band structure—localized versus delocalized states. Consider the Cu_3O_{10} cluster modeling the chains of $Y_1Ba_2Cu_3O_7$. Ionizing this cluster leads to two equivalent localized wavefunctions, Ψ_L and Ψ_R,

Ψ_L O—Cu—O—Cu—O—Cu—O **III**

Ψ_R O—Cu—O—Cu—O—Cu—O **IV**

where structure IV is shown in Fig. 2, c and d. The wavefunction is localized because the shape of a doubly occupied orbital needs to be more expanded (electron repulsion) than that of a singly occupied orbital and because in Ψ_L the other bonds polarize to stabilize a charge on the left, whereas in Ψ_R they polarize to stabilize a charge on the right. These two wavefunctions overlap with a sizeable matrix element between them,

$$\sigma_{LR} = \langle\Psi_L|\Psi_R\rangle = -0.1412 \quad (12)$$

$$H_{LR} = \langle\Psi_L|H|\Psi_R\rangle \quad (13)$$

In the resonating-GVB description of these states, the total wavefunction is written

$$\Psi_u = (\Psi_L + \Psi_R)/\sqrt{1 + S} \quad (14)$$

$$\Psi_g = (\Psi_L + \Psi_R)/\sqrt{1 - S} \quad (15)$$

We calculate these states using the R-GVB program (*13*), which allows every orbital of Ψ_L to overlap every orbital of Ψ_R. This many-electron resonating generalized valence bond (R-GVB) hole description of the ion states is equivalent to a polaron-hopping description in which the hole is completely dressed with polarization for each site. The R-GVB states in structures III and IV lead to a resonance stabilization of 0.33 eV for Ψ_g and destabilization of 0.43 eV for Ψ_u. This leads to a one-dimensional band with bandwidth = 1.62 eV. As a result, holes in the oxygen $2p\pi$ bonds of the Cu-O chains or Cu-O sheets lead to high mobility charge carriers for electrical conductivity.

N-Electron band theory. We report here a band calculations based on such localized N-electron valence bond wavefunctions rather than the traditional one-electron molecular orbitals (MO) or band orbitals. The N-electron band states Ψ_k are described as a linear combination of localized N-electron valence bond wavefunctions,

$$\Psi_k = C_{1k}\Phi_1 + C_{2k}\Phi_2 + \cdots = \sum_i C_{ik}\Phi_i \quad (16)$$

where each term Φ_i is an N-electron wavefunction describing a fully polarized description of the hole on a particular site i. Here the coefficients are calculated by solving

$$\sum_j H_{ij}C_{jk} = \sum_j S_{ij}C_{jk}\lambda_k \quad (17)$$

where the H_{ij} are the N-electron matrix elements (*13*) between oxidized sites i and j and S_{ij} is the N-electron overlap for sites i and j, as in Eqs. 12 and 13. This process is analogous to a tight-binding band calculation except that the matrix elements arise from N-electron valence bond calculations, $\langle\Psi_L|H|\Psi_R\rangle$, where H is the total N-electron Hamiltonian rather than from one-electron matrix elements, $\langle\Phi_L|H^{HF}|\Phi_R\rangle$, where H^{HF} is an effective one-particle Hamiltonian. A wavepacket constructed from the band states, Ψ_k in Eq. 16, describes the motion of a fully dressed polaron.

This contrasts with the tight-binding MO description where the coefficients describe a particular one-electron band orbital

$$\psi_k = C_{1k}\phi_1 + C_{2k}\phi_2 + \cdots = \sum_i C_{ik}\phi_i \quad (18)$$

(in terms of localized atomic-like orbitals ϕ_i), which is occupied along with the other band orbitals to construct a many-electron wavefunction,

$$\Psi^{MO} = \mathcal{A}[(\psi_1)^2(\psi_2)^2\cdots] \quad (19)$$

For the CuO sheets of $La_2Cu_1O_4$, we calculated the valence band shown in Fig. 3. This represents the Bloch N-electron states for a hole moving in the CuO sheets. The most stable ion state is at the M point (highest state in a standard band calculation). The least stable state is the X point. The total bandwidth is 1.38 eV.

For $La_{2-x}Sr_xCu_1O_4$, the maximum transition temperature T_c occurs for $x = 0.15$. Assuming all these holes go into the oxygen $2p\pi$ band leads to the Fermi energy at 0.16 eV below the top of the band, as indicated in Fig. 3. The density of states at the Fermi

energy is $N(0) = 1.14$ eV^{-1} per copper atom. For $Y_1Ba_2Cu_3O_7$ the band arising from the chains would be half full if all holes were in this band. This would lead to $N(0) = 0.21$ eV^{-1} per chain copper. These results are used in the accompanying report (*12*) to derive the T_c for superconductivity in cuprates.

The Hubbard model. As pointed out above, standard HF methods lead to a very bad description of systems such as these Cu^{II} systems having weakly overlapping orbitals. The result is a strong mixture of the singly occupied $d\sigma$ orbitals ($d_{y^2-z^2}$ pointing from Cu to O) with oxygen $p\sigma$ orbitals, leading to a partially filled band of mixed copper $d\sigma$ and oxygen $p\sigma$ character. With GVB, the electron correlation effects lead to singly occupied $d_{y^2-z^2}$ orbitals on each copper. In terms of band concepts this GVB description corresponds to half occupation of every orbital of the band constructed from $d_{y^2-z^2}$ on each center, whereas HF would start with half occupation of the band. The Hubbard approximation (*14*) to UHF builds in a similar improvement upon standard HF band theory by introducing a repulsive one-center term to split the HF band into up-spin and down-spin bands on separate sublattices (leading to spin waves). The GVB approach treats the electron correlation problem rigorously, leading to pure spin states. However, this leads to the complication that the band states must be calculated in terms of N-body wavefunctions (as presented above) rather than the usual one-particle orbitals.

Several standard one-electron band calculations (based on local density functionals) have been reported (*15*) on $La_2Cu_1O_4$. These band calculations suggest an overall population of d^9 on each copper, in agreement with the GVB results but, as expected, they all involve strong mixing of copper $d\sigma$ and oxygen $p\sigma$ character, leading to a partially occupied band of σ character. A properly parameterized Hubbard Hamiltonian might mimic the GVB results (with the copper $d\sigma$ orbitals forming a narrow band and a highest band that is oxygen $p\pi$–like).

REFERENCES AND NOTES

1. J. G. Bednorz and K. A. Müller, *Z. Phys. B* **64**, 189 (1986); J. M. Tarascon, L. H. Greene, W. R. McKinnon, G. W. Hull, T. H. Geballe, *Science* **235**, 1373 (1987).
2. M. K. Wu, *et al.*, *Phys. Rev. Lett.* **58**, 908 (1987).
3. W. J. Hunt, P. J. Hay, W. A. Goddard III, *J. Chem. Phys.* **57**, 738 (1972); W. A. Goddard III and T. C. McGill, *J. Vac. Sci. Technol.* **16**, 1308 (1979).
4. The geometries of these clusters are based on neutron diffraction data (*5*). The Dunning (9*s*5*p*/3*s*2*p*) double zeta contraction (*6*) of the Huzinaga Gaussian basis set is used for the oxygen atoms. The Los Alamos core effective potential (*7*) is used to replace the 18 core electrons of the copper atom. This leads to a (3*s*,2*p*,2*d*) Gaussian basis for the 11 valence electrons of the copper atom.
5. P. Day *et al.*, *J. Phys. C* **20**, L429 (1987); W. I. F. David *et al.*, *Nature (London)* **327**, 310 (1987).
6. T. H. Dunning, Jr., and P. J. Hay, in *Modern Theoretical Chemistry* (Plenum, New York, 1977), vol. 3, p. 1.
7. P. J. Hay and W. R. Wadt, *J. Chem. Phys.* **82**, 270 (1985).
8. N. D. Mermin and H. Wagner, *Phys. Rev. Lett.* **17**, 1133 (1966).
9. D. Vaknin *et al.*, *ibid.* **58**, 2802 (1987).
10. J. B. Torrance, Y. Tokura, A. Nazzal, S. S. P. Parkin, in preparation; Y. Tokura, J. B. Torrance, A. I. Nazzal, T. C. Huang, C. Ortiz, in preparation.
11. Superexchange involves mixing of charge transfer states (structures VI and VII) into the dominant wavefunction (top structure V diagram). This charge transfer is much less favorable if the oxygen is made more positive.

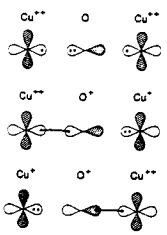

V VI VII

12. G. Chen and W. A. Goddard III, *Science* **239**, 899 (1988).
13. A. F. Voter and W. A. Goddard III, *J. Am. Chem. Soc.* **108**, 2830 (1986). The matrix elements as defined in Eq. 13 would depend on cluster size. We use instead

$$\bar{H}_{ij} = E^{N-1}S_{ij}^{N-1} - H_{ij}^{N-1} \quad (20)$$

where E^{N-1} is the energy of the cluster with one hole, and H_{ij}^{N-1} and S_{ij}^{N-1} are for systems with the hole localized on sites i and j, respectively. The sign chosen in $\bar{H}_{ij}$ is so that $E_k = -IP_k$, where IP_k is the ionization potential out of Bloch state k, leading to band diagrams analogous to one-electron band diagrams.
14. J. Hubbard, *Proc. R. Soc. London Ser. A.* **281**, 401 (1964).
15. L. F. Mattheiss, *Phys. Rev. Lett.* **58**, 1028 (1987); K. Takegahara, H. Harima, A. Yanase, *Jpn. J. Appl. Phys.* **26**, L352 (1987); T. Oguchi, *ibid.*, p. L417.

16. We thank the Office of Naval Research and the donors of the Petroleum Research Fund (administered by the American Chemical Society) for partial support of this research. We thank C. M. Kao and G. Chen for assistance and useful discussions. The GVB and R-GVB calculations were carried out on the Alliant FX8/8 and DEC VAX 8650 computers in the Caltech Materials Simulation Facility [funded by the National Science Foundation–Materials Research Groups (grant DMR-84-21119); the Office of Naval Research/Defense Advanced Research Projects Agency (contract N00014-86-K-0735); the Department of Energy–Energy Conversion and Utilization Technology (JPL code 49-242-E0403-0-3550), the National Science Foundation–Chemistry (grant CHE-8318041), and the Office of Naval Research (contract N00014-84-K-0637)].

7 December 1987; accepted 20 January 1988